

AB INITIO MOLECULAR DYNAMICS: APPLICATIONS TO DEFECTIVE SILICON
NANOCRYSTALS AND DEVELOPMENTS TOWARD DENSE MANIFOLD SYSTEMS

By

Wei-Tao Peng

A DISSERTATION

Submitted to
Michigan State University
in partial fulfillment of the requirements
for the degree of

Chemistry – Doctor of Philosophy

2019

ABSTRACT

AB INITIO MOLECULAR DYNAMICS: APPLICATIONS TO DEFECTIVE SILICON NANOCRYSTALS AND DEVELOPMENTS TOWARD DENSE MANIFOLD SYSTEMS

By

Wei-Tao Peng

Ab initio molecular dynamics (AIMD) methods consider the nuclear motions under the potential generated by electronic wavefunctions which are determined from ab initio quantum mechanical calculations on-the-fly. AIMD methods allow researchers to investigate chemical processes without prior knowledge or assumptions about the shape of the potential energy surface (PES). In this thesis, we applied AIMD methods to study silicon nanocrystals with dangling bond defects (DB-SiNCs). DB defects on SiNCs have been known as nonradiative (NR) decay centers. However, the atomistic mechanism for the decay process is unclear. Previously, researchers considered a pyramidalization mode surrounding the DB site involved in the process. Based on our AIMD calculations on the first excited state and the static analysis of the PESs of SiNC systems, we discovered that asymmetrical Si-Si bond stretching modes surrounding DB sites are important, in addition to pyramidalization. Most importantly, we found a low-lying defect-induced conical intersection (DICI) in the neutral DB system. The minimum energy conical intersection (MECI) is estimated to be 1.74 eV above the ground state minimum energy geometry by application of multi-state complete active space second-order perturbation theory (MS-CASPT2) to a small cluster model system. In addition, the roles of charged DBs on NR decay process are investigated. We found DICI for both positively and negatively charged DB systems. The MECI energies are 2.10 eV and 2.65 eV respectively. The rationalization of the existence of conical intersections and detailed dynamics after excitation of these systems are discussed in the thesis. Additionally, to study the possible defect-defect interactions during the

NR recombination process, we considered slab models with two DB defects at short ($\sim 4 \text{ \AA}$) and long ($\sim 10 \text{ \AA}$) separations. According to our simulations, the NR recombination process is localized on a single DB site, regardless the defect-defect distances. However, energy transfer between defect sites with short separations is possible.

For the defective SiNC systems, we demonstrated the power of the AIMD method to investigate the dynamics after excitations. However, the applications of AIMD to high-lying states are much more challenging, due to the dense manifold of states that cause immense computational effort. In the thesis, we developed several methods toward the application to such systems. First, we developed a time-dependent configuration interaction (TD-CI) method that can simulate the electron dynamics under a strong field efficiently. The method is based on the direct scheme to form the σ vector, $\sigma = \mathbf{Hc}$, which can be accelerated by a graphical processing unit. A TD-CI calculation with 853776 determinants requires only 20.1 hours to propagate to 100 fs with 1 attosecond (10^{-18} second) time steps. On the other hand, when the field is strong enough, the electrons can be driven to the boundary of the basis set, which would cause unphysical effects such as reflection. To account for this, we developed an analytical expression for a molecule-centered complex absorbing potential which can be evaluated efficiently to remove the unwanted effects. Finally, for the nuclear dynamics, we developed an Ehrenfest dynamics method based on the TD-CI wavefunction. In this approach, the nuclear motions are propagated under the averaged potential generated by TD-CI wave function, thus the approach is promising for application to systems with dense manifolds of states.

ACKNOWLEDGEMENTS

I would like to thank my advisor, Benjamin G. Levine, for his guidance, patience, and assistance throughout my PhD studies. I am grateful to him for offering the opportunity to join his scientific group. Besides the research, he taught me how to communicate effectively to other scientists. I am also inspired by his enthusiasm in science. I could not have imagined having a better advisor and mentor.

I would also like to thank my committee members, Katherine C. Hunt, Marcos Dantus, and Piotr Piecuch, for their invaluable comments.

I am thankful to my fellow labmates: Yinan, Garrett, Scott, Dmitry, Mike, Dylan, Andy, and Fangchun, for all the discussions, collaborations, and advices.

I greatly appreciate the continued support and warm love from my beloved family and friends. This dissertation would not have been possible without them.

TABLE OF CONTENTS

LIST OF TABLES	vii
LIST OF FIGURES	ix
CHAPTER 1 INTRODUCTION	1
1.1 Description of Chapters	3
REFERENCES	5
CHAPTER 2 DYNAMICS OF RECOMBINATION VIA CONICAL INTERSECTION IN A SEMICONDUCTOR NANOCRYSTAL	8
2.1 Introduction	8
2.2 Results and Discussion	10
2.3 Conclusions	19
APPENDIX	20
REFERENCES	44
CHAPTER 3 AB INITIO MOLECULAR DYNAMICS STUDY OF THE INTERACTION BETWEEN DEFECTS DURING NONRADIATIVE RECOMBINATION	52
3.1 Introduction	52
3.2 Method	54
3.3 Results and Discussions	58
3.4 Conclusions	68
APPENDIX	70
REFERENCES	91
CHAPTER 4 NONADIABATIC DYNAMICS STUDY OF SILICON DANGLING BOND DEFECTS AT DIFFERENT CHARGED STATES	97
4.1 Introduction	97
4.2 Method	99
4.3 Results and Discussion	101
4.3.1 Dynamical Simulations of the Neutral Si-DB	101
4.3.2 Static Analysis of the Potential Energy Surface on the Neutral Si-DB	104
4.3.3 Dynamical Simulations of the Cationic Si-DB	107
4.3.4 Static Analysis of the Potential Energy Surface on the Cationic Si-DB	109
4.3.5 Dynamical Simulations of the Anionic Si-DB	112
4.3.6 Static Analysis of the Potential Energy Surface on the Anionic Si-DB	115
4.3.7 Discussion	118
4.4 Conclusions	120

APPENDIX	121
REFERENCES	135
CHAPTER 5 SIMULATING ELECTRON DYNAMICS OF COMPLEX MOLECULES WITH TIME-DEPENDENT COMPLETE ACTIVE SPACE CONFIGURATION INTERACTION	141
5.1 Introduction	141
5.2 Method	143
5.3 Results and Discussion	148
5.3.1 Absorption Spectrum	148
5.3.2 Rabi Oscillations	150
5.3.3 Control by Shaped Pulses	154
5.3.4 Performance	161
5.4 Conclusions	161
APPENDIX	163
REFERENCES	173
CHAPTER 6 ANALYTICAL EXPRESSION FOR A MOLECULE-CENTERED COMPLEX ABSORBING POTENTIAL USING GAUSSIAN BASIS SETS	181
6.1 Introduction	181
6.2 Method	183
REFERENCES	188
CHAPTER 7 THE EHRENFEST MOLECULAR DYNAMICS IN CONJUNCTION WITH TIME-DEPENDENT CONFIGURATION INTERACTION ELECTRONIC WAVEFUNCTIONS	194
7.1 Introduction	194
7.2 Method	195
REFERENCES	199

LIST OF TABLES

Table 2.1.	The Si-Si bond lengths (\AA), Si-Si-Si bond angles (θ as indicated in Figure 1a; in degrees), and D_1 energies of differently sized silicon clusters at the Franck-Condon point (FC) and MECI. All energies are relative to the D_0 minimum energy. Energies are computed at the CASCI level of theory as described in the APPENDIX. When available, CASPT2 energies at CASCI geometries are presented in parenthesis.	12
Table 3.1.	Relevant geometric parameters surrounding the DB defect sites at several important geometries in each model. Parameters include Si-Si bond lengths ($R_{\text{Si-Si}}$ in \AA) and Si-Si-Si bond angles (θ in degrees) as illustrated in Figure 3.1. Si-Si bond lengths greater than 2.5 \AA are bolded. Result for the 1DB system ($\text{Si}_{72}\text{H}_{63}$) from reference 36 is also listed for comparison.	58
Table 3.2.	The vertical excitation energies (E_{ex} in eV) and excitation characters at the Franck-Condon point of the NN and TNN systems.	60
Table 3.3.	The energies (in eV) of the MECIs of the NN, TNN, and 1DB systems. Results for 1DB are drawn from reference 36. As the 1DB system has only one dangling bond, only one energy is listed. All energies are relative to ground state energy of the T_0 -optimized structure.	64
Table B1.	The minimum energy geometries of NN and TNN systems at the singlet ground state. The relative energies (R.E.; unit meV) are the energies relative to corresponding triplet ground state.	70
Table 4.1.	Optimized neutral DB cluster model FC point, D_1/D_0 MECI, and $D_{1\text{min}}$ energies (eV).	105
Table 4.2.	Optimized positive DB cluster model FC point, S_1/S_0 MECI, and $S_{1\text{min}}$ energies (eV).	110
Table 4.3.	Optimized negative DB cluster model FC point, S_1/S_0 MECI, and $S_{1\text{min}}$ energies (eV).	115
Table C1.	The excitation energies at Franck-Condon point (FC). The FC geometries are optimized with the B3LYP/6-31G(d,p) method. The IP-EOM-CCSD(2h,1p)/6-31G(d,p), EOM-CCSD/6-31G(d,p) and EOM-CCSD/6-31+G(d,p) energies are calculated for the neutral, cationic and anionic DB systems respectively.	121
Table C2.	The optimized cluster model FC, MECI, and $D_{1\text{min}}$ energies for the neutral DB system.	121

Table C3.	The optimized cluster model FC, MECI, and S ₁ min energies for the positive DB system.	122
Table C4.	The optimized cluster model FC, MECI, and S ₁ min energies for the negative DB system.	123
Table 5.1.	Comparison of the excitation energies (eV) of decacene calculated via TD-CISNO-CASCI and TI-CISNO-CASCI. Only the states with non-zero transition dipole moment in the polarization direction (μ_y ; atomic units) are listed. Absolute errors are reported in eV.	149
Table 5.2.	The error in the population (Pop. Err.), error in the Rabi oscillation period (ΔT) relative to the exact value (21.506 fs), and norm of the wave function after 100 fs of propagation for simulations of ethylene in a resonant CW field as a function of the integration time step. Simulation details are presented in the text.	153
Table 5.3.	The wall time to solution for several of the calculations. The propagation time is 100 femtosecond and the time step is 1 as for all simulations shown.	160
Table D1.	Comparison of the wave function norm at the end of 100 fs simulations of decacene after excitation by a δ -function pulse calculated using different time steps. Calculations are performed at the TD-CISNO-CASCI /6-31G(d) basis set with a (10,10) active space.	163
Table D2.	The first excitation energies (in eV) of decacene obtained with TI-CISNO-CASCI and TD-CISNO-CASCI methods with 6-31G(d) basis set and a (2,2) active space. TD-CISNO-CASCI calculations were performed with a series of time steps from 1 to 500 as. The norm at the end of the 100 fs simulations is also presented.	163

LIST OF FIGURES

- Figure 2.1. The P_b -containing silicon clusters studied in this work. (a) $Si_{10}H_{15}$ (sila-adamantane cluster), (b) $Si_{22}H_{27}$, (c) $Si_{26}H_{31}$, (d) $Si_{47}H_{49}$ (1.3-nm SiNC), and (e) $Si_{72}H_{63}$ (1.7-nm SiNC). One of the three symmetry-equivalent Si-Si bond lengths (R_{Si-Si}) and bond angles (θ) discussed herein are indicated in red in (a). The red arrows indicate the positions of dangling bond defects. 11
- Figure 2.2. Orbitals representative of the $D_0 \rightarrow D_1$ (${}^2A_1 \rightarrow {}^2E$) transition of the $Si_{72}H_{63}$ system. (a) The singly occupied molecular orbital (SOMO) is the nonbonding (n) orbital of the P_b center, and (b) the highest doubly occupied orbital (HDOMO) has Si-Si σ bonding character in the vicinity of the P_b defect (σ_{Si-Si}). Note that this HDOMO is approximately degenerate due to the local symmetry of the defect. We show only one of the two nearly degenerate orbitals. The red arrows indicate the locations of the P_b center. 13
- Figure 2.3. (a) The potential energies of the D_1 (red) and D_0 (black) electronic states as a function of time from the D_1 AIMD simulation of $Si_{72}H_{63}$. (b) The three Si-Si bond lengths (R_{Si-Si}) adjacent to the P_b defect as a function of time from the same AIMD calculation. (c) The three Si-Si-Si angles (θ , illustrated in Figure 1a) as a function of time from the same AIMD calculation. Each color represents one of the three symmetry equivalent bond lengths or angles in (b) and (c), respectively. 15
- Figure 2.4. (a) Schematic illustration of the dynamics of nonradiative recombination of an excitation at a P_b center. The PESs are plotted as a function of an asymmetric stretching coordinate about the P_b center (illustrated along the x-axis with the dangling bond site represented by a filled circle and the three adjacent silicon atoms represented by open circles). Insets show the orbital occupations of D_0 and D_1 and relative orbital energies at the FC point (left) and MECI (right). The n and σ_{Si-Si} orbitals of the smallest (sila-adamantane) system are shown on the bottom left. 16
- Figure A1. The potential energies of the first excited (red line) and ground states (black line) change with the time following the first excited state trajectory from an AIMD simulation where the force comes from the first excited state in $Si_{10}H_{15}$. 20
- Figure A2. The potential energies of the first excited (red line) and ground states (black line) change with the time following the first excited state trajectory from an AIMD simulation where the force comes from the first excited state in $Si_{22}H_{27}$. 21

Figure A3.	The potential energies of the first excited (red line) and ground states (black line) change with the time following the first excited state trajectory from an AIMD simulation where the force comes from the first excited state in $\text{Si}_{26}\text{H}_{31}$.	22
Figure A4.	The potential energies of the first excited (red line) and ground states (black line) change with the time following the first excited state trajectory from an AIMD simulation where the force comes from the first excited state in $\text{Si}_{47}\text{H}_{49}$.	23
Figure A5.	The three Si-Si bond lengths ($R_{\text{Si-Si}}$) of $\text{Si}_{10}\text{H}_{15}$ change with time from the AIMD calculation. Each color represents one Si-Si bond length.	24
Figure A6.	The three Si-Si bond lengths ($R_{\text{Si-Si}}$) of $\text{Si}_{22}\text{H}_{27}$ change with time from the AIMD calculation. Each color represents one Si-Si bond length.	25
Figure A7.	The three Si-Si bond lengths ($R_{\text{Si-Si}}$) of $\text{Si}_{26}\text{H}_{31}$ change with time from the AIMD calculation. Each color represents one Si-Si bond length.	26
Figure A8.	The three Si-Si bond lengths ($R_{\text{Si-Si}}$) of $\text{Si}_{47}\text{H}_{49}$ change with time from the AIMD calculation. Each color represents one Si-Si bond length.	27
Figure 3.1.	The $\text{Si}_{70}\text{H}_{68}$ slab model. The Si and H atoms are shown in blue and white, respectively. The left and right DB sites are labeled L and R, respectively. Site R is the same for both models. The nearest neighbor (NN), and third nearest neighbor (TNN) models are created by removing the capping H atoms from the yellow circled positions labeled L(NN) and L(TNN), respectively. The right panel illustrates the geometric parameters, θ and $R_{\text{Si-Si}}$, reported in Table 3.1 and discussed in the text.	55
Figure 3.2.	The singly occupied natural orbitals of the triplet ground state (T_0) of the TNN system. These are both n_{DB} orbitals, as described in the text.	59
Figure 3.3.	Natural orbitals with occupation numbers 1.00 (top) and 2.00 (bottom) of state T_1 at the NN FC geometry. The top and bottom orbitals are examples of $\sigma_{\text{Si-Si}}$ and n_{DB} orbitals, respectively, as described in the text.	61
Figure 3.4.	A simplified picture of the orbitals arrangement in the systems studied here. All excitations investigated in this work involve promotion of an electron from a $\sigma_{\text{Si-Si}}$ orbital to a n_{DB} orbital. In the low-lying excited states (T_1 - T_4) the majority of the excitation character is local to a single DB site. The dashed arrow indicates a possible charge-transfer excitation between two sites (e.g. T_5).	62

Figure 3.5.	Top panel: The T_1 - T_0 energy gap as a function of time for the NN system. Bottom panel: the T_1 - T_0 energy gap as a function of time for the TNN system. The light grey curves depict the individual trajectories and the red curves depict the average gap over 20 trajectories for each system.	63
Figure 3.6.	The MECI(L) geometries and natural orbitals for the NN and TNN systems. (a) The top view of the MECI(L) in NN. (b) The side view of MECI(L) in NN. (c) A natural orbital with occupation number 1.50 (n_{DB}) for MECI(L) in NN. (d) A natural orbital with occupation number 1.50 (σ_{Si-Si}) for MECI(L) in NN. (e) The top view of the MECI(L) in TNN. (f) The side view of MECI(L) in TNN. (g) A natural orbital with occupation number 1.50 (n_{DB}) for MECI(L) in TNN. (h) A natural orbital with occupation number 1.50 (σ_{Si-Si}) for MECI(L) in TNN. Panels c and d are adapted from reference 40 with permission from the PCCP Owner Societies.	65
Figure 3.7.	Top panel: the averaged Si-Si bond lengths around the DB sites for the NN system. Bottom panel: the averaged Si-Si bond lengths around the DB sites for the TNN system. The bond lengths are sorted as described in the main text. On-site (more distorted) and off-site (less distorted) bonds are shown on the left and right, respectively. Longest, middle, and shortest lengths are shown by yellow, orange, and blue lines, respectively.	66
Figure B1.	The ground state natural orbitals with occupation number 1.00 in the NN system.	71
Figure B2.	The T_1 state natural orbitals with occupation number 1.00 and sigma bonding character in the TNN system.	72
Figure B3.	The T_1 state natural orbitals with occupation number 2.00 and (majority) DB nonbonding character in the TNN system.	72
Figure B4.	The T_5 state (CT state) natural orbitals with occupation number 1.06 and sigma bonding character in the NN system.	73
Figure B5.	The T_5 state (CT state) natural orbitals with occupation number 1.94 and DB nonbonding character in the NN system.	73
Figure B6.	The T_5 state (CT state) natural orbitals with occupation number 1.00 and sigma bonding character in the TNN system.	74
Figure B7.	The T_5 state (CT state) natural orbitals with occupation number 2.00 and DB nonbonding character in the TNN system.	74

- Figure 4.1. (a) The Si_8H_{13} cluster model studied in this work. One of the three Si-Si bond lengths ($R_{\text{Si-Si}}$) and Si-Si-Si bond angles (θ) surrounding DB site are indicated in red. (b) The top view of the one nonbonding and two $\sigma_{\text{Si-Si}}$ bonding orbitals at the FC point in the neutral state system. (c) The side view of the diffused LUMO and nonbonding HOMO at the FC point in the negatively charged DB system. 102
- Figure 4.2. The time evolutions of the D_1 - D_0 energy gap (grey lines: 20 trajectories; red line: average) for the neutral DB system. 102
- Figure 4.3. The time evolutions of the population of the first excited and ground states for the neutral DB system. Cyan lines: excited state populations of 20 trajectories; magenta lines: ground state populations of 20 trajectories; thick blue line: averaged excited state population; thick red line: averaged ground state population. 103
- Figure 4.4. The time evolutions of (a) the averaged Si-Si bond lengths surrounding DB ($R_{\text{Si-Si}}$) and (b) the averaged Si-Si-Si bond angles surrounding DB (θ) for the neutral DB system. The bond lengths (bond angles) are sorted as the longest (largest), the middle, and the shortest (smallest) $R_{\text{Si-Si}}$ distances (θ degree) for each trajectory at each time step, then averaged, and are shown by yellow, orange and blue lines respectively. 104
- Figure 4.5. (a) The D_1/D_0 MECI geometry of the neutral DB cluster optimized by SA-CASSCF. (b) The D_1/D_0 MECI geometry of the neutral DB cluster optimized by MS-CASPT2. (c) and (d) Top view and side view of D_0 - D_1 state-averaged natural orbitals with occupation numbers 1.50 for the neutral DB at the MECI geometry. 106
- Figure 4.6. The time evolutions of (a) the averaged Si-Si bond lengths surrounding DB ($R_{\text{Si-Si}}$) and (b) the averaged Si-Si-Si bond angles surrounding DB (θ) for the positive DB system. The bond lengths (bond angles) are sorted as the longest (largest), the middle, and the shortest (smallest) $R_{\text{Si-Si}}$ distances (θ degree) for each trajectory at each time step, then averaged, and are shown by yellow, orange and blue lines respectively. 108
- Figure 4.7. The time evolutions of the S_1 - S_0 energy gap (grey lines: 20 trajectories; red line: average) for the positive DB system. 108
- Figure 4.8. The time evolutions of the population of the first excited and ground states for the positive DB system. Cyan lines: excited state populations of 20 trajectories; magenta lines: ground state populations of 20 trajectories; thick blue line: averaged excited state population; thick red line: averaged ground state population. 109

- Figure 4.9. (a) The S_1/S_0 MECI geometry of the positive DB cluster optimized by SA-CASSCF. (b) The S_1/S_0 MECI geometry of the positive DB cluster optimized by MS-CASPT2. (c) and (d) Top view and side view of S_0 - S_1 state-averaged natural orbitals with fractional occupation numbers 1.48 and 0.53 for the positive DB at the MECI geometry. 112
- Figure 4.10. The time evolutions of (a) the averaged Si-Si bond lengths surrounding DB (R_{Si-Si}) and (b) the averaged Si-Si-Si bond angles surrounding DB (θ) for the negative DB system. The bond lengths (bond angles) are sorted as the longest (largest), the middle, and the shortest (smallest) R_{Si-Si} distances (θ degree) for each trajectory at each time step, then averaged, and are shown by yellow, orange and blue lines respectively. 113
- Figure 4.11. The time evolutions of the S_1 - S_0 energy gap (grey lines: 20 trajectories; red line: average) for the negative DB system. 114
- Figure 4.12. The time evolutions of the population of the first excited and ground states for the negative DB system. Cyan lines: excited state populations of 20 trajectories; magenta lines: ground state populations of 20 trajectories; thick blue line: averaged excited state population; thick red line: averaged ground state population. 114
- Figure 4.13. (a) The S_1/S_0 MECI geometry of the negative DB cluster optimized by SA-CASSCF. (b) The S_1/S_0 MECI geometry of the negative DB cluster optimized by MS-CASPT2. (c) and (d) Top view and side view of S_0 - S_1 state-averaged natural orbitals with fractional occupation numbers 1.50 and 0.60 for the negative DB at the MECI geometry. 116
- Figure 4.14. The plot of three Si-Si bond lengths surrounding DB site changes with time for (a) the simulation where the one Si-Si bond stretch occurred at 200 fs, (b) the simulation where the one Si-Si bond stretch occurred at 900 fs. 118
- Figure C1. Optimized cluster model FC, MECI and S_1 min energies. The geometry optimizations were performed at B3LYP (dotted lines at FC point), SA-CASSCF (dash lines at MECI, S_1 min and D_1 min) and MS-CASPT2 (solid lines at MECI, S_1 min and D_1 min) levels of theory. Energy calculations were performed at SA-CASSCF (blue lines), MS-CASPT2 (red lines) and MRCI (yellow lines) levels of theory. (a) The neutral DB system. (b) The positive DB system. (c) The negative DB system. 124
- Figure C2. The orbitals of positively charged DB system at the ground state minimum energy geometry. 124
- Figure C3. The state-averaged natural orbitals with fractional occupation numbers for a negative DB at the S_1 min geometry. 125

Figure 5.1.	Molecule of decacene. Dark gray: carbons. Light gray: hydrogens.	148
Figure 5.2.	The absorption spectrum of decacene computed at the TD-CISNO-CASCI level as described in the text.	149
Figure 5.3.	The populations of the S_0 and S_1 states as a function of time from calculations of the dynamics of ethylene in a resonant CW field, as described in the text. Calculations are performed with time steps of 1 as (solid) and b) 10 as (dashed).	152
Figure 5.4.	The final state populations obtained from 100 fs simulations of decacene (TD-CISNO-CASCI(10/10)/6-31G(d)) in a series of laser pulses with chirp ranging from $\beta = -0.342 \text{ fs}^{-2}$ to $\beta = 0.342 \text{ fs}^{-2}$. All pulses have a FWHM of 10 fs and a maximum intensity of $3 \times 10^{12} \text{ W/cm}^2$. The populations of bright and dark states up to S_8 are shown with solid lines and dashed lines, respectively. The populations in all states above S_8 are summed into a single (purple) line. Populations of states with negligible population in all simulations (S_3 - S_5) are not shown. A Jablonski diagram on the right shows the energies of the populated states up to S_8 .	154
Figure 5.5.	The electronic state populations as a function of time for decacene (TD-CISNO-CASCI(10,10)/6-31G(d)) in 10 femtosecond (FWHM) TL pulses with maximum intensities of $1 \times 10^{12} \text{ W/cm}^2$ (middle panel) or $3 \times 10^{12} \text{ W/cm}^2$ (bottom panel). The electric field as a function of time is shown in the top panel (arbitrary units). This pulse is resonant with the $S_0 \rightarrow S_2$ transition. Only states up to S_8 that contain non-negligible population at the end of the simulations are shown. The sum of all population in states higher than S_8 is represented by a dotted purple line.	156
Figure 5.6.	The electronic state populations as a function of time for decacene (TD-CISNO-CASCI(10,10)/6-31G(d)) in 10 fs (FWHM) chirped pulses with $\beta = 0.256 \text{ fs}^{-2}$ and an intensity of $3 \times 10^{12} \text{ W/cm}^2$ are shown in the bottom panel. The electric field as a function of time is illustrated in the top panel. Only populations of states up to S_8 that contain non-negligible population at the end of the simulation are shown. The sum of all population in states higher than S_8 is represented by a dotted purple line.	157
Figure 5.7.	The electronic state populations as a function of time for decacene (TD-CISNO-CASCI(10,10)/6-31G(d)) in 10 fs (FWHM) chirped pulses with $\beta = -0.256 \text{ fs}^{-2}$ and an intensity of $3 \times 10^{12} \text{ W/cm}^2$ are shown in the bottom panel. The electric field as a function of time is illustrated in the top panel. Only populations of states up to S_8 that contain non-negligible population at the end of the simulation are shown. States that are dark with respect to the electronic ground state (S_1 , S_6 , and S_7) are shown with dashed lines. The sum of all population in states higher than S_8 is represented by a dotted purple line.	158

- Figure D1. The electronic state populations as a function of time for decacene (TD-CISNO-CASCI(12,12)/6-31G(d)) in 10 fs (FWHM) chirped pulses with $\beta = -0.256 \text{ fs}^{-2}$ and an intensity of $3 \times 10^{12} \text{ W/cm}^2$. Only populations of states up to S_9 that contain non-negligible population at the end of the simulation are shown. Note that S_9 in this active space corresponds to S_8 in the (10,10) active space used throughout this work. States that are dark with respect to the electronic ground state (S_1 , S_6 , and S_7) are shown with dashed lines. The sum of all population in states higher than S_9 is represented by a dotted purple line. 164
- Figure D2. The final population on S_0 for a simulation of decacene with a (10,10) active space in a pulse with a chirp rate of -0.256 fs^{-2} as a function of time step. All other simulation parameters are as described in the main text. 165
- Figure D3. The final population on S_1 for a simulation of decacene with a (10,10) active space in a pulse with a chirp rate of -0.256 fs^{-2} as a function of time step. All other simulation parameters are as described in the main text. 166
- Figure D4. The final population on S_2 for a simulation of decacene with a (10,10) active space in a pulse with a chirp rate of -0.256 fs^{-2} as a function of time step. All other simulation parameters are as described in the main text. 167
- Figure D5. The final population on S_6 for a simulation of decacene with a (10,10) active space in a pulse with a chirp rate of -0.256 fs^{-2} as a function of time step. All other simulation parameters are as described in the main text. 168
- Figure D6. The final population on S_7 for a simulation of decacene with a (10,10) active space in a pulse with a chirp rate of -0.256 fs^{-2} as a function of time step. All other simulation parameters are as described in the main text. 169
- Figure D7. The final population on S_8 for a simulation of decacene with a (10,10) active space in a pulse with a chirp rate of -0.256 fs^{-2} as a function of time step. All other simulation parameters are as described in the main text. 170
- Figure 6.1. A representation of a molecule-centered complex absorbing potential developed in this work. The radius r_0 from the center of the molecule is defined for the boundary (shown in red). Beyond the boundary, a quadratic form of absorbing potential is applied (shown in the green line and in the inserted figure). Within the boundary, the potential is zero. 183

Figure 7.1. The schematic representation of the Ehrenfest dynamics algorithm. The steps (i)-(vi) mentioned in the text are labeled. The orange and blue arrows indicate the velocity-Verlet algorithm with time steps Δt for propagating momentum and position respectively. The smaller green arrows indicate the time steps $\Delta\tau$ for propagating electronic dynamics in TD-CI calculations. For the feedback between electronic and nuclear dynamics, the force calculation and orbital diabatizing (both indicated in red words) are performed.

198

CHAPTER 1 INTRODUCTION

Ab initio molecular dynamics (AIMD) methods simulate the nuclear motions on the potential energy surface (PES) generated by electronic wavefunctions which are determined from quantum mechanical calculations on-the-fly. Such methods are extensively applied to understand various chemical processes in which the transient elementary steps are difficult (if possible) to investigate experimentally. In the 1970s, Karplus, Warshel and Levitt applied a combined quantum mechanical and molecular mechanical (QM/MM) approach, where the chemically relevant part of the system is treated quantum mechanically, to study the PESs of a conjugated organic molecule¹ and an enzyme.² Ever since, the QM/MM method has gradually gained popularity for understanding complex chemical and enzymatic reactions, and eventually Karplus, Warshel and Levitt shared the Nobel Prize in Chemistry 2013. On the other hand, Car and Parrinello proposed a method that employed density functional theory for the electronic structure and an extended Lagrangian scheme for the dynamics in 1985,³ which later became the most prevalent AIMD approach and is known as the CP method. For considering systems where multiple electronic states are involved, many nonadiabatic ab initio molecular dynamics (NAMD) methods have been developed. The ab initio multiple spawning (AIMS) method,⁴⁻⁵ surface hopping method⁶ and Ehrenfest dynamics⁷⁻⁹ are three popular NAMD methods being used. Starting from pioneering work by the Prezhdo¹⁰ and Batista¹¹ groups, growing numbers of studies are now applying NAMD methods to elucidate photochemical and photophysical processes in materials science. In this thesis, we applied AIMD and NAMD methods to semiconductor nanocrystals, specifically silicon nanocrystals (SiNCs), to investigate the photophysics of such systems when defects are present.

Semiconductor nanocrystals are promising in many applications such as light emitting diodes,¹² light harvesting materials¹³ and bioimaging applications,¹⁴ just to name a few. As one may notice, many applications take advantage of nanocrystals' ability to efficiently absorb and emit light, as well as the tunability of their band gaps. These optical properties are achieved by quantum confinement effects, which occur when the size of a semiconductor nanocrystal is smaller than its exciton Bohr radius. As the semiconductor nanocrystals have high surface-to-volume ratio, another route to tune their optical properties is based on surface modification.

Hence, it is important to understand how the composition of the surface of semiconductor nanocrystals affects their properties. In addition to artificially modified surface composition, many types of defects may exist on the surface as well. These defects generally cause unwanted effects to the devices. Understanding the effects is essential for device optimization and rational design of high-performance materials.

It is well-known that surface defects play important roles in nonradiative recombination (NRR) processes which convert excitation energy to useless heat. However, it is generally difficult to identify a specific defect as an NRR center by experimental means, not to mention to investigate the microscopic mechanism of the NRR process. Toward this aim, theoretical calculations are performed to complement the experiments and to give guidance toward new discoveries. A semiconductor nanocrystal usually contains more than a hundred atoms. Thus, theoretical study of photophysics based on quantum mechanics often relies on single-particle pictures (e.g. orbitals or band structures), and nuclear motions are often simplified or totally ignored. However, electron-hole interactions and local distortions of nuclear structure can be crucial, due to the localized nature of the defect states. Following advances in computer hardware, AIMD methods are now feasible for unprecedentedly large systems. AIMD explores the potential energy surface (PES), including many particle interactions and the full set of nuclear degrees of freedom. In this thesis, we apply state-of-the-art AIMD methods to understand the photophysics of defective semiconductor nanocrystals. With the aid of graphic processing units (GPUs), we are able to run Born-Oppenheimer AIMD in conjunction with the complete active space configuration interaction (CASCI-AIMD) level of theory. The CASCI-AIMD method allows us to explore the excited state PES, and representative points on the PES such as excited state minimum energy geometries and conical intersections (CIs) may be discovered and can be further optimized. Defect-induced conical intersections (DICIs)¹⁵⁻¹⁶ provide efficient pathways for NRR processes and microscopic mechanisms can be deduced from CASCI-AIMD simulations. On the other hand, methods that are suitable for studying photophysics with population transfer between adiabatic electronic states require going beyond Born-Oppenheimer approximation, e.g. NAMD methods. Since the local nature of DICIs supports the use of small cluster models,¹⁷ we also apply the AIMS method to include

nonadiabatic effects in cluster models to analyze the NRR process involving several electronic states in semiconductor nanocrystals.

In contrast to NAMD methods such as AIMS that are applicable to low-lying excited states, the tools for high-lying excited states including Rydberg and continuum states are less mature, due to the dense manifold of adiabatic electronic states. Conventional NAMD is not applicable since the computational cost grows immensely with the number of states involved and the need for considering the numerous nonadiabatic couplings between states. New developments for NAMD methods are required for these systems. Toward this goal, first we developed real-time time-dependent configuration interaction (TD-CI) methods to account for the electronic dynamics under different external fields. Then, in conjunction with the TD-CI method for computing the electronic wavefunction, we developed an Ehrenfest approach for ab initio nonadiabatic molecular dynamics. This approach avoids explicitly calculating each state in a dense manifold situation, in which the electronic wavefunction is expressed as a time-dependent CI vector. On the other hand, since the electronic wavefunction in TD-CI is expanded with Gaussian basis sets which are finite in the space, we developed a complex absorption potential (CAP) to eliminate unphysical effects that may appear from the finite boundary when an intense field is applied. The other advantage of the CAP is that the ionization rate from the intense field-matter interaction can be derived without explicitly simulating the continuum states. We endeavor to develop efficient methods that allow us to consider large systems. The TD-CI method is based on a direct CI scheme that can be greatly accelerated using GPUs. Thus, the computational cost of the most time-consuming step of Ehrenfest dynamics (electronic dynamics) is much reduced. In addition, analytical force calculations in the molecular dynamics portion can be completed in GPUs as well.¹⁸⁻¹⁹ For the CAP, we have identified an analytical expression of the potential that can be evaluated efficiently.

1.1 Description of Chapters

Dangling bond defects in silicon nanocrystals (DB-SiNCs) have been known to work as nonradiative (NR) decay center. However, the microscopic detail is unclear. In Chapter 2, we studied the photophysics of DB-SiNCs via AIMD in conjunction with a complete active space

configuration interaction (CASCI) electronic structure method to elucidate the NR decay mechanism. The extension to a situation with multiple DB defects and the study of possible interactions between defects during the NR decay process is presented in Chapter 3. To include nonadiabatic effects and consider how the different charge states of the DB affect the photophysical properties of silicon clusters, we present an AIMS study of charged DB systems in Chapter 4.

Toward theoretical studies of the photophysics of systems with dense manifolds of electronic states, method developments are required. We first present the development of an efficient time-dependent complete active space configuration interaction (TD-CASCI) approach for describing electronic dynamics in Chapter 5. An Ehrenfest dynamics method based on the TD-CASCI wavefunction (TD-CASCI-Ehrenfest) is presented in Chapter 6. We note that the extension of Ehrenfest dynamics to time-dependent multireference configuration interaction singles (TD-MRCIS-Ehrenfest) is straightforward if the force generated by a TD-MRCIS wavefunction can be evaluated efficiently. To consider the electron dynamics under intense laser fields, a molecule-centered CAP is developed in conjunction with the TD-MRCIS method as presented in Chapter 7.

REFERENCES

REFERENCES

1. Warshel, A.; Karplus, M., Calculation of Ground and Excited-State Potential Surfaces of Conjugated Molecules .1. Formulation and Parametrization. *J Am Chem Soc* **1972**, *94*, 5612-5625.
2. Warshel, A.; Levitt, M., Theoretical Studies of Enzymic Reactions - Dielectric, Electrostatic and Steric Stabilization of Carbonium-Ion in Reaction of Lysozyme. *J Mol Biol* **1976**, *103*, 227-249.
3. Car, R.; Parrinello, M., Unified Approach for Molecular-Dynamics and Density-Functional Theory. *Phys Rev Lett* **1985**, *55*, 2471-2474.
4. Ben-Nun, M.; Quenneville, J.; Martinez, T. J., Ab initio multiple spawning: Photochemistry from first principles quantum molecular dynamics. *J Phys Chem A* **2000**, *104*, 5161-5175.
5. Levine, B. G.; Coe, J. D.; Virshup, A. M.; Martinez, T. J., Implementation of ab initio multiple spawning in the MOLPRO quantum chemistry package. *Chem Phys* **2008**, *347*, 3-16.
6. Tully, J. C., Molecular-Dynamics with Electronic-Transitions. *J Chem Phys* **1990**, *93*, 1061-1071.
7. Andrade, X.; Castro, A.; Zueco, D.; Alonso, J. L.; Echenique, P.; Falceto, F.; Rubio, A., Modified Ehrenfest Formalism for Efficient Large-Scale ab initio Molecular Dynamics. *J Chem Theory Comput* **2009**, *5*, 728-742.
8. Hack, M. D.; Truhlar, D. G., Nonadiabatic trajectories at an exhibition. *J Phys Chem A* **2000**, *104*, 7917-7926.
9. Li, X. S.; Tully, J. C.; Schlegel, H. B.; Frisch, M. J., Ab initio Ehrenfest dynamics. *J Chem Phys* **2005**, *123*, 084106.
10. Stier, W.; Prezhdo, O. V., Nonadiabatic molecular dynamics simulation of light-induced, electron transfer from an anchored molecular electron donor to a semiconductor acceptor. *J Phys Chem B* **2002**, *106*, 8047-8054.
11. Rego, L. G. C.; Batista, V. S., Quantum dynamics simulations of interfacial electron transfer in sensitized TiO₂ semiconductors. *J Am Chem Soc* **2003**, *125*, 7989-7997.
12. Dai, X. L.; Deng, Y. Z.; Peng, X. G.; Jin, Y. Z., Quantum-Dot Light-Emitting Diodes for Large-Area Displays: Towards the Dawn of Commercialization. *Adv Mater* **2017**, *29*, 1607022.

13. Kundu, S.; Patra, A., Nanoscale Strategies for Light Harvesting. *Chem Rev* **2017**, *117*, 712-757.
14. Jaque, D.; Richard, C.; Viana, B.; Soga, K.; Liu, X. G.; Sole, J. G., Inorganic nanoparticles for optical bioimaging. *Adv Opt Photonics* **2016**, *8*, 1-103.
15. Shu, Y. N.; Fales, B. S.; Levine, B. G., Defect-Induced Conical Intersections Promote Nonradiative Recombination. *Nano Lett* **2015**, *15*, 6247-6253.
16. Shu, Y. N.; Fales, B. S.; Peng, W. T.; Levine, B. G., Understanding Nonradiative Recombination through Defect-Induced Conical Intersections. *J Phys Chem Lett* **2017**, *8*, 4091-4099.
17. Levine, B. G.; Peng, W. T.; Esch, M. P., Locality of Conical Intersections in Semiconductor Nanomaterials. *Phys Chem Chem Phys* **2019**, *21*, 10870.
18. Hohenstein, E. G.; Bouduban, M. E. F.; Song, C. C.; Luehr, N.; Ufimtsev, I. S.; Martinez, T. J., Analytic first derivatives of floating occupation molecular orbital-complete active space configuration interaction on graphical processing units. *J Chem Phys* **2015**, *143*, 014111.
19. Fales, B. S.; Shu, Y. N.; Levine, B. G.; Hohenstein, E. G., Complete active space configuration interaction from state-averaged configuration interaction singles natural orbitals: Analytic first derivatives and derivative coupling vectors. *J Chem Phys* **2017**, *147*, 094104.

CHAPTER 2 DYNAMICS OF RECOMBINATION VIA CONICAL INTERSECTION IN A SEMICONDUCTOR NANOCRYSTAL

Reproduced with permission from “Dynamics of Recombination via Conical Intersection in a Semiconductor Nanocrystal”, W.-T. Peng, B. S. Fales, Y. Shu, B. G. Levine, *Chem. Sci.* 9, 681, 2018. Published by The Royal Society of Chemistry.

2.1 Introduction

Conical intersections (CIs) are points of degeneracy between the potential energy surfaces (PESs) of two or more adiabatic electronic states.¹⁻⁶ It is now well established that molecules that undergo efficient, ultrafast nonradiative transitions between electronic states of the same spin often do so by passing through CIs connecting those states. CIs can therefore be thought of in analogy to transition states; transition states are representative of paths that connect reactant and product wells on the same PES, whereas CIs are representative of nonradiative pathways connecting different electronic states. Theoretical predictions of CIs have provided insights into many important photochemical phenomena, e.g photoisomerization,^{4,7} photodissociation,⁸⁻¹⁰ vision,^{11,12} and nonradiative decay of nucleic acids.^{13,14} Identification of CIs is now a routine part of the computational molecular photochemistry toolbox.¹⁵ However, only recently and through the use of advanced computing technology¹⁶ has the role that CIs play in the nonradiative recombination of excitations in semiconductors come to light.^{17,18}

Here we investigate the role of CIs in the photophysics of silicon nanocrystals (SiNCs) with dangling bond defects. SiNCs and other low-dimensional silicon systems have received intense attention due to their unique photophysical properties. Unlike bulk silicon, which has an indirect band gap, low-dimensional silicon materials can efficiently emit visible light¹⁹ with a wavelength that can be tuned via quantum confinement²⁰⁻²³ or surface modification.²⁴⁻²⁷ This tunable emission enables their application in optoelectronic devices,²⁸⁻³⁰ biological imaging,³¹ and silicon lasers.^{32,33} Under ambient conditions, however, SiNCs are prone to oxidize quickly upon exposure to O₂ and/or H₂O. Oxidation generates various defects on the surfaces of SiNCs, including dangling bonds (DBs) and some silicon oxide species (Si-O-Si bridges and Si-OH).

Among them, silicon dangling bond defects have been studied extensively.³⁴⁻³⁸ In general, there are two common types of dangling bond defects: P_b centers, which are dangling bonds on a three-coordinated silicon atom on the surface, and D centers, which are DB defects located in amorphous silicon.³⁹ DB defects have been known to degrade the performance of silicon-based devices for both photovoltaic^{40, 41} and light emission^{38, 42-44} applications.

Thus, it is well-known that silicon DB defects are nonradiative centers in SiNCs. It is also established that electronic movement at DB centers is strongly coupled to local vibrational motions.^{45, 46} The widely accepted mechanism for recombination involves the sequential capture of electron and hole into the non-bonding orbital of the P_b center. Each change in the oxidation state of the P_b center is accompanied by nuclear relaxation along a bending mode that maintains local C_{3v} symmetry; reduction results in the defect silicon atom taking on a less planar structure (i.e. less sp²-like) while oxidation results in a more planar structure. The line of thinking that yields this mechanism arises from the assumption that each change in charge state is instantaneous, however. It neglects a) the fact that electrons and holes are strongly confined in SiNCs and therefore may interact strongly with one another and with the defect site before localization to the P_b center, and b) the interaction of electron and hole with the defect is not instantaneous and may, instead, involve complex electron-nuclear dynamics. The CI theory of recombination considers these interactions and dynamics explicitly, therefore it would be instructive to reinvestigate this recombination process from a CI point of view.

In this work we a) investigate whether nonradiative dynamics at P_b centers can be attributed to CIs between the ground and first excited electronic states, and b) inform our fundamental physical intuition for recombination processes in general by analysis of the CIs associated with the dangling bond defect. To these ends we will bring to bear novel ab initio molecular dynamics (AIMD) tools capable of modeling the dynamics of electronically excited SiNCs as they approach CIs with the ground electronic state. In AIMD simulations, the nuclear dynamics are computed on PESs that are solved on the fly via electronic structure calculations. AIMD has recently become a tool of choice for the theoretical study of the photophysics of nanomaterials when either direct knowledge of excited state dynamics or extensive thermodynamic sampling are required, shedding light on various aspects of the charge carrier

dynamics of SiNCs.⁴⁷⁻⁵⁶ The current study is the first to apply an AIMD approach based on a multireference description of the electronic structure to a true nanocrystal (diameter 1.7 nm). The advantage of multireference electronic structure approaches such as the complete active space configuration interaction (CASCI) approach used here^{57, 58} is that they can accurately describe the PES in the vicinity of CIs between the ground and first excited electronic states. This is in contrast to single reference electronic structure methods—such as time-dependent density functional theory—which cannot accurately describe the potential energy surface near CIs involving the ground electronic state.⁵⁹ The below study illustrates how applying CASCI-AIMD to model the dynamics of a semiconductor nanocluster from excitation to the neighborhood of a conical intersection can inform our fundamental understanding of nonradiative recombination.

2.2 Results and Discussion

The methodological and computational specifics of our CASCI-AIMD simulations are presented in APPENDIX, but here we outline our study. We have performed a single CASCI-AIMD simulation for each of a series of five silicon clusters. Each cluster has a single P_b defect on the surface. The clusters (pictured in Figure 2.1) range in size from a single sila-adamantine unit ($Si_{10}H_{15}$) to a 1.7-nm particle ($Si_{72}H_{63}$). All simulations were run on the first excited electronic PES starting from a structure in the Franck-Condon region. (Structures are presented in APPENDIX.) All surface silicon atoms aside from the defect site were capped with hydrogen atoms. We emphasize that these simulations are performed in the Born-Oppenheimer approximation.

Geometries of near-zero energy gap were drawn from the AIMD trajectories and the minimal energy CIs (MECIs; the local minima on the CI seam) were optimized. Because CASCI lacks dynamic electron correlation, complete active space second-order perturbation theory (CASPT2) calculations⁶⁰ were performed on the smallest cluster to estimate errors in our CASCI energies. Static CASCI and CASCI-AIMD calculations were performed in the TeraChem software package,^{16, 61-63} which enables these demanding calculations through the use of graphics processing units—high performance computer processors designed for graphical applications

such as video games. CASPT2 calculations were performed in MolPro,⁶⁴⁻⁶⁸ coupled cluster calculations were performed in GAMESS,⁶⁹⁻⁷¹ and conical intersection optimizations were performed with CIOpt.⁷² Through this work we prefer adiabatic state labels: D_0 and D_1 to indicate the ground and first excited spin doublet electronic states of the clusters, respectively. However, when useful and appropriate we also include term symbols 2A_1 and 2E to reflect the approximate symmetry of the states with respect to the local C_{3v} symmetry of the defect site.

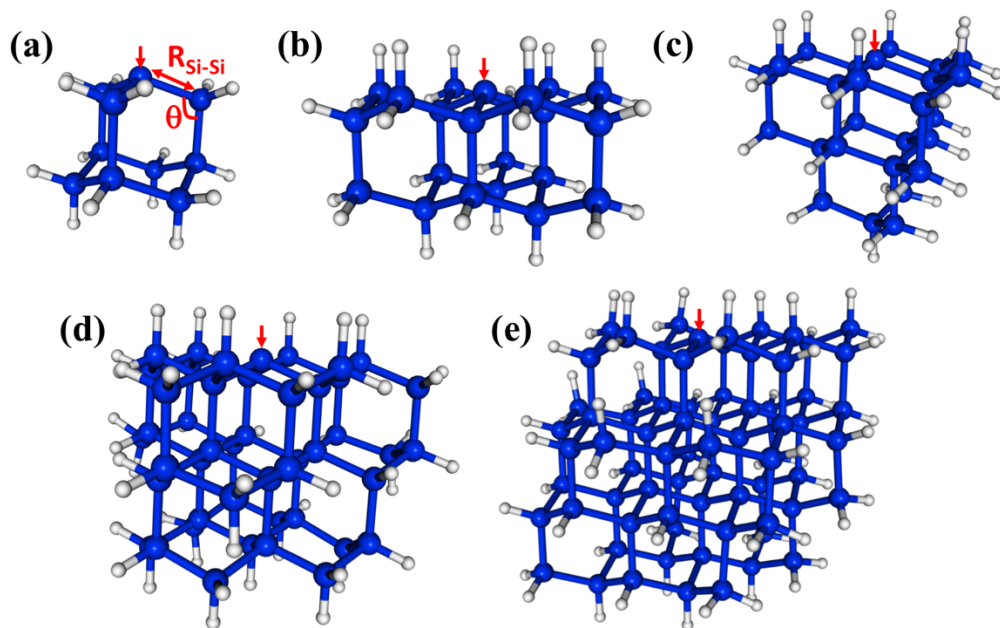
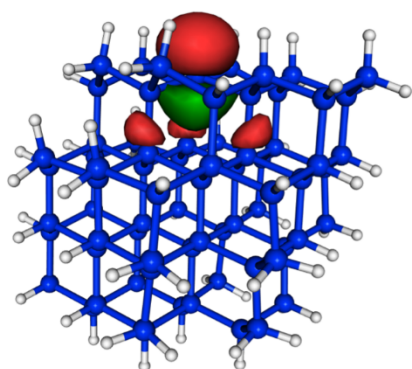


Figure 2.1. The P_b -containing silicon clusters studied in this work. (a) $Si_{10}H_{15}$ (sila-adamantane cluster), (b) $Si_{22}H_{27}$, (c) $Si_{26}H_{31}$, (d) $Si_{47}H_{49}$ (1.3-nm SiNC), and (e) $Si_{72}H_{63}$ (1.7-nm SiNC). One of the three symmetry-equivalent Si-Si bond lengths (R_{Si-Si}) and bond angles (θ) discussed herein are indicated in red in (a). The red arrows indicate the positions of dangling bond defects.

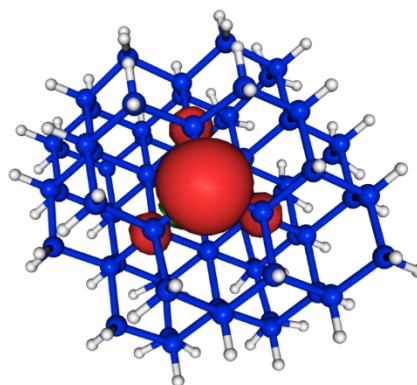
Table 2.1. The Si-Si bond lengths (\AA), Si-Si-Si bond angles (θ as indicated in Figure 2.1a; in degrees), and D_1 energies of differently sized silicon clusters at the Franck-Condon point (FC) and MECI. All energies are relative to the D_0 minimum energy. Energies are computed at the CASCI level of theory as described in the APPENDIX. When available, CASPT2 energies at CASCI geometries are presented in parenthesis.

	FC			MECI		
	$R_{\text{Si-Si}} / \text{\AA}$	θ / Degree	$D_1 \text{ Energy} / \text{eV}$	$R_{\text{Si-Si}} / \text{\AA}$	θ / Degree	$D_1 \text{ Energy} / \text{eV}$
$\text{Si}_{10}\text{H}_{15}$	2.34	107.2	4.23	2.43	123.8	2.67
	2.34	107.2	(3.53)	2.45	123.7	(2.69)
	2.34	107.2		2.94	124.0	
$\text{Si}_{22}\text{H}_{27}$	2.36	105.2		2.46	122.6	
	2.36	105.2	4.25	2.46	121.9	2.52
	2.36	105.2		2.89	123.5	
$\text{Si}_{26}\text{H}_{31}$	2.36	104.9		2.43	122.0	
	2.36	104.9	4.29	2.51	123.2	2.52
	2.36	104.9		2.83	123.6	
$\text{Si}_{47}\text{H}_{49}$	2.36	105.6		2.43	122.4	
	2.36	105.6	3.99	2.54	123.6	2.44
	2.36	105.6		2.81	123.6	
$\text{Si}_{72}\text{H}_{63}$	2.35	105.7		2.44	122.4	
	2.35	105.7	4.00	2.48	122.9	2.38
	2.35	105.7		2.82	124.3	

(a)

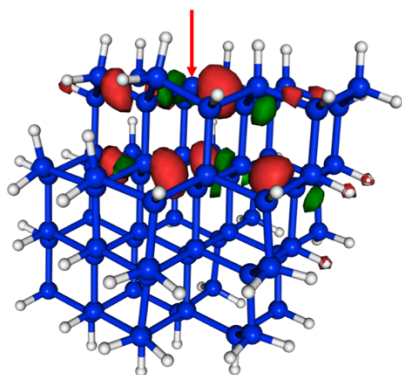


side view

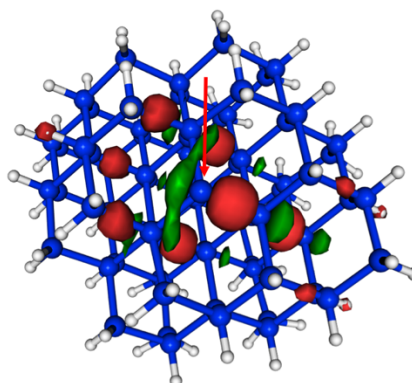


top view

(b)



side view



top view

Figure 2.2. Orbitals representative of the $D_0 \rightarrow D_1$ (${}^2A_1 \rightarrow {}^2E$) transition of the $\text{Si}_{72}\text{H}_{63}$ system. (a) The singly occupied molecular orbital (SOMO) is the nonbonding (n) orbital of the P_b center, and (b) the highest doubly occupied orbital (HDOMO) has Si-Si σ bonding character in the vicinity of the P_b defect ($\sigma_{\text{Si-Si}}$). Note that this HDOMO is approximately degenerate due to the local symmetry of the defect. We show only one of the two nearly degenerate orbitals. The red arrows indicate the locations of the P_b center.

The D_0 (2A_1) minimum energy structures of our five clusters are presented in Figure 2.1. Bond lengths and bond angles around the P_b defect (as indicated in Figure 2.1a) at these structures are listed in the Table 2.1, labeled FC (Franck-Condon point). In these initial structures the three Si-Si bond lengths surrounding the DB and the associated bond angles are symmetric. The vertical excitation energies (Table 2.1) of the five clusters are very similar to one another, varying by only 0.3 eV, and there is not a strong trend with system size. This absence of quantum confinement effects suggests the locality of the excitation. This locality can be seen in the orbitals involved in the excitation (pictured in Figure 2.2). The excitation occurs from the highest doubly occupied molecular orbital (HDOMO) to the singly occupied molecular orbital (SOMO). The HDOMO is a Si-Si σ bonding orbital ($\sigma_{\text{Si-Si}}$; e), which is relatively local to the region of the defect, while the SOMO is the dangling bond itself: the nonbonding (n; a_1) sp^3 orbital of the defect silicon atom. Note that there is a nearly degenerate pair of HDOMOs due to the local C_{3v} symmetry of the defect. We present only one of the two degenerate $\sigma_{\text{Si-Si}}$ orbitals in Figure 2.2.

Now we consider the results of the excited state AIMD simulations initiated on the D_1 (2E ; $\sigma_{\text{Si-Si}} \rightarrow n$) state. The time-dependent D_1 and D_0 potential energies, Si-Si bond lengths ($R_{\text{Si-Si}}$ as defined in Figure 2.1a), and bond angles (θ as illustrated in Figure 2.1a) of the 1.7-nm SiNC are presented in Figure 2.3. The dynamics of the smaller clusters were nearly identical; similar graphs for these cases are reported in Figures A1-A12. In all five cases the D_1/D_0 energy gap approaches zero (<0.1 eV) in the first 40-60 fs after excitation (Figure 2.3a). The vanishing energy gaps strongly suggest the existence of low-lying D_1/D_0 CIs.⁷³

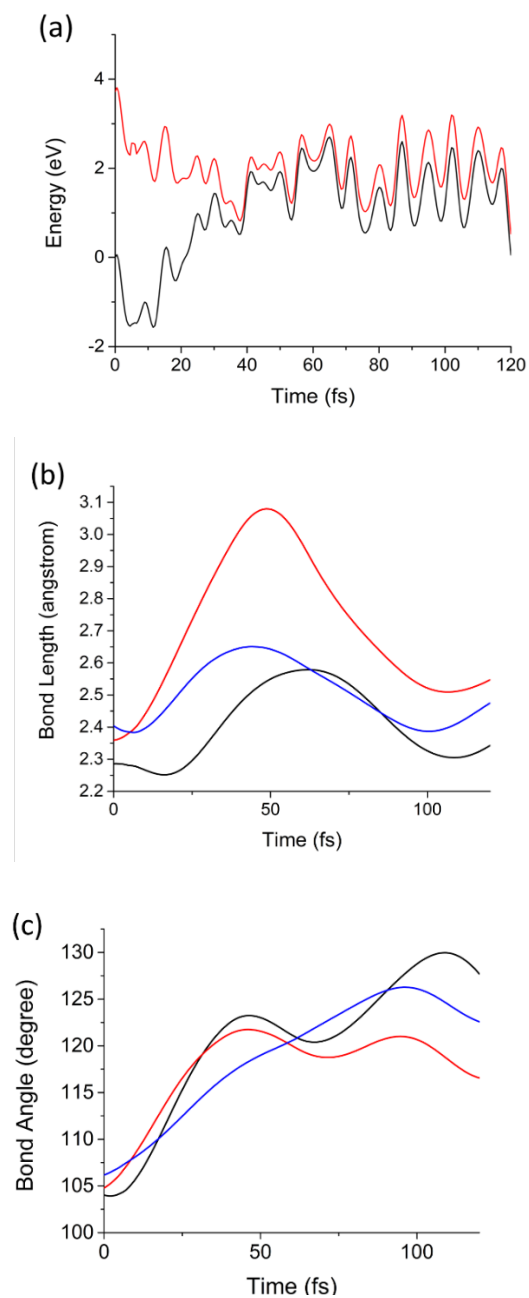


Figure 2.3. (a) The potential energies of the D_1 (red) and D_0 (black) electronic states as a function of time from the D_1 AIMD simulation of $\text{Si}_{72}\text{H}_{63}$. (b) The three Si-Si bond lengths ($R_{\text{Si-Si}}$) adjacent to the P_b defect as a function of time from the same AIMD calculation. (c) The three Si-Si-Si angles (θ , illustrated in Figure 2.1a) as a function of time from the same AIMD calculation. Each color represents one of the three symmetry equivalent bond lengths or angles in (b) and (c), respectively.

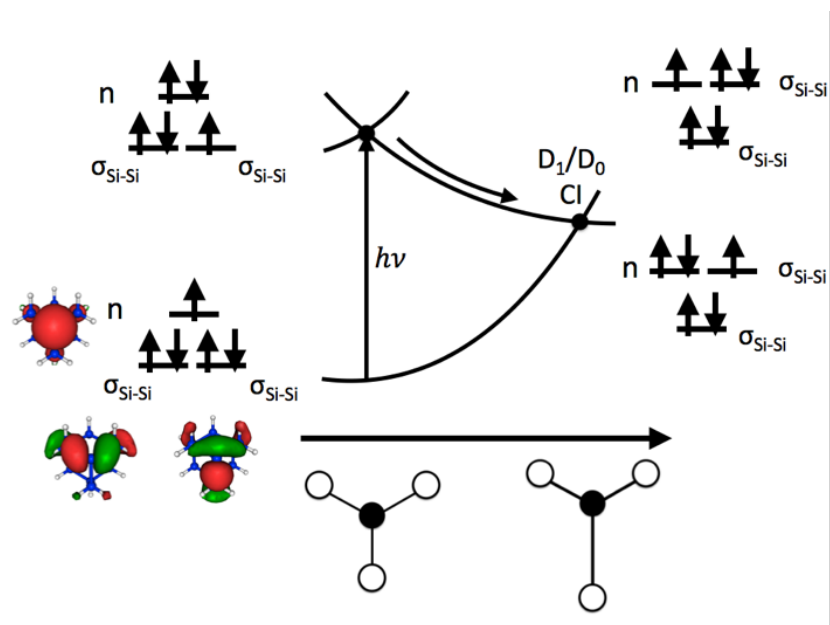


Figure 2.4. (a) Schematic illustration of the dynamics of nonradiative recombination of an excitation at a P_b center. The PESs are plotted as a function of an asymmetric stretching coordinate about the P_b center (illustrated along the x-axis with the dangling bond site represented by a filled circle and the three adjacent silicon atoms represented by open circles). Insets show the orbital occupations of D_0 and D_1 and relative orbital energies at the FC point (left) and MECI (right). The n and $\sigma_{\text{Si-Si}}$ orbitals of the smallest (sila-adamantane) system are shown on the bottom left.

Using low-gap structures from the AIMD trajectories as starting guesses, MECIs were optimized in all five systems. The energies and structural details of these MECIs are reported in Table 2.1. Full structures are presented in APPENDIX. Comparing the structures of MECIs to the Franck-Condon points, one can see that both bond lengths and bond angles around the DB defects increase at the MECIs. The three Si-Si bonds surrounding the DB are asymmetrically stretched in all five clusters; one Si-Si bond grows longer (2.81-2.94 angstrom) than the other two (2.43-2.54 angstrom). Similar asymmetric stretching is observed in the AIMD simulations of all five systems (Figures 2.3b and Figure A5-A8) on the same 40-60 fs time scale on which the D_1/D_0 energy gap approaches zero. Much smaller changes in bond length are observed for Si-Si bonds not immediately adjacent to the P_b defect. Consistent with past work on dangling bond defects,⁴⁵ symmetric bending motion is also observed to be important; the θ angles are observed to increase significantly both in the AIMD simulations (Figures 2.3c and Figure A9-A12) and in the optimized MECI structures (Table 2.1). Taken together, these calculations suggest that upon excitation of the lowest defect-localized excited state, the P_b defect moves ballistically to the CI region in 40-60 fs. It is also noteworthy that the trajectories remain in a region of small energy gap after 40-60 fs, suggesting that it may pass over the intersection multiple times, enabling efficient decay.

The role that symmetry breaking plays in these nonradiative dynamics can be intuitively understood through analysis of the orbitals occupied during excitation. Figure 2.4 is a schematic diagram summarizing these dynamics. As described above, excitation to D_1 involves the promotion of an electron from one of the degenerate $\sigma_{\text{Si-Si}}$ orbitals to the n orbital. This reduces the Si-Si bond order, resulting in a lengthening of one of the Si-Si bonds (as observed in the AIMD simulations of all five clusters). In the locally C_{3v} -symmetric FC structure the D_1 (2E) state is doubly degenerate by symmetry, thus this symmetry-breaking motion is a Jahn-Teller distortion. The lengthening of a single Si-Si bond (moving from left to right along the D_1 PES in Figure 2.4) brings the molecule towards the MECI structure. This symmetry breaking raises the energy of one of the $\sigma_{\text{Si-Si}}$ orbitals into near degeneracy with the n orbital, bringing about a CI between the D_0 and D_1 states. That a Jahn-Teller distortion in D_1 drives the molecules directly towards the D_1/D_0 CI provides a straightforward explanation for the ultrafast nonradiative process that follows creation of the defect-localized excitation.

The MECIs of the defective silicon clusters studied here are all accessible at energies in the visible range (2.38-2.67 eV above the ground state minimum structure; Table 2.1) and therefore capable of quenching visible light emission. The MECIs show a slight decrease in energy with increasing system size; the energy decreases from 2.67 eV for the small sila-adamantane cluster to 2.38 eV for the 1.7-nm SiNC. This small energy decrease of 0.29 eV is consistent with the localized nature of the defect-localized excited state. Calculations at the dynamically correlated CASPT2 level confirm the accuracy of the MECI energies predicted by CASCI, though vertical excitation energies are somewhat overestimated. All five clusters have D_1 minimum energy structures distinct from the MECIs. In all cases this minimum is 0.05-0.06 eV below the MECI, compared to the 1.6-1.9 eV released during relaxation on the excited states. Thus the MECI is energetically accessible upon excitation. Energies and structures of D_1 minima are presented in APPENDIX.

The existence of defect-induced CIs with energies in the 2.4-2.7 eV range is consistent with several experimental observations of the photoluminescence (PL) of SiNCs after oxidation. The MECI energies suggest that the PL of SiNCs with emission energies larger than ~ 2.4 -2.7 eV is likely to be quenched by the DB defects. Indeed the quantum yield of PL from oxidized SiNCs is observed to drop with increasing energy,⁷⁴ and single particle experiments on oxidized SiNCs show no emissive particles with PL maxima above 2.5 eV.⁷⁵ In addition, the PL lifetime of oxidized SiNCs decreases with increasing PL energy, and a dramatic decrease is observed in the 2.0-2.2 eV energy range.⁷⁶ This decreasing PL lifetime suggests the existence of an efficient nonradiative recombination pathway accessible above these energies, consistent with our computed CI energies. Finally, as noted in our previous studies of oxygen-containing defects, the unusual size-insensitive orange (S-band) emission of oxidized SiNCs observed in ensemble PL measurements⁷⁷ is consistent with the presence of CIs accessible in this energy range. We argue that the size-insensitivity of the observed ensemble emission arises not because the emission energy of individual oxidized SiNCs becomes insensitive to particle size, but instead because the rate of nonradiative recombination is strongly size sensitive, dramatically reducing the PL yields of smaller SiNCs with shorter wavelengths. This argument reconciles the observation of size-insensitive emission with PL lifetime, linewidth, and polarization measurements suggesting that the S-band arises from quantum-confined excitons.^{75, 78, 79}

2.3 Conclusions

Thus, we have elucidated the mechanism of nonradiative recombination via a dangling bond defect by application of AIMD simulations based on a multireference description of the electronic structure to SiNCs up to 1.7-nm in diameter. Within 40-60 fs after excitation of a defect-localized electronic excited state, a CI between the D_0 and D_1 states is accessed. This CI is accessible at energies in the 2.4-2.7 eV range, and thus is detrimental to visible PL, consistent with the fact that DBs are well-known nonradiative centers. The ultrafast recombination process is driven both by Jahn-Teller distortion in the D_1 state and by totally symmetric bending of the DB center. The role that symmetry-breaking plays in this mechanism underlines the importance of treating coupled electron-nuclear dynamics in the study of recombination.

APPENDIX

SUPPORTING INFORMATION FOR: DYNAMICS OF RECOMBINATION VIA CONICAL INTERSECTION IN A SEMICONDUCTOR NANOCRYSTAL

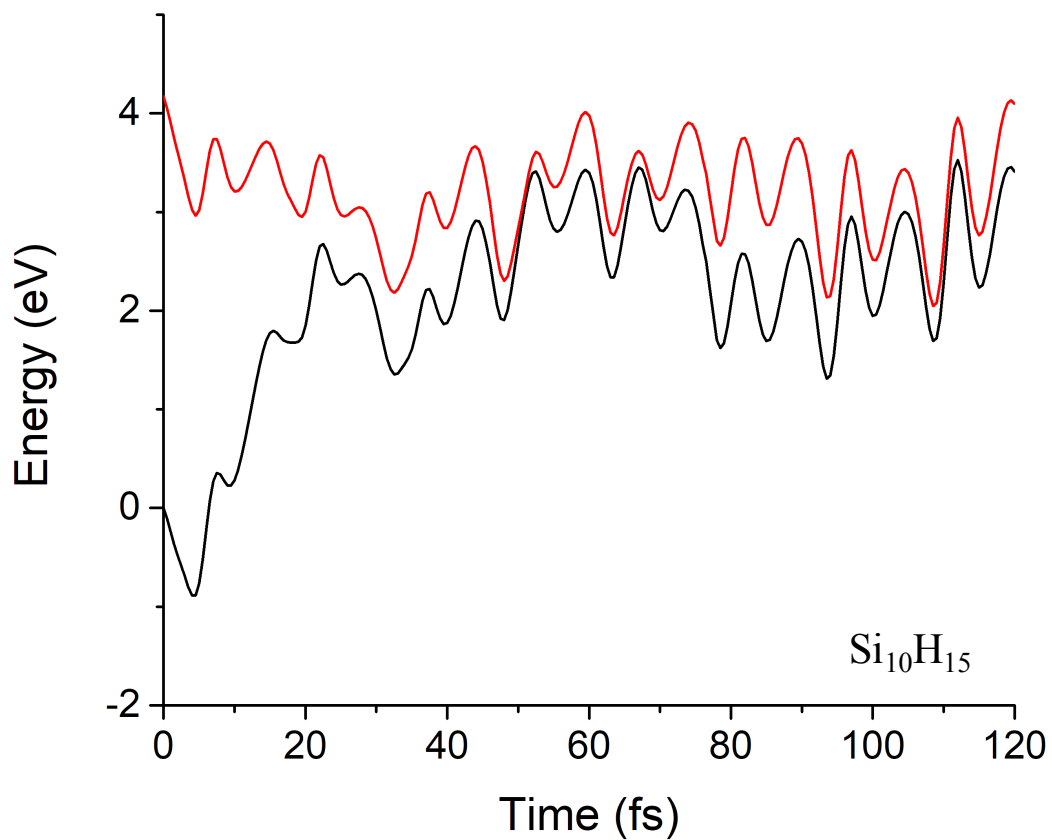


Figure A1. The potential energies of the first excited (red line) and ground states (black line) change with the time following the first excited state trajectory from an AIMD simulation where the force comes from the first excited state in Si₁₀H₁₅.

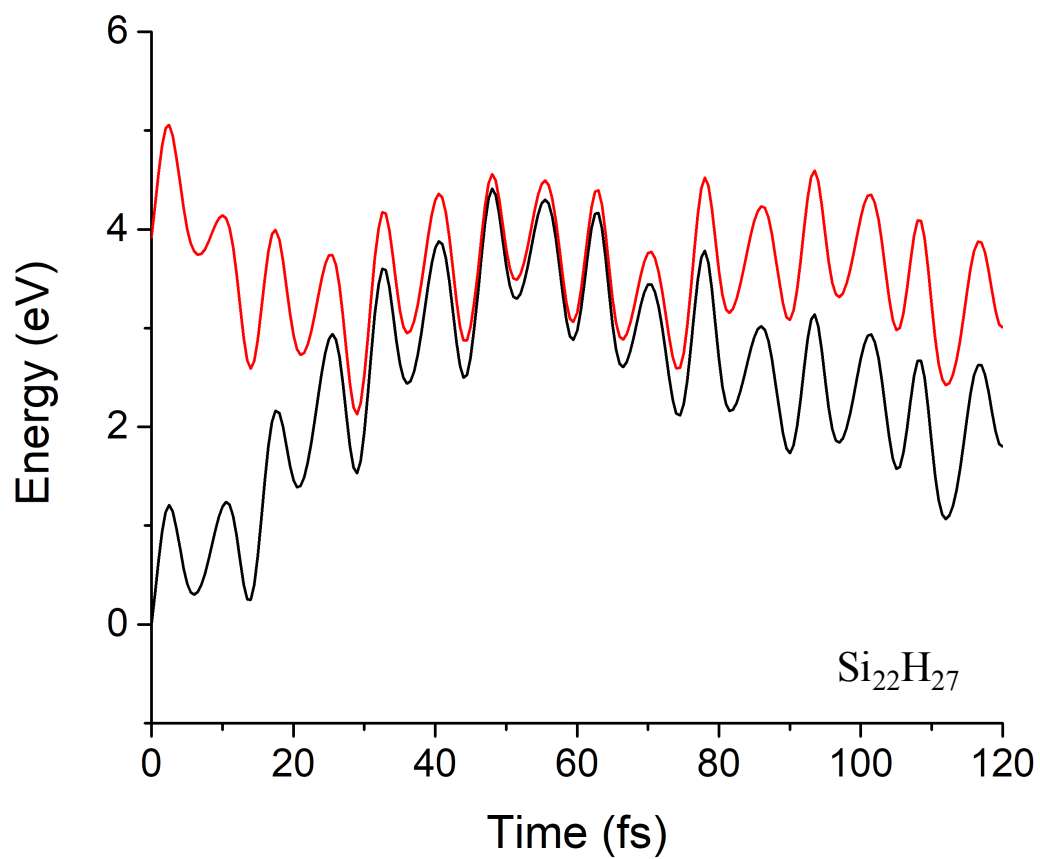


Figure A2. The potential energies of the first excited (red line) and ground states (black line) change with the time following the first excited state trajectory from an AIMD simulation where the force comes from the first excited state in $\text{Si}_{22}\text{H}_{27}$.

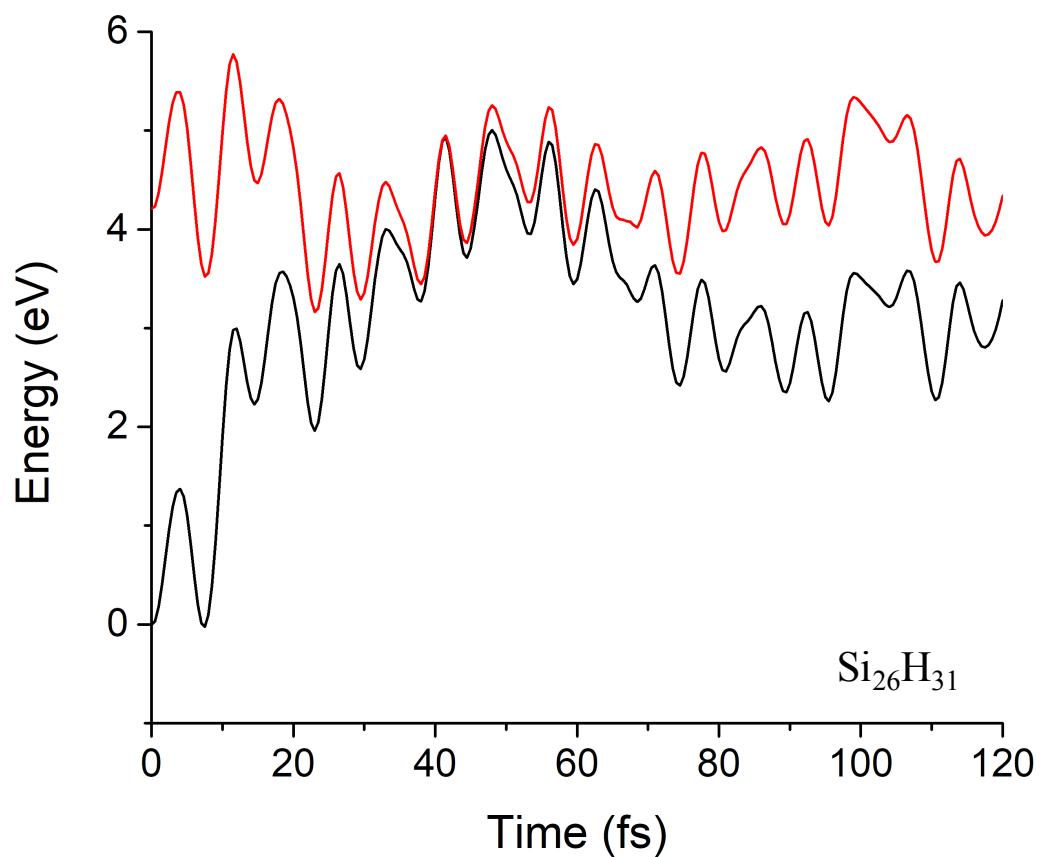


Figure A3. The potential energies of the first excited (red line) and ground states (black line) change with the time following the first excited state trajectory from an AIMD simulation where the force comes from the first excited state in $\text{Si}_{26}\text{H}_{31}$.

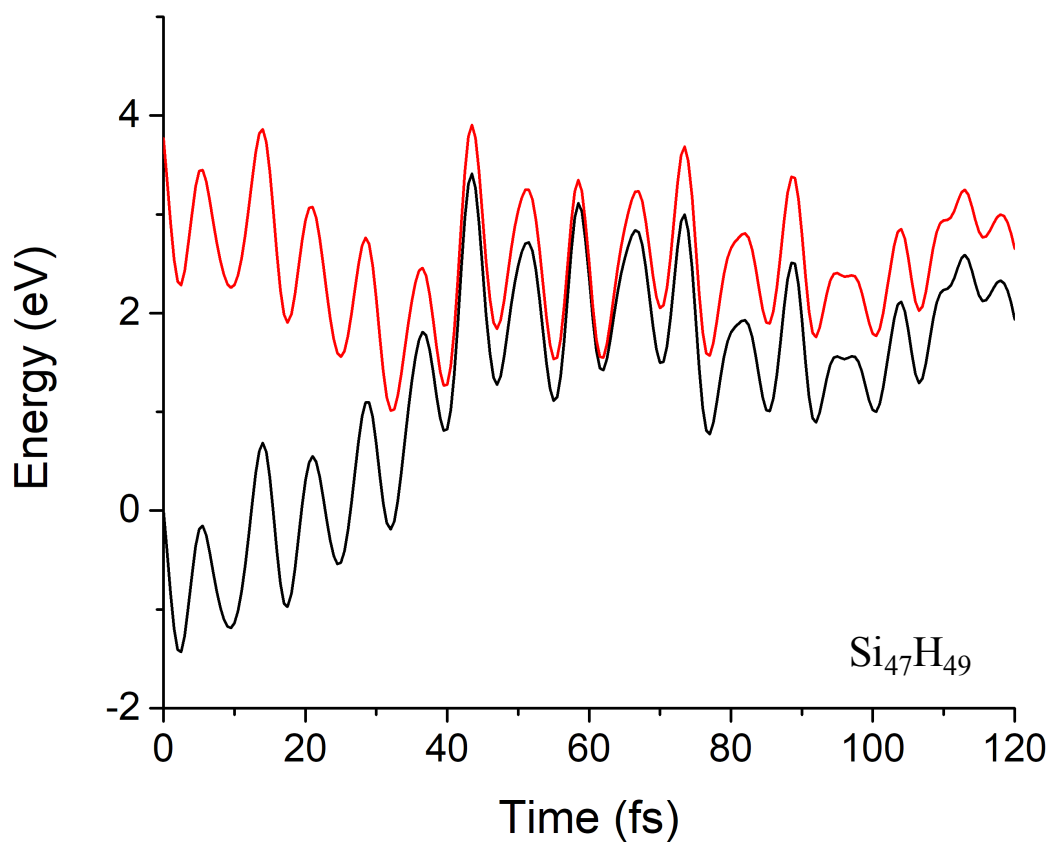


Figure A4. The potential energies of the first excited (red line) and ground states (black line) change with the time following the first excited state trajectory from an AIMD simulation where the force comes from the first excited state in $\text{Si}_{47}\text{H}_{49}$.

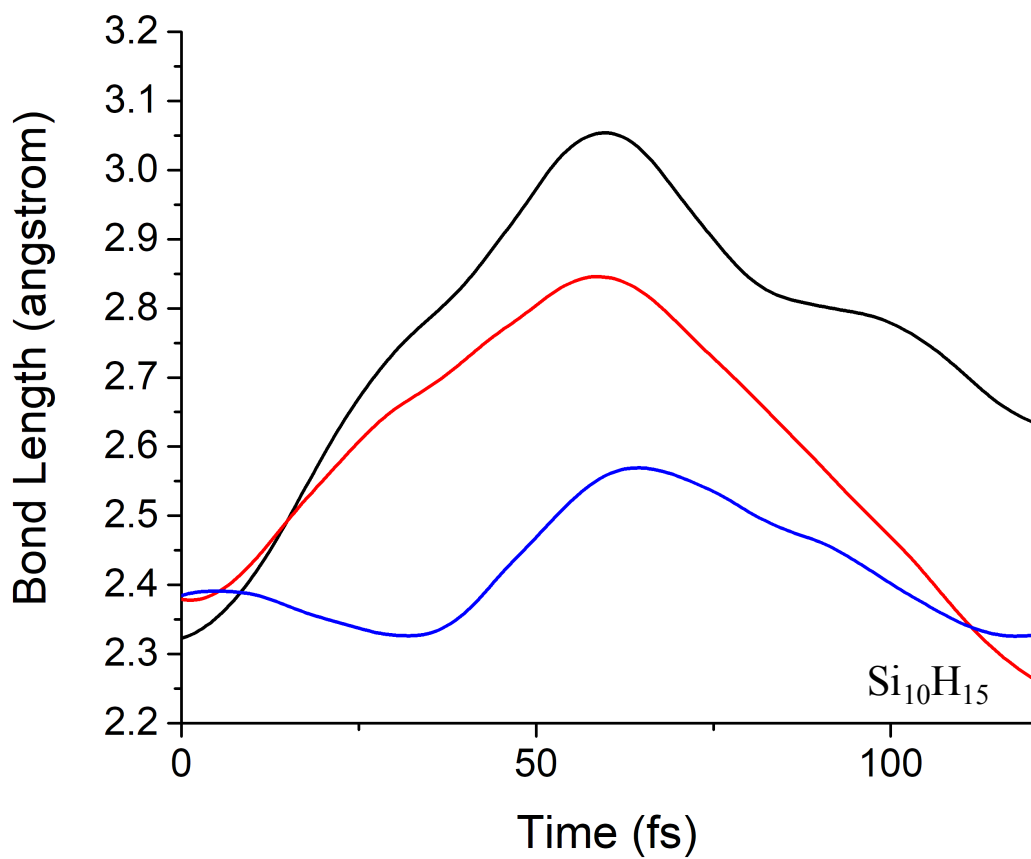


Figure A5. The three Si-Si bond lengths ($R_{\text{Si-Si}}$) of $\text{Si}_{10}\text{H}_{15}$ change with time from the AIMD calculation. Each color represents one Si-Si bond length.

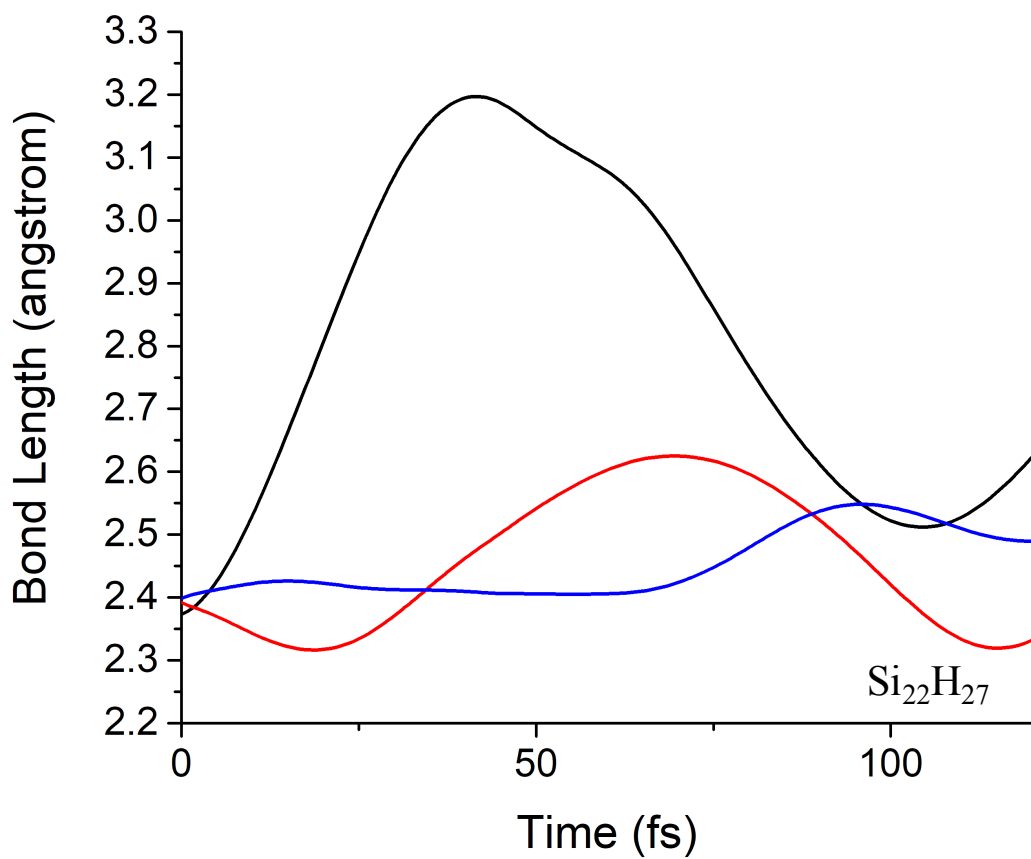


Figure A6. The three Si-Si bond lengths ($R_{\text{Si-Si}}$) of $\text{Si}_{22}\text{H}_{27}$ change with time from the AIMD calculation. Each color represents one Si-Si bond length.

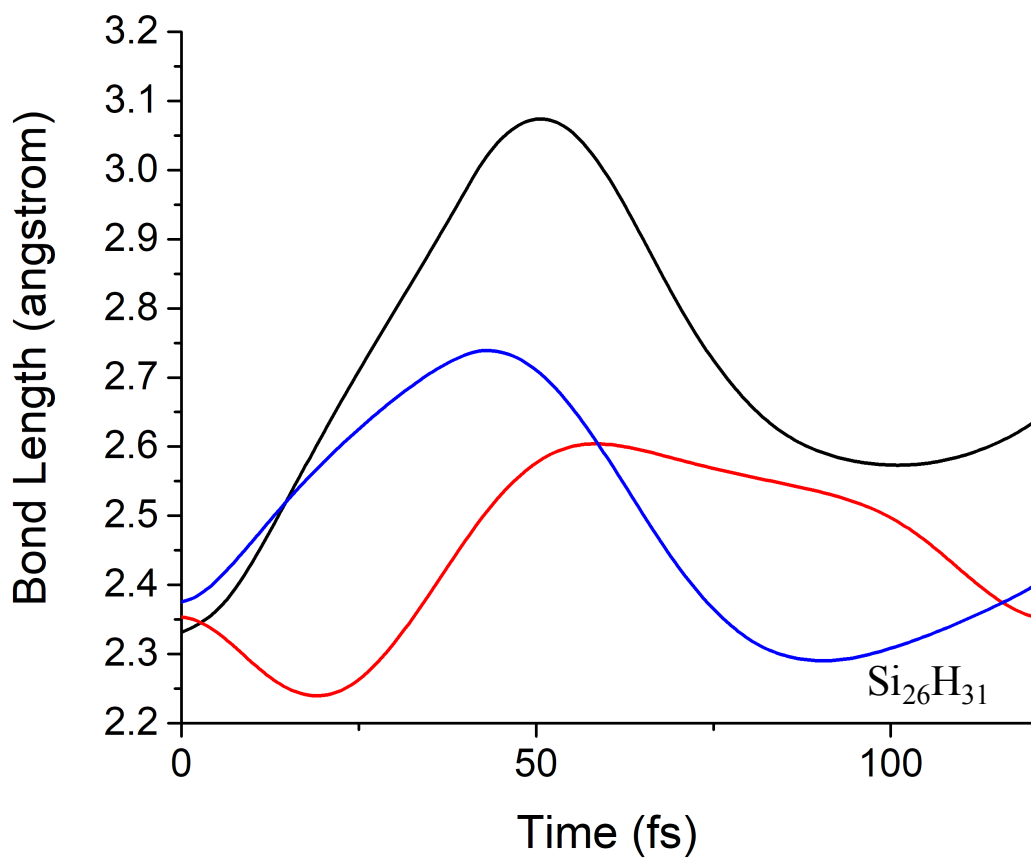


Figure A7. The three Si-Si bond lengths ($R_{\text{Si-Si}}$) of $\text{Si}_{26}\text{H}_{31}$ change with time from the AIMD calculation. Each color represents one Si-Si bond length.

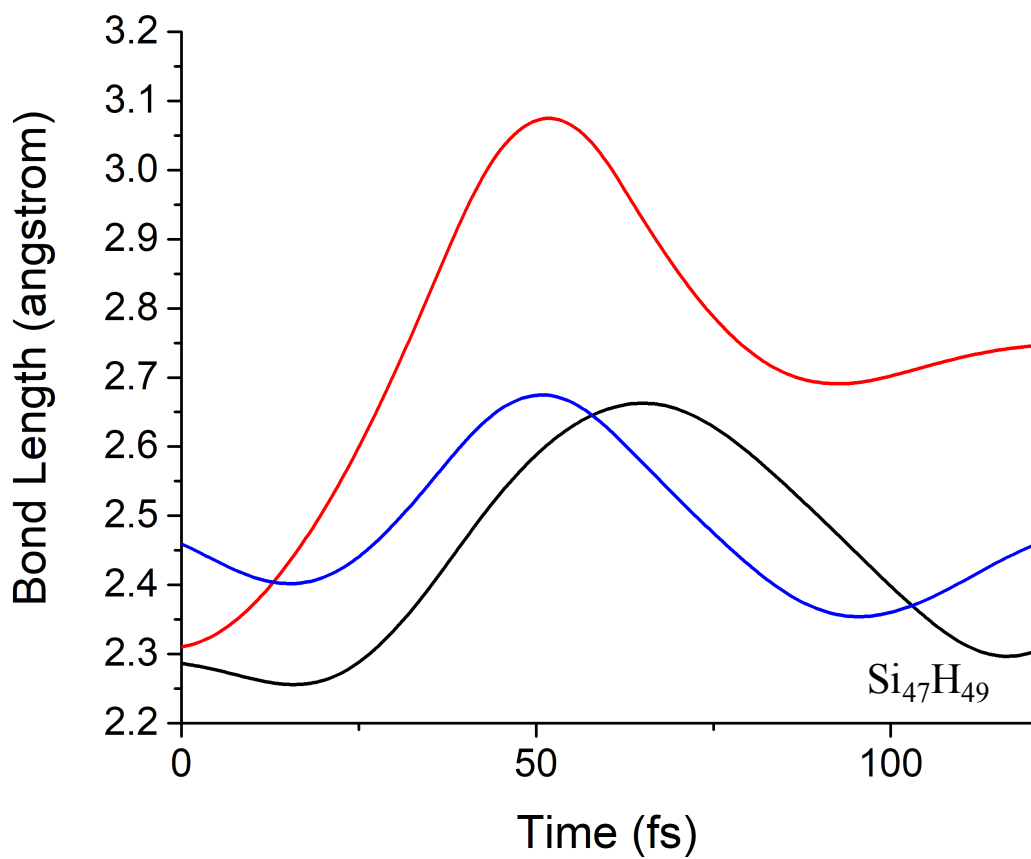


Figure A8. The three Si-Si bond lengths ($R_{\text{Si-Si}}$) of $\text{Si}_{47}\text{H}_{49}$ change with time from the AIMD calculation. Each color represents one Si-Si bond length.

Ground State Minimum Energy Geometries (in Angstrom)

Si₁₀H₁₅

Si	-0.5174205979	-0.8348349814	-0.7170299444
Si	1.8349944728	-0.8348264311	-0.7034572298
Si	-1.2975571211	1.2346984879	0.0845084533
Si	-1.3052009638	-2.5548459701	0.6728075910
Si	2.6315781484	-0.4801811161	1.4813624363
Si	-0.5177122134	1.6008056015	2.2734868246
Si	-0.4846934236	-2.1343753473	2.8284603389
Si	1.8346837138	1.5893845329	2.2660259352
Si	-1.3047721410	-0.1085476518	3.6768972784
Si	1.8582635743	-2.1980831303	2.8819602955
H	-0.9982771294	-1.0362895976	-2.0995241051
H	2.3315062053	0.2372717958	-1.5870674988
H	2.3323357458	-2.1296624310	-1.2075209264
H	-0.8158399009	2.3161803939	-0.7958276067
H	-2.7733368421	1.2426787832	0.0773677090
H	-0.8177833037	-3.8633496961	0.1999671071
H	-2.7792581411	-2.5648306177	0.6939505559
H	-0.9987009985	2.9137881883	2.7507928354
H	4.1089148884	-0.4613933574	1.4662466180
H	2.3329439541	-3.5078878963	2.3998373351
H	2.3309456347	-1.9888831636	4.2626165112
H	2.3362682403	1.8278307131	3.6333053374
H	2.3268252019	2.6684318023	1.3883697280
H	-2.7788325440	-0.1308235029	3.6830320283
H	-0.8167544595	0.0893645920	5.0538623924

Si₂₂H₂₇

Si	-0.3972569683	-0.5830501301	-0.8321377189
Si	1.9547937034	-0.5351843517	-0.9261372969
Si	-1.2673419317	1.4207876463	0.0460120336
Si	-1.0925993707	-2.3994500329	0.5183564137
Si	2.7958091258	-0.1644944637	1.2417357013
Si	-0.3752694178	1.7597885391	2.1984031749
Si	-0.1842263064	-1.9641860638	2.6552086261
Si	1.9772606786	1.8458715325	2.1539087435
Si	-1.0702013941	0.0005215740	3.6226425378
Si	2.1782576455	-1.9705589033	2.6428534318
Si	2.7795135709	-2.5536488064	-1.7967200647
Si	-3.6115798856	1.3295809584	0.1346450351
Si	-0.2244978466	-4.4218911388	-0.3137364596
Si	-3.4407387476	-2.4674922803	0.6496570015
Si	2.9663271290	-4.0003233853	1.7513439153

Si	2.9839993170	-1.6272021648	4.8265803683
Si	2.8285758589	2.1711593733	4.3176421018
Si	-3.4187750187	-0.1309944319	3.6768518851
Si	-0.1810162833	0.2952618485	5.7809228431
Si	-4.2716600504	-0.4512847041	1.5148443519
Si	2.1615665176	0.3909193270	5.6953479926
Si	2.1178154977	-4.3296505758	-0.4110542982
H	-0.9337269855	-0.7896112302	-2.1955426474
H	2.3691472072	0.5899615504	-1.7909698734
H	-0.8415282220	2.5392852707	-0.8219118306
H	-0.8977627692	3.0310669206	2.7461811431
H	4.2733117579	-0.1072635696	1.1868895734
H	2.3912495084	2.9635134242	1.2792119398
H	-3.9472753343	1.1236982662	4.2472869753
H	-3.8212391577	-1.2485943134	4.5520456397
H	-3.8462215043	-3.5953227101	1.5100842802
H	-3.9802870975	-2.6951354357	-0.7054811742
H	-4.1531920071	1.1338546260	-1.2239303759
H	-4.1379983402	2.5986143590	0.6729439203
H	-5.7471969680	-0.5132427112	1.5733383063
H	4.3019464522	2.2360897950	4.2671192792
H	2.3201495689	3.4431803692	4.8659126820
H	-0.6127148144	-0.8236447730	6.6402960867
H	-0.7170649358	1.5506740166	6.3428263104
H	2.6949058479	0.5920344669	7.0590176458
H	4.4592270578	-1.5942712095	4.7840164407
H	2.5658146727	-2.7557007535	5.6801035554
H	2.5562723179	-5.1101149082	2.6328987217
H	4.4413386301	-3.9540895487	1.7126277108
H	-0.7772667381	-4.6525748767	-1.6630173745
H	-0.6526344611	-5.5288472442	0.5627333459
H	2.2482628661	-2.7601367084	-3.1579086455
H	2.6373504254	-5.6026008335	-0.9535717420
H	4.2524071997	-2.5002016047	-1.8694102124

Si₂₆H₃₁

Si	-0.4398719991	-0.7667028184	-0.7199895311
Si	1.9169358250	-0.7102511493	-0.8312161401
Si	-1.2842117817	1.2742724470	0.1134434767
Si	-1.1519899237	-2.5663199225	0.6420641284
Si	2.7467564604	-0.3525062221	1.3493626084
Si	-0.4030484240	1.6007804485	2.2788258343
Si	-0.2411305565	-2.1134912524	2.7735430173
Si	1.9549530372	1.6951550095	2.2168084688
Si	-1.1143735472	-0.1348854308	3.7214863010
Si	2.1205673899	-2.1406940490	2.7673489807

Si	2.5808280743	1.0741374168	-2.2171839705
Si	2.7206385134	-2.7580946669	-1.6618975200
Si	-0.5758336726	3.0366740558	-1.2791141000
Si	-3.6319488280	1.1820443817	0.2162064221
Si	-0.2954349561	-4.6001904717	-0.1743329304
Si	-3.5014485152	-2.6102368358	0.7637577222
Si	2.8953657268	-4.1835792702	1.8939246403
Si	2.9336981691	-1.7727609553	4.9446198572
Si	2.7933177311	2.0180727279	4.3902694973
Si	2.6249274101	3.4471592811	0.7924887629
Si	-3.4640844554	-0.2442985623	3.7712029892
Si	-0.2241290923	0.1787678782	5.8764729334
Si	-4.3127756716	-0.5794774241	1.6108681831
Si	2.1180184114	0.2574945304	5.7888243180
Si	2.0465897874	-4.5213280144	-0.2660075568
Si	1.7682817395	3.1040968674	-1.3651261280
H	-0.9710306912	-0.9743469029	-2.0862548834
H	-0.9125347485	2.8871119676	2.8058286964
H	4.2250326162	-0.2987073289	1.2882133424
H	-3.9815046875	1.0217478641	4.3266353671
H	-3.8782921805	-1.3483119622	4.6582253502
H	-3.9239118392	-3.7293332623	1.6276877574
H	-4.0350424388	-2.8398208301	-0.5934380726
H	-4.1745620243	0.9810230975	-1.1417621168
H	-4.1499058706	2.4610358238	0.7401823545
H	-5.7892884662	-0.6267279777	1.6662030424
H	4.2673825755	2.0803816423	4.3433956334
H	2.2896985737	3.2989120615	4.9235788132
H	-0.6650489031	-0.9268836631	6.7483800987
H	-0.7519640874	1.4446426595	6.4226048641
H	2.6526019450	0.4719867603	7.1502497667
H	4.4087895903	-1.7412117524	4.8934142895
H	2.5199654199	-2.8906287069	5.8143326491
H	2.4749943262	-5.2824727349	2.7844520881
H	4.3707110737	-4.1490727793	1.8578148437
H	-0.8470104930	-4.8355329683	-1.5231914466
H	-0.7338434828	-5.6984209044	0.7083249666
H	2.1950252878	-2.9729417343	-3.0243594431
H	2.5597543707	-5.8007898857	-0.8000298153
H	4.1941915726	-2.7136854510	-1.7327245565
H	2.0535348997	0.8514849939	-3.5776806851
H	4.0546489524	1.1107737335	-2.2886280827
H	4.0994803269	3.4969360510	0.7470832498
H	2.1324462611	4.7286577853	1.3346293894
H	-1.0982839833	4.3110636678	-0.7480806102
H	-1.1253410139	2.8371986564	-2.6344226252
H	2.1962402666	4.2121840809	-2.2460944904

Si₄₇H₄₉

Si	-0.4818420248	-0.8450923780	-0.7475587158
Si	1.8949966387	-0.7996570386	-0.8162480058
Si	-1.3303573489	1.1989091972	0.1229132491
Si	-1.1755107650	-2.6314669539	0.6580713694
Si	2.7614439979	-0.4119190912	1.3642498020
Si	-0.4519139512	1.5792950376	2.3000190220
Si	-0.2666834627	-2.1565037493	2.7818217331
Si	1.9249267731	1.6337651392	2.2426335061
Si	-1.1507491115	-0.1861076156	3.7293841351
Si	2.0914212410	-2.1910813469	2.7903429621
Si	2.5944697213	0.9792177906	-2.2208695306
Si	2.6807903266	-2.8867062136	-1.6183781784
Si	-0.6396160161	2.9597268145	-1.3085314684
Si	-3.6934319714	1.0790379800	0.2576922038
Si	-0.3592695126	-4.6827916917	-0.1669116664
Si	-3.5194482202	-2.7278756784	0.8443536220
Si	2.8187629272	-4.2757194561	1.9759099962
Si	2.9301101245	-1.8520950816	4.9666858546
Si	2.7611918722	1.9254265007	4.4408754043
Si	2.5933201778	3.4148528825	0.8257341579
Si	-3.5040148649	-0.2787133612	3.8207359208
Si	-0.2819005257	0.0623623586	5.9022623346
Si	-4.3339422246	-0.6953247292	1.6627258444
Si	2.0523344301	0.1543695273	5.8169624287
Si	1.9890879841	-4.6167839264	-0.1827316245
Si	1.7198854433	2.9780875672	-1.3223194444
Si	-1.2293428774	-1.2217303113	-2.9608951612
Si	-1.3483726738	3.6343239864	3.0567823960
Si	5.1213861172	-0.2397435357	1.3416418125
Si	-4.3098523751	1.7613445134	4.6729575549
Si	-4.6890509186	3.0164105966	1.1418196883
Si	5.1086338144	1.9596228770	4.5621460617
Si	5.2805681378	-1.7903940128	4.8715997533
Si	-1.2243641113	-5.0282761474	-2.3278736369
Si	1.8776437223	-3.4401584042	-3.7572951465
Si	1.7262588436	0.8642730044	-4.4080798826
Si	4.9482378499	1.0368641185	-2.2746888332
Si	4.9242128824	3.5630397462	0.5161719393
Si	1.7495958374	5.4389799618	1.6845076927
Si	-1.2604001518	5.1026231602	-0.5512120553
Si	-1.4934024518	2.5742142430	-3.4692906229
Si	-3.6959958783	3.4970237055	3.2138417689
Si	-0.4661705185	-3.3110225378	-3.7401762309
Si	5.9458367901	0.0225087435	3.5339836191
Si	-0.6022266357	0.5836609780	-4.3350375041

Si	-0.5963768059	5.3900298442	1.6809182656
Si	5.7841121117	1.4765960150	-0.1266699457
H	-3.8859362855	-1.3863572271	4.7222133972
H	-3.8751739213	-3.8373381830	1.7492600550
H	-4.1024051055	-2.9992501783	-0.4831471239
H	-4.2257575946	0.8246175845	-1.0975283260
H	-5.8114485808	-0.7338762132	1.7199904631
H	2.2201947541	3.1900623677	4.9819150730
H	-0.7316548092	-1.0779557287	6.7230349423
H	-0.8074568981	1.3055273298	6.4973343607
H	2.5953744091	0.3739229220	7.1751601098
H	2.4903655432	-2.9835896413	5.8103323133
H	2.3456272198	-5.3308164031	2.8918611470
H	4.2934703939	-4.3011898528	1.9519397105
H	-0.8198921900	-5.7579406416	0.7371122698
H	2.4978651041	-5.8980430385	-0.7187408229
H	4.1583325695	-2.8521895154	-1.6392676432
H	2.1484598895	4.0858135310	-2.2077360361
H	5.8188261508	-1.6159927180	6.2346614169
H	5.7881138508	-3.0612517576	4.3228916287
H	7.4217518662	0.0823595037	3.4814031858
H	5.6723371414	3.1793836881	3.9643513991
H	5.4854232127	1.9284875125	5.9895040901
H	7.2611244374	1.5332093712	-0.1601782368
H	5.1514627665	4.5188882624	-0.5866263415
H	5.5993602751	4.0868526713	1.7143465869
H	2.2204062097	6.5560069793	0.8417857946
H	2.2662621744	5.6382663286	3.0518565379
H	-1.1300152265	6.6670161657	2.2009631224
H	-2.7008934004	5.3455417253	-0.7285938053
H	-0.5298639645	6.0806816764	-1.3827483960
H	5.3854025508	2.1001812319	-3.2007537064
H	5.4533967566	-0.2546809505	-2.7779471062
H	2.0179429905	2.1596918784	-5.0549396069
H	2.3796383149	-0.1920363209	-5.1973426781
H	-1.1206506992	0.3484369495	-5.6995239532
H	-2.9654398079	2.5027405608	-3.4032652102
H	-1.1211729008	3.7027132892	-4.3453394285
H	-2.7078395095	-1.2758026474	-2.9411079642
H	-0.9888588572	-3.5273706027	-5.1057061256
H	-0.7499465958	-6.3283618900	-2.8404151937
H	-2.6976049557	-5.0513664116	-2.2743048301
H	5.6675240594	-1.5113586086	0.8181947097
H	2.4616213138	-2.5854439499	-4.8020046494
H	2.2644308634	-4.8378826380	-4.0348252662
H	-4.2125441458	4.7821908724	3.7297934077
H	-5.7812647245	1.7014364729	4.7701212832

H	-3.7568532536	1.9887112059	6.0206386615
H	-6.1186061319	2.7239426360	1.3678727238
H	-4.5935550529	4.1551233989	0.2159800954
H	-0.8325825741	3.8833259734	4.4210475184

Si₇₂H₆₃

Si	0.0142241203	-0.0252846567	0.0768646407
Si	0.0346997444	-0.0401227583	2.4414756915
Si	2.2575291124	0.0123854838	-0.7170080344
Si	2.2269845101	0.0275667081	-3.0942123496
Si	-1.1397905465	-1.9564352762	-0.6992361571
Si	-1.1169672063	1.9175074904	-0.7219432065
Si	-1.1576391126	-1.9337091445	-3.0764343523
Si	-1.1324828590	1.9214860268	-3.1022953316
Si	-0.0089272882	-3.9048106254	0.0565840655
Si	3.3922990567	-1.9333970945	0.0397311433
Si	0.1940503141	-3.9783251531	2.4053931311
Si	3.3725782305	-2.1323839650	2.3904206130
Si	1.1645852039	-1.9837872048	3.1851727340
Si	2.1719975613	-3.7553835232	-0.8169293028
Si	-2.2920927412	0.0014049753	-3.8884208992
Si	1.1039942636	1.9690430258	-3.9065620857
Si	1.0810055341	-1.9030507914	-3.8870353468
Si	-2.2562654975	3.8547204996	-3.8945861082
Si	-2.2523561113	3.8298838715	-6.2620365959
Si	-3.2746325565	1.9127465058	-7.1625716490
Si	-0.0873905138	3.7590490879	-7.1778926271
Si	-2.2720068559	-0.0211748796	-6.2610696976
Si	1.0957859215	1.9290465522	-6.2793755974
Si	-0.0320338637	-0.0131251069	-6.9886978399
Si	2.2152395250	-3.8524750271	-3.1670272271
Si	1.0921088668	-1.9443224955	-6.2520793138
Si	4.4427814737	-3.8277688209	-3.9601626326
Si	1.0801913498	-5.7764320480	-3.9430256700
Si	-0.0277910630	-3.8859502178	-7.0011095015
Si	3.3277638978	-1.9428613762	-7.0186636634
Si	1.1244517982	-5.8027701264	-6.2915397414
Si	4.4240250368	-3.8917365542	-6.3083633081
Si	-2.1977898930	-0.0016194395	3.2279762350
Si	1.1169638634	1.9200254425	3.2102560129
Si	-3.3323125511	1.9406687411	0.0998412176
Si	-0.0299565104	3.8550378699	0.0823035009
Si	-4.4656082230	3.8534117935	-3.0446885343
Si	-1.1513717485	5.7750655685	-3.0612606269
Si	-1.1762957101	5.7675193883	-0.7060102251
Si	-0.0357924735	3.8276198904	2.4463205355

Si	-3.2877847392	1.9422087721	2.4634526806
Si	-4.4280516160	3.8823805864	-0.6896083457
Si	-2.2404689841	3.8899128591	3.2469016364
Si	-3.3632035610	5.8002105993	0.1424363872
Si	-3.3561099228	5.8082547919	2.4877000092
Si	-3.2346696447	-1.9598306240	-7.1869488927
Si	-4.5119858403	0.0107269519	-3.0502515018
Si	-2.2855978847	-3.8606541916	-3.8567065167
Si	-2.2513791794	-3.8642965448	-6.2236791040
Si	-0.8955075372	-5.9242935790	-0.7746374599
Si	-1.1208204174	-5.7807103101	-3.1080003619
Si	-3.3716697116	-1.9319512400	0.1174679077
Si	-4.4188517815	0.0157331836	-0.6965260507
Si	-5.7050631671	-1.9219747662	-3.6746701917
Si	-4.6082953956	-3.7695972942	-0.6839547211
Si	-4.5055505891	-3.8415351567	-3.0323898522
Si	3.3305469068	-5.8146847986	-7.0861842545
Si	3.3516360758	1.9656919225	0.0810170439
Si	2.2048992291	3.9044161170	-3.0867247941
Si	2.1740340752	3.8374616935	-0.7321670002
Si	5.5467840461	-1.9157290608	-3.1431640868
Si	4.4204942138	0.0008111951	-6.2597663805
Si	4.4530841503	0.0452328946	-3.8933023715
Si	5.5530377927	2.1292009520	-0.7417784001
Si	4.4668496462	3.9741396258	-3.7395437411
Si	5.5449466650	1.9867753683	-3.0894829012
Si	3.3181220300	2.1616378953	2.4267966383
Si	-3.5049464308	-1.7968665710	2.4637278514
Si	-5.7141847553	1.9520801125	-3.6304626877
Si	1.1144103948	5.9111350362	-3.6642925358
Si	5.5792623203	-2.1661673277	-0.8079868935
Si	3.2457820888	1.7901203204	-7.2287832961
H	3.3294258772	-5.8252786239	-8.5612795450
H	4.0307907851	-7.0197495786	-6.6024741603
H	0.4050367645	-7.0063137169	-6.7596789923
H	5.8219188057	-3.8683799275	-6.7884697769
H	5.1240361038	-5.0278012291	-3.4280182341
H	3.2963233770	-1.9090342418	-8.4975059835
H	1.7881197862	-6.9612758834	-3.4116902747
H	-0.0536240787	-3.8489242016	-8.4800230480
H	5.8167341193	-0.0151380906	-6.7475452777
H	6.9331944217	-1.9182992981	-3.6588470167
H	-1.8125536084	-6.9866563461	-3.6131456451
H	-2.9350844591	-5.0857433756	-6.7016869713
H	-2.1557407259	-6.2670192120	-0.0989349870
H	0.0871465362	-6.9843394534	-0.4760635219
H	6.0213639124	-3.5406422807	-0.5015065070

H	6.5032141846	-1.2316573450	-0.1481688338
H	6.9356944424	1.9835493131	-3.5927156454
H	3.9780637396	3.0617076432	-7.1306394516
H	3.0675395064	1.4785931668	-8.6614519288
H	-0.0411831528	-0.0134110108	-8.4687141404
H	-4.6999164117	-1.9622589549	-7.0598473957
H	-2.9039391886	-1.9676912736	-8.6263084957
H	-5.1969421500	-5.0532431888	-3.5235604103
H	-4.7423551943	5.8140120304	2.9928249244
H	-2.6674336406	7.0156105574	2.9826317342
H	-4.0607410847	6.9988572255	-0.3698020210
H	-2.2171476938	3.8637572827	4.7248940991
H	0.6998669372	5.0226699930	2.9150575824
H	-0.4382281706	6.9596104243	-0.2336173924
H	-5.8260067600	3.8380805016	-0.2071350442
H	-4.6871330116	1.8988753859	2.9420646976
H	-5.1509848247	5.0727391089	-3.5265212821
H	-1.8734201042	6.9726348975	-3.5439614291
H	1.1062881603	1.9122852253	4.6893452109
H	-2.1725010493	0.0108612683	4.7068002061
H	-5.8108147169	0.0085511911	-0.1934183682
H	1.1762166089	-1.9931735808	4.6641121260
H	2.8760695207	5.0435095895	-0.2390188285
H	-2.9545763086	5.0395554241	-6.7433972762
H	-6.9459872919	1.9565329808	-2.8154325006
H	-6.1104039164	1.9502023130	-5.0469435022
H	-3.1458340514	-3.0703875536	3.1066082790
H	-4.9125327652	-1.5013802083	2.7997225986
H	3.7592771113	3.5334495751	2.7510222232
H	4.2523940966	1.2240063210	3.0689281187
H	1.3031452370	6.2513511597	-5.0826892336
H	1.7300593092	6.9826652672	-2.8553742254
H	-6.9727762757	-1.9227277101	-2.9166639727
H	-6.0367596186	-1.9134730067	-5.1072716468
H	-6.0192835367	-3.5491531073	-0.3072968675
H	-4.1663172785	-5.0244648727	-0.0568752474
H	-1.1082197360	-4.2653518755	3.0242925262
H	1.1108720070	-5.0877008497	2.7332951953
H	4.2684436566	-1.1365254850	2.9963154923
H	3.8878706450	-3.4748230174	2.7238099150
H	6.0576241624	3.4696070179	-0.3803899101
H	6.4348812122	1.1326402387	-0.1150591964
H	4.6026455996	4.2472009580	-5.1780569907
H	5.1086291622	5.0838120453	-3.0059758344
H	-0.2259383858	3.5249706989	-8.6295609701
H	-4.7322154567	1.8993213135	-6.9687363699
H	0.6525473782	5.0161682626	-6.9926420676

H -3.0110230539 1.9082580693 -8.6158982183

Minimum Energy Conical Intersection Geometries (in Angstrom)

Si₁₀H₁₅

C	-0.66500	0.00000	0.00000
C	0.66500	0.00000	0.00000
H	-1.23780	0.92380	0.00000
H	-1.23780	-0.92380	0.00000
H	1.23780	0.92380	0.00000
H	1.23780	-0.92380	0.00000

Si₂₂H₂₇

Si	-0.5940904555	0.3616540930	-2.6805104047
Si	1.7550557026	0.3451103256	-2.7684170382
Si	-1.5027579220	2.3288649207	-1.7751423935
Si	-1.2363980971	-1.3821862538	-1.2579914285
Si	2.5206230408	0.6194792255	-0.5644464069
Si	-0.6223138325	2.5199713053	0.3938666098
Si	-0.4579089825	-1.5426175774	1.5170891127
Si	1.7245842491	2.6301537011	0.3484312496
Si	-1.3506481163	0.7376816209	1.7665783944
Si	1.8628161468	-1.2060408196	0.7832590069
Si	2.5461552059	-1.6991291200	-3.6242685779
Si	-3.8514324626	2.2437742855	-1.6661730014
Si	-0.4247163217	-3.5030297102	-1.9302512060
Si	-3.5791973509	-1.5494718203	-0.9617691224
Si	2.8249455405	-3.1520779670	-0.0992648329
Si	2.7487814160	-0.8237789737	2.9529312344
Si	2.5349274167	2.9812440810	2.5229366042
Si	-3.6910275005	0.7951223070	1.9014831982
Si	-0.4546834633	1.1098872702	3.9372683172
Si	-4.5159400527	0.4813907617	-0.2645026140
Si	1.8943416151	1.1669942115	3.8653316176
Si	1.8987730682	-3.4713343033	-2.2243944500
H	-1.1738164171	0.0618354369	-4.0103226054
H	2.2233553657	1.4609977905	-3.6174114922
H	-1.0820628018	3.4851591718	-2.5921224151
H	-1.1311402304	3.7742085309	0.9937682765
H	4.0018056655	0.6405725429	-0.5772747866
H	2.1293714308	3.7505192376	-0.5264611276
H	-4.1254793892	2.0894975839	2.4583237127
H	-4.1668349098	-0.2920070314	2.7764718682
H	-3.8383227001	-2.5917138873	0.0476790966

H	-4.1193916952	-2.0109926956	-2.2573476752
H	-4.4356372698	2.0805794118	-3.0109482601
H	-4.3364463599	3.5202373987	-1.1044861996
H	-5.9877693936	0.3535617047	-0.2719996540
H	4.0030027383	3.1287090971	2.5078782075
H	1.9425424050	4.2228044921	3.0585507558
H	-0.9253699345	0.0416400900	4.8396980552
H	-0.9556362606	2.4037068863	4.4380001433
H	2.4287965302	1.3521745496	5.2300637492
H	4.2176666815	-0.7304585330	2.8561902564
H	2.4024285512	-1.9715876941	3.8136684006
H	2.5335709937	-4.3015705297	0.7756058785
H	4.2865059047	-2.9763295786	-0.1977124321
H	-1.1439095982	-3.8178919403	-3.1822540359
H	-0.8091058287	-4.5011490261	-0.9158392080
H	2.0444184474	-1.9098346826	-4.9950265229
H	2.3212195488	-4.7585025460	-2.8135108121
H	4.0213152921	-1.6561013422	-3.6660899702

Si₂₆H₃₁

Si	-0.8709514730	-0.3598917130	-2.0828395194
Si	1.4823861941	-0.2789482831	-2.2262195021
Si	-1.6831631158	1.7131541168	-1.3094300428
Si	-1.5977718188	-2.1626259592	-0.7260862307
Si	2.2821092473	0.0710462959	-0.0416083340
Si	-0.7651574189	2.0238896069	0.8369561429
Si	-0.7775062319	-2.4802385376	1.5423288250
Si	1.5822403453	2.1618023327	0.7837201548
Si	-1.3487698321	0.2169484084	2.1926419629
Si	1.5922199337	-1.6737971224	1.4009136994
Si	2.1646156980	1.5112801588	-3.6026943390
Si	2.2969119331	-2.3259796636	-3.0571230367
Si	-0.9842011486	3.4975404496	-2.6770488297
Si	-4.0307472157	1.5972344900	-1.1998517686
Si	-0.7713897166	-4.1491739554	-1.7161888286
Si	-3.9439556631	-2.2201736091	-0.7473688103
Si	2.3617564939	-3.7438706793	0.4895905362
Si	2.6102222265	-1.3463988678	3.4886051800
Si	2.4636911274	2.4588818875	2.9486233415
Si	2.2114977237	3.9375761211	-0.6283823029
Si	-3.7076080092	-0.0511014420	2.2855585972
Si	-0.5015946718	0.4729089195	4.3859688209
Si	-4.6845264202	-0.1965039420	0.1607605823
Si	1.8297625042	0.6823955693	4.3450127862
Si	1.5742804039	-4.0905601260	-1.6929007380
Si	1.3591846132	3.5565108056	-2.7795380134

H	-1.4073674926	-0.5684896309	-3.4496704212
H	-1.3490389563	3.2289711340	1.4692127677
H	3.7644290172	0.0548104427	-0.0649945724
H	-4.1704624446	1.1502893567	3.0117263703
H	-4.0343093484	-1.2369843982	3.0927944156
H	-4.4178112064	-3.3310711416	0.0992663737
H	-4.4646432358	-2.4064381830	-2.1154486182
H	-4.5419809386	1.3756796591	-2.5674395666
H	-4.5831572180	2.8708142273	-0.7042138547
H	-6.1513746662	-0.1828351849	0.3306144362
H	3.9362662048	2.4941836154	2.8362571721
H	2.0078884660	3.7443755151	3.5105071943
H	-0.9084620468	-0.6879045272	5.1994562432
H	-1.1453619760	1.6853577445	4.9310994383
H	2.3187925948	0.9236854608	5.7190456407
H	4.0740747003	-1.3101987721	3.3012266728
H	2.2631580003	-2.4466056823	4.4043910733
H	1.9224478461	-4.8306326005	1.3810335170
H	3.8377664341	-3.7039342450	0.4879548551
H	-1.2469650110	-4.2642562735	-3.1099497042
H	-1.2601676749	-5.3146501793	-0.9542517928
H	1.8007534500	-2.5184073326	-4.4331022372
H	2.1255415115	-5.3622769010	-2.2051764996
H	3.7718890467	-2.2797622740	-3.0910929885
H	1.6593084830	1.2970602796	-4.9716520939
H	3.6410598188	1.5412274457	-3.6495792725
H	3.6850194558	4.0547529181	-0.6581450301
H	1.6556030870	5.1877645473	-0.0748261669
H	-1.4967916662	4.7544655035	-2.0988753773
H	-1.5549736226	3.3403509844	-4.0286969087
H	1.7878591380	4.6513070455	-3.6752175997

Si₄₇H₄₉

Si	-1.0805163359	-1.0841087306	-1.5771394436
Si	1.2730095406	-0.9859890166	-1.7430896817
Si	-1.9594752751	0.9470017532	-0.7123441710
Si	-1.6589471478	-2.8792031405	-0.1364528900
Si	2.0880606584	-0.6022105005	0.4419824348
Si	-1.0984706687	1.3060060935	1.4686582831
Si	-1.3804333890	-2.8005157439	2.3870804849
Si	1.2683286793	1.4243584888	1.3688853256
Si	-1.7771225778	-0.4590647147	2.9127505529
Si	1.3296261654	-2.3642270603	1.7788367191
Si	1.9617901828	0.8030323164	-3.1233441522
Si	2.0464527242	-3.0811023566	-2.5566238023
Si	-1.2934364012	2.7131259106	-2.1499938956

Si	-4.3221979913	0.7942518029	-0.5793705540
Si	-0.9578634906	-4.9268210788	-1.0549409057
Si	-4.0423729610	-2.9647157019	0.0474973477
Si	2.0728757438	-4.4821870866	1.0554050198
Si	2.0727929308	-2.0901249390	4.0184129425
Si	2.1132758642	1.6834184735	3.5736166516
Si	1.9374420562	3.2072371833	-0.0381341679
Si	-4.1441316747	-0.4707314865	3.0172867845
Si	-0.9811062610	-0.0807160889	5.0871890812
Si	-4.9347988066	-0.9608767073	0.8595411802
Si	1.3437084607	-0.0626814944	4.9472014678
Si	1.3816834996	-4.8382216827	-1.1383153100
Si	1.0660892172	2.7744967477	-2.1896031643
Si	-1.8831327919	-1.4559480238	-3.7776353409
Si	-1.9900298926	3.3792715186	2.1963822061
Si	4.4504997352	-0.4894696345	0.4675275650
Si	-4.9733493506	1.5799704030	3.8131647647
Si	-5.3301868663	2.7401201315	0.2670210574
Si	4.4570073061	1.6408014720	3.7311366905
Si	4.4377669585	-2.1416630484	3.9257200319
Si	-1.9192139135	-5.2443957890	-3.1752871020
Si	1.1823430219	-3.6304848912	-4.6768476540
Si	1.0536428443	0.6843412662	-5.2949068780
Si	4.3173762793	0.8901516243	-3.1395463639
Si	4.2763493778	3.3357630484	-0.2907762346
Si	1.0888224525	5.2398163413	0.7928676092
Si	-1.9335359852	4.8526776727	-1.3982258975
Si	-2.1844718619	2.3162024613	-4.2934647126
Si	-4.3399731709	3.2795803135	2.3258884482
Si	-1.1598151429	-3.5402635970	-4.5974557428
Si	5.2293212478	-0.3104764429	2.6811935871
Si	-1.2672353588	0.3455136613	-5.1679846886
Si	-1.2531340657	5.1447482067	0.8263630714
Si	5.1283771411	1.2546600126	-0.9636777148
H	-4.5410739400	-1.5527447654	3.9414566464
H	-4.4132789808	-4.1170622451	0.8835354701
H	-4.5443977790	-3.1928530189	-1.3233510096
H	-4.8489659278	0.5087864537	-1.9299454459
H	-6.4110597236	-1.0611176823	0.8637645288
H	1.6019677579	2.9674342594	4.0976149243
H	-1.4217452843	-1.1851764240	5.9599788476
H	-1.4740269899	1.1945435757	5.6385436616
H	1.9863308135	0.0710480392	6.2723721381
H	1.5854836010	-3.2320282823	4.8181754077
H	1.5128891733	-5.5038430003	1.9570823058
H	3.5439865828	-4.5100082724	1.1674269714
H	-1.3713293053	-5.9978611291	-0.1252088080

H	1.9394899825	-6.1000218844	-1.6724705328
H	3.5230393488	-3.0477836767	-2.6168140070
H	1.4680869818	3.8983849995	-3.0666762460
H	4.9536837759	-2.0575831999	5.3060639554
H	4.8917680998	-3.4094448704	3.3275131468
H	6.7061679720	-0.3313278428	2.6696083416
H	5.0798531411	2.8482242990	3.1655885680
H	4.8032574466	1.5671980584	5.1638241966
H	6.6065763308	1.2946260092	-0.9809404479
H	4.5496874851	4.3150942039	-1.3615471258
H	4.9195002642	3.8184897069	0.9413822324
H	1.5260529822	6.3323746583	-0.0981388439
H	1.6370103274	5.4909909487	2.1384758784
H	-1.8049075597	6.4106298028	1.3535310979
H	-3.3780801353	5.0692193935	-1.5694749264
H	-1.2220214589	5.8330583512	-2.2439817550
H	4.7506917211	2.0135698284	-3.9945777156
H	4.8577461308	-0.3604920813	-3.7019150527
H	1.2881991394	1.9930697710	-5.9379331725
H	1.7155626434	-0.3462410152	-6.1101109085
H	-1.7992275312	0.0898288593	-6.5242289285
H	-3.6487859746	2.1975276122	-4.1788151979
H	-1.8744855797	3.4545300305	-5.1816022029
H	-3.3609887150	-1.4838066585	-3.7390219633
H	-1.7061774496	-3.7383832448	-5.9560181943
H	-1.5130379633	-6.5612865860	-3.7046082800
H	-3.3884394172	-5.2092047319	-3.0705168464
H	4.9740742875	-1.7599180691	-0.0794442084
H	1.7112405500	-2.7498540184	-5.7291302974
H	1.5977190621	-5.0151450158	-4.9778606456
H	-4.8437189582	4.5882517738	2.7933657081
H	-6.4469617364	1.5309177546	3.8902858626
H	-4.4407775950	1.8372424359	5.1631119043
H	-6.7536859424	2.4284330714	0.5069765306
H	-5.2588745496	3.8495503069	-0.6942662775
H	-1.4887048558	3.6433093787	3.5632932730

Si₇₂H₆₃

Si	0.0076002773	0.0056878681	2.3708277395
Si	0.0388678163	-0.0271752787	4.7433961007
Si	2.2231615770	0.0460193503	1.5502747400
Si	2.2309883884	0.0643150535	-0.8191592070
Si	-1.0660751180	-1.9621135920	1.6143122203
Si	-1.1177450367	1.9420816251	1.5795860257
Si	-1.1044802497	-1.9183219249	-0.7636832829
Si	-1.1208353745	1.9503635050	-0.8034979572

Si	0.1301609942	-3.8721305426	2.3984874764
Si	3.2514668906	-1.9332589739	2.2374923626
Si	0.1938841260	-3.9748777120	4.7475493911
Si	3.2965035309	-2.2402336536	4.5774371711
Si	1.1580409709	-1.9724038170	5.4960694492
Si	2.3655890295	-4.5148827101	1.5266609144
Si	-2.2569459388	0.0077989005	-1.5797008146
Si	1.1153121864	2.0032212908	-1.6160278910
Si	1.1360977731	-1.9045997432	-1.5552269043
Si	-2.2511119269	3.8774231123	-1.5941466582
Si	-2.2501982494	3.8445155187	-3.9618836196
Si	-3.2920693497	1.9173367229	-4.8158434595
Si	-0.0928976178	3.7689470538	-4.8972864592
Si	-2.2405977541	-0.0088411470	-3.9540753312
Si	1.1066941992	1.9557245775	-3.9887394326
Si	-0.0006399813	-0.0063687198	-4.6770408721
Si	2.3185666224	-3.8253030086	-0.8165559723
Si	1.1236974130	-1.9327837569	-3.9235026057
Si	4.4958219790	-3.8050515651	-1.7201730349
Si	1.1355267989	-5.7329503979	-1.6297484031
Si	0.0065071529	-3.8673699020	-4.6944504959
Si	3.3412608519	-1.9179429734	-4.7380920371
Si	1.1533283460	-5.7808705948	-3.9757829612
Si	4.4533693174	-3.8700665055	-4.0619187771
Si	-2.1949866705	0.0001916491	5.5231179376
Si	1.1284092509	1.9269302186	5.5090838101
Si	-3.3322328673	1.9562066057	2.4007970846
Si	-0.0237825128	3.8758716038	2.3893989698
Si	-4.4575359232	3.8719699829	-0.7385149150
Si	-1.1484542182	5.7960154540	-0.7560246118
Si	-1.1731836457	5.7859797714	1.5991457948
Si	-0.0237546411	3.8378079940	4.7535862745
Si	-3.2837909112	1.9457248444	4.7646212878
Si	-4.4248951462	3.8996783235	1.6152457231
Si	-2.2309368513	3.8895113349	5.5538717009
Si	-3.3566633100	5.8107704624	2.4557169506
Si	-3.3302852151	5.8197767295	4.8004680732
Si	-3.2028966949	-1.9481115614	-4.8772995077
Si	-4.4790396219	0.0235634836	-0.7441136282
Si	-2.2451393375	-3.8397815971	-1.5492493921
Si	-2.2134434203	-3.8462197707	-3.9151866920
Si	-0.8836131062	-5.8534195153	1.5537186624
Si	-1.0657385351	-5.7445897805	-0.7845133043
Si	-3.3038699787	-1.9449390977	2.4087992635
Si	-4.3733830466	0.0025995986	1.6076930327
Si	-5.6731813604	-1.8985494286	-1.3957598948
Si	-4.6061115241	-3.7353471865	1.5981350578

Si	-4.4727910760	-3.8151922249	-0.7483541829
Si	3.3527705657	-5.8108167116	-4.7878257736
Si	3.3613180139	1.9594758698	2.3734002379
Si	2.2145542231	3.9343855207	-0.7782135698
Si	2.1840045051	3.8467346744	1.5780379879
Si	5.5596252189	-1.8869396835	-0.8781057869
Si	4.4330166157	0.0269401859	-3.9732774914
Si	4.4654595593	0.0797696298	-1.6059128755
Si	5.5664383491	2.1185873056	1.5530678480
Si	4.4843011713	4.0193135439	-1.4035332562
Si	5.5559306464	2.0161316189	-0.7953483948
Si	3.3374274601	2.0774630361	4.7257763447
Si	-3.4698393347	-1.8138707218	4.7520130667
Si	-5.7067968479	1.9610214077	-1.2849404613
Si	1.1164724177	5.9340999367	-1.3612258894
Si	5.4567684811	-2.2195877210	1.4342453542
Si	3.2727534258	1.8417241656	-4.9073993858
H	3.3462226780	-5.8757488699	-6.2611360495
H	4.0575605465	-6.9974131540	-4.2653154696
H	0.4228055487	-6.9830750383	-4.4318051355
H	5.8422355555	-3.8476807973	-4.5691446044
H	5.2102235349	-4.9867614124	-1.1908601692
H	3.2799795304	-1.8593258373	-6.2154633257
H	1.8291913638	-6.9283667253	-1.1067286987
H	-0.0154167020	-3.8158962458	-6.1729377676
H	5.8327736596	0.0170082342	-4.4530938889
H	6.9723057679	-1.8441731863	-1.3124276253
H	-1.7585878451	-6.9531071087	-1.2812313213
H	-2.9032559171	-5.0686477947	-4.3807009684
H	-2.1844335052	-6.0562979790	2.2059284518
H	-0.0150511567	-6.9901711361	1.9069712129
H	5.8870691918	-3.5932552577	1.7485806756
H	6.3022436936	-1.2959688665	2.2096049735
H	6.9452124135	2.0191709680	-1.3015674417
H	4.0005769785	3.1068692531	-4.7317832803
H	3.1327486158	1.6046783296	-6.3575156110
H	-0.0016345125	-0.0220192205	-6.1575893667
H	-4.6671523728	-1.9458092559	-4.7508424050
H	-2.8772262187	-1.9489619377	-6.3169131662
H	-5.1555624499	-5.0268163064	-1.2509614564
H	-4.7102404438	5.8521220266	5.3196531593
H	-2.6175022376	7.0185907091	5.2819160604
H	-4.0566770432	7.0082452598	1.9460349560
H	-2.2052634557	3.8626155354	7.0317085293
H	0.7059525339	5.0379451000	5.2204600205
H	-0.4382938287	6.9799115442	2.0708599351
H	-5.8250762583	3.8570148611	2.0895292391

H	-4.6828899720	1.9096361080	5.2445886612
H	-5.1430227770	5.0896711229	-1.2222828390
H	-1.8732032858	6.9925601329	-1.2366616102
H	1.1242799976	1.9194311872	6.9886279421
H	-2.1651284030	0.0089185832	7.0020961362
H	-5.7634210639	-0.0330270519	2.1141907802
H	1.2504730830	-1.9317926481	6.9711231104
H	2.8891912936	5.0488410902	2.0776013812
H	-2.9546652615	5.0520111482	-4.4453260526
H	-6.8950611115	1.9573002189	-0.4079777109
H	-6.1781871239	1.9567266320	-2.6774575875
H	-3.0851761039	-3.0750013580	5.4004318088
H	-4.8856594205	-1.5534437255	5.0779006530
H	3.9015265915	3.3834234507	5.1201352677
H	4.1801146605	1.0226093507	5.3116647741
H	1.3022243533	6.2609355322	-2.7832235299
H	1.7278151306	7.0146696742	-0.5620914299
H	-6.9431511311	-1.8982149961	-0.6415467730
H	-5.9946246761	-1.8668044024	-2.8305640124
H	-6.0076561482	-3.4240960396	1.9446632936
H	-4.2523785059	-5.0110984204	2.2369987743
H	-1.1261220549	-4.2683107540	5.3193262742
H	1.1095911072	-5.0671351093	5.1264859133
H	4.3286681026	-1.3456454741	5.1233086827
H	3.7317896234	-3.6251365369	4.8298737253
H	6.0826344429	3.4463483278	1.9415354394
H	6.4345468528	1.0977060015	2.1602235847
H	4.6428605522	4.3511312951	-2.8268045320
H	5.1054058241	5.1007843207	-0.6119526705
H	-0.2471736554	3.5114448810	-6.3440957393
H	-4.7330203240	1.8914639066	-4.5237388865
H	0.6437048613	5.0321223019	-4.7344943837
H	-3.1272290280	1.9148404136	-6.2833083349

REFERENCES

REFERENCES

1. J. Michl and V. Bonacic-Koutecky, *Electronic Aspects of Organic Photochemistry*, Wiley, New York, 1990.
2. D. R. Yarkony, *Rev. Mod. Phys.*, Diabolical conical intersections. 1996, **68**, 985-1013.
3. F. Bernardi, M. Olivucci and M. A. Robb, Potential energy surface crossings in organic photochemistry. *Chem. Soc. Rev.*, 1996, **25**, 321-328.
4. B. G. Levine and T. J. Martinez, Isomerization through conical intersections. *Annu. Rev. Phys. Chem.*, 2007, **58**, 613-634.
5. S. Matsika and P. Krause, Nonadiabatic events and conical intersections. *Annu. Rev. Phys. Chem.*, 2011, **62**, 621-643.
6. D. R. Yarkony, Nonadiabatic quantum chemistry – past, present, and future. *Chem. Rev.*, 2012, **112**, 481-498.
7. R. Gonzalez-Luque, M. Garavelli, F. Bernardi, M. Merchan, M. A. Robb and M. Olivucci, Computational evidence in favor of a two-state, two-mode model of the retinal chromophore photoisomerization. *Proc. Natl. Acad. Sci. U. S. A.*, 2000, **97**, 9379-9384.
8. M. L. Hause, Y. H. Yoon, A. S. Case and F. F. Crim, Dynamics at conical intersections: The influence of O–H stretching vibrations on the photodissociation of phenol. *J. Chem. Phys.*, 2008, **128**, 104307-104309.
9. K. R. Yang, X. F. Xu, J. J. Zheng and D. G. Truhlar, Full-dimensional potentials and state couplings and multidimensional tunneling calculations for the photodissociation of phenol. *Chem. Sci.*, 2014, **5**, 4661-4680.
10. X. L. Zhu and D. R. Yarkony, Fitting coupled potential energy surfaces for large systems: Method and construction of a 3-state representation for phenol photodissociation in the full 33 internal degrees of freedom using multireference configuration interaction determined data. *J. Chem. Phys.*, 2014, **140**, 024112.
11. D. Polli, P. Altoe, O. Weingart, K. M. Spillane, C. Manzoni, D. Brida, G. Tomasello, G. Orlandi, P. Kukura, R. A. Mathies, M. Garavelli and G. Cerullo, Conical Intersection Dynamics of the Primary Photoisomerization Event in Vision. *Nature*, 2010, **467**, 440-U488.
12. M. Liebel, C. Schnedermann and P. Kukura, Vibrationally Coherent Crossing and Coupling of Electronic States During Internal Conversion in B-Carotene. *Phys. Rev. Lett.*, 2014, **112**, 198302.

13. S. Matsika, Radiationless decay of excited states of uracil through conical intersections. *J. Phys. Chem. A*, 2004, **108**, 7584-7590.
14. M. Merchan and L. Serrano-Andres, Ultrafast internal conversion of excited cytosine via the lowest $\pi\pi^*$ electronic singlet state. *J. Am. Chem. Soc.*, 2003, **125**, 8108-8109.
15. I. Schapiro, F. Melaccio, E. N. Laricheva and M. Olivucci, Using the computer to understand the chemistry of conical intersections. *Photochem. Photobiol. Sci.*, 2011, **10**, 867-886.
16. B. S. Fales and B. G. Levine, Nanoscale multireference quantum chemistry: full configuration interaction on graphical processing units. *J. Chem. Theory Comput.*, 2015, **11**, 4708-4716.
17. Y. N. Shu, B. S. Fales and B. G. Levine, Defect-induced conical intersections promote nonradiative recombination. *Nano Lett*, 2015, **15**, 6247-6253.
18. Y. N. Shu, B. S. Fales, W.-T. Peng and B. G. Levine, Understanding nonradiative recombination through defect-induced conical intersections. *J. Phys. Chem. Lett.*, 2017, **8**, 4091-4099.
19. L. T. Canham, Silicon quantum wire array fabrication by electrochemical and chemical dissolution of wafers. *Appl. Phys. Lett.*, 1990, **57**, 1046-1048.
20. V. Kocevski, O. Eriksson and J. Ruzs, Transition Between Direct and Indirect Band Gap in Silicon Nanocrystals. *Phys. Rev. B*, 2013, **87**, 245401.
21. M. L. Mastronardi, F. Hennrich, E. J. Henderson, F. Maier-Flaig, C. Blum, J. Reichenbach, U. Lemmer, C. Kubel, D. Wang, M. M. Kappes and G. A. Ozin, Preparation of Monodisperse Silicon Nanocrystals Using Density Gradient Ultracentrifugation. *J. Am. Chem. Soc.*, 2011, **133**, 11928-11931.
22. B. Delley and E. F. Steigmeier, Quantum confinement in Si nanocrystals. *Phys. Rev. B*, 1993, **47**, 1397-1400.
23. S. Furukawa and T. Miyasato, Quantum size effects on the optical band gap of microcrystalline Si:H. *Phys. Rev. B*, 1988, **38**, 5726-5729.
24. Z. Y. Zhou, L. Brus and R. Friesner, Electronic structure and luminescence of 1.1- and 1.4-nm silicon nanocrystals: Oxide shell versus hydrogen passivation. *Nano Lett*, 2003, **3**, 163-167.
25. D. Konig, J. Rudd, M. A. Green and G. Conibeer, Impact of interface on the effective bandgap of Si quantum dot. *Sol. Energy Mater. Sol. Cells*, 2009, **93**, 753-758.

26. M. Dasog, G. B. De los Reyes, L. V. Titova, F. A. Hegmann and J. G. C. Veinot, Size vs surface: Tuning the photoluminescence of freestanding silicon nanocrystals across the visible spectrum via surface groups. *ACS Nano*, 2014, **8**, 9636-9648.
27. H. S. Li, Z. G. Wu, T. L. Zhou, A. Sellinger and M. T. Lusk, Tailoring the Optical Gap of Silicon Quantum Dots Without Changing Their Size. *Phys. Chem. Chem. Phys.*, 2014, **16**, 19275-19281.
28. B. Gelloz and N. Koshida, Electroluminescence with High and Stable Quantum Efficiency and Low Threshold Voltage From Anodically Oxidized Thin Porous Silicon Diode. *J. Appl. Phys.*, 2000, **88**, 4319-4324.
29. C. Y. Liu, Z. C. Holman and U. R. Kortshagen, Hybrid Solar Cells From P3HT and Silicon Nanocrystals. *Nano Lett*, 2009, **9**, 449-452.
30. J. Valenta, N. Lalic and J. Linnros, Electroluminescence Microscopy and Spectroscopy of Silicon Nanocrystals in Thin SiO₂ Layers. *Opt. Mater.*, 2001, **17**, 45-50.
31. J. H. Park, L. Gu, G. von Maltzahn, E. Ruoslahti, S. N. Bhatia and M. J. Sailor, Biodegradable Luminescent Porous Silicon Nanoparticles for in Vivo Applications. *Nat. Mater.*, 2009, **8**, 331-336.
32. L. Pavesi, L. Dal Negro, C. Mazzoleni, G. Franzo and F. Priolo, Optical Gain in Silicon Nanocrystals. *Nature*, 2000, **408**, 440-444.
33. D. Liang and J. E. Bowers, Recent Progress in Lasers on Silicon. *Nat. Photonics*, 2010, **4**, 511-517.
34. M. A. Tischler, R. T. Collins, J. H. Stathis and J. C. Tsang, Luminescence degradation in porous silicon. *Appl. Phys. Lett.*, 1992, **60**, 639-641.
35. C. Delerue, G. Allan and M. Lannoo, Theoretical aspects of the luminescence of porous silicon. *Phys. Rev. B*, 1993, **48**, 11024-11036.
36. M. Schoisswohl, J. L. Cantin, H. J. Vonbardeleben and G. Amato, Electron Paramagnetic Resonance Study of Luminescent Stain Etched Porous Silicon. *Appl. Phys. Lett.*, 1995, **66**, 3660-3662.
37. R. N. Pereira, D. J. Rowe, R. J. Anthony and U. Kortshagen, Oxidation of freestanding silicon nanocrystals probed with electron spin resonance of interfacial dangling bonds. *Phys. Rev. B*, 2011, **83**, 155327.
38. N. P. Brawand, M. Voros and G. Galli, Surface Dangling Bonds Are a Cause of B-Type Blinking in Si Nanoparticles. *Nanoscale*, 2015, **7**, 3737-3744.

39. E. H. Poindexter, P. J. Caplan, B. E. Deal and R. R. Razouk, Interface States and Electron Spin Resonance Centers in Thermally Oxidized (111) and (100) Silicon Wafers.. *J. Appl. Phys.*, 1981, **52**, 879-884.
40. S. Niesar, A. R. Stegner, R. N. Pereira, M. Hoeb, H. Wiggers, M. S. Brandt and M. Stutzmann, Defect Reduction in Silicon Nanoparticles by Low-Temperature Vacuum Annealing. *Appl. Phys. Lett.*, 2010, **96**, 193112.
41. H. S. Li, Z. G. Wu and M. T. Lusk, Dangling Bond Defects: the Critical Roadblock to Efficient Photoconversion in Hybrid Quantum Dot Solar Cells. *J. Phys. Chem. C*, 2014, **118**, 46-53.
42. B. K. Meyer, V. Petrovakocho, T. Muschik, H. Linke, P. Omling and V. Lehmann, Electron Spin Resonance Investigations of Oxidized Porous Silicon. *Appl. Phys. Lett.*, 1993, **63**, 1930-1932.
43. B. G. Fernandez, M. Lopez, C. Garcia, A. Perez-Rodriguez, J. R. Morante, C. Bonafos, M. Carrada and A. Claverie, Influence of Average Size and Interface Passivation on the Spectral Emission of Si Nanocrystals Embedded in SiO₂. *J. Appl. Phys.*, 2002, **91**, 798-807.
44. X. D. Pi, L. Mangolini, S. A. Campbell and U. Kortshagen, Room-Temperature Atmospheric Oxidation of Si Nanocrystals After HF Etching. *Phys. Rev. B*, 2007, **75**, 177.
45. C. Delerue and M. Lannoo, *Nanostructure: Theory and Modelling*, Springer-Verlag, Berlin, 2004.
46. M. Lannoo, C. Delerue and G. Allan, Nonradiative recombination on dangling bonds in silicon crystallites. *J. Lumines.*, 1993, **57**, 243-247.
47. J. C. Chen, A. Schmitz, T. Inerbaev, Q. G. Meng, S. Kilina, S. Tretiak and D. S. Kilin, First-principles study of p-n-doped silicon quantum dots: Charge transfer, energy dissipation, and time-resolved emission. *J. Phys. Chem. Lett.*, 2013, **4**, 2906-2913.
48. J. Liu, A. J. Neukirch and O. V. Prezhdo, Phonon-Induced Pure-Dephasing of Luminescence, Multiple Exciton Generation, and Fission in Silicon Clusters.. *J. Chem. Phys.*, 2013, **139**, 164303.
49. Y. A. Shu and B. G. Levine, Communication: Non-Radiative Recombination via Conical Intersection at a Semiconductor Defect. *J. Chem. Phys.*, 2013, **139**, 081102.
50. J. Liu, A. J. Neukirch and O. V. Prezhdo, Non-Radiative Electron-Hole Recombination in Silicon Clusters: Ab Initio Non-Adiabatic Molecular Dynamics. *J. Phys. Chem. C*, 2014, **118**, 20702-20709.

51. Y. A. Shu and B. G. Levine, Do Excited Silicon–Oxygen Double Bonds Emit Light? *J. Phys. Chem. C*, 2014, **118**, 7669-7677.
52. Y. Han, D. A. Micha and D. S. Kilin, Ab initio study of the photocurrent at the Au/Si metal-semiconductor nanointerface. *Mol. Phys.*, 2015, **113**, 327-335.
53. K. G. Reeves, A. Schleife, A. A. Correa and Y. Kanai, Role of surface termination on hot electron relaxation in silicon quantum dots: A first-principles dynamics simulation study. *Nano Lett*, 2015, **15**, 6429-6433.
54. Y. N. Shu and B. G. Levine, Nonradiative Recombination via Conical Intersections Arising at Defects on the Oxidized Silicon Surface. *J. Phys. Chem. C*, 2015, **119**, 1737-1747.
55. Y. N. Shu and B. G. Levine, First-principles study of nonradiative recombination in silicon nanocrystals: The role of surface silanol. *J. Phys. Chem. C*, 2016, **120**, 23246-23253.
56. N. P. Brawand, M. B. Goldey, M. Voros and G. Galli, Defect states and charge transport in quantum dot solids. *Chem. Mat.*, 2017, **29**, 1255-1262.
57. G. Granucci, M. Persico and A. Toniolo, Direct semiclassical simulation of photochemical processes with semiempirical wave functions. *J. Chem. Phys.*, 2001, **114**, 10608-10615.
58. P. Slavicek and T. J. Martinez, Ab Initio Floating Occupation Molecular Orbital-Complete Active Space Configuration Interaction: an Efficient Approximation to CASSCF. *J. Chem. Phys.*, 2010, **132**, 234102.
59. B. G. Levine, C. Ko, J. Quenneville and T. J. Martinez, Conical Intersections and Double Excitations in Time-Dependent Density Functional Theory.. *Mol. Phys.*, 2006, **104**, 1039-1051.
60. J. Finley, P. A. Malmqvist, B. O. Roos and L. Serrano-Andres, The multi-state CASPT2 method. *Chem. Phys. Lett.*, 1998, **288**, 299-306.
61. I. S. Ufimtsev and T. J. Martinez, Quantum Chemistry on Graphical Processing Units. 3. Analytical Energy Gradients, Geometry Optimization, and First Principles Molecular Dynamics. *J. Chem. Theory Comput.*, 2009, **5**, 2619-2628.
62. E. G. Hohenstein, M. E. F. Bouduban, C. C. Song, N. Luehr, I. S. Ufimtsev and T. J. Martinez, Analytic First Derivatives of Floating Occupation Molecular Orbital-Complete Active Space Configuration Interaction on Graphical Processing Units. *J. Chem. Phys.*, 2015, **143**, 014111.

63. C. C. Song, L. P. Wang and T. J. Martinez, Automated code engine for graphical processing units: Application to the effective core potential integrals and gradients. *J. Chem. Theory Comput.*, 2016, **12**, 92-106.
64. P. J. Knowles and H. J. Werner, An efficient second-order MC SCF method for long configuration expansions. *Chem. Phys. Lett.*, 1985, **115**, 259-267.
65. H.-J. Werner and P. J. Knowles, A second order multiconfiguration SCF procedure with optimum convergence. *J. Chem. Phys.*, 1985, **82**, 5053-5063.
66. H. J. Werner, Third-order multireference perturbation theory: The CASPT3 method. *Mol. Phys.*, 1996, **89**, 645-661.
67. P. Celani and H. J. Werner, Multireference perturbation theory for large restricted and selected active space reference wave functions. *J. Chem. Phys.*, 2000, **112**, 5546-5557.
68. H. J. Werner, P. J. Knowles, G. Knizia, F. R. Manby and M. Schutz, Molpro: a general-purpose quantum chemistry program package. *Wires Comput. Mol. Sci.*, 2012, **2**, 242-253.
69. M. W. Schmidt, K. K. Baldridge, J. A. Boatz, S. T. Elbert, M. S. Gordon, J. H. Jensen, S. Koseki, N. Matsunaga, K. A. Nguyen, S. Su, T. L. Windus, M. Dupuis and J. A. Montgomery, General atomic and molecular electronic structure system. *J. Comput. Chem.*, 1993, **14**, 1347-1363.
70. J. R. Gour, P. Piecuch and M. Wloch, Active-space equation-of-motion coupled-cluster methods for excited states of radicals and other open-shell systems: EA-EOMCCSDt and IP-EOMCCSDt. *J. Chem. Phys.*, 2005, **123**, 134113.
71. J. R. Gour and P. Piecuch, Efficient formulation and computer implementation of the active-space electron-attached and ionized equation-of-motion coupled-cluster methods. *J. Chem. Phys.*, 2006, **125**, 234107.
72. B. G. Levine, J. D. Coe and T. J. Martinez, Optimizing Conical Intersections Without Derivative Coupling Vectors: Application to Multistate Multireference Second-Order Perturbation Theory (MS-CASPT2). *J. Phys. Chem. B*, 2008, **112**, 405-413.
73. D. G. Truhlar and C. A. Mead, Relative Likelihood of Encountering Conical Intersections and Avoided Intersections on the Potential Energy Surfaces of Polyatomic Molecules. *Phys. Rev. A*, 2003, **68**, 457.
74. D. Jurbergs, E. Rogojina, L. Mangolini and U. Kortshagen, Silicon Nanocrystals with Ensemble Quantum Yields Exceeding 60%. *Appl. Phys. Lett.*, 2006, **88**, 233116.

75. T. Schmidt, A. I. Chizhik, A. M. Chizhik, K. Potrick, A. J. Meixner and F. Huisken, Radiative exciton recombination and defect luminescence observed in single silicon nanocrystals. *Phys. Rev. B*, 2012, **86**, 125302.
76. F. Huisken, G. Ledoux, O. Guillois and C. Reynaud, Light-emitting silicon nanocrystals from laser pyrolysis. *Adv. Mater.*, 2002, **14**, 1861-1865.
77. M. V. Wolkin, J. Jorne, P. M. Fauchet, G. Allan and C. Delerue, Electronic states and luminescence in porous silicon quantum dots: The role of oxygen. *Phys. Rev. Lett.*, 1999, **82**, 197-200.
78. C. Garcia, B. Garrido, P. Pellegrino, R. Ferre, J. A. Moreno, J. R. Morante, L. Pavesi and M. Cazzanelli, Size dependence of lifetime and absorption cross section of Si nanocrystals embedded in SiO₂. *Appl. Phys. Lett.*, 2003, **82**, 1595-1597.
79. I. Sychugov, R. Juhasz, J. Valenta and J. Linnros, Narrow luminescence linewidth of a silicon quantum dot. *Phys. Rev. Lett.*, 2005, **94**, 087405.

CHAPTER 3 AB INITIO MOLECULAR DYNAMICS STUDY OF THE INTERACTION BETWEEN DEFECTS DURING NONRADIATIVE RECOMBINATION

Reproduced with permission from “Ab Initio Molecular Dynamics Study of the Interaction Between Defects During Nonradiative Recombination”, W.-T. Peng, B. G. Levine, *J. Phys. Chem. C.*, 123, 16588, 2019. Copyright 2019 American Chemical Society.

3.1. Introduction

As a result of quantum confinement effects, low-dimensional silicon materials such as porous silicon and silicon nanocrystals (SiNCs) have desirable optoelectronic properties, including efficient emission of visible light.¹⁻³ As such, SiNCs have gained attention as potential materials for light emitting diodes,⁴⁻⁷ solar cells,⁸⁻⁹ and semiconductor lasers.¹⁰⁻¹¹ Though they have desirable optical properties, hydrogen-terminated SiNCs are prone to oxidation under ambient conditions, dramatically changing both the color and yield of photoluminescence (PL).¹²⁻¹³ Several defects arising during oxidation have been experimentally characterized, including dangling bonds (DB), silanol groups (Si-OH), bridging oxygen atoms, and silicon epoxide rings.¹⁴⁻¹⁸ DB defects, in particular, have been determined to be important nonradiative (NR) decay centers.¹⁴⁻¹⁵ The certainty of this determination was possible because DB defects are easily observable in electron paramagnetic resonance experiments, and this signal shows a strong inverse correlation with PL yields. However, due to the complex heterogeneous nature of the interface and the lack of experimental techniques that can unambiguously connect atomistic structure to function in nanomaterials, the role of many other defects remains unclear, as does the detailed NR decay mechanism in real nanoparticles. Theoretical and computational methods offer the opportunity to gain microscopic insights into the decay process that can guide future experiments and material design.

Theoretically, nonradiative recombination is most often viewed through the lens of electronic band theory. In this theory, the exciton is generated by creation of an electron and a hole in the conduction and valence bands, respectively. Most often interactions between charge carriers and with the lattice are neglected, though techniques for incorporation of both of these

effects exist and have been applied in the study of silicon nanomaterials.¹⁹⁻²² Neglect of these interactions is a good approximation when one considers spatially delocalized excitations (e.g. quantum-confined excitons). However, in band theory recombination involving defects (Shockley-Read-Hall or SRH recombination²³⁻²⁴) requires the localization of charge carriers to mid-gap states centered on the defect site. One might expect interactions between charge carriers and with the lattice to be stronger in these more localized states, requiring a many-body treatment of the electronic structure and an explicit treatment of local geometric distortions to obtain an accurate picture of recombination dynamics. Indeed the importance of lattice relaxation during NR recombination at DB defects has been known for several decades.¹⁹

Recently, our group has proposed the notion of defect induced conical intersections (DICIs): points of degeneracy between the potential energy surfaces (PESs) of materials that arise through local distortions of the nuclear and electronic structures at defect sites.²⁵⁻²⁷ Conical intersections (CIs) are a textbook concept in molecular photochemistry, where they are known to facilitate ultrafast transitions between electronic states.²⁸⁻³¹ In the context of silicon PL, identification of DICIs has yielded insights into the effect of surface chemistry on both yield and color of luminescence. Our group has identified intersections associated with various silicon surface defects, including silicon epoxide rings,^{25, 32-33} silicon-oxygen double bonds,^{25, 34} and hypervalent silyl defects.³⁵ Most recently, we identified DICIs associated with the NR decay process occurring in SiNCs with surface DB defects.³⁶ We found that upon excitation to the first excited electronic state, energetically favorable geometric distortions bring the system near a CI with the ground state, resulting in an ultrafast NR decay process. The predicted geometric relaxations observed include both a long-known symmetric pyramidalization motion ($sp^2 \leftrightarrow sp^3$ hybridization) of the DB site¹⁹ and a Jahn-Teller distortion arising from the approximate C_{3v} symmetry of the DB site.³⁶ The theoretical investigation of DICIs associated with DB and epoxide defects shed light on several important experimental findings. Most notably, the existence of low-lying DICIs in defective SiNCs reconciles two seemingly contradictory experimental observations regarding the slow- (S-) band PL in oxidized SiNCs; the observed PL energy is insensitive to particle size,¹² although various evidence suggests that it arises from a quantum-confined exciton.³⁷⁻³⁹

With the exception of a preliminary report of the present work included in a recent perspective article,⁴⁰ to date our studies of DICIs have focused exclusively on idealized particles containing a single defect site. Nanocrystals are likely to contain more than one surface defect after oxidation, however. Herein we will investigate how neighboring defects interact with each other during recombination. Specifically, we ask whether interactions between neighboring defect modify the mechanism of recombination.

At the same time, we will examine the possibility of energy transfer between dangling bond sites. Pairs (or larger sets) of interacting silicon DB sites with net charge have been proposed as potential quantum bits (qubits) for quantum information processing.⁴¹⁻⁴⁴ In principle, an extra electron can sit in one or the other of a pair of degenerate DB defect states or it can be in a quantum mechanical superposition of these two states. However, it is known that charge transfer between surface defects can be strongly influenced by interactions with local lattice vibrations.^{42, 45} As a natural consequence of the simulations reported below, we can comment here on the possibility of a related process: energy transfer (exciton hopping) between DB sites, taking interactions with the lattice fully into account.

In this study, we applied ab initio molecular dynamics simulations in conjunction with a multireference electronic structure method to nanoscale slab models of the silicon (111) surface containing pairs of interacting dangling bonds at varying distance. The results shed light both on the effect of defect-defect interactions on the nonradiative recombination mechanism and the prospect of exciton transfer between neighboring defects.

3.2 Method

In this work we studied slab models of the silicon (111) surface with dimension 2.5×1.0 nm ($\text{Si}_{70}\text{H}_{68}$; Figure 3.1). This slab consists of a single layer of sila-adamantane units with two DB defects on the surface. These models allow us to study the effect of distance on the interaction between two defects. Here we studied two different configurations in which the DB defects are either nearest neighbors (NN) or third nearest neighbors (TNN), with defect-defect distances of 3.90 \AA and 10.25 \AA , respectively, in their ground state minimum energy structures.

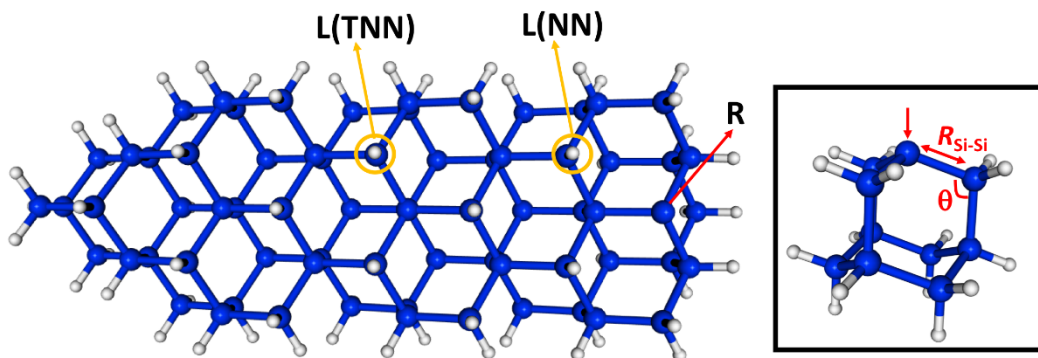


Figure 3.1. The Si₇₀H₆₈ slab model. The Si and H atoms are shown in blue and white, respectively. The left and right DB sites are labeled L and R, respectively. Site R is the same for both models. The nearest neighbor (NN), and third nearest neighbor (TNN) models are created by removing the capping H atoms from the yellow circled positions labeled L(NN) and L(TNN), respectively. The right panel illustrates the geometric parameters, θ and $R_{\text{Si-Si}}$, reported in Table 3.1 and discussed in the text.

To investigate the photophysics of these models, we applied a floating occupation molecular orbital complete active space configuration interaction (FOMO-CASCI) description of the electronic structure.⁴⁶⁻⁴⁸ A multireference electronic structure approach was chosen because it can accurately describe dynamics in the vicinity of CIs.⁴⁹ The FOMO-CASCI method has several advantages over the more widely used state-averaged complete active space self-consistent field (SA-CASSCF)⁵⁰ approach. First, unlike SA-CASSCF, FOMO-CASCI provides a size-intensive description of electronic excitations.⁵¹ That is, in systems composed of multiple excitable subsystems the error does not increase with the number of subsystems. This property is especially important in the present application, because we will compare the present results for slabs with two interacting DB defects with our previous work on systems containing a single isolated DB defect. In addition, FOMO-CASCI alleviates many of the convergence issues arising from the simultaneous optimization of the orbitals and configuration interaction coefficients in SA-CASSCF and in most cases is less computationally expensive. It is noteworthy that the scaling of complete active space calculations with the size of the one-electron basis is, in general, the same

as Hartree-Fock ($O(N^4)$). Thus extension to nanoscale systems does not require extraordinary effort unless the system necessitates a large active space.

In our previous work on an isolated DB defect³⁶ we found that an active space of 5 electrons in 3 orbitals provided an accurate description of the low-lying excited states of interest when compared to accurate multi-state complete active space second order perturbation theory (CASPT2)⁵² calculations. Here we chose an active space of 10 electrons in 6 orbitals by simply doubling this active space so that we can accurately describe the excitations of two DB defects. The LANL2DZ basis set and effective core potentials⁵³ were used throughout this study. The ground state geometries were optimized for both singlet and triplet states. The ground state was found to be the triplet, 40 and 0.1 meV below the lowest singlet state for the NN and TNN systems, respectively. Neglecting spin orbit effects, we have only modeled dynamics on the excited triplet states in this work. (See Table B.1 for optimized geometric parameters and energies of the singlet state.)

We applied Born-Oppenheimer (adiabatic) ab initio molecular dynamics (AIMD) to model the nuclear dynamics of the electronically excited system. The PES was computed on-the-fly at the FOMO-CASCI level described above (CASCI-AIMD). Initial nuclear positions and momenta were sampled from the ground state vibrational Wigner distribution computed in the harmonic approximation. Trajectories were propagated with the velocity Verlet algorithm on the first triplet excited state (T_1) PES using a 0.5 fs time step. Twenty trajectories were propagated for both the NN and TNN systems. All quantum chemical and AIMD calculations were performed with the TeraChem software package.^{46, 54-57}

Points where the energy gap between the ground (T_0) and T_1 states approaches zero were chosen as the starting points for minimal energy conical intersection (MECI) optimization calculations. For this purpose, the CIOpt software package⁵⁸ was applied in conjunction with TeraChem. All MECI calculations were performed using the same FOMO-CASCI PES described above.

In one out of twenty of the trajectories for each system (NN and TNN), the excitation was observed to transfer between DB sites. In both cases this energy transfer occurred at structure where the T_1 state became nearly degenerate with the next higher energy triplet state (T_2). Our AIMD simulations neglect nonadiabatic effects, which may result in the diabatic passage through such a crossing, therefore this transfer may or may not be physical. To quantify the probability of energy transfer in these trajectories, we applied the norm-preserving interpolation (NPI) method to compute time derivative nonadiabatic couplings (TDC) and population transfer probabilities at the crossing points associated with these two trajectories.⁵⁹ The NPI method is designed to accurately evaluate the population transfer probability from the overlap between adiabatic electronic wave functions at different times, even when the TDC spikes very sharply, e.g. at trivial unavoided crossings that arise during long-range energy transfer.⁶⁰⁻⁶¹ Time steps ranging from 0.5 to 4.0 fs were used to ensure convergence of the computed probabilities.

Table 3.1. Relevant geometric parameters surrounding the DB defect sites at several important geometries in each model. Parameters include Si-Si bond lengths ($R_{\text{Si-Si}}$ in Å) and Si-Si-Si bond angles (θ in degrees) as illustrated in Figure 3.1. Si-Si bond lengths greater than 2.5 Å are bolded. Result for the 1DB system ($\text{Si}_{72}\text{H}_{63}$) from reference 36 is also listed for comparison.

NN	FC		MECI (L)		MECI (R)	
	$R_{\text{Si-Si}}/\text{Å}$	θ/degree	$R_{\text{Si-Si}}/\text{Å}$	θ/degree	$R_{\text{Si-Si}}/\text{Å}$	θ/degree
L ^a	2.35	106.7	2.44	123.5	2.34	106.7
	2.36	106.4	2.45	123.2	2.36	106.7
	2.36	107.2	3.00	121.4	2.35	106.3
R ^a	2.37	106.4	2.39	108.7	2.43	123.0
	2.37	106.5	2.36	106.5	2.74	126.0
	2.36	106.6	2.41	106.5	2.52	125.2
TNN	FC		MECI (L)		MECI (R)	
L ^a	2.36	106.4	2.90	124.6	2.36	106.4
	2.36	106.3	2.44	123.1	2.35	106.1
	2.36	106.3	2.50	123.3	2.36	106.4
R ^a	2.35	106.1	2.35	105.7	2.47	122.7
	2.36	106.5	2.36	106.4	2.44	123.5
	2.37	106.4	2.37	106.3	2.86	125.0
1DB ^b	FC		MECI			
	2.35	105.7	2.44	122.4	---	---
	2.35	105.7	2.48	122.9	---	---
	2.35	105.7	2.82	124.3	---	---

^a The local geometries of left and right DB sites as oriented in Figure 3.1

^b See $\text{Si}_{72}\text{H}_{63}$ in reference ³⁶

3.3. Results and Discussions

First, we optimized the geometries of both slab models in their triplet ground states. Hereafter the optimized structures will be referred to as the Franck-Condon (FC) points. The most relevant geometric parameters (illustrated in the inset of Figure 3.1) can be found in Table 3.1. Although the two defects are not equivalent on our slab models because the model is asymmetric, the differences in local structure surrounding the left (L) and right (R) DB defects are very small at the FC point. (L and R labels are shown in Figure 3.1.) In both the NN and TNN cases the Si-Si bond distances ($R_{\text{Si-Si}}$) differ by only 0.02 Å and the Si-Si-Si bond angles (θ) are within 1 degree. At this minimum energy structure, natural orbital analysis demonstrates the unpaired electrons to

reside in the nonbonding orbitals at the dangling bond sites, n_{DB} (Figure 3.2 for TNN and Figure B1 for NN).

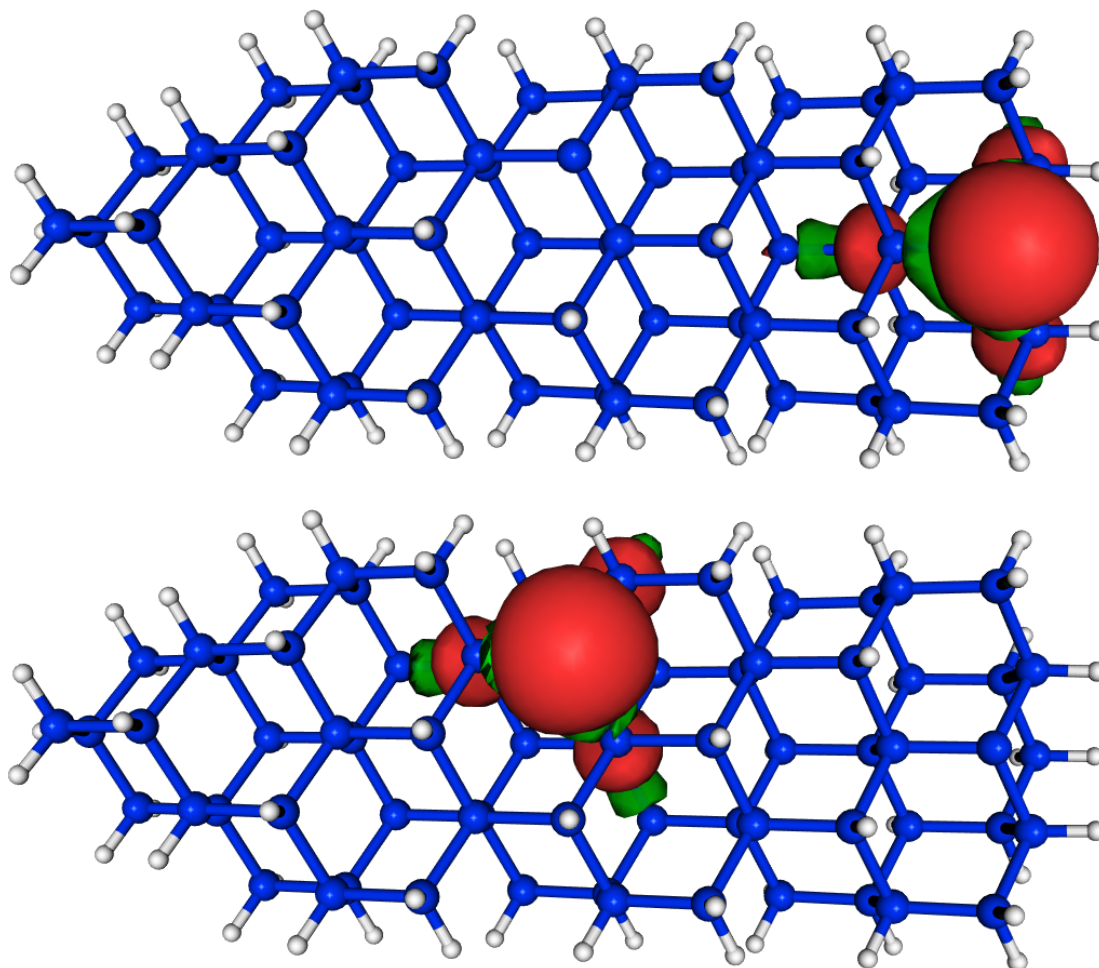


Figure 3.2. The singly occupied natural orbitals of the triplet ground state (T_0) of the TNN system. These are both n_{DB} orbitals, as described in the text.

Table 3.2. The vertical excitation energies (E_{ex} in eV) and excitation characters at the Franck-Condon point of the NN and TNN systems.

NN		TNN	
$E_{\text{ex}} / \text{eV}$	Character	$E_{\text{ex}} / \text{eV}$	Character
3.89	Local	4.00	Local
4.08	Local	4.22	Local
4.11	Local	4.32	Local
4.30	Local	4.41	Local
5.19	CT	5.53	CT

The excitation energies and chemical characters of the lowest five electronic excited states (T_1 - T_5) at the FC point are reported in Table 3.2. States T_1 to T_4 are characterized by local excitations on an individual DB site. In all four cases, an electron is excited from a partially localized Si-Si σ bonding orbital, $\sigma_{\text{Si-Si}}$, to the n_{DB} orbital on the same DB site. (Natural orbitals are presented in Figure 3.3 for NN and Figures B2 and B3 for TNN. An orbital scheme is shown in Figure 3.4.) Four excitations of this type (T_1 - T_4) exist because each DB site has two nearly degenerate $\sigma_{\text{Si-Si}}$ orbitals from which an electron can be excited. The energies of these excitations vary over a range of 0.41 eV, indicating coupling between DB sites at the FC point.

On the other hand, the highest excitations computed (T_5) involve charge transfer (CT) between the DB sites, with an electron excited from a $\sigma_{\text{Si-Si}}$ orbital on one DB site to the n_{DB} orbital on the other site (as depicted by the blue arrow in Figure 3.4; see Figures B4-B7 for natural orbitals). The CT states are higher in energy due to the larger spatial separation and thus smaller Coulombic interaction between the electron and hole. It is noteworthy that for the NN system a nonnegligible CT contribution can be mixed with lower-lying excited states (T_1 - T_4 states) due to the shorter distance between the two DB sites and the partially delocalized nature of the $\sigma_{\text{Si-Si}}$ orbitals (as can be seen in the natural orbitals in Figures 3.3, B2, and B3). Nevertheless, the excited electron is always localized on one of the n_{DB} orbitals at the FC point.

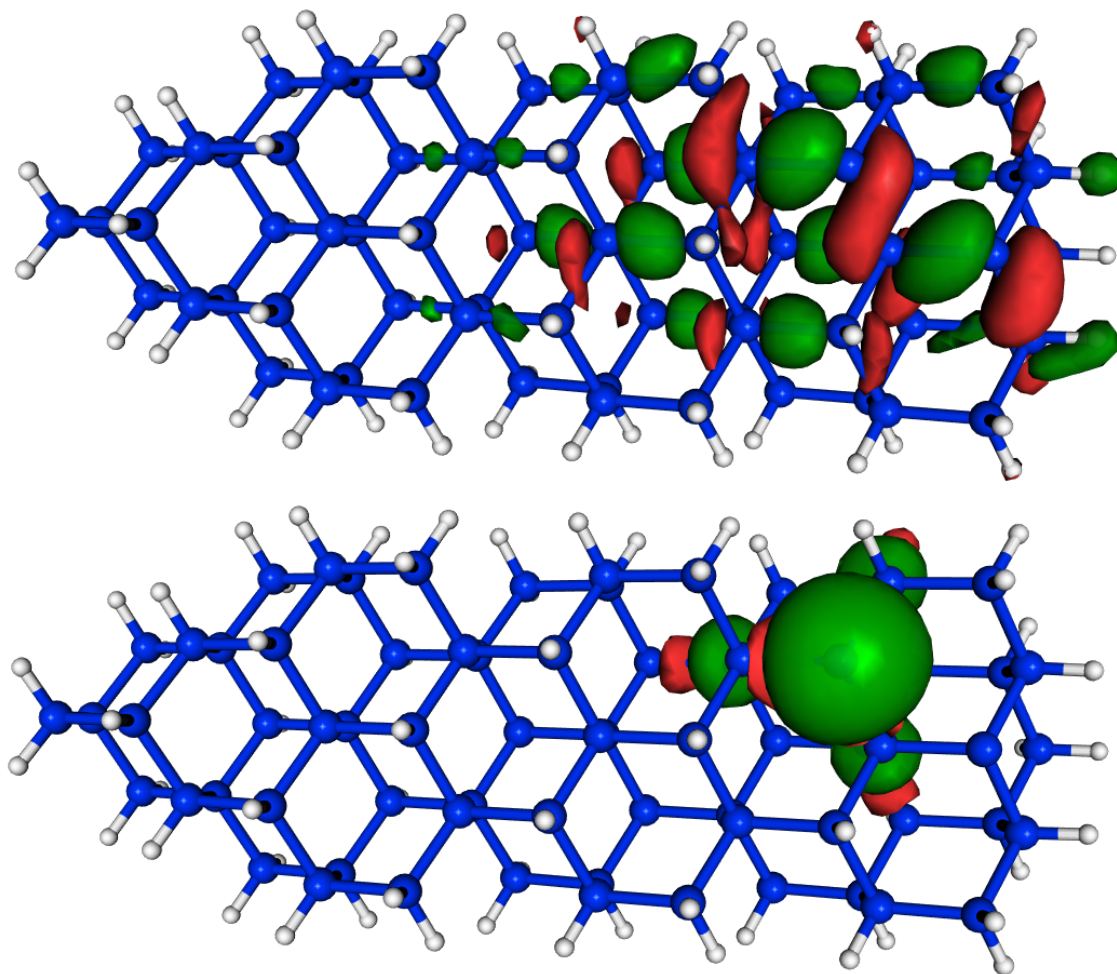


Figure 3.3. Natural orbitals with occupation numbers 1.00 (top) and 2.00 (bottom) of state T_1 at the NN FC geometry. The top and bottom orbitals are examples of $\sigma_{\text{Si-Si}}$ and n_{DB} orbitals, respectively, as described in the text.

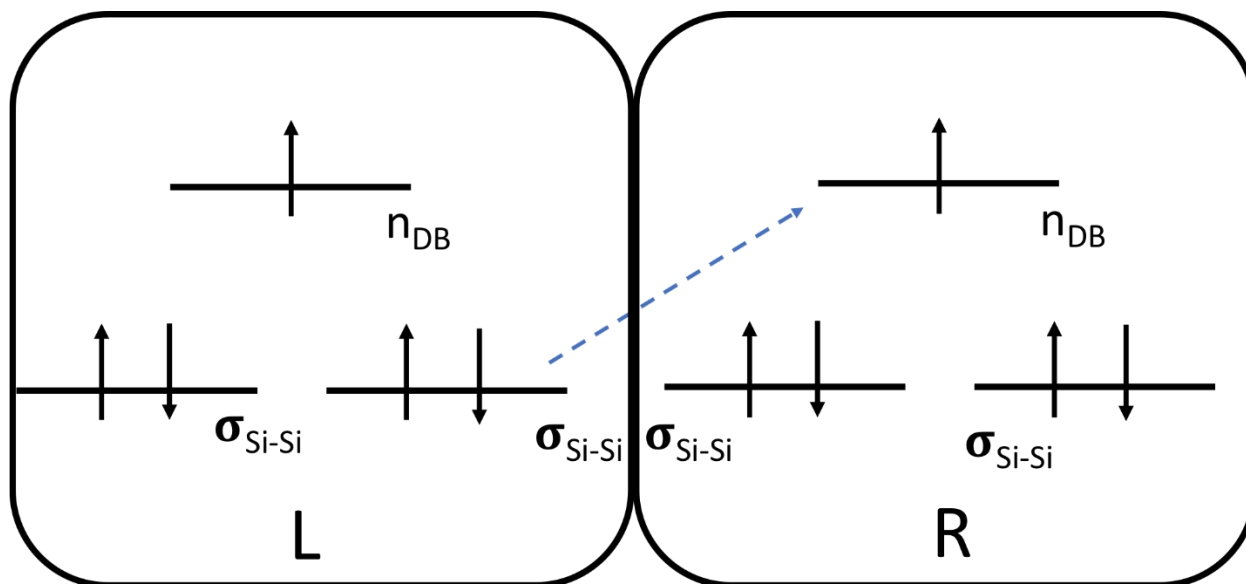


Figure 3.4. A simplified picture of the orbitals arrangement in the systems studied here. All excitations investigated in this work involve promotion of an electron from a $\sigma_{\text{Si-Si}}$ orbital to a n_{DB} orbital. In the low-lying excited states (T_1 - T_4) the majority of the excitation character is local to a single DB site. The dashed arrow indicates a possible charge-transfer excitation between two sites (e.g. T_5).

Adiabatic CASCI-AIMD calculations were performed on the T_1 state, as described in the previous section. Although the low-lying excited states are close in energy in the FC region, the gap between T_1 and the higher energy states increases rapidly in all simulations. This splitting was previously observed in our study of an isolated DB defect (referred to as 1DB hereafter).³⁶ It can be understood as the Jahn-Teller splitting between the nearly degenerate states that arise from the two $\sigma_{\text{Si-Si}} \rightarrow n_{\text{DB}}$ states localized to a particular DB site.

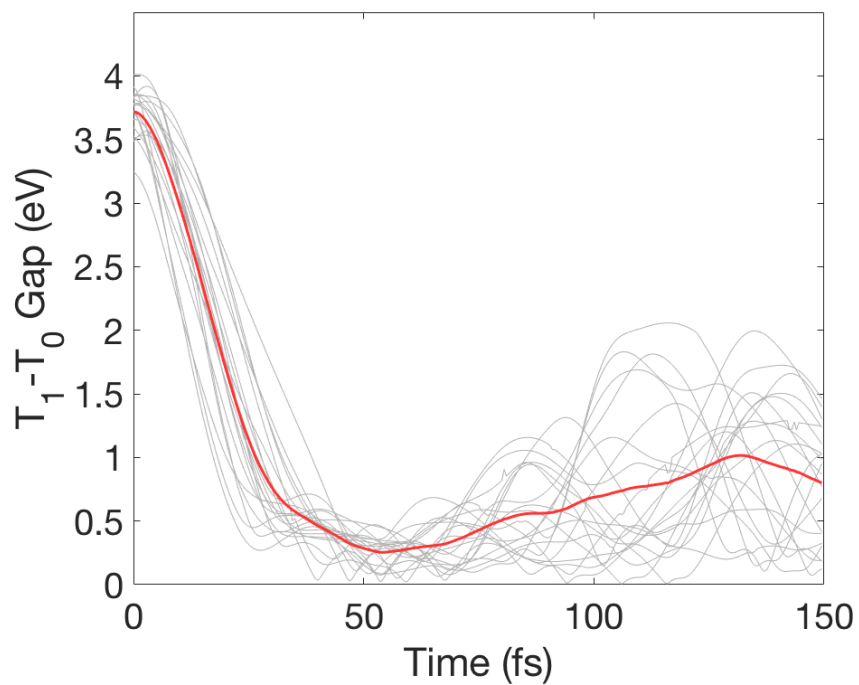
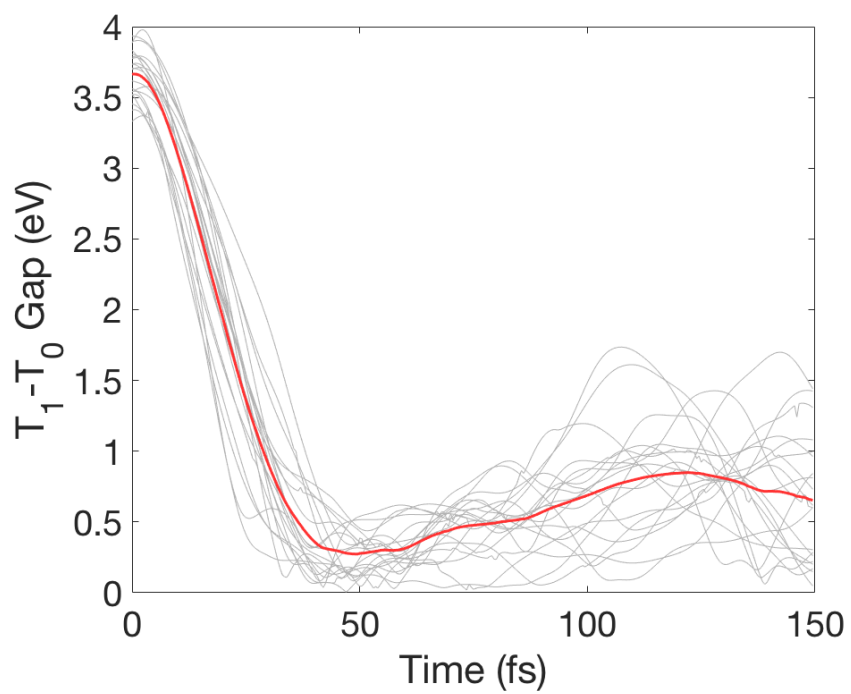


Figure 3.5. Top panel: The T_1-T_0 energy gap as a function of time for the NN system. Bottom panel: the T_1-T_0 energy gap as a function of time for the TNN system. The light grey curves depict the individual trajectories and the red curves depict the average gap over 20 trajectories for each system.

Table 3.3. The energies (in eV) of the MECIs of the NN, TNN, and 1DB systems. Results for 1DB are drawn from reference 36. As the 1DB system has only one dangling bond, only one energy is listed. All energies are relative to ground state energy of the T_0 -optimized structure.

	MECI(L)	MECI(R)
NN	2.33	2.42
TNN	2.41	2.42
1DB	2.38	---

The T_0 - T_1 energy gap as a function of time is presented in Figure 3.5. This gap approaches zero for both the NN and TNN systems 40-60 fs after excitation, with all trajectories exploring regions of near-zero energy gap. This suggests that, as in the 1DB case,³⁶ there are CIs between the ground and first excited electronic states in these systems. To explore this possibility, MECI optimization calculations have been performed starting from points of near-zero energy gap drawn from the AIMD simulations. The optimized MECI geometries are shown in Figures 3.6a-b and e-f with important geometric parameters reported in Table 3.1. The energies of the MECIs are presented in Table 3.3. Two different MECIs were located for each of the model systems (NN and TNN). These MECIs are labeled MECI(L) and MECI(R), indicating that the nuclear distortions bringing about degeneracy are local to either the left or right DB site. Taking as an example MECI(L) of the NN system, one of the Si-Si bond lengths adjacent to the left DB site is stretched to 3.00 Å, while all Si-Si bond lengths surrounding the right DB site (2.41, 2.39, and 2.36 Å) remain near their ground state minimum values. The asymmetric bond stretching and increased θ angles surrounding the left DB site are consistent with those observed in previous work for 1DB (see Table 3.1) and described in the introduction. Similarly localized bond length distortions are observed in the other three MECI structures as well (see bold values in Table 3.1). The MECI energies for all four intersections reported here are very similar to one another, ranging from 2.33 to 2.42 eV above the ground state minimum energy (Table 3.3). These energies are, again, similar to that previously reported for 1DB (2.38 eV).

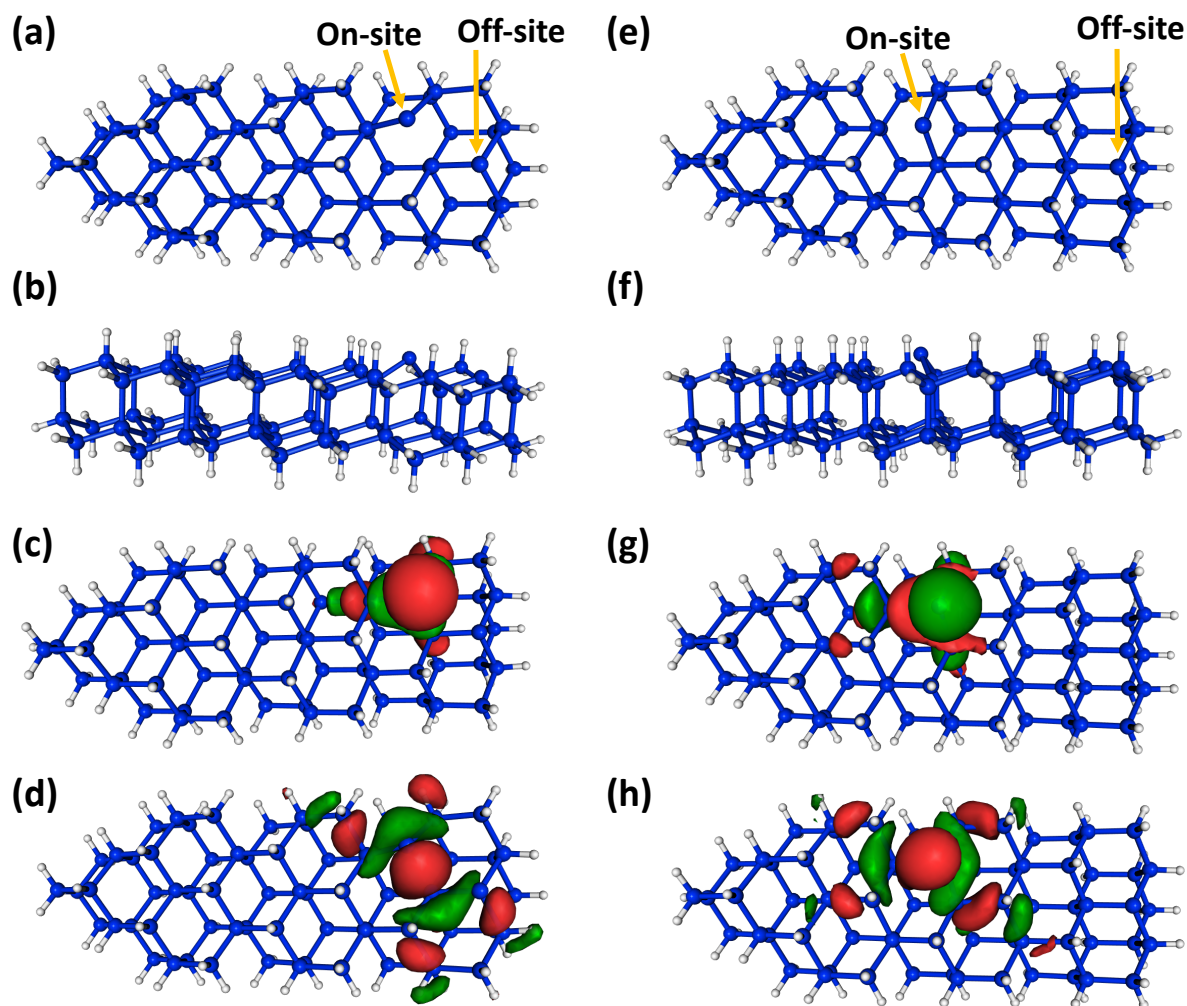


Figure 3.6. The MECI(L) geometries and natural orbitals for the NN and TNN systems. (a) The top view of the MECI(L) in NN. (b) The side view of MECI(L) in NN. (c) A natural orbital with occupation number 1.50 (n_{DB}) for MECI(L) in NN. (d) A natural orbital with occupation number 1.50 (σ_{Si-Si}) for MECI(L) in NN. (e) The top view of the MECI(L) in TNN. (f) The side view of MECI(L) in TNN. (g) A natural orbital with occupation number 1.50 (n_{DB}) for MECI(L) in TNN. (h) A natural orbital with occupation number 1.50 (σ_{Si-Si}) for MECI(L) in TNN. Panels c and d are adapted from reference 40 with permission from the PCCP Owner Societies.

At each MECI, T_0 - T_1 state-averaged natural orbitals were computed to investigate the nature of the electronic transition enabled by these intersections. In all cases two natural orbitals with occupation numbers ~ 1.5 are observed. It is transitions of a single electron between these pairs of orbitals that are facilitated by the MECIs. In all cases, these orbitals are localized to a

single DB site, as can be seen in Figures 3.6c-d and g-h, which show the partially occupied natural orbitals for MECI(L) of NN and TNN, respectively.

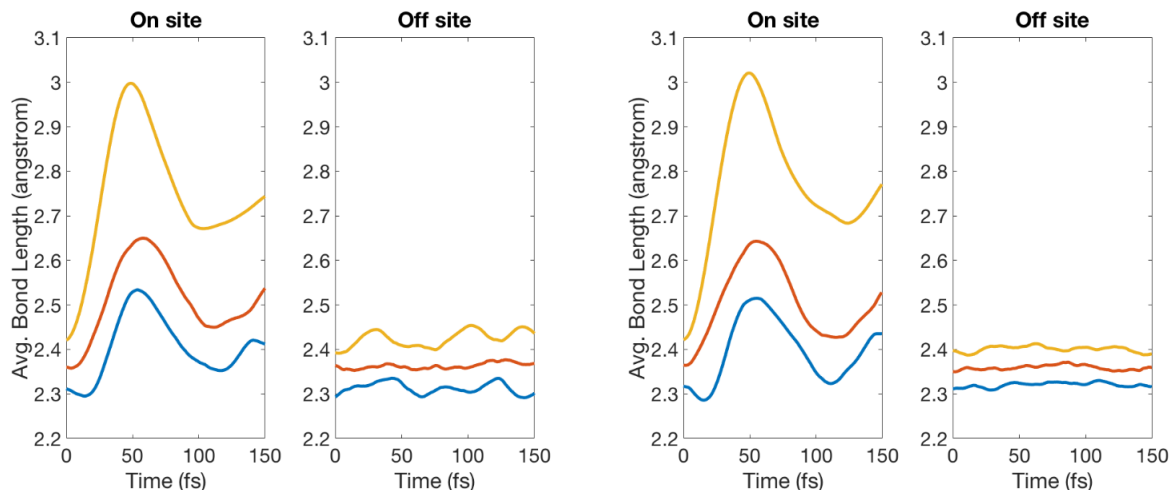


Figure 3.7. Top panel: the averaged Si-Si bond lengths around the DB sites for the NN system. Bottom panel: the averaged Si-Si bond lengths around the DB sites for the TNN system. The bond lengths are sorted as described in the main text. On-site (more distorted) and off-site (less distorted) bonds are shown on the left and right, respectively. Longest, middle, and shortest lengths shown by yellow, orange, and blue lines, respectively.

We now return to the AIMD data to assess whether the optimized MECIs accurately reflect the predicted dynamics. The Si-Si bond lengths, averaged over all 20 trajectories for NN and TNN respectively, are reported as a function of time in Figure 3.7. For each trajectory, the DB sites are sorted as either on-site or off-site, with the on-site DB defined as the one with the more distorted Si-Si bond lengths. Then, within each site, the three adjacent Si-Si bonds are sorted by length. Then, six averages are performed over the sorted bonds (that is, the longest on-site bond lengths from the twenty trajectories are averaged to produce the yellow curve on the left, etc.). Clearly the on-site bonds distort significantly in the first 50 fs after excitation, while the off-site bonds remain very near to their ground state minimum values. This emphasizes the local nature of the dynamics; the coupled electron-nuclear motions of NR recombination occur largely at a single DB site, with the other DB site relatively unperturbed. This is even true for the NN configuration where DB sites are separated by only two Si-Si bonds (though very modest oscillations in the off-site bond lengths are observed in this case). The ratio of trajectories with larger distortions on the

left DB to those with larger distortions on the right DB is 11:9 for both the NN and TNN systems, which is statistically indistinguishable from 50%. Thus, the exciton appears to have roughly equal probability of undergoing NR recombination at either DB site.

To briefly summarize, we have found that during the first 40-60 fs after excitation of a defect-localized excitation in our model slabs the bond lengths surrounding the DB defects undergo asymmetric stretching and the energy gap between T_1 and T_0 approaches zero, suggesting a pathway for NR recombination via DICl. Optimization of MECIs confirms this suggestion. Several factors suggest that neighboring DB defects behave essentially independently: a) The geometric distortions observed in the AIMD simulations are local to a single defect site (Figure 3.7), b) the electronic transitions facilitated by the MECIs are local to a single defect site (Figure 3.6), and c) the observed dynamics and MECI energetics are very similar to those predicted in our previous work on a single isolated DB site.³⁶ The localized nature of the DICl supports the extrapolation of the NR decay mechanism and dynamics from the simulations of idealized models containing a single isolated defect to realistic systems with multiple defects.

Though in all forty simulations reported here NR recombination occurred upon dynamics that were local to a single defect site, we did observe communication between defect sites in two simulations (one out of twenty for each of NN and TNN). Specifically, within the first ~ 10 fs after excitation we observed crossing of the T_1 and T_2 excited states. In our adiabatic AIMD simulations, this resulted in the transfer of the exciton between DB sites. Because nonadiabatic effects are neglected, however, it is unclear whether this energy transfer process (an adiabatic process) is physical or not. In order to study this nonadiabatic event, we applied NPI⁵⁹ to evaluate the TDC and population transfer probability associated with these PES crossings. Below we present the computed energy transfer probabilities, defined such that 0% corresponds to the excitation remaining on the same DB site and 100% corresponds to the transfer of the excitation between dangling bonds with unit probability.

First, we evaluate the probability of energy transfer in the NN trajectory. We expect that the exciton transfer is more likely to occur in this system due to the shorter DB-DB distance. The energy transfer probability is computed to be 98.5%. It is important to remember that this is the

probability of transfer for only one out of twenty trajectories. No evidence of transfer was observed in the other nineteen trajectories. This suggests a significant probability of energy transfer between DB defects separated by two Si-Si bonds (nearest neighbors) on the Si (111) surface in the first femtoseconds after excitation. However, without a larger sample size we hesitate to quantify the probability of such transfer.

Now we consider whether energy transfer can occur over a longer distance (~ 10 Å; the TNN case). An energy transfer probability of 0% is predicted by NPI in this case. Not surprisingly, the probability of energy transfer between DB defects separated by ~ 10 Å is much lower than in the NN case. Given the sampling of our present study (twenty trajectories), the probability cannot be discerned from zero. Further insights into the probability of energy transfer could also be gained through full nonadiabatic molecular dynamics simulations.

3.4. Conclusions

In this study, we applied CASCI-AIMD to investigate NR recombination in slab models of the silicon (111) surface containing two dangling bond defects. All trajectories, initiated on the lowest triplet electronic excited state, explored regions of near-zero energy gap with the triplet ground electronic state within 40-60 fs after excitation. Conical intersections were identified in these regions, suggesting that these systems decay to the electronic ground state via DICI. The nuclear distortions associated with recombination were found to be nearly completely localized to a single defect site, as were the electronic transitions associated with the MECIs. The mechanism, timescale, and energetics of recombination were all in nearly perfect agreement with our past work on a single isolated dangling bond defect.³⁶ Thus, even when separated by a mere two Si-Si bonds, the presence of a second defect has negligible effect on the NR decay mechanism and dynamics. This is consistent with a growing body of evidence that even in large systems, energetically accessible conical intersections tend to involve relatively local distortions of electronic and geometric structure.⁴⁰

On the other hand, based on the NPI calculations of the nonadiabatic coupling, we found that a localized exciton on one defect site can transfer to a nearest-neighbor DB site (separated by two Si-Si bonds, ~ 4 Å) with significant probability. This process occurs within the first 10 fs after

excitation. After this short window, Jahn-Teller distortion of the excited DB stabilizes the localized excitation, breaking the degeneracy of the states involved and disfavoring transfer. In fact, this distortion appears to disfavor electronic communication of any kind, as evidenced by the local mechanism of NR recombination observed in our AIMD simulations. Nuclear relaxation of the defect site thus plays a crucial role in determining the degree of communication between defect sites.

APPENDIX

SUPPORTING INFORMATION FOR: AB INITIO MOLECULAR DYNAMICS STUDY OF THE INTERACTION BETWEEN DEFECTS DURING NONRADIATIVE RECOMBINATION

Table B1. The minimum energy geometries of NN and TNN systems at the singlet ground state. The relative energies (R.E.; unit meV) are the energies relative to corresponding triplet ground state.

NN	$R_{\text{Si-Si}}/\text{\AA}$	θ/degree	R.E./meV
L	2.35	106.9	40.5
	2.36	106.6	
	2.36	106.8	
R	2.37	106.0	
	2.37	106.5	
	2.36	106.6	
TNN	$R_{\text{Si-Si}}/\text{\AA}$	θ/degree	
L	2.36	106.4	0.1
	2.36	106.3	
	2.36	106.3	
R	2.35	106.1	
	2.36	106.5	
	2.37	106.4	

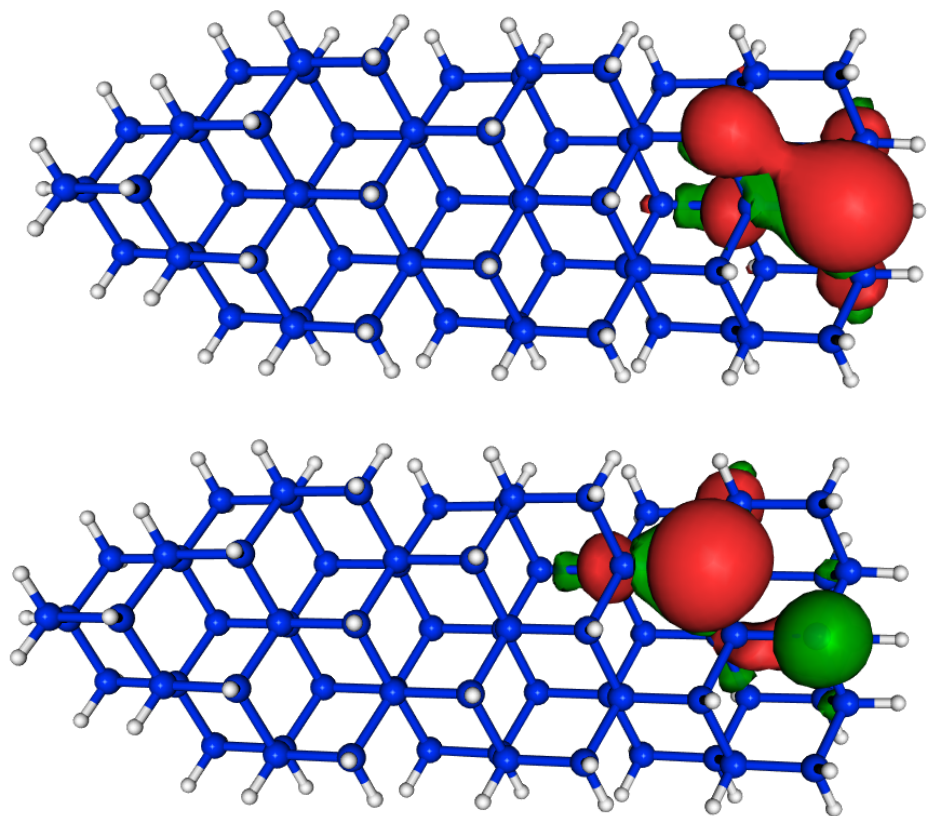


Figure B1. The ground state natural orbitals with occupation number 1.00 in the NN system.

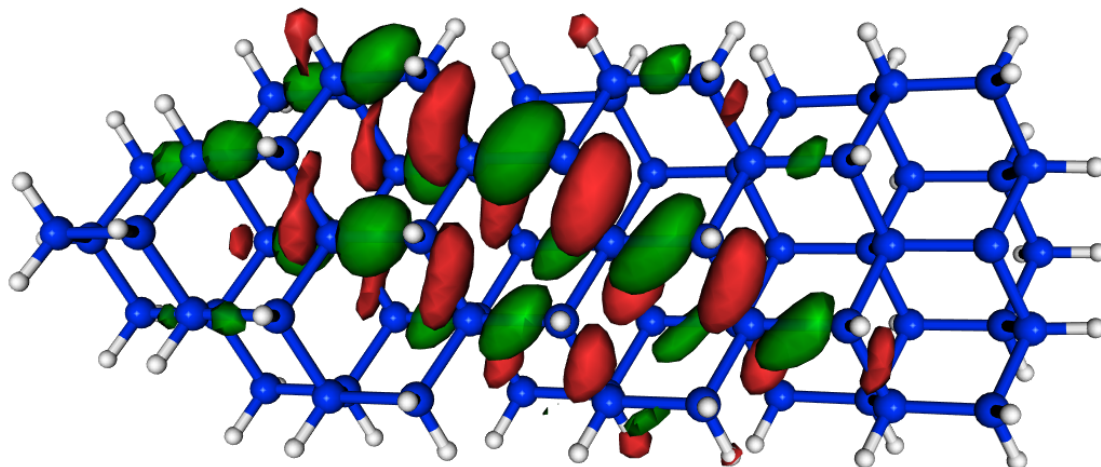


Figure B2. The T_1 state natural orbitals with occupation number 1.00 and sigma bonding character in the TNN system.

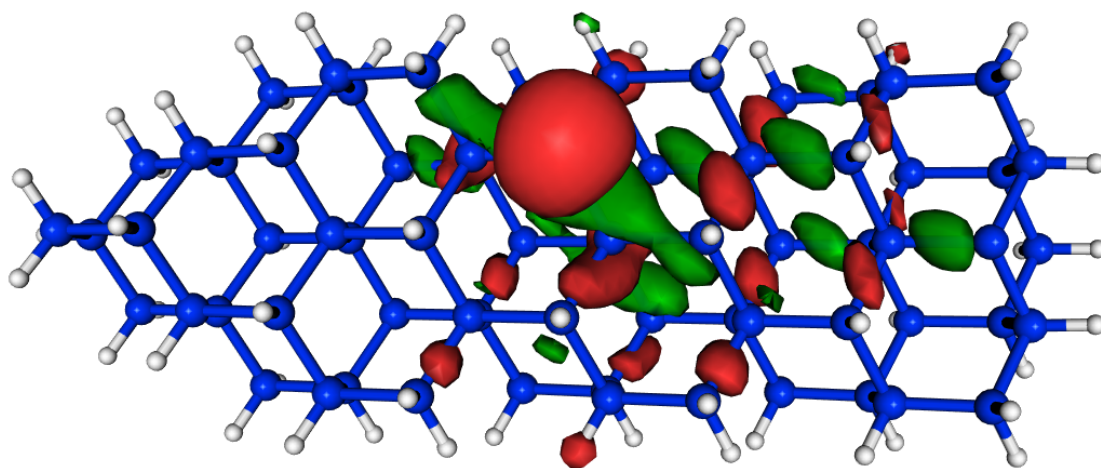


Figure B3. The T_1 state natural orbitals with occupation number 2.00 and (majority) DB nonbonding character in the TNN system.

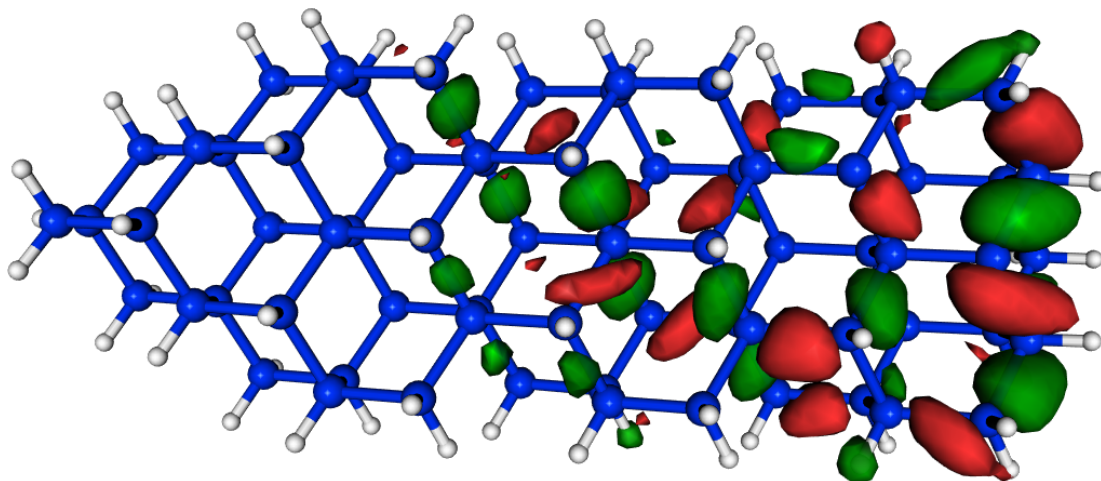


Figure B4. The T_5 state (CT state) natural orbitals with occupation number 1.06 and sigma bonding character in the NN system.

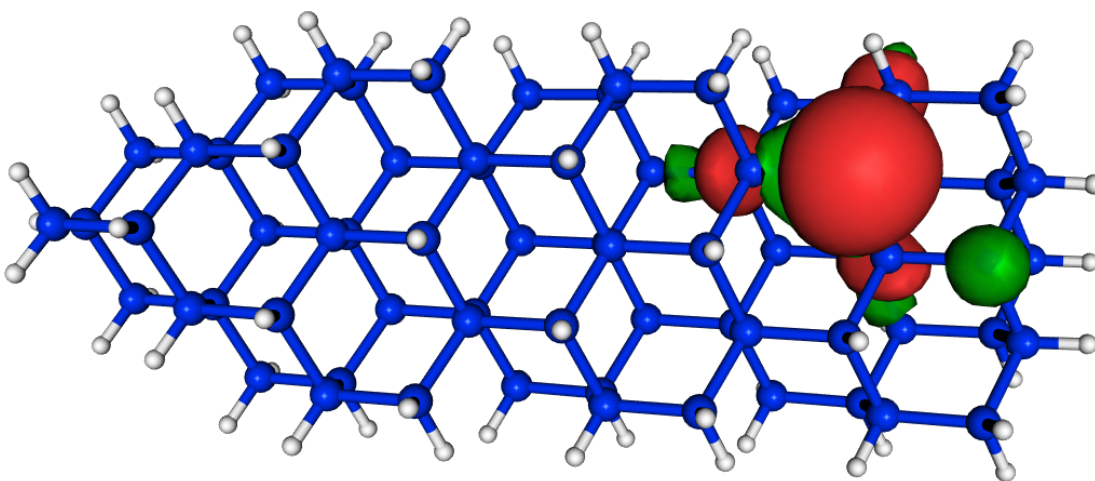


Figure B5. The T_5 state (CT state) natural orbitals with occupation number 1.94 and DB nonbonding character in the NN system.

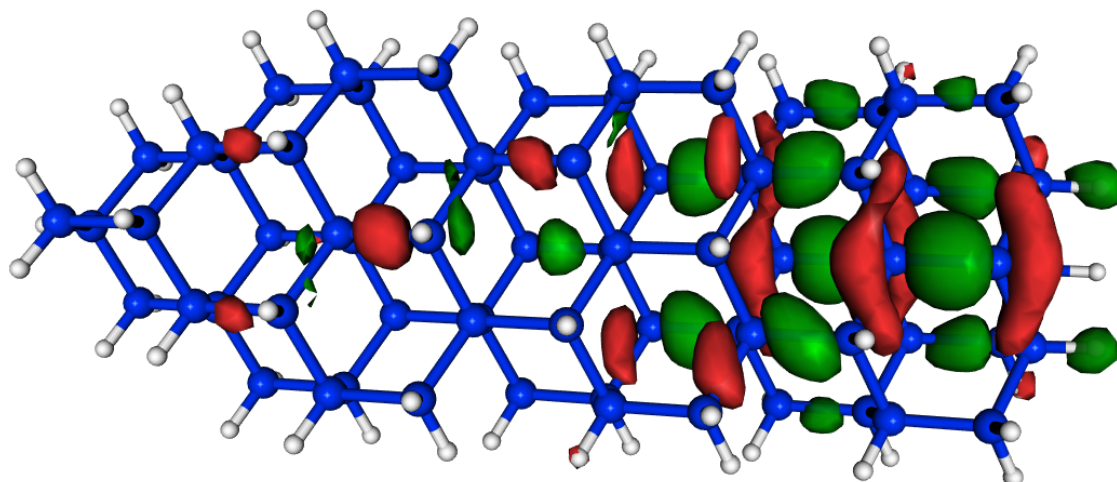


Figure B6. The T_5 state (CT state) natural orbitals with occupation number 1.00 and sigma bonding character in the TNN system.

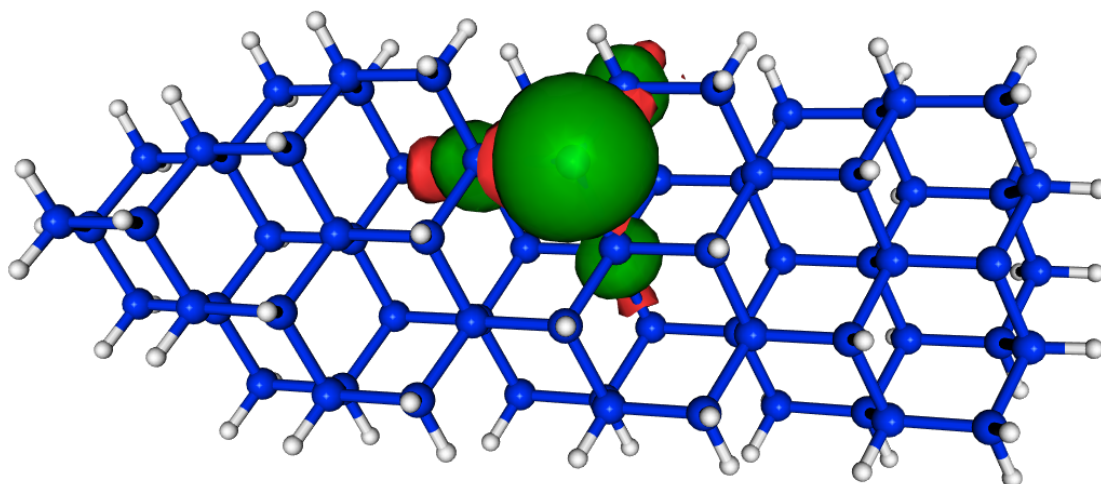


Figure B7. The T_5 state (CT state) natural orbitals with occupation number 2.00 and DB nonbonding character in the TNN system.

Ground State Minimum Energy Geometries (in Angstrom)

NN System

Si	-0.5576323185	-0.4696373504	-0.5920927866
Si	1.7982390365	-0.4053398800	-0.6923731798
Si	-1.3882497620	1.5214595289	0.3701750119
Si	-1.2003660670	-2.2968807090	0.7710967586
Si	2.7173630701	-0.0880106730	1.4569051027
Si	-0.4763805609	1.8269212341	2.5275452825
Si	-0.2786724268	-1.9805410724	2.9206367854
Si	1.8814725610	1.9029682772	2.4165588267
Si	-1.1189093405	0.0012536655	3.8939505339
Si	2.0776452179	-1.9138966149	2.8227829129
Si	2.6415292250	-2.3941707900	-1.6707089170
Si	-3.7366811353	1.4614762050	0.5208380030
Si	-0.3626797296	-4.2860183150	-0.1833238623
Si	-3.5464471644	-2.3773792303	0.9456521969
Si	2.9037944108	-3.9048424014	1.8607442295
Si	2.9302289348	-1.6234465941	4.9976737530
Si	2.7524891647	2.2166515582	4.5808543680
Si	-3.4764822610	-0.0641955087	4.0129501094
Si	-0.2154120340	0.3149323036	6.0532480155
Si	-4.3593719693	-0.3726185292	1.8547087982
Si	2.1315931173	0.3832053206	5.9162064436
Si	1.9936334351	-4.2153625381	-0.2940768224
Si	-1.4075070276	-0.7565346349	-2.7688484997
Si	-1.3125710618	3.8198073673	3.4936178410
Si	5.0629271458	0.0001101856	1.2799415000
Si	-4.2763144538	1.9291161430	4.9741008362
Si	-4.5450946429	3.4623058112	1.4449741377
Si	1.9401980985	4.2171572139	5.5032025071
Si	-1.0628042904	2.3030513314	6.9848411982
Si	5.2490416295	-3.8410275138	1.7206068239
Si	-1.2399322676	-4.6021421023	-2.3416343407
Si	1.7287816830	-2.7114489087	-3.8226895601
Si	4.9971015644	-2.3259029052	-1.7771136286
Si	-0.4059388753	4.1369106062	5.6516568587
Si	-3.4103580532	2.2375656600	7.1407680258
Si	-3.6711092086	3.7572841617	3.6088468836
Si	-1.2471164516	6.1283088965	6.5878541095
Si	-4.4780071726	5.7525079399	4.5662494995
Si	-4.2278638526	4.2317891021	8.0767151627
Si	-3.5891890630	6.0373409174	6.7202937516
Si	-0.6186298447	-2.7700746853	-3.6811378161
Si	2.5571324453	-4.6943659362	-4.7900243331
Si	2.8252055923	-6.2078585836	-1.2698629294

Si	5.8368727134	-4.3043818329	-2.7414682383
Si	5.8770241451	-2.0106771597	0.3823343804
Si	4.9144119023	-4.6363397590	-4.8935381648
Si	1.7089649397	-4.9943167450	-6.9670099521
Si	1.9164935926	-6.5251401342	-3.4273936374
Si	5.1860822102	-6.1253893522	-1.3642700019
Si	8.1865772037	-4.2420546785	-2.9145066326
Si	5.7589957025	-6.6067363966	-5.8776706610
Si	2.7391957410	-8.5198508731	-4.3779360615
Si	-0.4305348654	-6.6103001264	-3.2424394666
Si	6.0437936056	-5.8520304613	0.8140231237
Si	6.0384950426	-8.0721329346	-2.3689642716
Si	1.8824390046	-8.8353761344	-6.5516086567
Si	5.0938183318	-8.4293272900	-4.4979872935
Si	8.1185561160	-6.5632894354	-5.9795625201
Si	4.8499671066	-6.9351539396	-8.0324447258
Si	8.3955804019	-8.0832834301	-2.4845307107
Si	5.9617609270	-10.3838492954	-5.5116091091
Si	2.5051407308	-6.9992956164	-7.8859603824
Si	2.6824743731	-10.8459319379	-7.4607099382
Si	5.7057951090	-8.9111943531	-8.9846913032
Si	9.0055701737	-6.2433466499	-3.8257289182
Si	8.9341893308	-8.5437837372	-6.9538611383
Si	8.3255527972	-10.3525051971	-5.5715515702
Si	8.0496359933	-8.8239770055	-9.1120547260
Si	5.0233458608	-10.7290979016	-7.6479289929
Si	9.1573662458	-10.1152198844	-3.3850550543
H	2.2001335667	0.7360245708	-1.5455014028
H	-0.9816770730	2.6662277540	-0.4744106725
H	2.2727295033	3.0454472848	1.5617507574
H	-3.8666939418	-1.2050822360	4.8698987011
H	-3.9298092492	-3.5076632351	1.8141844735
H	-4.1411519133	-2.5947676003	-0.3873964147
H	-4.2995922878	1.2843203605	-0.8350249369
H	-5.8347961530	-0.4204646210	1.9472034751
H	4.2278454712	2.2765493879	4.5008344911
H	-0.6237710338	-0.8281446857	6.8987422351
H	2.6828782165	0.5704603009	7.2759196757
H	4.4053662762	-1.5994068007	4.9596039536
H	2.5070179777	-2.7588351152	5.8406664321
H	2.5019206059	-5.0493628477	2.7081258975
H	-0.7543509857	-5.4286605224	0.6715190550
H	2.3340934675	5.3570870406	4.6521483024
H	2.5121138241	4.4185095282	6.8490031991
H	-0.4908202058	2.4853547393	8.3372971077
H	-0.9114702631	4.9612371618	2.6407864224
H	-5.7532520736	1.8734442045	5.0451234968

H	-6.0192505415	3.4266196499	1.5107898261
H	-4.1421134494	4.6034076531	0.5997173702
H	-3.8031007814	1.0875473818	7.9826919403
H	-3.6778751698	4.4053640989	9.4351835082
H	-5.6995140515	4.1701033676	8.1698199675
H	-0.8331521112	7.2749573280	5.7557014399
H	-0.6750140319	6.3019962449	7.9377859788
H	-5.9512988836	5.6886680249	4.6366715294
H	-4.1018826616	6.8949930667	3.7106201361
H	-0.6767516118	-3.1243023916	3.7719546699
H	-4.0992418482	7.2975827836	7.3018247284
H	-2.7146449053	-4.6684845300	-2.2621626262
H	2.1363982577	-1.5737572936	-4.6768375556
H	-0.9666456780	0.3717261557	-3.6128734602
H	-2.8825589451	-0.7652495304	-2.7402760248
H	-1.1800995540	-2.9547605316	-5.0365762350
H	5.4406572592	1.1197078644	0.3948282949
H	5.6667264578	0.2330507438	2.6057496156
H	5.8180207153	-3.6728725369	3.0746722574
H	5.3988397550	-1.1898031762	-2.6357695408
H	7.3526476399	-1.9598092334	0.3027177591
H	2.4413704354	-7.3586811063	-0.4228194773
H	5.3232273773	-3.5019031494	-5.7518133290
H	-0.7950323986	-7.7386914549	-2.3627483483
H	-1.0231029269	-6.8491257821	-4.5724890292
H	7.5182816968	-5.8507165600	0.7651055016
H	5.6034526590	-6.9921989442	1.6407294255
H	2.3684814930	-9.6704876043	-3.5274940655
H	2.1390156994	-3.8663419802	-7.8160777206
H	0.2344738536	-5.0191460617	-6.9342550812
H	0.4083951655	-8.8983403833	-6.4715768617
H	5.2555750973	-5.7888917733	-8.8744987772
H	8.5118132963	-5.4214214052	-6.8335009029
H	8.9385412519	-7.9133494092	-1.1222454397
H	8.7844458953	-4.0255371025	-1.5836435562
H	8.5778376055	-3.1215191311	-3.7912126136
H	1.9512693950	-7.1967380072	-9.2427724652
H	10.4811063744	-6.1958232822	-3.9179143530
H	10.4103589846	-8.4847452129	-7.0160214701
H	5.1356172052	-9.0900147871	-10.3368997656
H	8.7869177860	-11.6242768900	-6.1650494012
H	8.4561438895	-7.6846713673	-9.9558894073
H	8.5676733133	-10.0690202845	-9.7095783170
H	5.5695396847	-11.9889181176	-8.1930065681
H	2.1102862447	-11.0674258434	-8.8021508748
H	2.3229042234	-11.9823711446	-6.5931469846
H	10.6320766370	-10.1198007873	-3.4290076038

H 8.6976407448 -11.2437879293 -2.5569553201

TNN System

Minimum Energy Conical Intersection Geometries (in Angstrom)

NN System: MECI-L

Si	-2.5494918535	2.3235668108	-0.0549987860
Si	-0.1914314307	2.3883635899	-0.1554164091
Si	-3.3669027310	4.3165608112	0.9164746452
Si	-3.1669471560	0.4786940695	1.2934084170
Si	0.7250925855	2.6722030321	2.0022133404
Si	-2.4560477814	4.5994036279	3.0754027150
Si	-2.2650610336	0.7789074480	3.4527830952
Si	-0.0991431039	4.6602024772	2.9663381062
Si	-3.1026733591	2.7662487965	4.4280306862
Si	0.0952199915	0.8290701649	3.3459502368
Si	0.6470279101	0.4155919359	-1.1620426143
Si	-5.7163610498	4.2701782875	1.0670872664
Si	-2.3117380917	-1.5086861341	0.3249884882
Si	-5.5213639660	0.4180485870	1.4433837818
Si	0.9512693088	-1.1465499949	2.3651867483
Si	0.9401941436	1.1000582858	5.5285236991
Si	0.7760526156	4.9476982891	5.1322322392
Si	-5.4618376068	2.7192068332	4.5483669845
Si	-2.2050646539	3.0648048062	6.5902551803
Si	-6.3288699695	2.4178148482	2.3812231030
Si	0.1422854123	3.1069928399	6.4516518737
Si	0.0579219822	-1.4280501094	0.1987730939
Si	-3.4160891956	2.0387091444	-2.2286051006
Si	-3.2778985118	6.5923855118	4.0470320935
Si	3.0702817020	2.7816446962	1.8256369625
Si	-6.2506487087	4.7175844311	5.5207090751
Si	-6.5382470390	6.2561658208	2.0173397516
Si	-0.0177862386	6.9489888659	6.0658090705
Si	-3.0347270496	5.0593921621	7.5273973315
Si	3.2955371135	-1.0541438496	2.2057684440
Si	-3.2181823099	-1.8022439013	-1.8244373445
Si	-0.2719954401	0.0996153136	-3.3188597927
Si	2.9973146695	0.5331228703	-1.2757632595
Si	-2.3643303443	6.8958864368	6.2041953474
Si	-5.3822786162	5.0162211049	7.6884764155
Si	-5.6366490747	6.5515062968	4.1688312687
Si	-3.1791092503	8.9010553042	7.1329152246

Si	-6.4145231972	8.5563935450	5.1328733573
Si	-6.1612726081	7.0198171519	8.6407964836
Si	-5.5198111738	8.8264004827	7.2868095954
Si	-2.6185164848	0.0393153436	-3.1571279484
Si	0.5570422467	-1.8781518916	-4.2850550974
Si	0.9238245155	-3.4302387849	-0.8171632460
Si	3.8622805620	-1.4112856595	-2.2868800346
Si	3.8863497183	0.7981828923	0.8843346658
Si	2.9091971304	-1.8152953262	-4.4024835169
Si	-0.2858800123	-2.2020558426	-6.4625268186
Si	-0.0689164520	-3.7193401570	-2.9348858934
Si	3.3357050813	-3.2582355105	-0.9383696597
Si	6.1999307232	-1.2715869772	-2.4459799062
Si	3.7300034833	-3.8441294484	-5.2576050667
Si	0.6897219828	-5.7356018630	-3.8866682088
Si	-2.4095689415	-3.8040295131	-2.7268406967
Si	4.1595846675	-3.0205672397	1.2512928415
Si	3.7408857035	-5.8608523472	-1.5516160498
Si	-0.1415107714	-6.0543563293	-6.0593107788
Si	3.0366641869	-5.6352791614	-3.8610181700
Si	6.0810492998	-3.7547722054	-5.3564316351
Si	2.8675845843	-4.1667991396	-7.4369531582
Si	6.1897069470	-5.0603512606	-1.7596967360
Si	3.9060064180	-7.5744416406	-4.8998897282
Si	0.5181381104	-4.2136416448	-7.3640512730
Si	0.6946841100	-8.0727419470	-6.9181061764
Si	3.7387469952	-6.1393126452	-8.3748361816
Si	6.9181863623	-3.3572259019	-3.1978603391
Si	6.9301055093	-5.7436936107	-6.2720830208
Si	6.2755792821	-7.4960326774	-4.8405548042
Si	6.0844354461	-6.0479514479	-8.4469918730
Si	3.0375378933	-7.9556025604	-7.0510141870
Si	6.9991186234	-7.1240882273	-2.6327116189
H	0.2225624500	3.5425605266	-0.9841947267
H	-2.9436170875	5.4640186084	0.0838677245
H	0.3050630494	5.7957013285	2.1079437103
H	-5.8625625790	1.5807197776	5.4033349618
H	-5.9426447437	-0.7294039356	2.2701684465
H	-6.0963833733	0.2548989976	0.0940661979
H	-6.2790907192	4.1073317078	-0.2905535658
H	-7.8046272879	2.3599085867	2.4576791185
H	2.2514908275	4.9911921471	5.0517448231
H	-2.6330591101	1.9238237024	7.4284685200
H	0.6980497986	3.2819799570	7.8106251125
H	2.4153672515	1.1164003114	5.4938166289
H	0.5067613537	-0.0426842967	6.3562852853
H	0.5509367361	-2.3117196565	3.1843911830

H	-2.6946428678	-2.6536896500	1.1799814353
H	0.3951830411	8.0904056769	5.2262837082
H	0.5494008218	7.1325169911	7.4161225673
H	-2.4562922368	5.2228996252	8.8793984108
H	-2.8676751299	7.7295607171	3.1928941435
H	-7.7280913642	4.6661445445	5.5874886784
H	-8.0094755391	6.1821120324	2.1174684057
H	-6.1846025447	7.4110710659	1.1692989884
H	-5.7846904860	3.8709722500	8.5319835578
H	-5.5812430519	7.1754854756	9.9891286515
H	-7.6311915856	6.9757550093	8.7628426308
H	-2.7721415246	10.0318409049	6.2755779082
H	-2.5863252785	9.0919301574	8.4712687331
H	-7.8889788994	8.5243024263	5.1968976879
H	-6.0133656018	9.6919480042	4.2792208674
H	-2.6730433056	-0.3671535571	4.2963990515
H	-6.0175575884	10.0899514143	7.8717941989
H	-4.6904113900	-1.8705288526	-1.7122351219
H	0.1313410029	1.2465696545	-4.1624715981
H	-2.9953525510	3.1761955846	-3.0684940635
H	-4.8909869704	2.0186116717	-2.1774713307
H	-3.1819726509	-0.1438955192	-4.5120355672
H	3.4404729574	3.9247013156	0.9692276617
H	3.6704720437	2.9792208676	3.1585390305
H	3.8713316920	-0.8827541513	3.5571251808
H	3.3776139821	1.6977240175	-2.1060714413
H	5.3600019432	0.8620965683	0.7866748512
H	0.5848652839	-4.5755949432	0.0541161731
H	3.3119658323	-0.7261667509	-5.3192822189
H	-2.7784315614	-4.9308373562	-1.8486985032
H	-2.9924009990	-4.0419891211	-4.0613398678
H	5.6312079519	-2.9353398557	1.2339833729
H	3.7634092376	-4.1991648110	2.0438142033
H	0.2641811273	-6.8526570783	-3.0161723615
H	0.1410662633	-1.0754561190	-7.3146108856
H	-1.7607484194	-2.2239204695	-6.4212050627
H	-1.6171189873	-6.1221394016	-6.0081669301
H	3.2949929510	-3.0128120662	-8.2580732801
H	6.4680414001	-2.6157764968	-6.2179999532
H	6.7234329762	-4.8673604693	-0.3947297596
H	6.7828152979	-0.9847317303	-1.1221147469
H	6.5949143798	-0.2083573148	-3.3867193074
H	0.0001132116	-4.3862696022	-8.7381788206
H	8.3933786752	-3.4566882151	-3.2139884423
H	8.4069334888	-5.6799583200	-6.3122426586
H	3.1976251910	-6.3041485836	-9.7407714680
H	6.8183725899	-8.7801560598	-5.3277315026

H	6.5065298128	-4.9098770022	-9.2851430332
H	6.6244935495	-7.2909730049	-9.0303494809
H	3.5911151547	-9.2151723334	-7.5895842241
H	0.1436749275	-8.3362876257	-8.2602140779
H	0.3226692427	-9.1833152287	-6.0213001763
H	8.4684350997	-6.9864996270	-2.6447179622
H	6.6262859502	-8.2487058553	-1.7569559627

NN System: MECI-R

Si	-2.5661827184	2.3238226837	-0.0440001497
Si	-0.2060317901	2.4043199539	-0.1605815227
Si	-3.4191313529	4.3007570081	0.9211827851
Si	-3.1974388685	0.4916271772	1.3166452717
Si	0.7136522709	2.7203831543	1.9882673639
Si	-2.4890877036	4.6224747041	3.0672978859
Si	-2.2686125718	0.8156268621	3.4684353195
Si	-0.1304554761	4.7112069977	2.9333654463
Si	-3.1017738946	2.7973617066	4.4460676533
Si	0.0863910247	0.8928534652	3.3543872366
Si	0.6536940573	0.4238206171	-1.1430971152
Si	-5.7662077708	4.2105473779	1.1066338751
Si	-2.3555779962	-1.4810343303	0.3384292274
Si	-5.5440751432	0.3995116131	1.4988971520
Si	0.9038788867	-1.0953783317	2.3866263544
Si	0.9667114585	1.1999569514	5.5190916865
Si	0.7648785476	5.0410973052	5.0857917091
Si	-5.4550302630	2.7031361007	4.6056974027
Si	-2.1738621124	3.1273747245	6.5934606988
Si	-6.3584152568	2.3796007248	2.4575378352
Si	0.1697968538	3.2086747418	6.4350226382
Si	-0.0020460895	-1.3953154583	0.2278020650
Si	-3.3861015090	2.0594143772	-2.2364465852
Si	-3.3346419573	6.6085293306	4.0338110711
Si	3.0613502856	2.8167262399	1.8046958739
Si	-6.2571296520	4.6947875140	5.5717252948
Si	-6.5921342247	6.2007405622	2.0334187645
Si	-0.0483202382	7.0454198301	5.9977875348
Si	-3.0169991147	5.1182603187	7.5253005534
Si	3.2500173971	-1.0227418673	2.2615597963
Si	-3.2286762176	-1.7797475960	-1.8284934326
Si	-0.2468625372	0.1190800149	-3.3027962529
Si	3.0148396375	0.4920925739	-1.2424841704
Si	-2.3926837613	6.9484635545	6.1726792127
Si	-5.3597112941	5.0375028119	7.7212977846
Si	-5.6914161567	6.5185716986	4.1833248627
Si	-3.2364220849	8.9465590925	7.0900812411

Si	-6.5217285286	8.5030030287	5.1423941317
Si	-6.1806393597	7.0367357736	8.6455579371
Si	-5.5743291101	8.8341669813	7.2643625455
Si	-2.5939696202	0.0529440906	-3.1597205191
Si	0.5918225642	-1.8674405973	-4.2659816434
Si	0.8265723258	-3.3848091038	-0.7435666642
Si	3.8596913930	-1.5025077087	-2.1885254601
Si	3.8808502749	0.8033164568	0.9192646664
Si	2.9496580808	-1.8354322835	-4.3385481313
Si	-0.2163542662	-2.1589195231	-6.4558261213
Si	-0.0704478775	-3.6861600724	-2.9045405365
Si	3.1807757791	-3.3048690915	-0.8068757356
Si	6.2140939437	-1.4923635869	-2.3171174064
Si	3.7703837841	-3.8377746653	-5.2959397081
Si	0.7451798010	-5.6786216377	-3.8379553116
Si	-2.4146500314	-3.7769022604	-2.7494219449
Si	4.0488251517	-3.0360165594	1.3637695131
Si	3.9874969505	-5.2586423842	-1.8040481003
Si	-0.0428885093	-6.0244089726	-6.0339705699
Si	3.1097752487	-5.6694513688	-3.9449306198
Si	6.1215566859	-3.7197203054	-5.4261751993
Si	2.9093900137	-4.1253737991	-7.4742520414
Si	6.3403253057	-5.3676851432	-1.9886897378
Si	3.5665018678	-7.9818069642	-4.5372985122
Si	0.5629743326	-4.1805352375	-7.3639133652
Si	0.8449577492	-8.0212104361	-6.9008057041
Si	3.7859487385	-6.0927624133	-8.4176698740
Si	7.0085388543	-3.4994911371	-3.2606705736
Si	6.9234217745	-5.6491855634	-6.4940744486
Si	6.1673354244	-7.4824608864	-5.2521490106
Si	6.1024038435	-5.9012826253	-8.6697610889
Si	3.2276032518	-7.9061981979	-7.0295101971
Si	6.8473707574	-7.4390803098	-2.9792934714
H	0.1815408808	3.5552280871	-1.0075656673
H	-3.0386439496	5.4491861632	0.0706493562
H	0.2500815949	5.8467554628	2.0641018281
H	-5.8140971331	1.5584984990	5.4711739153
H	-5.9262368765	-0.7684444486	2.3162130974
H	-6.1344242996	0.2320762241	0.1569222382
H	-6.3423226245	4.0135562174	-0.2403224393
H	-7.8324909556	2.3178427722	2.5607961725
H	2.2385586958	5.1057784103	4.9854125814
H	-2.5678976019	1.9888332919	7.4510020257
H	0.7320127997	3.4019928877	7.7896285762
H	2.4404997076	1.2387714076	5.4516764356
H	0.5684593768	0.0672954903	6.3769552947
H	0.4915686803	-2.2415379127	3.2271332090

H	-2.7367249108	-2.6387655955	1.1772153636
H	0.3297414198	8.1785159497	5.1308881208
H	0.5354868926	7.2668011071	7.3358249464
H	-2.4231226148	5.3077593425	8.8673322813
H	-2.9629985548	7.7506782597	3.1690906321
H	-7.7318355037	4.6237684882	5.6669485823
H	-8.0635675570	6.1297247629	2.1265568466
H	-6.2268414177	7.3444297027	1.1752294401
H	-5.7263031883	3.8962879225	8.5859534269
H	-5.6205479325	7.2228980767	9.9981668295
H	-7.6509767503	6.9651903708	8.7484046715
H	-2.8471146696	10.0794266196	6.2277286746
H	-2.6454404653	9.1563976845	8.4268800059
H	-7.9877568847	8.3822606339	5.2735408700
H	-6.2222125456	9.6448792544	4.2571060850
H	-2.6600886245	-0.3230768881	4.3296215111
H	-6.0849155790	10.0950500293	7.8437153491
H	-4.7044139897	-1.8356315655	-1.7602051538
H	0.1607850428	1.2639051721	-4.1474732749
H	-2.9164649428	3.1959460673	-3.0544815152
H	-4.8603462833	2.0597952386	-2.2329753068
H	-3.1541534999	-0.1224593654	-4.5171958932
H	3.4288997171	3.9315449624	0.9091262332
H	3.6696995163	3.0596661216	3.1256511739
H	3.8062313865	-0.8332419228	3.6176574407
H	3.4170571585	1.6260421229	-2.1038525247
H	5.3570323972	0.8534619233	0.8463362803
H	0.4240767033	-4.5280621266	0.1045934683
H	3.3842047029	-0.7145398634	-5.2034446450
H	-2.7933897672	-4.9253802910	-1.9039588449
H	-2.9844081220	-3.9815208753	-4.0956456635
H	5.5228965852	-3.0220198749	1.3088418585
H	3.6221712332	-4.1728759295	2.2017525609
H	0.3332263073	-6.8206468926	-2.9963325570
H	0.2678134347	-1.0438450374	-7.2937611156
H	-1.6915369568	-2.1471201139	-6.4649296390
H	-1.5158879655	-6.1456829192	-6.0020349090
H	3.3439365986	-2.9715390499	-8.2903381216
H	6.4891192959	-2.5311962689	-6.2247224267
H	6.9548320019	-5.3184592426	-0.6462341012
H	6.8010405714	-1.3153877920	-0.9756427116
H	6.6617904129	-0.3742007289	-3.1700537250
H	0.0261934365	-4.3699162405	-8.7282293599
H	8.4860416762	-3.4807796225	-3.3356184619
H	8.4009946059	-5.6785568073	-6.4520947886
H	3.1370536864	-6.3329000653	-9.7253682529
H	6.5027900001	-8.7660898652	-5.9019892926

H	6.4554095140	-4.7439418591	-9.5104618949
H	6.6662922523	-7.1260688264	-9.2656103253
H	3.7508348494	-9.1615846512	-7.5994264703
H	0.3535894879	-8.2490654724	-8.2743845353
H	0.4611462352	-9.1621686321	-6.0534603829
H	8.2997413196	-7.6939998779	-2.9749847472
H	6.1695113579	-8.5182506463	-2.2442934527

TNN System: MECI-L

Si	-2.5669511322	2.3588724045	-0.1039824540
Si	-0.2068270253	2.4304001037	-0.2222780248
Si	-3.3738896706	4.3441631451	0.8775815437
Si	-3.2305189881	0.5260126410	1.2369977139
Si	0.7382260785	2.7841501906	1.9012892757
Si	-2.4620642587	4.6222010053	3.0398749090
Si	-2.2660257003	0.8029933374	3.3570501901
Si	-0.1107851083	4.7288236526	2.9301033045
Si	-3.0963474243	2.7738533086	4.3789765678
Si	0.0905378264	0.9397455297	3.1794511427
Si	0.6166126598	0.3900096743	-1.0549971279
Si	-5.7215336890	4.2907351379	1.0182502188
Si	-2.4381069102	-1.4874382376	0.3291135093
Si	-5.5727371896	0.4374829063	1.4581830496
Si	0.8373613910	-1.8059074834	2.6100046726
Si	0.9486448079	1.0708549509	5.3863497435
Si	0.7717701641	4.9568497214	5.0993510227
Si	-5.4603495332	2.7311410752	4.4980817856
Si	-2.2011273014	3.0448852769	6.5478325235
Si	-6.3584551679	2.4579476719	2.3448211131
Si	0.1484801442	3.0734970920	6.3652743924
Si	-0.0952765027	-1.3856402171	0.3309975683
Si	-3.4354548747	2.0489072477	-2.2718503423
Si	-3.2798036709	6.6028432664	4.0320604163
Si	3.0871782916	2.8205713276	1.8109199886
Si	-6.2527372659	4.7218310523	5.4688830457
Si	-6.5077695729	6.2962605724	1.9469617978
Si	-0.0301482047	6.9285127803	6.0864805915
Si	-3.0500711261	5.0264590910	7.5052433677
Si	3.1517497581	-1.0683966993	2.4100816256
Si	-3.2719225873	-1.8005501277	-1.8399523123
Si	-0.2687230032	0.0846763456	-3.2272185629
Si	2.9744587898	0.4448437944	-1.1302665039
Si	-2.3793823855	6.8776499076	6.2020882120
Si	-5.4042775579	5.0054693596	7.6459330365
Si	-5.6396324751	6.5612051782	4.1187365372
Si	-3.2086315601	8.8681324528	7.1501981625

Si	-6.4031717298	8.5799467636	5.0582973822
Si	-6.2494405861	7.0066103350	8.5487082791
Si	-5.5538026237	8.8210679037	7.2322843509
Si	-2.6169797136	0.0351328804	-3.1543025126
Si	0.5575764974	-1.8943952819	-4.1906309378
Si	0.8192518387	-3.3983009716	-0.6583553306
Si	3.8229781052	-1.5085490948	-2.1303980489
Si	3.8124874763	0.7350855332	1.0504027648
Si	2.9072952917	-1.8147067596	-4.2820383189
Si	-0.3002759893	-2.1656644330	-6.3628784450
Si	-0.0967422344	-3.7119276838	-2.8219099275
Si	3.1814350562	-3.3293051240	-0.7569271973
Si	6.1681553724	-1.4175969412	-2.3197187662
Si	3.7396125931	-3.7839064236	-5.2782271392
Si	0.7345653677	-5.7053115261	-3.7875047378
Si	-2.4442301610	-3.8135362474	-2.7045231187
Si	4.0572995071	-3.0202035964	1.4081148990
Si	4.0072068223	-5.3210062092	-1.7320547213
Si	-0.1311804806	-6.0084195376	-5.9579549672
Si	3.0904071884	-5.6021006527	-3.8936030797
Si	6.0976670383	-3.7257542993	-5.4008654150
Si	2.8313700130	-4.1043135442	-7.4359100582
Si	6.3560452328	-5.2584674773	-1.9132510999
Si	3.9512535030	-7.5284609937	-4.9271861997
Si	0.4837243636	-4.1711485659	-7.2930506840
Si	0.6696886785	-8.0039688095	-6.8967985752
Si	3.6849169998	-6.0736040986	-8.4045771226
Si	6.9796917264	-3.4171655171	-3.2412724884
Si	6.9165090151	-5.6986991491	-6.3867242391
Si	6.3132281557	-7.5150361141	-5.0156677782
Si	6.0288824613	-5.9692226276	-8.5454710008
Si	3.0113696664	-7.8927805074	-7.0688991026
Si	7.1667753943	-7.2574313182	-2.8401263516
H	0.1913300610	3.5275229660	-1.1309188780
H	-2.9540715876	5.4916865934	0.0434529436
H	0.2735806900	5.8986768279	2.1087964369
H	-5.8628714928	1.5838864515	5.3402906921
H	-5.9093968108	-0.6667565419	2.3779394077
H	-6.1893213403	0.1599137247	0.1473843493
H	-6.2722355412	4.1158787964	-0.3423650556
H	-7.8331244651	2.4323641758	2.4516649298
H	2.2456325016	5.0168417726	5.0107913721
H	-2.6132378570	1.8885793992	7.3729652145
H	0.7377535940	3.1914716758	7.7179490699
H	2.4206869018	1.0752478676	5.3743397381
H	0.4759382335	-0.0844121117	6.1708856711
H	-2.8715914975	-2.6008963753	1.1977672957

H	0.4027499871	8.0861695977	5.2804153756
H	0.5243217069	7.0710050595	7.4469750848
H	-2.4795142925	5.1861642569	8.8611385912
H	-2.8513787389	7.7484088582	3.1986544245
H	-7.7299432670	4.6603397443	5.5251563273
H	-7.9826673802	6.2855509570	1.9983809674
H	-6.0781567176	7.4339291661	1.1103246111
H	-5.8351123869	3.8619095198	8.4785112851
H	-5.7893834659	7.1821643419	9.9400343253
H	-7.7235019779	6.9391123099	8.5478426420
H	-2.7535859407	10.0148966252	6.3412742873
H	-2.6656081257	9.0146540328	8.5155250301
H	-7.8787992814	8.5879338549	5.0798236109
H	-5.9450310664	9.6981685310	4.2101198055
H	-2.6050373309	-0.3551236393	4.2111662762
H	-6.0553721326	10.0828808659	7.8169688021
H	-4.7469169839	-1.8578595427	-1.7725045249
H	0.1646239096	1.2319614262	-4.0553360903
H	-3.0322025039	3.1737070505	-3.1376712995
H	-4.9094073163	2.0121827253	-2.2095419656
H	-3.1343059409	-0.1428958439	-4.5277267301
H	3.5244803284	3.8833956529	0.8868727823
H	3.6241277430	3.1197060487	3.1522037453
H	3.7797708977	-0.9367160417	3.7450595457
H	3.3692289681	1.6170402951	-1.9426659639
H	5.2907821349	0.7347429897	0.9845154225
H	0.4079038568	-4.5391863000	0.1891903983
H	3.3002410038	-0.6676212276	-5.1308940493
H	-2.8492590695	-4.9386044503	-1.8398457669
H	-2.9969984640	-4.0460920870	-4.0531378942
H	5.5244971827	-2.8780761725	1.3249400301
H	3.7472203310	-4.2052551261	2.2312553976
H	0.3625822824	-6.8630962665	-2.9456632719
H	3.6027147403	-6.4795400696	-0.9071623713
H	0.1369217710	-1.0325752657	-7.2009678181
H	-1.7747200993	-2.1777042560	-6.3285870246
H	-1.6056966723	-6.0814539745	-5.8781560641
H	3.2343086783	-2.9550224359	-8.2749374442
H	6.4680232453	-2.5802014819	-6.2597847671
H	6.9351385076	-5.0961971783	-0.5629566626
H	6.7886204920	-1.1966825025	-1.0003572200
H	6.5355608590	-0.2917507241	-3.2007450993
H	-0.0741497151	-4.3568591985	-8.6497673675
H	8.4553368743	-3.3792569123	-3.3312797821
H	8.3928042705	-5.6310065172	-6.4504763653
H	3.1135114108	-6.2460529197	-9.7583795228
H	6.7735732984	-8.7798252021	-5.6239421389

H	6.4130673907	-4.8179214730	-9.3822237371
H	6.5525646401	-7.2036456996	-9.1618612127
H	3.5591650778	-9.1535344048	-7.6078725754
H	0.1135862402	-8.1826848852	-8.2519690843
H	0.2874701688	-9.1605456381	-6.0666195872
H	8.6391970083	-7.2146530585	-2.9234350639
H	6.7650491470	-8.4106203675	-2.0142726972

TNN System: MECI-R

Si	-2.5723092236	2.3222655077	-0.0500938233
Si	-0.2122571571	2.3765305788	-0.1641646118
Si	-3.3965441807	4.3058861496	0.9254849318
Si	-3.2098556510	0.4915084585	1.3104341606
Si	0.7095007280	2.6939324364	1.9867610139
Si	-2.4695074955	4.6136672908	3.0757359504
Si	-2.2922378257	0.7965687093	3.4644976604
Si	-0.1096742984	4.6875214755	2.9448152879
Si	-3.1040581462	2.7871443560	4.4459688172
Si	0.0642343755	0.8758004407	3.3611467945
Si	0.6316238096	0.3958191770	-1.1556379299
Si	-5.7432000430	4.2447552695	1.1025666305
Si	-2.3915913357	-1.4965625135	0.3439329946
Si	-5.5567220789	0.4091135924	1.5154891870
Si	0.9034392882	-1.0686420564	2.3274481460
Si	0.9535488737	1.1466786686	5.5299970496
Si	0.7892350693	5.0040120010	5.0989175236
Si	-5.4643685767	2.7148794357	4.5947505031
Si	-2.1698280069	3.1027789191	6.5914325902
Si	-6.3590658842	2.4099914967	2.4399270011
Si	0.1752639664	3.1691262119	6.4352887077
Si	-0.0326018276	-1.4384916914	0.1963723615
Si	-3.4169084949	2.0460326936	-2.2338909770
Si	-3.2944432104	6.6012095065	4.0499037165
Si	3.0587510450	2.7583110713	1.8311468748
Si	-6.2486710277	4.7096840499	5.5612637757
Si	-6.5359672777	6.2461975031	2.0348952270
Si	-0.0182470954	7.0005092666	6.0359306362
Si	-3.0105047778	5.0904108015	7.5321419043
Si	3.2549792230	-1.0894988553	2.2378129864
Si	-3.2611858861	-1.7937195225	-1.8255063409
Si	-0.2780983120	0.0980112602	-3.3155724260
Si	2.9928845201	0.4499238524	-1.2513750306
Si	-2.3653137219	6.9306830193	6.1961872266
Si	-5.3567726366	5.0179916636	7.7163187269
Si	-5.6501948496	6.5338666205	4.1926963532
Si	-3.2093558932	8.9310627688	7.1141043546

Si	-6.4746129623	8.5104353835	5.1637499394
Si	-6.1426253122	7.0128866178	8.6759684296
Si	-5.5480093700	8.8160680043	7.2987436131
Si	-2.6244966450	0.0387377788	-3.1549044764
Si	0.5495637536	-1.8854934670	-4.2912787851
Si	0.8080909118	-3.4257070938	-0.7799283931
Si	3.8244101775	-1.5399275230	-2.2134549541
Si	3.8735052558	0.7566248508	0.9105062212
Si	2.9101136802	-1.8504691856	-4.3660504013
Si	-0.2529127531	-2.1548950189	-6.4906788957
Si	-0.1178738045	-3.7042394669	-2.9359290531
Si	3.1676033093	-3.3707510310	-0.8700017873
Si	6.1694522103	-1.4566027115	-2.4038227595
Si	3.7409153788	-3.8498959322	-5.3310355290
Si	0.6980988809	-5.6932449575	-3.8802488292
Si	-2.4583900619	-3.8021134418	-2.7290658045
Si	3.9915107381	-3.1201951430	1.3202951736
Si	3.9919780722	-5.3671677108	-1.8334363813
Si	-0.0928381701	-6.0130981046	-6.0710175524
Si	3.0402814696	-5.6777599634	-4.0017685557
Si	6.0961746278	-3.7968190645	-5.4490988564
Si	2.8804184691	-4.0649748206	-7.5114896372
Si	6.3495723371	-5.3117977420	-1.9754137953
Si	3.9329128778	-7.9642938990	-4.2981922876
Si	0.5343491306	-4.1729310604	-7.4048752549
Si	0.8484671077	-8.0330630278	-6.8026543596
Si	3.7810581927	-6.0041722983	-8.4721630682
Si	6.9773447415	-3.4696852183	-3.2959381053
Si	6.8911561585	-5.8002179209	-6.4020195732
Si	6.2267838349	-7.6157112134	-5.0522062044
Si	6.1144886886	-5.9768162247	-8.6029953684
Si	3.1683420989	-7.7471723982	-7.0474675930
Si	7.2132605328	-7.2833863991	-2.9281774910
H	0.1915304316	3.5207565604	-1.0116315566
H	-3.0006835404	5.4546596796	0.0820529129
H	0.2841361898	5.8195080185	2.0766319615
H	-5.8435319667	1.5731711403	5.4557410404
H	-5.9205252903	-0.7288274370	2.3821889479
H	-6.1612749234	0.2016798041	0.1860624802
H	-6.3155971549	4.0651008315	-0.2487087827
H	-7.8348472217	2.3626656217	2.5329192339
H	2.2639711843	5.0652162808	5.0036150948
H	-2.5596508625	1.9554705850	7.4386534316
H	0.7346381857	3.3441891556	7.7928697002
H	2.4274535506	1.1508860628	5.4665890219
H	0.5246553799	0.0177916074	6.3777967711
H	-2.7743033774	-2.6452352184	1.1936705750

H	0.3872570506	8.1468756637	5.1988586880
H	0.5558549761	7.1789754572	7.3834875792
H	-2.4279399909	5.2609956001	8.8816038396
H	-2.9097860317	7.7371692894	3.1825213839
H	-7.7252216254	4.6631451093	5.6429702520
H	-8.0096457130	6.2257586385	2.1110065999
H	-6.1215450962	7.3833529828	1.1904996745
H	-5.7341421778	3.8657074916	8.5620070174
H	-5.5373331400	7.1857981441	10.0105228249
H	-7.6091882363	6.9555575110	8.8256657415
H	-2.8344050818	10.0607384979	6.2409444173
H	-2.6076807782	9.1562168659	8.4430390287
H	-7.9449341763	8.4110490803	5.2599943553
H	-6.1375828333	9.6587592027	4.3008725139
H	-2.6882807608	-0.3494037099	4.3124731713
H	-6.0602713166	10.0733946578	7.8840278804
H	-4.7365908514	-1.8368413760	-1.7436160240
H	0.1257226429	1.2481491478	-4.1530271978
H	-2.9724604728	3.1831526915	-3.0634774618
H	-4.8922159152	2.0361459610	-2.2124649250
H	-3.1880656116	-0.1416833071	-4.5093815617
H	3.4543055393	3.8946948670	0.9770476770
H	3.6392711983	2.9595978253	3.1724661965
H	3.7789781032	-0.9232539605	3.6089449320
H	3.4016532524	1.5918205168	-2.0978834140
H	5.3488150232	0.8187494903	0.8330421663
H	0.3870570611	-4.5729175596	0.0537398471
H	3.3347772847	-0.7150878077	-5.2170881525
H	-2.8048551127	-4.9229578534	-1.8330698118
H	-3.0726883600	-4.0503299897	-4.0479977188
H	5.4664358243	-3.1481879396	1.3173979773
H	3.5012700075	-4.2348444144	2.1529194742
H	0.2762794078	-6.8388318135	-3.0484862700
H	3.5749291887	-6.5077683861	-0.9904052114
H	0.2603347361	-1.0419914294	-7.3133473467
H	-1.7273907631	-2.1148754064	-6.5182795211
H	-1.5649639561	-6.1364180038	-6.0758542197
H	3.2925744561	-2.8861025729	-8.3018023866
H	6.4796110401	-2.6609460226	-6.3167685577
H	6.8928272730	-5.1333163158	-0.6119001409
H	6.7805447459	-1.2074736503	-1.0838113455
H	6.5238440901	-0.3413586674	-3.3027386604
H	-0.0018181131	-4.3499005217	-8.7717211250
H	8.4525571781	-3.4226370572	-3.3851544083
H	8.3698310940	-5.7548695546	-6.3995889792
H	3.1402483571	-6.2637169912	-9.7807948769
H	6.7463241337	-8.8745543858	-5.6298951347

H	6.5678867497	-4.8359908308	-9.4187574252
H	6.5789679511	-7.2313389440	-9.2237997540
H	3.8735349027	-9.0094652895	-7.3515427269
H	0.3228028070	-8.4513310034	-8.1177670783
H	0.5843788080	-9.0982207508	-5.8203560830
H	8.6732608324	-7.1324011383	-3.0735420578
H	6.9305561184	-8.4339798853	-2.0513334176

REFERENCES

REFERENCES

1. Canham, L. T., Silicon Quantum Wire Array Fabrication by Electrochemical and Chemical Dissolution of Wafers. *Appl Phys Lett* **1990**, *57*, 1046-1048.
2. Takagi, H.; Ogawa, H.; Yamazaki, Y.; Ishizaki, A.; Nakagiri, T., Quantum Size Effects on Photoluminescence in Ultrafine Si Particles. *Appl Phys Lett* **1990**, *56*, 2379-2380.
3. Li, Q.; Luo, T. Y.; Zhou, M.; Abroshan, H.; Huang, J. C.; Kim, H. J.; Rosi, N. L.; Shao, Z. Z.; Jin, R. C., Silicon Nanoparticles with Surface Nitrogen: 90% Quantum Yield with Narrow Luminescence Bandwidth and the Ligand Structure Based Energy Law. *ACS Nano* **2016**, *10*, 8385-8393.
4. Walters, R. J.; Bourianoff, G. I.; Atwater, H. A., Field-effect electroluminescence in silicon nanocrystals. *Nat Mater* **2005**, *4*, 143-146.
5. Gelloz, B.; Koshida, N., Electroluminescence with high and stable quantum efficiency and low threshold voltage from anodically oxidized thin porous silicon diode. *J Appl Phys* **2000**, *88*, 4319-4324.
6. Lalic, N.; Linnros, J., Characterization of a porous silicon diode with efficient and tunable electroluminescence. *J Appl Phys* **1996**, *80*, 5971-5977.
7. Valenta, J.; Lalic, N.; Linnros, J., Electroluminescence microscopy and spectroscopy of silicon nanocrystals in thin SiO₂ layers. *Opt Mater* **2001**, *17*, 45-50.
8. Liu, C. Y.; Holman, Z. C.; Kortshagen, U. R., Hybrid Solar Cells from P3HT and Silicon Nanocrystals. *Nano Lett* **2009**, *9*, 449-452.
9. Conibeer, G.; Green, M.; Corkish, R.; Cho, Y.; Cho, E. C.; Jiang, C. W.; Fangsuwannarak, T.; Pink, E.; Huang, Y. D.; Puzzer, T.; Trupke, T.; Richards, B.; Shalav, A.; Lin, K. L., Silicon nanostructures for third generation photovoltaic solar cells. *Thin Solid Films* **2006**, *511*, 654-662.
10. Liang, D.; Bowers, J. E., Recent progress in lasers on silicon. *Nat Photonics* **2010**, *4*, 511-517.
11. Pavesi, L.; Dal Negro, L.; Mazzoleni, C.; Franzo, G.; Priolo, F., Optical gain in silicon nanocrystals. *Nature* **2000**, *408*, 440-444.
12. Wolkin, M. V.; Jorne, J.; Fauchet, P. M.; Allan, G.; Delerue, C., Electronic states and luminescence in porous silicon quantum dots: The role of oxygen. *Phys Rev Lett* **1999**, *82*, 197-200.

13. Jurbergs, D.; Rogojina, E.; Mangolini, L.; Kortshagen, U., Silicon nanocrystals with ensemble quantum yields exceeding 60%. *Appl Phys Lett* **2006**, *88*, 2331-16.
14. Meyer, B. K.; Petrovakocho, V.; Muschik, T.; Linke, H.; Omling, P.; Lehmann, V., Electron-Spin-Resonance Investigations of Oxidized Porous Silicon. *Appl Phys Lett* **1993**, *63*, 1930-1932.
15. Fernandez, B. G.; Lopez, M.; Garcia, C.; Perez-Rodriguez, A.; Morante, J. R.; Bonafos, C.; Carrada, M.; Claverie, A., Influence of average size and interface passivation on the spectral emission of Si nanocrystals embedded in SiO₂. *J Appl Phys* **2002**, *91*, 798-807.
16. Belomoin, G.; Therrien, J.; Nayfeh, M., Oxide and hydrogen capped ultrasmall blue luminescent Si nanoparticles. *Appl Phys Lett* **2000**, *77*, 779-781.
17. Svrcek, V.; Mariotti, D.; Nagai, T.; Shibata, Y.; Turkevych, I.; Kondo, M., Photovoltaic Applications of Silicon Nanocrystal Based Nanostructures Induced by Nanosecond Laser Fragmentation in Liquid Media. *J Phys Chem C* **2011**, *115*, 5084-5093.
18. Stefanov, B. B.; Gurevich, A. B.; Weldon, M. K.; Raghavachari, K.; Chabal, Y. J., Silicon epoxide: Unexpected intermediate during silicon oxide formation. *Phys Rev Lett* **1998**, *81*, 3908-3911.
19. Lannoo, M.; Delerue, C.; Allan, G., NONRADIATIVE RECOMBINATION ON DANGLING BONDS IN SILICON CRYSTALLITES. *J. Lumines.* **1993**, *57*, 243-247.
20. Williamson, A. J.; Grossman, J. C.; Hood, R. Q.; Puzder, A.; Galli, G., Quantum Monte Carlo calculations of nanostructure optical gaps: Application to silicon quantum dots. *Phys Rev Lett* **2002**, *89*, 4196803.
21. Brawand, N. P.; Voros, M.; Galli, G., Surface dangling bonds are a cause of B-type blinking in Si nanoparticles. *Nanoscale* **2015**, *7*, 3737-3744.
22. Liu, J.; Neukirch, A. J.; Prezhdo, O. V., Non-Radiative Electron-Hole Recombination in Silicon Clusters: Ab Initio Non-Adiabatic Molecular Dynamics. *J Phys Chem C* **2014**, *118*, 20702-20709.
23. Hall, R. N., Electron-Hole Recombination in Germanium. *Phys Rev* **1952**, *87*, 387-387.
24. Shockley, W.; Read, W. T., Statistics of the Recombinations of Holes and Electrons. *Phys Rev* **1952**, *87*, 835-842.
25. Shu, Y. N.; Fales, B. S.; Levine, B. G., Defect-Induced Conical Intersections Promote Nonradiative Recombination. *Nano Lett* **2015**, *15*, 6247-6253.

26. Shu, Y. N.; Fales, B. S.; Peng, W. T.; Levine, B. G., Understanding Nonradiative Recombination through Defect-Induced Conical Intersections. *J Phys Chem Lett* **2017**, *8*, 4091-4099.
27. Levine, B. G.; Esch, M. P.; Fales, B. S.; Hardwick, D. T.; Peng, W. T.; Shu, Y., Conical Intersections at the Nanoscale: Molecular Ideas for Materials. *Annu Rev Phys Chem* **2019**, *70*, 21-43.
28. Bernardi, F.; Olivucci, M.; Robb, M. A., Potential energy surface crossings in organic photochemistry. *Chem Soc Rev* **1996**, *25*, 321.
29. Yarkony, D. R., Diabolical conical intersections. *Rev Mod Phys* **1996**, *68*, 985-1013.
30. Yarkony, D. R., Nonadiabatic Quantum Chemistry-Past, Present, and Future. *Chem Rev* **2012**, *112*, 481-498.
31. Levine, B. G.; Martinez, T. J., Isomerization through conical intersections. *Annu Rev Phys Chem* **2007**, *58*, 613-634.
32. Shu, Y. A.; Levine, B. G., Communication: Non-radiative recombination via conical intersection at a semiconductor defect. *J Chem Phys* **2013**, *139*, 081102.
33. Shu, Y. N.; Levine, B. G., Nonradiative Recombination via Conical Intersections Arising at Defects on the Oxidized Silicon Surface. *J Phys Chem C* **2015**, *119*, 1737-1747.
34. Shu, Y. A.; Levine, B. G., Do Excited Silicon-Oxygen Double Bonds Emit Light? *J Phys Chem C* **2014**, *118*, 7669-7677.
35. Shu, Y. N.; Kortshagen, U. R.; Levine, B. G.; Anthony, R. J., Surface Structure and Silicon Nanocrystal Photoluminescence: The Role of Hypervalent Silyl Groups. *J Phys Chem C* **2015**, *119*, 26683-26691.
36. Peng, W. T.; Fales, B. S.; Shu, Y. N.; Levine, B. G., Dynamics of recombination via conical intersection in a semiconductor nanocrystal. *Chem Sci* **2018**, *9*, 681-687.
37. Schmidt, T.; Chizhik, A. I.; Chizhik, A. M.; Potrick, K.; Meixner, A. J.; Huisken, F., Radiative exciton recombination and defect luminescence observed in single silicon nanocrystals. *Phys Rev B* **2012**, *86*, 125302.
38. Garcia, C.; Garrido, B.; Pellegrino, P.; Ferre, R.; Moreno, J. A.; Morante, J. R.; Pavese, L.; Cazzanelli, M., Size dependence of lifetime and absorption cross section of Si nanocrystals embedded in SiO₂. *Appl Phys Lett* **2003**, *82*, 1595-1597.
39. Sychugov, I.; Juhasz, R.; Valenta, J.; Linnros, J., Narrow luminescence linewidth of a silicon quantum dot. *Phys Rev Lett* **2005**, *94*, 087405.

40. Levine, B. G.; Peng, W. T.; Esch, M. P., Locality of Conical Intersections in Semiconductor Nanomaterials. *Phys Chem Chem Phys* **2019**, *21*, 10870.
41. Haider, M. B.; Pitters, J. L.; DiLabio, G. A.; Livadaru, L.; Mutus, J. Y.; Wolkow, R. A., Controlled Coupling and Occupation of Silicon Atomic Quantum Dots at Room Temperature. *Phys Rev Lett* **2009**, *102*, 046805.
42. Livadaru, L.; Xue, P.; Shaterzadeh-Yazdi, Z.; DiLabio, G. A.; Mutus, J.; Pitters, J. L.; Sanders, B. C.; Wolkow, R. A., Dangling-bond charge qubit on a silicon surface. *New J Phys* **2010**, *12*, 083018.
43. Kawai, H.; Ample, F.; Wang, Q.; Yeo, Y. K.; Saeys, M.; Joachim, C., Dangling-bond logic gates on a Si(100)-(2 x 1)-H surface. *J Phys-Condens Mat* **2012**, *24*, 13095011.
44. Schofield, S. R.; Studer, P.; Hirjibehedin, C. F.; Curson, N. J.; Aeppli, G.; Bowler, D. R., Quantum engineering at the silicon surface using dangling bonds. *Nat Commun* **2013**, *4*, 71649.
45. Berthe, M.; Urbieto, A.; Perdigo, L.; Grandidier, B.; Deresmes, D.; Delerue, C.; Stievenard, D.; Rurali, R.; Lorente, N.; Magaud, L.; Ordejon, P., Electron transport via local polarons at interface atoms. *Phys Rev Lett* **2006**, *97*, 206801.
46. Hohenstein, E. G.; Bouduban, M. E. F.; Song, C. C.; Luehr, N.; Ufimtsev, I. S.; Martinez, T. J., Analytic first derivatives of floating occupation molecular orbital-complete active space configuration interaction on graphical processing units. *J Chem Phys* **2015**, *143*, 014111.
47. Slavicek, P.; Martinez, T. J., Ab initio floating occupation molecular orbital-complete active space configuration interaction: An efficient approximation to CASSCF. *J Chem Phys* **2010**, *132*, 234102.
48. Granucci, G.; Persico, M.; Toniolo, A., Direct semiclassical simulation of photochemical processes with semiempirical wave functions. *J Chem Phys* **2001**, *114*, 10608-10615.
49. Hollas, D.; Sistik, L.; Hohenstein, E. G.; Martinez, T. J.; Slavicek, P., Nonadiabatic Ab Initio Molecular Dynamics with the Floating Occupation Molecular Orbital-Complete Active Space Configuration Interaction Method. *J Chem Theory Comput* **2018**, *14*, 339-350.
50. Roos, B. O.; Taylor, P. R., A COMPLETE ACTIVE SPACE SCF METHOD (CASSCF) USING A DENSITY-MATRIX FORMULATED SUPER-CI APPROACH. *Chem Phys* **1980**, *48*, 157-173.
51. Shu, Y. A.; Hohenstein, E. G.; Levine, B. G., Configuration interaction singles natural orbitals: An orbital basis for an efficient and size intensive multireference description of electronic excited states. *J Chem Phys* **2015**, *142*, 024102.

52. Finley, J.; Malmqvist, P. A.; Roos, B. O.; Serrano-Andres, L., The multi-state CASPT2 method. *Chem Phys Lett* **1998**, *288*, 299-306.
53. Wadt, W. R.; Hay, P. J., Abinitio Effective Core Potentials for Molecular Calculations - Potentials for Main Group Elements Na to Bi. *J Chem Phys* **1985**, *82*, 284-298.
54. Ufimtsev, I. S.; Martinez, T. J., Quantum Chemistry on Graphical Processing Units. 3. Analytical Energy Gradients, Geometry Optimization, and First Principles Molecular Dynamics. *J Chem Theory Comput* **2009**, *5*, 2619-2628.
55. Fales, B. S.; Levine, B. G., Nanoscale Multireference Quantum Chemistry: Full Configuration Interaction on Graphical Processing Units. *J Chem Theory Comput* **2015**, *11*, 4708-4716.
56. Song, C. C.; Wang, L. P.; Martinez, T. J., Automated Code Engine for Graphical Processing Units: Application to the Effective Core Potential Integrals and Gradients. *J Chem Theory Comput* **2016**, *12*, 92-106.
57. Fales, B. S.; Hohenstein, E. G.; Levine, B. G., Robust and Efficient Spin Purification for Determinantal Configuration Interaction. *J Chem Theory Comput* **2017**, *13*, 4162-4172.
58. Levine, B. G.; Coe, J. D.; Martinez, T. J., Optimizing conical intersections without derivative coupling vectors: Application to multistate multireference second-order perturbation theory (MS-CASPT2). *J Phys Chem B* **2008**, *112*, 405-413.
59. Meek, G. A.; Levine, B. G., Evaluation of the Time-Derivative Coupling for Accurate Electronic State Transition Probabilities from Numerical Simulations. *J Phys Chem Lett* **2014**, *5*, 2351-2356.
60. Fernandez-Alberti, S.; Roitberg, A. E.; Nelson, T.; Tretiak, S., Identification of unavoided crossings in nonadiabatic photoexcited dynamics involving multiple electronic states in polyatomic conjugated molecules. *J Chem Phys* **2012**, *137*, 014512.
61. Nelson, T.; Fernandez-Alberti, S.; Roitberg, A. E.; Tretiak, S., Artifacts due to trivial unavoided crossings in the modeling of photoinduced energy transfer dynamics in extended conjugated molecules. *Chem Phys Lett* **2013**, *590*, 208-213.

CHAPTER 4 NONADIABATIC DYNAMICS STUDY OF SILICON DANGLING BOND DEFECTS AT DIFFERENT CHARGED STATES

4.1 Introduction

Dangling bond (DB) defects on the surfaces of SiNCs have been an intriguing subject to study. The low-dimensional silicon materials such as SiNCs were found to emit light as a result of quantum confinement effects.¹⁻² However, DB defects in such systems were deemed detrimental and unwanted since they have the ability to quench photoluminescent (PL) effectively.³⁻⁶ Besides, the fluorescence intermittency in SiNCs has recently been connected to the existence and the charging/discharging of surface DBs.⁷ Both effects impair the potential employment of SiNCs for light emitting applications, in spite of the great advantage of its compatibility to modern silicon technology and infrastructure.⁸⁻¹¹ In addition, DBs work as deep-level charge traps in photovoltaic materials, which impose limits on the performance of SiNCs in optoelectronic devices as well.¹² However, there is renewed interest among researchers who are now taking advantages to make useful applications out of DBs, based on the unique electronic properties and chemical reactivity as well as the experimental techniques to precisely pattern DBs on surfaces.¹³⁻¹⁴ For example, DBs can be engineered to work as coupled quantum wells for quantum computing qubits.¹⁵ Besides, the DB on the surface of SiNCs can initialize and direct chain reactions of organic molecules,¹⁶ and different mechanisms for a chemical reaction occur on surfaces with DBs of different charge states.¹⁷

Our group is particularly interested in the photophysics of SiNCs (along with other semiconductor nanocrystals¹⁸) with various kinds of defects.¹⁹⁻²⁵ Although it is well known that defects play an important role in nonradiative (NR) decay processes, it is generally hard to identify a specific defect as a NR decay center, and the atomistic details of NR decay processes are not completely understood. Knowledge of such mechanisms is the key for rational design and device optimization. In view of this, we applied ab initio molecular dynamics (AIMD) to simulate electronic and nuclear dynamics after excitation. Without assuming a particular reaction coordinate coupled to the NR decay processes, our studies bring new insights into the photophysics of defective SiNCs via the notion of defect-induced conical intersections (DICIs) that facilitate NR

recombination.²⁶ For the neutral DB-SiNCs, we reveal a previously unknown NR decay mechanism in DB-SiNCs. In addition to the conventional wisdom that a pyramidalization mode where Si-Si bonds surrounding DB undergo symmetrical stretching is involved in the NR decay process,^{7,27} we found asymmetrical stretching modes (one Si-Si bond or two Si-Si bonds stretching) surrounding the DB site that are important to the NR recombination process. These vibrational modes are driven by the Jahn-Teller effect on the doubly degenerate first excited state, which drives the system toward a DICI between the first excited and the ground states. Due to the accessibility of the DICI, the excitation energy will dissipate to heat efficiently when the vertical excitation energy of an SiNC is larger than the energy of its DICI (estimated 2.4 eV by a complete active space configuration interaction method in a SiNC model). The discovery of conical intersections in defective SiNCs is consistent with several experimental findings. Most importantly, the existence of energetically and kinetically accessible DICIs between the first excited and ground states in defective SiNCs reconciles the experimental observations of slow (S-) band in SiNCs after oxidation. Some experiments found the emission of S-band is independent of the size of SiNCs,²⁸ but others suggested that the size-independent red-shifted PL (S-band) is from quantum-confined states rather than defect states.²⁹⁻³¹ Based on our DICI concept, when an SiNC has an energy gap larger than the energy of DICI, the PL of oxidized SiNCs becomes susceptible to the CI since it is energetically accessible. Thus, the unusual features of the S-band originates from the quenching of smaller wavelength emitters in an ensemble of SiNCs after oxidation, which causes an overall red-shifted and size-insensitive PL spectra.

Silicon DBs can exist in positive (DB^+) and negative (DB^-) charged states other than the neutral (DB^0) state, adjusting to the environment (e.g. electrochemical potential). The attachment/removal of an electron to/from the DB alters its electronic structure, that in turn changes the properties and achievable applications as introduced in the first paragraph. To obtain a thorough picture for the photophysics of SiNCs with DB defects, we consider different charged states of DBs, including nonadiabatic effects to the simulations. We apply the ab initio multiple spawning (AIMS) method to study the dynamics of the neutral as well as charged silicon DBs after excitation using small cluster models. As mentioned above, the dynamical simulations give us valuable insights into the atomistic details of photophysical processes. The important points on the potential energy surfaces (PESs), such as minimum energy geometries on the excited state

and conical intersections (CIs), can be explored by the dynamical simulations, and further extraction of the energies and locations are performed by geometry optimization with higher order methods that include both static and dynamical electron correlation. It is worth mentioning that most of our previous simulations examine the NR recombination processes between the defect localized state and ground state. For the energy transfer process from the delocalized excitonic state to the defect localized state, we have estimated the transfer rate based on a Marcus-like theory.²⁴ The consideration of negatively charged DB will give us some insight of this process from direct dynamics simulations for the first time. Based on our results, experimental means to observe NR decay via DB is briefly discussed.

We have shown in previous studies that CIs are generally localized in nature,^{25, 32} thus a small cluster model can give us a reasonable estimate of the geometry and energy of first excited/ground states MECI, and the results can be applied to understand the NR decay process via DICIs in defective SiNCs. The other merit of using small cluster models is that by reducing the dimensionality of the SiNC the important reaction coordinates related to the NR decay process are easier to extract. When the full dimensionality is applied, the analysis of structural dynamics can be projected to the reaction coordinates extracted from the cluster models to understand the process. The caveat is that the estimated rate might be affected by the overestimation of the excitation energy and the reduced rate of energy dissipation due to the reduced dimensionality of the small cluster model.

4.2 Method

The cluster model (Si_8H_{13}) for dynamic study is shown in Figure 4.1a. All silicon atoms are passivated to full valency with hydrogen atoms except one silicon with only trivalent coordination (surrounded by three silicon atoms) to represent the dangling bond defect. Thus, the defect can be deemed as a P_b center, which commonly appears on the interfaces of bulk silicon and SiNCs. In this study, we investigate the DB defect in different charged states, which are the neutral, the positively charged (the cationic), and the negatively charged (the anionic) states. The geometry of the clusters at their ground state (Frank-Condon point) are optimized via B3LYP³³⁻³⁴ with the 6-31G(d,p) basis set for the neutral and cationic states and the 6-31+G(d,p) basis set for

the anionic state. We applied the ab initio multiple spawning (AIMS) method,³⁵⁻³⁶ which allows us to calculate full time-dependent wave functions of molecules after excitation, to study the photophysics of the Si clusters with DB defects. The electronic wave functions are described at state averaged complete active space self-consistent field (SA-CASSCF)³⁷⁻³⁹ level with LANL2DZdp basis sets.⁴⁰ It is worth mentioning that the LANL2DZdp basis contains diffuse gaussian functions for properly describing negatively charged states. For example, the most diffuse gaussian exponent on the p shell of the Si atom is 0.0237 for LANL2DZdp basis, where it is 0.0331 for the 6-31+G(d) basis set. For the neutral state, we averaged three states to optimize the orbitals and used an active space with five electrons and three orbitals in the SA-CASSCF calculations (abbreviated as SA3-CASSCF(5,3)). For the charged states, the SA3-CASSCF(4,3) and SA2-CASSCF(6,4) have been used for the cationic and anionic states, respectively. These active spaces are chosen because of their agreement to the excitation energies and excitation characters predicted by high level methods, such as (ionization potential) equation-of-motion coupled cluster with single and double excitations (EOM-CCSD⁴¹⁻⁴³ for charged states and IP-EOM-CCSD(2h,1p)⁴⁴⁻⁴⁷ for the neutral state), multi-state complete active space second order perturbation theory (MS-CASPT2)⁴⁸⁻⁵⁰ and multireference configuration interaction method (MRCI) with the Davidson correction⁵¹⁻⁵³ using the same state average and active space as above (the energies can be found below and in APPENDIX). Twenty simulations are conducted in the AIMS calculations with each simulation initiated with one nuclear basis function. The initial positions and momenta for each nuclear wavepacket are sampled from the ground state vibrational Wigner distribution. The time-derivative coupling is evaluated via the norm-preserving interpolation method developed by Meek et al.⁵⁴⁻⁵⁵ In this paper, we adopted adiabatic state labels, in which D_0 (S_0) denotes the doublet (singlet) ground state, D_1 (S_1) is the doublet (singlet) first excited state, etc. The important points on the potential energy surfaces (PES), which include the energy minimum on the first excited state (denote as D_{1min} and S_{1min}) and the minimal energy point on the CI seam (MECI), are optimized at the SA-CASSCF and MS-CASPT2 levels of theory. The SA-CASSCF, MS-CASPT2, MRCI and EOM-CCSD electronic structure calculations are performed in the Molpro software package,⁵⁶ and the AIMS dynamic simulations are performed using FMS-Molpro.³⁶ The IP-EOM-CCSD calculations are performed in the GAMESS program.^{44-47, 57-58} On the other hand, the MECI geometry optimization is

performed using the CIOpt software package, which uses the sequential penalty method to optimize the minimum on the seam of conical intersections.⁵⁹

4.3 Results and Discussion

4.3.1 Dynamical Simulations of the Neutral Si-DB

At the ground state, the three Si-Si bond lengths, $R_{\text{Si-Si}}$, and Si-Si-Si bond angles, θ , surrounding the DB site (as illustrated in Figure 4.1a) are practically identical for all three charge states. For the DB neutral state, the bond lengths $R_{\text{Si-Si}}$ are 2.36 Å and bond angles θ are 109°. We run AIMS in conjunction with the SA3-CASSCF(5,3) electronic structure method to study the photodynamics after excitation in the neutral DB system. The dynamics after excitation are essentially the same as our previous work on real nanometer-sized models of DB-SiNCs.²⁵ To shortly summarize, the averaged (over twenty trajectories) D₁-D₀ energy gap approaches zero at 40-60 fs with many (if not all) trajectories exploring regions of near-zero energy gap (Figure 4.2), suggesting an accessible D₁/D₀ CI in the system. The ultrafast population transfer from the D₁ to the D₀ state (Figure 4.3) further suggests the existence of CIs. More than 60% of the initially prepared D₁ state population is transferred to the ground state within the first hundred fs. For the structural dynamics, all three averaged bond lengths, $R_{\text{Si-Si}}$, and bond angles, θ , increase within 50 fs (Figure 4.4), where one bond length is significantly elongated more than the other two, resulting in an asymmetric bond stretching motion surrounding the DB. The structural dynamics after excitation can be attributed to the Jahn-Teller effect. As the orbital arrangements show in Figure 4.1b, the first excited state at the FC point is a doubly degenerate state corresponding to the excitation of one electron from one of the two $\sigma_{\text{Si-Si}}$ bonding orbitals surrounding the DB site to the DB nonbonding orbital (n_{DB}). As a result, the structure undergoes Jahn-Teller distortion on the first excited state at the FC point, in which the asymmetric bond stretching of $R_{\text{Si-Si}}$ breaks the degeneracy and stabilizes the structure.

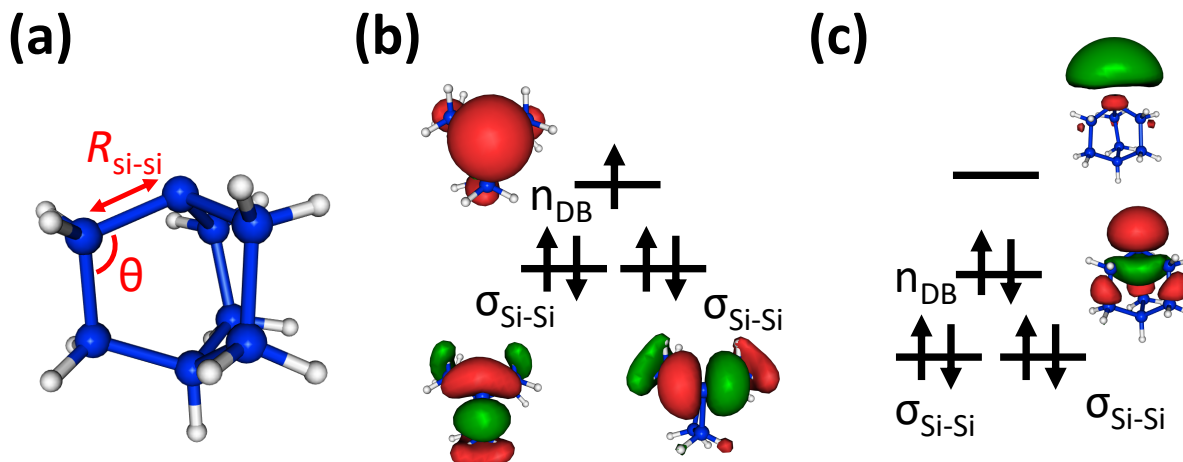


Figure 4.1. (a) The Si_8H_{13} cluster model studied in this work. One of the three Si-Si bond lengths ($R_{\text{Si-Si}}$) and Si-Si-Si bond angles (θ) surrounding the DB site are indicated in red. (b) The top view of the one nonbonding and two $\sigma_{\text{Si-Si}}$ bonding orbitals at the FC point in the neutral state system. (c) The side view of the diffuse LUMO and nonbonding HOMO at the FC point in the negatively charged DB system.

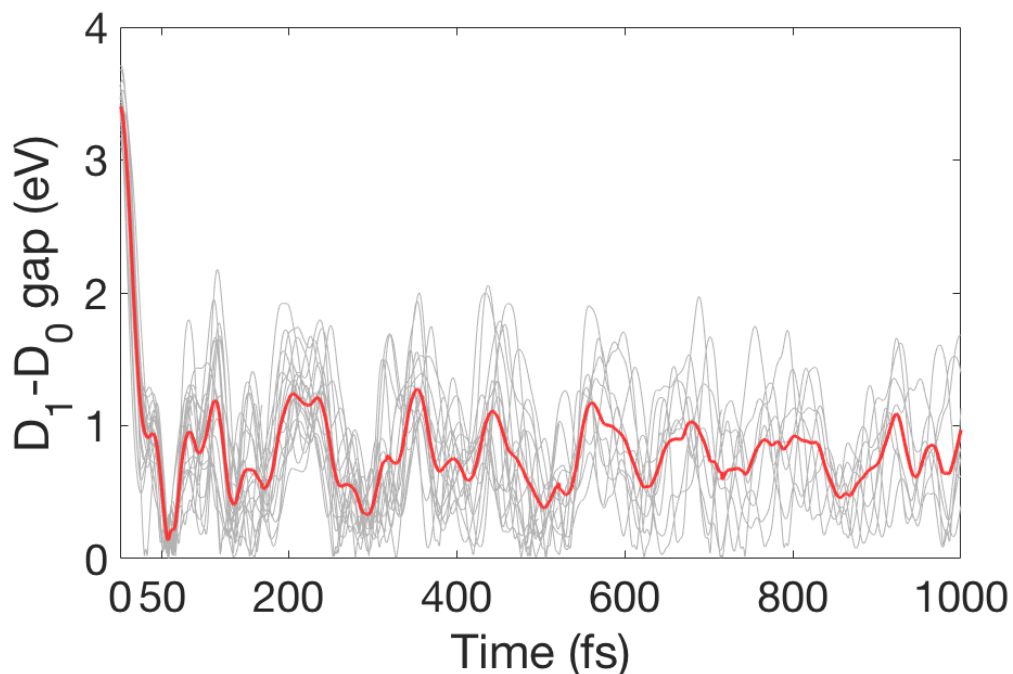


Figure 4.2. The time evolutions of the D_1 - D_0 energy gap (grey lines: 20 individual trajectories; red line: average) for the neutral DB system.

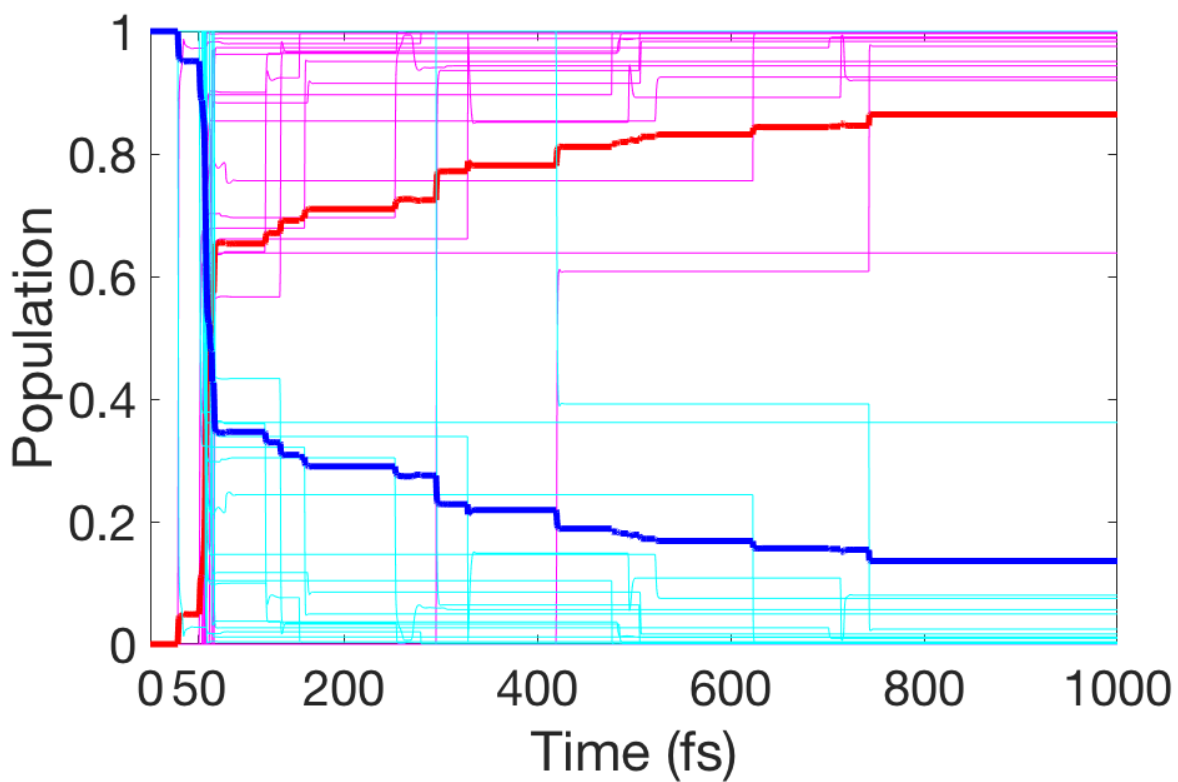


Figure 4.3. The time evolution of the population of the first excited and ground states of the neutral DB system. Cyan lines: excited state populations of 20 trajectories; magenta lines: ground state populations of 20 trajectories; thick blue line: averaged excited state population; thick red line: averaged ground state population.

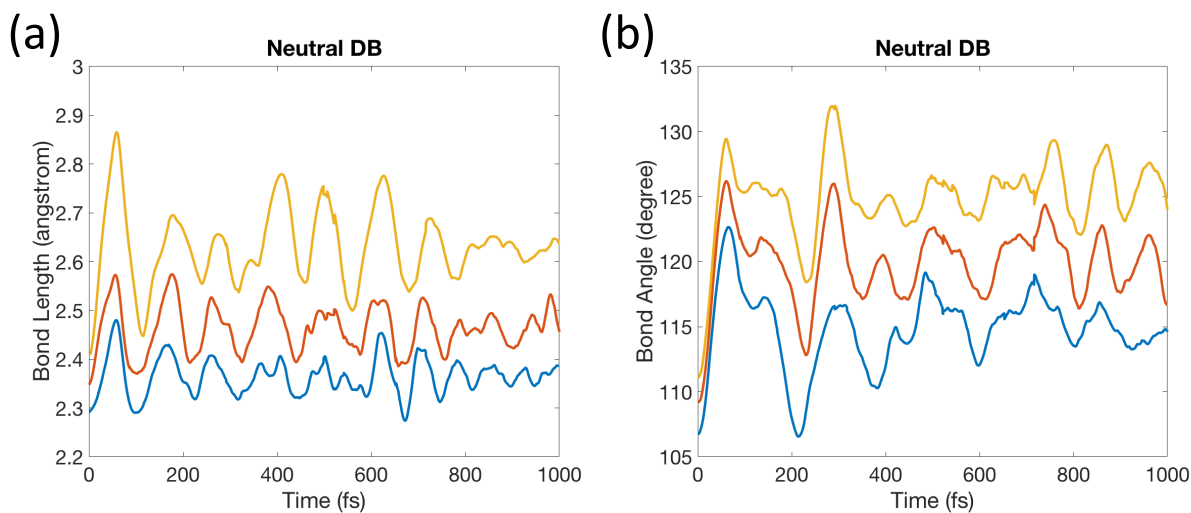


Figure 4.4. The time evolutions of (a) the averaged Si-Si bond lengths surrounding the DB ($R_{\text{Si-Si}}$) and (b) the averaged Si-Si-Si bond angles surrounding the DB (θ) for the neutral DB system. The bond lengths (bond angles) are sorted as the longest (largest), the middle and the shortest (smallest) $R_{\text{Si-Si}}$ distances (θ degree) for each trajectory at each time step, then averaged, and are shown by yellow, orange and blue lines, respectively.

4.3.2 Static Analysis of the Potential Energy Surface on the Neutral Si-DB

To calibrate and qualify the accuracy of SA-CASSCF as well to gain chemical insight through analysis of the PES, we applied higher order methods and geometry optimizations for important points on the PES. At the FC point, we compared the vertical excitation energies to those computed at the IP-EOM-CCSD level of theory (see Table C1) at the minimum energy geometry of the ground state, optimized by B3LYP/6-31G(d,p). IP-EOM-CCSD predicts a doubly-degenerated first excited state with a 3.08 eV excitation energy at the FC point, and the SA3-CASSCF(5,3) excitation energy for the doubly-degenerated D_1 state is 3.63 eV (Table 4.1). The discrepancy between the SA-CASSCF and IP-EOM-CCSD is most likely due to the lack of dynamical correlation in the SA-CASSCF method. After inclusions of dynamical correlation, MS-CASPT2 and MRCI methods with the same active space gave excitation energies of 3.12 and 3.29 eV, respectively, as shown in Table 4.1 and APPENDIX, which are in good agreement with the IP-EOM-CCSD result.

Table 4.1. Optimized neutral DB cluster model FC point, D₁/D₀ MECI, and D₁min energies (eV).

	SA3-CASSCF(5,3)		MS-CASPT2	
	D ₀ Energy	D ₁ Energy	D ₀ Energy	D ₁ Energy
FC	0	3.63	0	3.12
D ₁ /D ₀ MECI	2.35	2.35	1.73	1.74
D ₁ min	1.87	2.33	---	---

The AIMS trajectories exploring near-zero gap region and the population transfer from the D₁ to D₀ state suggest that there is a CI in the neutral DB system. To characterize the decay pathways, we applied geometry optimization using SA-CASSCF and MS-CASPT2 methods to search for the D₁/D₀ MECI as well as the D₁min. Single point energy calculations are performed at these optimized geometries with the MRCI method and are presented in the APPENDIX. With the initial guess geometries drawn from the near-zero gap region, we found the D₁/D₀ MECI at both level of theories. The geometry of the MECI (Figure 4.5) shows the asymmetrically stretched Si-Si bonds surrounding the DB site ($R_{\text{Si-Si}} = 2.38 \text{ \AA}, 2.52 \text{ \AA}, 2.53 \text{ \AA}; \theta = 122^\circ, 128^\circ, 117^\circ$ optimized at SA-CASSCF level of theory; $R_{\text{Si-Si}} = 2.37 \text{ \AA}, 2.45 \text{ \AA}, 2.46 \text{ \AA}; \theta = 123^\circ, 129^\circ, 119^\circ$ optimized at MS-CASPT2 level of theory). The MECI energy is estimated to be 2.35 eV and 1.74 eV above the D₀ state minimum at the SA-CASSCF and MS-CASPT2 levels, respectively (Table 4.1). The nature of the electronic transition between the D₁ and D₀ states via MECI can be examined by computing state-averaged natural orbitals (NOs) at the D₁/D₀ MECI geometry. As shown in the Figure 4.5, the NOs with occupation number 1.5 have the characters of the n_{DB} and one of the $\sigma_{\text{Si-Si}}$ orbitals, thus these two orbitals become near-degenerated, introducing the MECI. For the D₁min, we found a minimum energy structure at the SA-CASSCF level of theory, which is very close to the D₁/D₀ MECI with geometric differences less than 0.02 Å for $R_{\text{Si-Si}}$ ($R_{\text{Si-Si}} = 2.38 \text{ \AA}, 2.50 \text{ \AA}, 2.51 \text{ \AA}$) and 3° for θ ($\theta = 121^\circ, 125^\circ, 117^\circ$), and a 0.02 eV difference for the D₁ state energy (Table 4.1). We cannot find a distinct D₁min geometry near the D₁/D₀ MECI at the MS-CASPT2 level. The results suggest that the Jahn-Teller distortion at the FC point bring the system toward the D₁/D₀ CI directly, which facilitates the ultrafast NR recombination for the neutral DB system. The accuracy of the dynamical simulations with the SA-CASSCF PES can be qualified by comparing the difference between the D₁ state energies at FC and MECI points to the results from higher level of theories. SA-CASSCF predicts an 1.28

eV energy difference, where MS-CASPT2 and MRCI (with an MS-CASPT2-optimized geometry) gave 1.38 eV and 1.33 eV, respectively. Hence, agreement is very good and the dynamical simulations are trustworthy. Also, it is worth mentioning that the results for the neutral DB system support the use of a small cluster model. The structural dynamics after excitation, the time scale for reaching the near-zero gap region, and the electronic and geometric structures in the study of this small cluster model agree well with the previous DB-SiNCs results.²⁵

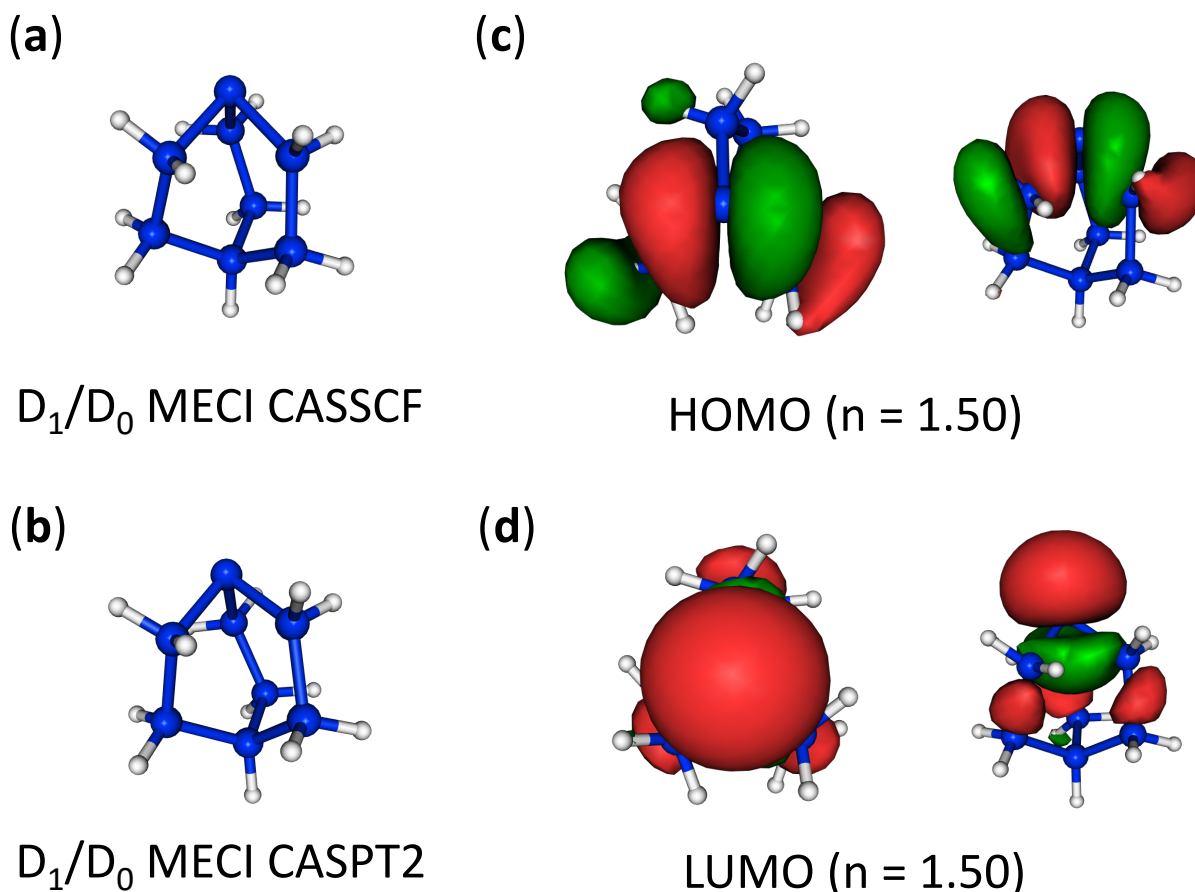


Figure 4.5. (a) The D_1/D_0 MECI geometry of the neutral DB cluster optimized by SA-CASSCF. (b) The D_1/D_0 MECI geometry of the neutral DB cluster optimized by MS-CASPT2. (c) and (d). Top view and side view of D_0 - D_1 state-averaged natural orbitals with occupation numbers 1.50 for the neutral DB at the MECI geometry.

4.3.3 Dynamical Simulations of the Cationic Si-DB

After removing one electron from the neutral DB, the positively charged DB cluster has smaller bond lengths ($R_{\text{Si-Si}} = 2.34 \text{ \AA}$) and a more planar geometry ($\theta = 99^\circ$) surrounding the DB site at the minimum energy geometry on its ground state. We applied AIMS in conjunction with the SA3-CASSCF(4,3) electronic structure method to study the photophysical dynamics in the DB^+ system after excitation. Similar to the DB^0 system, the first excited state at the FC point is a doubly degenerated excited state characterized by an electronic excitation from one of the $\sigma_{\text{Si-Si}}$ orbitals to the n_{DB} orbital (see Figure C2). Thus, the dynamics after excitation are also driven by the Jahn-Teller effect at FC geometry, where the asymmetric Si-Si bond stretching modes surrounding the DB defect break the degeneracy on the first excited state. As shown in Figure 4.6, the averaged bond lengths, $R_{\text{Si-Si}}$, as well as bond angles, θ , increase to their maximum at $\sim 50 \text{ fs}$, where one of the Si-Si bonds grows significantly longer than the other two. The time evolution of the energy gap is shown in the Figure 4.7, in which a few trajectories (gray lines) occasionally explore near-zero gap region suggesting an accessible CI in the positive DB system. Although the structural dynamics after excitations are similar to the DB^0 system and the trajectories explore near-zero gap region in both cases, the nonadiabatic transition rate to the ground state is much slower in the DB^+ system as estimated by AIMS simulations (Figure 4.8). Only 3% of the averaged population is transferred to the ground state after 1 ps based on the simulations. Nonetheless, the time-scales are not directly relevant to realistic nanocrystals, but the location and energy of the MECI play more important roles in our interpretation of our simulations.

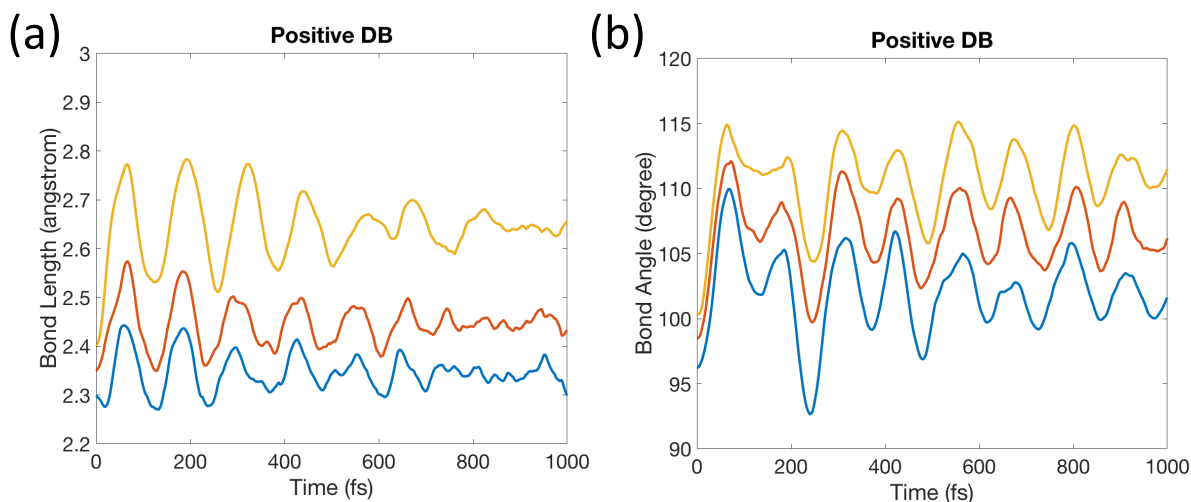


Figure 4.6. The time evolutions of (a) the averaged Si-Si bond lengths surrounding the DB (R_{Si-Si}) and (b) the averaged Si-Si-Si bond angles surrounding DB (θ) for the positive DB system. The bond lengths (bond angles) are sorted as the longest (largest), the middle and the shortest (smallest) R_{Si-Si} distances (θ degree) for each trajectory at each time step, then averaged, and are shown by yellow, orange and blue lines respectively.

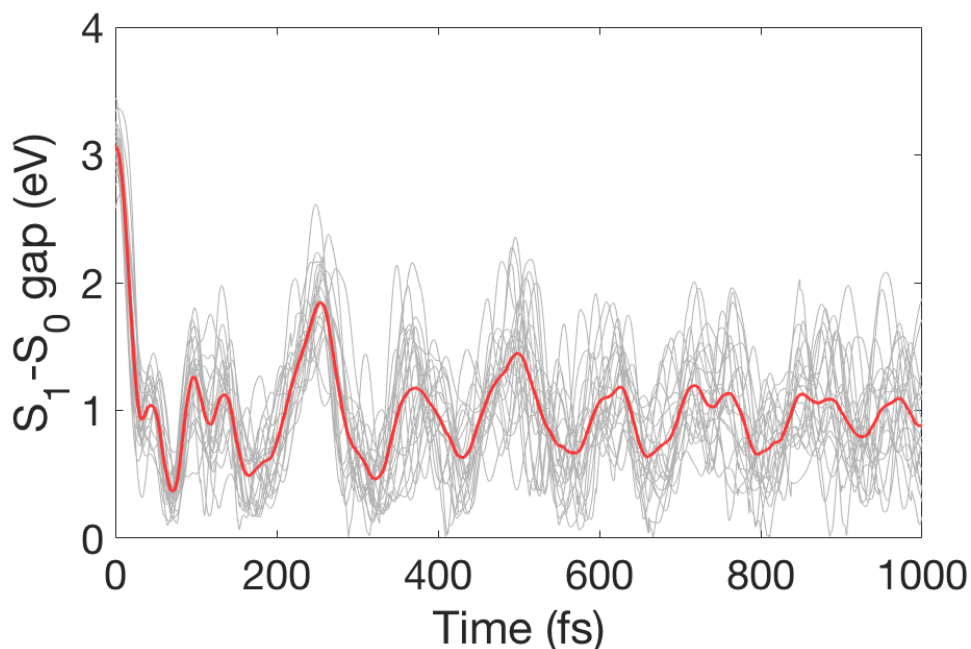


Figure 4.7. The time evolutions of the S_1-S_0 energy gap (grey lines: 20 trajectories; red line: average) for the positive DB system.

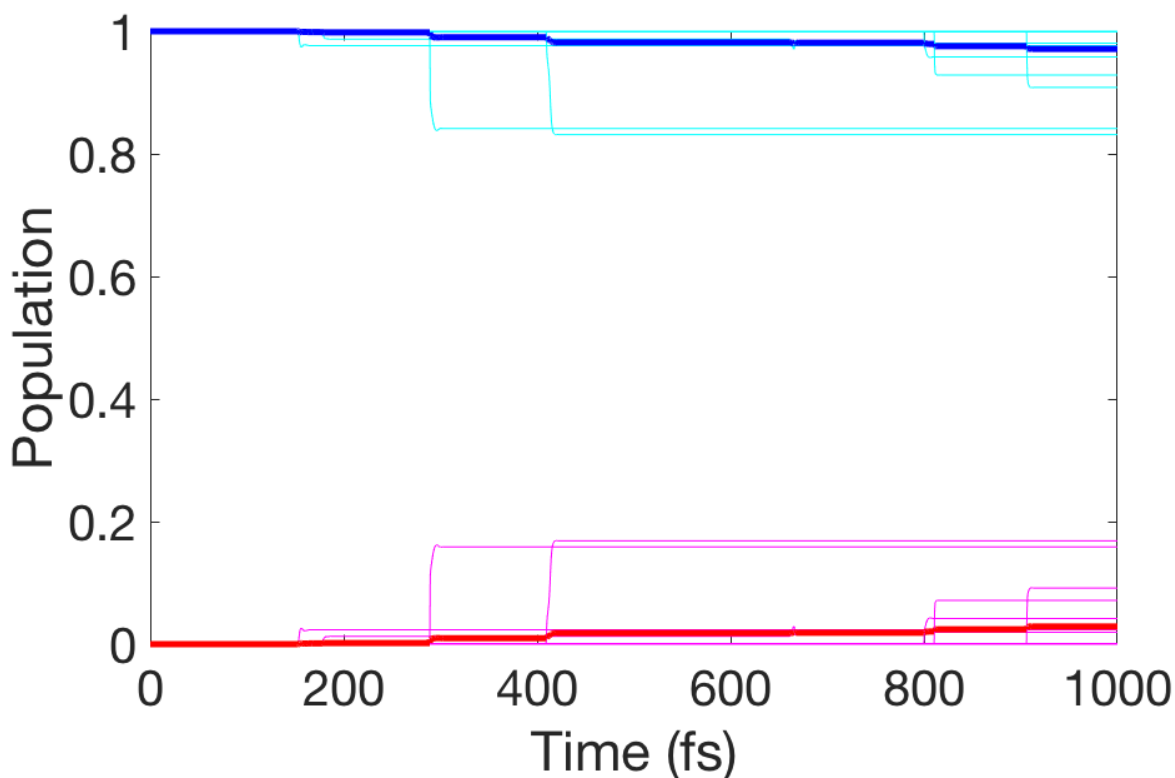


Figure 4.8. The time evolutions of the population of the first excited and ground states for the positive DB system. Cyan lines: excited state populations of 20 trajectories; magenta lines: ground state populations of 20 trajectories; thick blue line: averaged excited state population; thick red line: averaged ground state population.

4.3.4 Static Analysis of the Potential Energy Surface on the Cationic Si-DB

The PES of SA-CASSCF method for the positive DB system is calibrated with higher order methods. In addition, chemical insight can be obtained through static analysis of the important points on the PES. Thus, we applied EOM-CCSD, MS-CASPT2 and MRCI levels of theories for these purposes. At the FC point, EOM-CCSD method is performed at the minimum energy geometry (see Table C1) of the ground state (B3LYP/6-31G(d,p) optimized). The first excited state is a doubly-degenerated state with excitation energy 2.89 eV calculated by EOM-CCSD. SA3-CASSCF(4,3) predicts the excitation energy to be 3.32 eV (Table 4.2). After inclusion of dynamical correlation, MS-CASPT2 and MRCI with the same active space predict

excitation energies of 2.61 and 3.00 eV, respectively, as shown in Table 4.2 and APPENDIX. These are in good agreement with the EOM-CCSD result.

Table 4.2. Optimized positive DB cluster model FC point, S_1/S_0 MECI, and $S_{1\text{min}}$ energies (eV).

	SA3-CASSCF(4,3)		MS-CASPT2	
	S_0 Energy	S_1 Energy	S_0 Energy	S_1 Energy
FC	0	3.32	0	2.61
S_1/S_0 MECI	2.43	2.45	2.08	2.10
$S_{1\text{min}}$	1.40	2.26	1.16	1.83

The AIMS trajectories for the DB^+ cluster occasionally explore regions of near-zero gap suggesting the existence of a S_1/S_0 CI in the system. Geometry optimizations at the SA-CASSCF and MS-CASPT2 levels are applied to search for the S_1/S_0 MECI as well as the $S_{1\text{min}}$. MRCI single point calculations are performed at these geometries and are presented in the APPENDIX. Using a geometry from the region of near-zero gap from the AIMS simulations as an initial guess, we discovered a low-lying S_1/S_0 MECI for the DB^+ cluster at both the SA-CASSCF and MS-CASPT2 levels of theories. As shown in Figure 4.9, the MECI geometry shows asymmetrical stretching of the Si-Si bonds surrounding the DB defect, with three $R_{\text{Si-Si}}$ as 2.37 Å, 2.39 Å, 2.75 Å for the SA-CASSCF method and 2.34 Å, 2.35 Å, 2.51 Å for the MS-CASPT2 method. The three θ are 111°, 113°, 110° and 112°, 119°, 111°, respectively. The MECI energies are estimated to be 2.45 eV and 2.10 eV at the SA-CASSCF and MS-CASPT2 levels, respectively (Table 4.2). The S_0 - S_1 state-averaged NOs show the nature of the electronic transition facilitated by the MECI, in which the transition is between the n_{DB} orbital (occupation number 0.53) and one of the $\sigma_{\text{Si-Si}}$ orbitals surrounding the DB (occupation number 1.48), as shown in Figure 4.9. For the $S_{1\text{min}}$, we found the minimum energy geometries at both level of theories, in which the three $R_{\text{Si-Si}}$ are estimated 2.37 Å, 2.38 Å, 2.67 Å at SA-CASSCF and 2.33 Å, 2.41 Å, 2.42 Å at MS-CASPT2, and the energies are 2.26 and 1.83 eV respectively (Table 4.2). As can be seen from the results of both methods, the S_1/S_0 MECI geometry exhibits significant stretching of one Si-Si bond surrounding the DB from $S_{1\text{min}}$ geometry. The S_0 - S_1 energy gap at the $S_{1\text{min}}$ is large, estimated to be 0.86 eV at the SA-CASSCF level and 0.67 eV at the MS-CASPT2 level. As a result, the Jahn-Teller distortion at the FC point in the DB^+ cluster drives the system toward the $S_{1\text{min}}$, which has a large energy gap between the first excited and

ground states. The S_0 - S_1 energy gap remains large near the S_1 min region, with no driving force toward the MECI, resulting in a much slower NR decay rate compared to the DB^0 system. In addition, the energy difference between the S_1 min and S_1/S_0 MECI (0.19 eV for SA-CASSCF and 0.27 eV for MS-CASPT2) can be deemed as an energy barrier for the system to reach the near-zero energy gap region. Nevertheless, the estimated NR decay rate is still orders of magnitudes faster than the typically time scale for radiative decay process in SiNCs ($\sim\mu$ s), and we expect that SiNCs with energy gaps larger than the MECI energy do not efficiently emit light when positively charged DBs are present. The energy difference between the S_1 energies at the FC and MECI points is 0.87 eV for SA-CASSCF, and it is 0.51 eV and 0.62 eV for MS-CASPT2 and MRCI (at the MS-CASPT2 optimized geometry), respectively. The agreement between methods are reasonable, thus the dynamical simulations can be deemed as reliable.

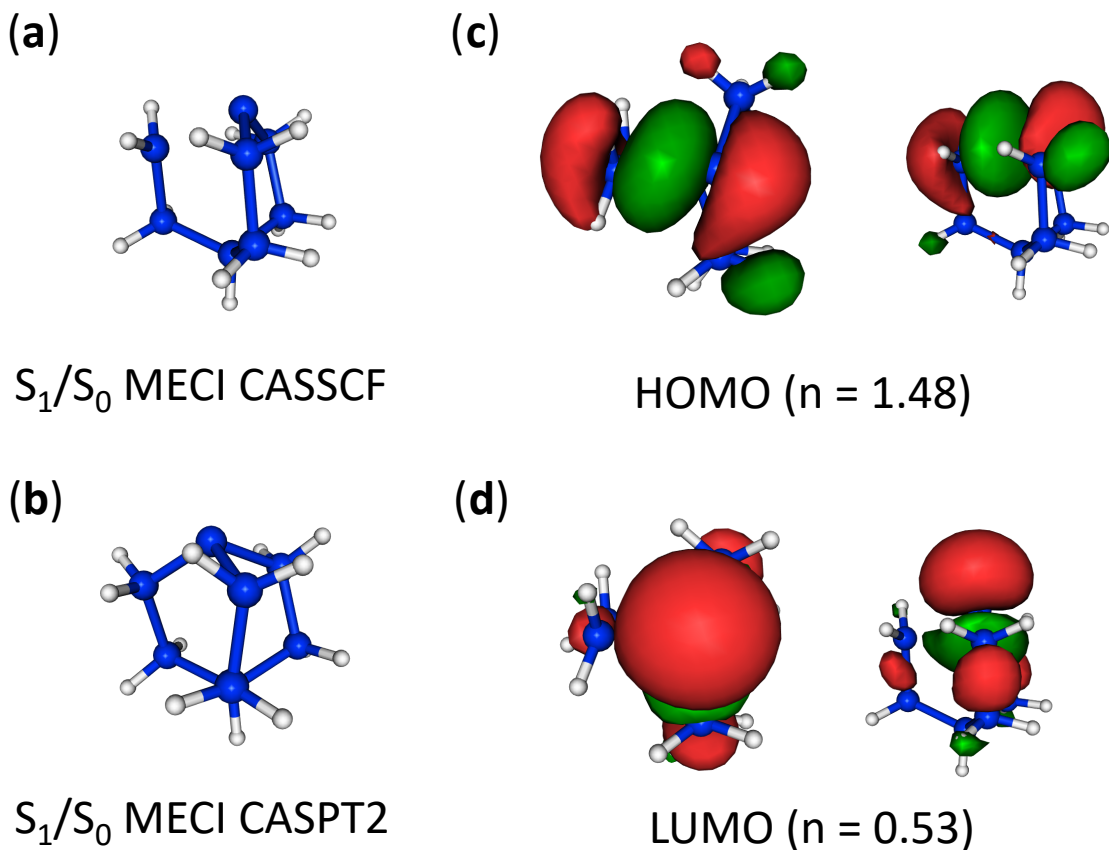


Figure 4.9. (a) The S_1/S_0 MECI geometry of the positive DB cluster optimized by SA-CASSCF. (b) The S_1/S_0 MECI geometry of the positive DB cluster optimized by MS-CASPT2. (c) and (d) Top view and side view of the S_0 - S_1 state-averaged natural orbitals, with fractional occupation numbers 1.48 and 0.53, for the positive DB at the MECI geometry.

4.3.5 Dynamical Simulations of the Anionic Si-DB

Opposite to the DB^+ , the minimum energy structure of the ground state of the negatively charged DB system has the longest bond lengths ($R_{Si-Si} = 2.39 \text{ \AA}$) and the largest bond angles ($\theta = 121^\circ$) surrounding the DB site, due to charge congestion. The excitation character of the DB^- cluster at the FC point is one electron excited from the n_{DB} orbital to a diffuse orbital (Figure 4.1c). Because the excitation character is different from that in the DB^0 and DB^+ systems, the DB^- system has distinct dynamics after excitation. In the first 30 fs, both the averaged bond lengths, R_{Si-Si} , and the averaged bond angles, θ , decrease with time, as shown in the Figure 4.10.

After this decreasing stage, the averaged bond lengths, $R_{\text{Si-Si}}$, shows a prominent stretching in one Si-Si bond with the other two bonds remaining relatively unchanged. The averaged energy gap between the first excited and ground states never approach zero (always > 0.7 eV as the red line in Figure 4.11), but many trajectories (gray lines in Figure 4.11) explore regions of near-zero gap. The AIMS simulations predict population transfer between first excited and ground states (Figure 4.12), which suggests an accessible S_1/S_0 CI in the DB^- system as well.

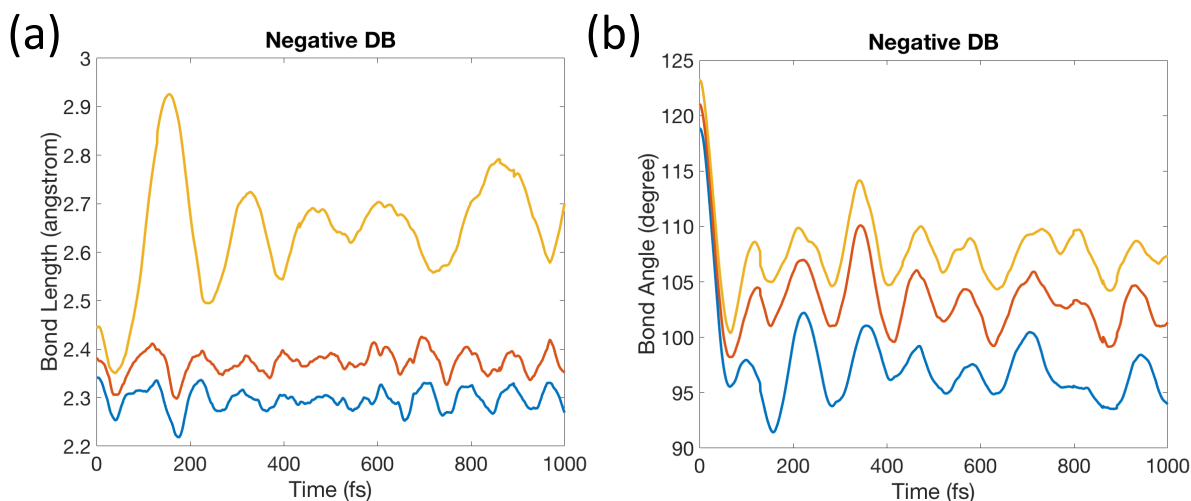


Figure 4.10. The time evolutions of (a) the averaged Si-Si bond lengths surrounding the DB ($R_{\text{Si-Si}}$) and (b) the averaged Si-Si-Si bond angles surrounding the DB (θ) for the negative DB system. The bond lengths (bond angles) are sorted as the longest (largest), the middle, and the shortest (smallest) $R_{\text{Si-Si}}$ distances (θ degree) for each trajectory at each time step, then averaged, and are shown by yellow, orange and blue lines respectively.

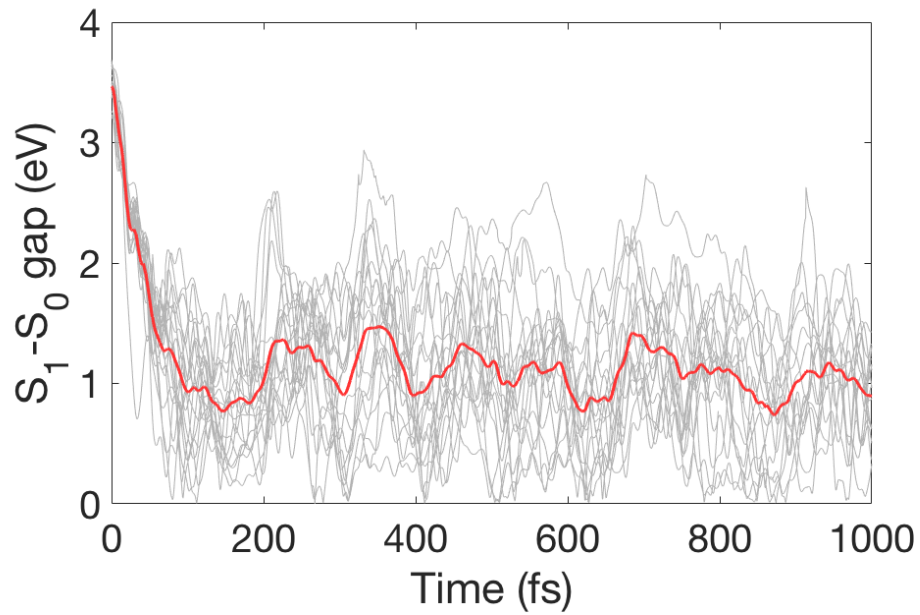


Figure 4.11. The time evolutions of the S_1 - S_0 energy gap (grey lines: 20 trajectories; red line: average) for the negative DB system.

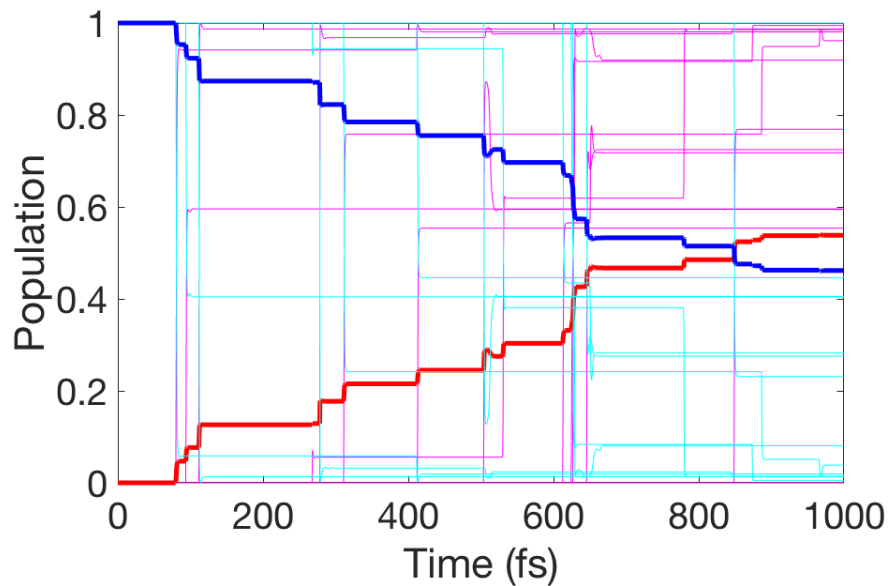


Figure 4.12. The time evolutions of the population of the first excited and ground states for the negative DB system. Cyan lines: excited state populations of 20 trajectories; magenta lines: ground state populations of 20 trajectories; thick blue line: averaged excited state population; thick red line: averaged ground state population.

4.3.6 Static Analysis of the Potential Energy Surface on the Anionic Si-DB

To calibrate the SA-CASSCF method and gain chemical insight through static analysis of PES, we applied higher order methods such as EOM-CCSD, MS-CASPT2 and MRCI level of theories to the negative DB system. The SA-CASSCF method for the DB⁻ system is calibrated by the EOM-CCSD level of theory (Table C1) on the ground state minimum energy geometry (B3LYP/6-31+G(d,p) optimized). EOM-CCSD predicted a 3.54 eV excitation energy for the first excited state, and SA2-CASSCF(6,4), MS-CASPT2 and MRCI methods gave 3.51 eV, 3.79 eV and 3.79 eV, respectively (Table 4.3 and APPENDIX). These are in good agreement with EOM-CCSD result. Thus, we applied SA2-CASSCF(6,4) as the electronic structure method for the AIMS dynamical simulations.

Table 4.3. Optimized negative DB cluster model FC point, S₁/S₀ MECI, and S₁min energies (eV).

	SA2-CASSCF(6,4)		MS-CASPT2	
	S ₀ Energy	S ₁ Energy	S ₀ Energy	S ₁ Energy
FC	0	3.51	0	3.79
S ₁ min-1	0.54	2.64	0.57	2.91
S ₁ /S ₀ MECI	2.70	2.72	2.63	2.65
S ₁ min	1.84	2.65	1.57	2.38

Many of the AIMS trajectories explore regions of near-zero gap and exhibit population transfer between the first excited and ground states suggesting the existence of a low-lying S₁/S₀ CI in the DB⁻ system. We applied geometry optimization to search for the S₁/S₀ MECI in this system with both the SA-CASSCF and MS-CASPT2 electronic structure methods. The single point energy calculations on the optimized geometries are carried out at the MRCI level of theory and presented in APPENDIX. The low-lying MECI has been found at both levels of theory, where the estimated energies are 2.72 eV and 2.65 eV for SA-CASSCF and MS-CASPT2 levels of theory, respectively (Table 4.3). The important geometry parameters, $R_{\text{Si-Si}}$, are 2.32 Å, 2.32 Å, 2.77 Å for SA-CASSCF and 2.31 Å, 2.33 Å, 2.56 Å for MS-CASPT2, and the three θ are estimated 103°, 98°, 91° and 105°, 98°, 94°, respectively (see the MECI geometry also in Figure 4.13). Thus, the geometry at the S₁/S₀ MECI of the negative DB system is a local distortion of one of the Si-Si bonds surrounding the DB. The electronic structure at the MECI

geometry can be examined by calculating the state-averaged NOs. The NR recombination can be characterized as a transition between a $\sigma_{\text{Si-Si}}^*$ orbital and the n_{DB} orbital, as shown in Figure 4.13. The $\sigma_{\text{Si-Si}}^*$ orbital is an antibonding orbital for one of the Si-Si bonds surrounding the DB site. Thus, the significant elongation of one Si-Si bond is caused by the repulsive potential from the antibonding electronic character in this bond.

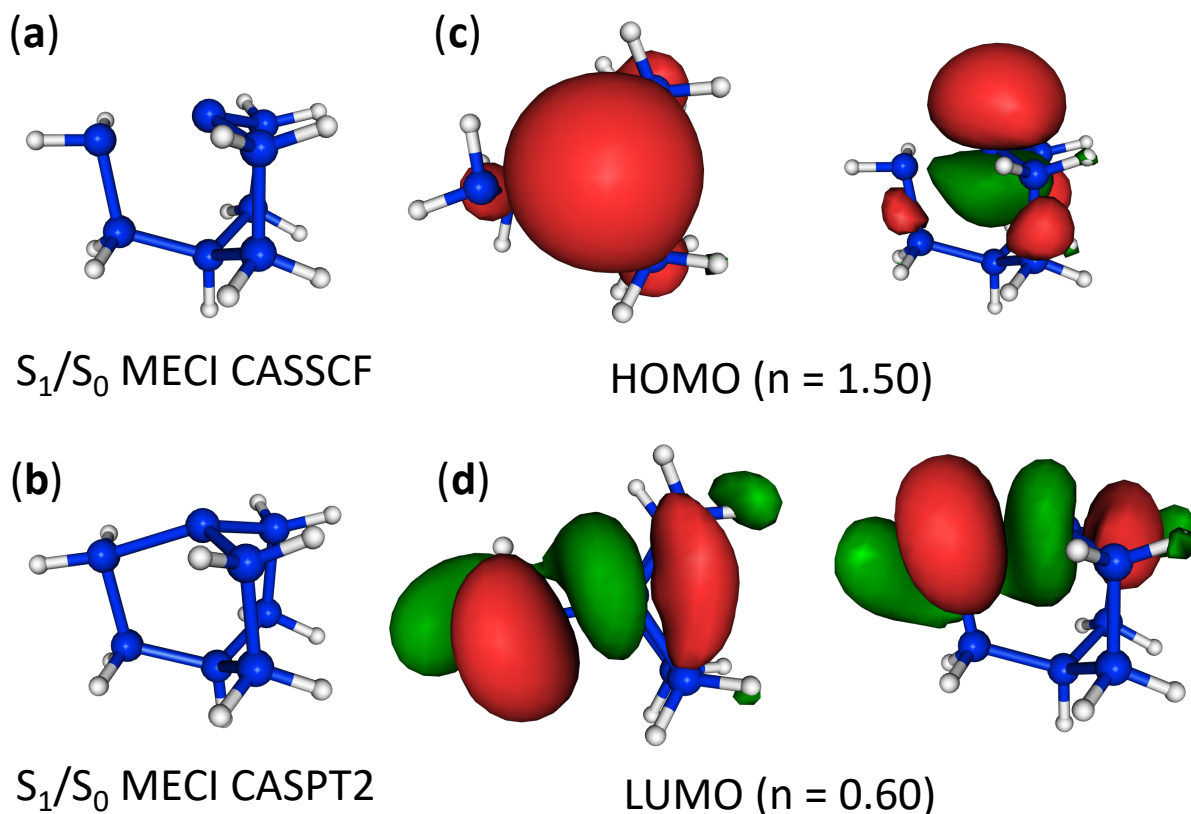


Figure 4.13. (a) The S_1/S_0 MECI geometry of the negative DB cluster optimized by SA-CASSCF. (b) The S_1/S_0 MECI geometry of the negative DB cluster optimized by MS-CASPT2. (c) and (d) Top view and side view of the S_0 - S_1 state-averaged natural orbitals with fractional occupation numbers 1.50 and 0.60 for the negative DB cluster at the MECI geometry.

For the excited state PES in the DB^- system, we searched for the minimum energy geometries at two regions: region where the bond lengths, $R_{\text{Si-Si}}$ and bond angles, θ , are relaxed and the region nearby the S_1/S_0 MECI structure. Thus, the initial structures for the two regions are taken from the AIMS trajectories at ~ 30 fs and the optimized MECI geometry. Distinct

minimum energy geometries are found in both regions at both the SA-CASSCF and MS-CASPT2 levels. In the relaxed region (denoted as $S_{1\text{min-1}}$), both bond lengths, $R_{\text{Si-Si}}$, and bond angles, θ , are smaller than in the structure at the FC point. The $R_{\text{Si-Si}}$ are estimated to be 2.34 Å, 2.34 Å, 2.35 Å by SA-CASSCF and 2.31 Å, 2.31 Å, 2.36 Å by MS-CASPT2, and the three θ are estimated 107°, 108°, 106° and 105°, 107°, 101°, respectively. Thus, the exploration from the FC point to the nearby $S_{1\text{min-1}}$ region is responsible for the first ~30 fs of dynamics after excitation in the AIMS simulations, where the geometry is relaxed from the charge-congested DB structure. The energy at $S_{1\text{min-1}}$ is estimated to be 2.64 eV at the SA-CASSCF level and 2.91 eV at the MS-CASPT2 level (Table 4.3). On the other hand, the minimum energy geometry near the MECI region (denoted as $S_{1\text{min}}$) contains similar electronic character to the S_1/S_0 MECI (see Figure C3). The geometry surrounding the DB is 2.32 Å, 2.33 Å, 2.63 Å for $R_{\text{Si-Si}}$ and 106°, 103°, 97° for θ at the SA-CASSCF level, and is 2.31 Å, 2.39 Å, 2.41 Å for $R_{\text{Si-Si}}$ and 106°, 99°, 102° for θ at the MS-CASPT2 level. Thus, in the MECI geometry one Si-Si bond surrounding DB site is stretched further relative to the $S_{1\text{min}}$ region. The antibonding character of $\sigma_{\text{Si-Si}}^*$ provides the driving force for the system to reach the $S_{1\text{min}}$ region, which is near the S_1/S_0 CI. To qualify the SA-CASSCF PES used in the AIMS simulations, the difference in S_1 energy between the FC and MECI points is considered. It is 0.79 eV at the SA-CASSCF level, and 1.14 eV and 0.93 eV for MS-CASPT2 and MRCI (at the MS-CASPT2 optimized geometry), respectively. Thus, the agreement between methods are reasonable and the dynamical simulations can be deemed as reliable.

The fact that the dynamics explore two regions in negative DB system can also be seen upon examining the individual trajectories. Unlike the DB^0 and DB^+ systems, where the individual trajectories follow the averaged time evolution of the energy gap (red line in Figure 4.2 and Figure 4.7) reasonably well, the individual trajectories diverge from averaged value after the first few tens of fs (relaxation process) and span the range 0-2 eV throughout the simulations in the DB^- system. In addition, although the averaged structural dynamics show a prominent one Si-Si bond ($R_{\text{Si-Si}}$) stretching mode after the relaxation process (Figure 4.10), this one bond stretching mode occurs at different times for individual trajectories. For instance, Figure 4.14a presents a trajectory where a single $R_{\text{Si-Si}}$ stretches at 200 fs, which is similar to the averaged

dynamics. However, in Figure 4.14b the other trajectory has three $R_{\text{Si-Si}}$ oscillating roughly in between 2.2-2.5 Å from 0-800 fs, followed by the stretching of a single $R_{\text{Si-Si}}$ at 900 fs.

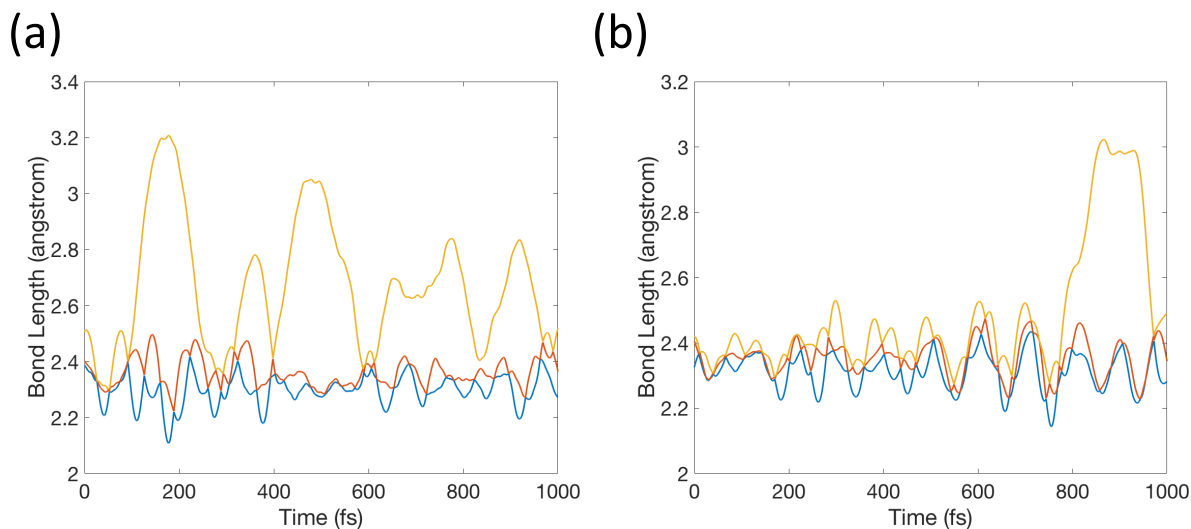


Figure 4.14. The plot of three Si-Si bond lengths surrounding DB site changes with time for (a) the simulation where the one Si-Si bond stretch occurred at 200 fs, (b) the simulation where the one Si-Si bond stretch occurred at 900 fs.

4.3.7 Discussion

According to the results, DBs with different charged states all undergo NR decay via DICIs. We found low-lying MECIs between the first excited and ground states for all three systems, with MS-CASPT2 energies 1.74 eV, 2.10 eV and 2.65 eV above the minimum energy of the ground state for the neutral, positively and negatively charged states respectively. The estimated MECI energies are within the visible light range, thus the DB DICIs are capable of quenching visible photoluminescence. Along with our dynamical simulations and static analysis of the PESs, we investigated the NR decay mechanisms between the first and ground states for all three charged states. Although the microscopic mechanisms are related, with the asymmetric bond stretching mode(s) surrounding DB site appear to be important for the NR decay processes, the detailed mechanisms and dynamics are distinct. For the DB^0 and DB^+ systems, the asymmetrical stretching modes can be either elongations of one or two Si-Si bonds surrounding the DB. Although similar structural dynamics are observed after excitation, the recombination rates of these cluster models are estimated $\text{DB}^0 \gg \text{DB}^+$ based on the dynamical simulations as well as

the static analysis of the PES. For the DB^- system, it is stretching of a single Si-Si bond mode launched by the repulsive potential of an occupied $\sigma_{\text{Si-Si}}^*$ orbital surrounding the DB site that brings the system toward the DICl.

It is interesting to compare our results to the related study by Brawand et al.,⁷ where the authors proposed that the changing charge state of the DB might be responsible for the fluorescence intermittency in SiNCs. The authors considered four elementary pathways. First, the $\text{DB}^0 \rightarrow \text{DB}^+$ pathway corresponds to the electron transitioning from a singly occupied n_{DB} nonbonding orbital to the valence band (σ bonding orbital in our study), which we denoted as $(\sigma)^1(n_{\text{DB}})^1 \rightarrow (\sigma)^2(n_{\text{DB}})^0$. Second, the $\text{DB}^0 \rightarrow \text{DB}^-$ pathway corresponds to the electron transition from the conduction band (σ^* antibonding orbital in our study) to the singly occupied n_{DB} , which can be denoted as $(n_{\text{DB}})^1(\sigma^*)^1 \rightarrow (n_{\text{DB}})^2(\sigma^*)^0$. Third, the $\text{DB}^- \rightarrow \text{DB}^0$ pathway corresponds to the electron transition from doubly occupied n_{DB} nonbonding orbital to the σ bonding orbital, which we denoted as $(\sigma)^1(n_{\text{DB}})^2 \rightarrow (\sigma)^2(n_{\text{DB}})^1$. And finally, the $\text{DB}^+ \rightarrow \text{DB}^0$ pathway considers the electron transition from σ^* antibonding orbital to an unoccupied n_{DB} , thus we denoted as $(n_{\text{DB}})^0(\sigma^*)^1 \rightarrow (n_{\text{DB}})^1(\sigma^*)^0$. They applied Fermi's golden rule to evaluate both the nonradiative and radiative recombination rates for these four processes. Our simulations of neutral, positive and negative DB systems correspond to $(\sigma)^1(n_{\text{DB}})^2 \rightarrow (\sigma)^2(n_{\text{DB}})^1$, $(\sigma)^1(n_{\text{DB}})^1 \rightarrow (\sigma)^2(n_{\text{DB}})^0$ and $(n_{\text{DB}})^1(\sigma^*)^1 \rightarrow (n_{\text{DB}})^2(\sigma^*)^0$ pathways respectively, in which we found low-lying DICIs for all three systems. Brawand, et al. predicted these pathways to be NR processes as well. Thus, the two studies are in agreement with each other regarding the identification of the NR decay pathways in DB-SiNCs. We do not consider the radiative pathway $(n_{\text{DB}})^0(\sigma^*)^1 \rightarrow (n_{\text{DB}})^1(\sigma^*)^0$ they suggested because it is not the lowest energy mechanisms in our cluster model. For the neutral DB cluster at the FC point, the low-lying excitations predicted by the IP-EOM-CCSD level of theory compose of excitations from valence electron to the n_{DB} orbital. Thus, the excitations of one electron to virtual orbitals of the neutral DB cluster are higher in energy. The merit of our method is that we use dynamical simulations to explore the PES of different charged DB directly, where Brawand et al. assumed the same symmetric stretching mode (pyramidalization) surrounding the DB for NR decay processes in all pathways. We found that for the NR decay processes the excitation energies of differently charged DB systems are dumped to similar

vibrational mode (asymmetric stretching mode), but occur via different mechanisms. These local distortion mode(s) can work as the signature for the NR decay processes via DB DICIs. If a time-resolved spectra for monitoring the asymmetrically vibrational mode surrounding DB is available, the NR decay via differently charged DB sites may be identifiable. In turn, it may provide a chance to validate the proposed blinking mechanism as well. One can imagine that the four pathways investigated by Brawand et al. can be distinguished from the structural dynamics of the processes $((\sigma)^1(n_{\text{DB}})^2 \rightarrow (\sigma)^2(n_{\text{DB}})^1)$, $(\sigma)^1(n_{\text{DB}})^1 \rightarrow (\sigma)^2(n_{\text{DB}})^0$ and $(n_{\text{DB}})^1(\sigma^*)^1 \rightarrow (n_{\text{DB}})^2(\sigma^*)^0$ and the radiative signal $((n_{\text{DB}})^0(\sigma^*)^1 \rightarrow (n_{\text{DB}})^1(\sigma^*)^0)$.

4.4 Conclusions

In this study, we investigated the nonadiabatic dynamics occurring upon excitation of differently charged silicon DB defects using the ab initio multiple spawning method in conjunction with a SA-CASSCF description of the electronic structure. In addition, energy calculations at the Franck-Condon geometries, the excited state minimum energy geometries and the minimal energy conical intersection geometries are performed with higher order levels of theory such as EOM-CCSD, MS-CASPT2 and MRCI methods. We found low-lying conical intersections which can facilitate nonradiative decay in all three systems. The nonradiative decay processes involve signature asymmetrical Si-Si bond stretching mode(s) surrounding the DB site in all three cases. However, the microscopic mechanisms are distinct. For the neutral DB, the excited state force drives the system toward the low-lying conical intersection directly, thus result to ultrafast NR decay. The cationic DB has similar structural dynamics after excitation as in the neutral state DB. However, the excited state force does not drive the system to the conical intersection directly but to the $S_{1\text{min}}$ region with larger S_0/S_1 energy gap. As a result, the NR decay is much slower in the positive DB system than the neutral DB system. For the anionic DB, the dynamics explore two regions after excitation. First, a relaxation process brings the system to approach an excited state minimum $S_{1\text{min}-1}$. Then, the other region of the $S_{1\text{min}}$ can be accessed, with the S_0/S_1 MECI located nearby. The signature asymmetric Si-Si bond stretching mode(s) and different microscopic mechanisms provide opportunities to examine the NR decay processes via DB DICIs, if the experimental means are available.

APPENDIX

SUPPORTING INFORMATION FOR: NONADIABATIC DYNAMICS STUDY OF SILICON DANGLING BOND DEFECT AT DIFFERENT CHARGED STATES

Table C1. The excitation energies at Franck-Condon point (FC). The FC geometries are optimized with the B3LYP/6-31G(d,p) method. The IP-EOM-CCSD(2h,1p)/6-31G(d,p), EOM-CCSD/6-31G(d,p) and EOM-CCSD/6-31+G(d,p) energies are calculated for the neutral, cationic and anionic DB systems respectively.

State	Neutral	Cationic	Anionic
	IP-EOM-CCSD(2h,1p)	EOM-CCSD	EOM-CCSD
E _{S1} (FC)	3.08	2.89	3.54
E _{S2} (FC)	3.08	2.89	3.78
E _{S3} (FC)	3.96	3.40	3.78
E _{S4} (FC)	3.96	3.40	3.94

Table C2. The optimized cluster model FC, MECI and D₁min energies for the neutral DB system.

geometry	optimization method	SA-CASSCF D ₀ energy	SA-CASSCF D ₁ energy	MS-CASPT2 D ₀ energy	MS-CASPT2 D ₁ energy	MRCI D ₀ energy	MRCI D ₁ energy
FC	B3LYP	0	3.63	0	3.12	0	3.29
D ₀ /D ₁ MECI	SA-CASSCF	2.35	2.35	1.78	1.81	1.96	1.98
	MS-CASPT2	2.39	2.41	1.73	1.74	1.93	1.96
D ₁ min	SA-CASSCF	1.87	2.33	1.40	1.83	1.55	1.99

Table C3. The optimized cluster model FC, MECI and S₁min energies for the positive DB system.

geometry	optimization method	CASSCF S ₀ energy	CASSCF S ₁ energy	MS-CASPT2 S ₀ energy	MS-CASPT2 S ₁ energy	MRCI S ₀ energy	MRCI S ₁ energy
FC	B3LYP	0	3.32	0	2.61	0	3.00
S ₀ /S ₁ MECI	SA-CASSCF	2.43	2.45	1.87	2.20	2.18	2.36
	MS-CASPT2	2.62	2.78	2.08	2.10	2.36	2.38
S ₁ min	SA-CASSCF	1.40	2.26	1.23	1.98	1.26	2.22
	MS-CASPT2	1.54	2.41	1.16	1.83	1.25	2.19

Table C4. The optimized cluster model FC, MECI and S₁min energies for the negative DB system.

geometry	optimization method	CASSCF S ₀ energy	CASSCF S ₁ energy	MS-CASPT2 S ₀ energy	MS-CASPT2 S ₁ energy	MRCI S ₀ energy	MRCI S ₁ energy
FC	B3LYP	0	3.51	0	3.79	0	3.79
S ₀ /S ₁ MECI	SA-CASSCF	2.70	2.72	2.54	3.05	2.87	2.90
	MS-CASPT2	2.69	2.86	2.63	2.65	2.71	2.86
S ₁ min	SA-CASSCF	1.84	2.65	1.98	2.66	2.00	2.77
	MS-CASPT2	1.57	2.78	1.57	2.38	1.58	2.65
S ₁ min-1	SA-CASSCF	0.54	2.64	0.50	2.99	0.53	3.02
	MS-CASPT2	0.75	2.74	0.57	2.91	0.66	3.01

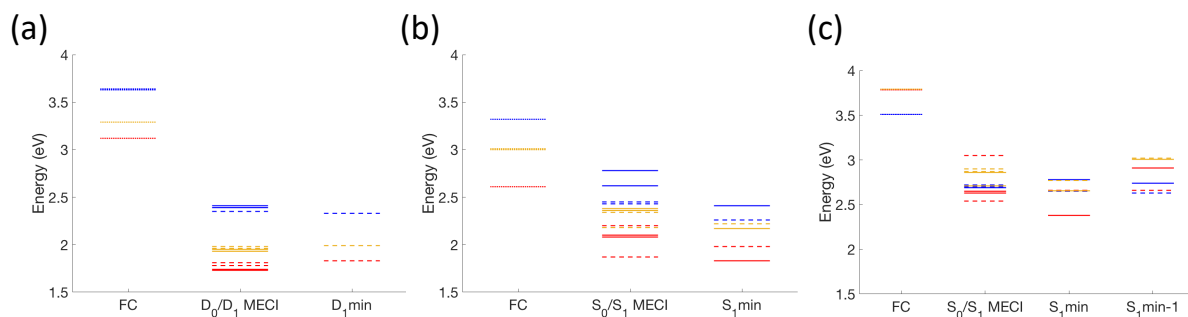


Figure C1. Optimized cluster model FC, MECI and S1min energies. The geometry optimizations were performed at B3LYP (dotted lines at FC point), SA-CASSCF (dash lines at MECI, S1min and D1min) and MS-CASPT2 (solid lines at MECI, S1min and D1min) levels of theory. Energy calculations were performed at SA-CASSCF (blue lines), MS-CASPT2 (red lines) and MRCI (yellow lines) levels of theory. (a) The neutral DB system. (b) The positive DB system. (c) The negative DB system.

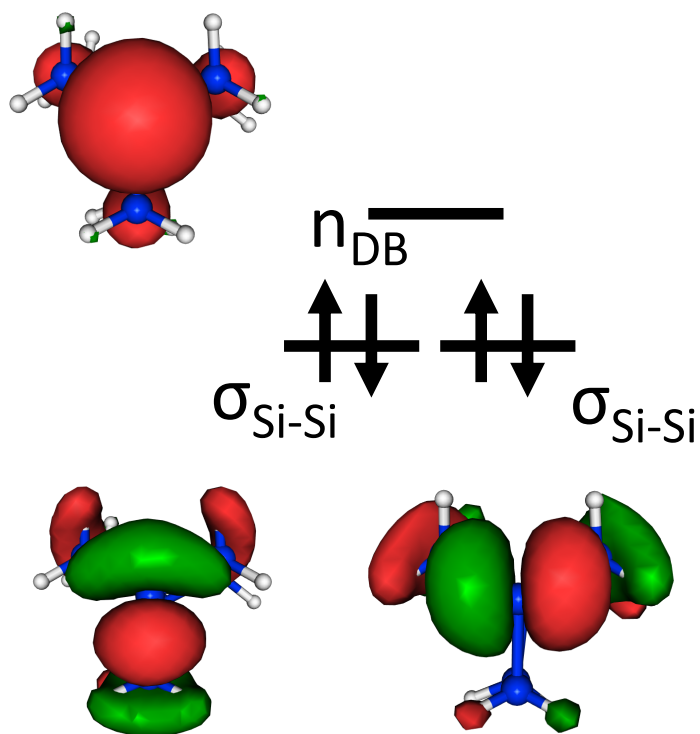
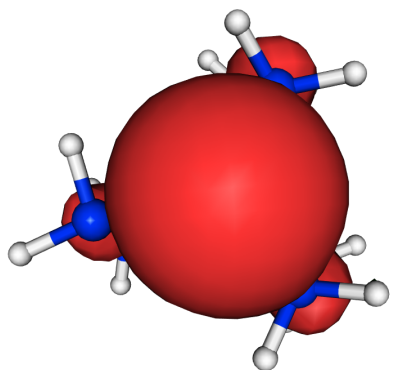
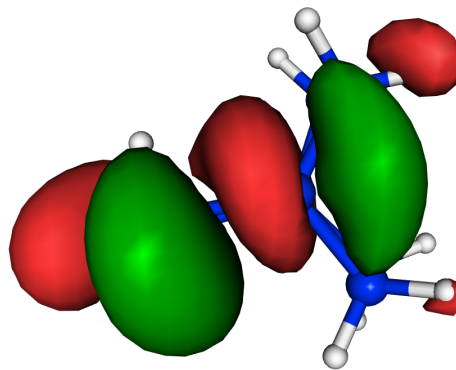


Figure C2. The orbitals of positively charged DB system at the ground state minimum energy geometry.



HOMO ($n = 1.50$)



LUMO ($n = 0.56$)

Figure C3. The state-averaged natural orbitals with fractional occupation numbers for a negative DB at the S_1 min geometry.

Geometries of The Neutral DB System (in Angstrom)

Ground State Minimum Energy Geometry

Si	-0.0579090190	0.7238324132	0.1042865142
Si	0.3657420222	-0.8333928145	-1.6145610716
Si	2.6985762443	-1.3099096917	-1.6746996734
Si	3.7153711667	-0.5297483840	0.3137181686
Si	3.6315299358	1.8341432481	0.3258389525
Si	1.4094732879	2.5527180190	-0.1410316088
Si	0.3331325220	-0.3007616982	2.1919290247
Si	2.4778581283	-1.3358763777	2.1614726856
H	5.1314729465	-0.9998314378	0.3915796047
H	1.3378027850	3.0624622057	-1.5409615497
H	1.0349641645	3.6706953612	0.7708006873
H	4.5826563416	2.4027536847	-0.6728957720
H	4.0343098133	2.3377239517	1.6717453983
H	3.3079552061	-0.6173102136	-2.8477691588
H	2.9256051279	-2.7743777580	-1.8451517078
H	-0.0796091432	-0.3084103746	-2.9365345764
H	-0.3899971294	-2.0908103723	-1.3456338329
H	3.2014073091	-1.0703849883	3.4387352567
H	0.2982215441	0.7336236063	3.2657474441
H	-0.7159858705	-1.3131632297	2.5007487475
H	2.3051386170	-2.8128031495	2.0366824672

Minimum Energy Conical Intersection Geometry: CASSCF

Si	-0.5369052956	0.6502415455	-0.1137860198
Si	0.4590676533	-1.0255215720	-1.4823532049
Si	2.7859718583	-1.2174490250	-1.7482536524
Si	3.8110726273	-0.6542633577	0.2817785920
Si	3.6747317923	1.6683911455	0.4786009756
Si	1.4215225806	2.2197591462	0.0850534681
Si	0.6261955238	0.1381125419	2.0747493690
Si	2.4207790981	-1.3761064322	2.0165675671
H	5.1964466062	-1.1558776039	0.4110567331
H	1.2666090529	2.5648258830	-1.3497436667
H	0.9501378971	3.3398031955	0.9164149807
H	4.4899945098	2.3852419454	-0.5246774166
H	4.0686911914	2.1189380324	1.8303703906
H	3.2757994047	-0.2884427222	-2.7925585018
H	3.1527066130	-2.5946001502	-2.1455220075
H	-0.1486328997	-0.9308697896	-2.8305102272
H	0.0181273471	-2.3216679853	-0.9050379698
H	3.0992192601	-1.3307851473	3.3302077654
H	1.0162170223	1.3457988569	2.8299347822

H	-0.5697873436	-0.4352380661	2.7301638770
H	1.8986307275	-2.7395219757	1.7916145788

Minimum Energy Conical Intersection Geometry: CASPT2

Si	-0.5081918375	0.6672491083	-0.0984449772
Si	0.4847916399	-1.0027820640	-1.4547331259
Si	2.7882479577	-1.2014513494	-1.7337089611
Si	3.7943264514	-0.6471272260	0.2828840516
Si	3.6551514451	1.6557010895	0.4861964297
Si	1.4130108979	2.1748832711	0.1016775182
Si	0.6332993341	0.1432755088	2.0151306468
Si	2.4084398266	-1.3696713755	1.9923772480
H	5.1854180650	-1.1483794634	0.4111019122
H	1.2682508494	2.5094348531	-1.3517254472
H	0.9453524082	3.3194639199	0.9208268066
H	4.4727209013	2.3704171882	-0.5273664981
H	4.0561591864	2.1057124187	1.8430585012
H	3.2719213377	-0.2702509209	-2.7870399192
H	3.1535628183	-2.5873633648	-2.1287883816
H	-0.1497954911	-0.9220269927	-2.8009611465
H	0.0347236759	-2.3007040691	-0.8662436901
H	3.0965913366	-1.3189092679	3.3099703421
H	1.0425907715	1.3441974475	2.7920649800
H	-0.5626288165	-0.4186188236	2.7110024145
H	1.8926524361	-2.7422814270	1.7667922895

Excited State Minimum Geometry (D₁min): CASSCF

Si	-0.4778264450	0.6607938151	-0.1050761809
Si	0.4540660846	-1.0278833102	-1.4917040415
Si	2.7815234224	-1.2312312852	-1.7472312054
Si	3.7998183232	-0.6468741346	0.2806128438
Si	3.6717071614	1.6782541859	0.4698697246
Si	1.4301480369	2.2656215181	0.0624495104
Si	0.6037389549	0.0987162480	2.0899315876
Si	2.4237092852	-1.3831489673	2.0217752393
H	5.1877964847	-1.1426154160	0.4077915710
H	1.2908637403	2.6599841815	-1.3607406950
H	0.9569670838	3.3586419437	0.9285043996
H	4.5070452457	2.3819861875	-0.5262147301
H	4.0620181094	2.1243940206	1.8244034904
H	3.2749381741	-0.3156403461	-2.8014605312
H	3.1471892021	-2.6140039317	-2.1260058301
H	-0.1545814922	-0.9183670679	-2.8374715632
H	-0.0042935553	-2.3167625745	-0.9130677850

H	3.1103328570	-1.3318105710	3.3308844853
H	0.9717541566	1.3148825928	2.8418708976
H	-0.5829344943	-0.4998285672	2.7401316983
H	1.9226148916	-2.7543400568	1.7948175275

Geometries of The Positive DB System (in Angstrom)

Ground State Minimum Energy Geometry

Si	0.2912724992	0.6092868581	0.1227163020
Si	0.3723970070	-0.8207057892	-1.7307374400
Si	2.7092926620	-1.4021395927	-1.6375485506
Si	3.7368292360	-0.5347982428	0.3164006413
Si	3.6815030572	1.8352372844	0.2348353554
Si	1.4328881324	2.6467195394	-0.0660803788
Si	0.2915558143	-0.4097158743	2.2320051507
Si	2.5391556052	-1.2777146046	2.2237552877
H	5.1469103166	-1.0024419380	0.3919814623
H	1.2034442963	3.2165354095	-1.4152676150
H	1.0072408483	3.5653943914	1.0162433169
H	4.4714634268	2.3610431729	-0.9077911283
H	4.1525770040	2.4167629909	1.5183441700
H	3.3190843458	-0.8101471002	-2.8562707673
H	2.7738929080	-2.8854070012	-1.6782484017
H	0.0212029655	-0.0731324232	-2.9614981176
H	-0.5199416722	-1.9814551194	-1.4982639828
H	3.1728719505	-0.8122310339	3.4836650017
H	0.0753909061	0.6181999945	3.2783874205
H	-0.7323389511	-1.4810910309	2.2721418946
H	2.4010236422	-2.7570278907	2.2152763789

Minimum Energy Conical Intersection Geometry: CASSCF

Si	-0.1153874180	0.8005373208	-0.2822600633
Si	0.4996714569	-1.1356114803	-1.5050225459
Si	2.8352908845	-1.3308836549	-1.6664646127
Si	3.7846655368	-0.5646574152	0.3388539822
Si	3.6711654536	1.7807656044	0.3202003739
Si	1.4311430657	2.5077204370	0.3536858835
Si	0.4811343269	-0.2941915689	2.1711063155
Si	2.4700071937	-1.5200852081	2.0369069577
H	5.1761612108	-1.0249236742	0.5186803905
H	1.1506237671	3.4639658331	-0.7404761737
H	0.9831367218	3.0642992848	1.6371043652
H	4.2355491729	2.2669325294	-0.9528281003
H	4.3876603824	2.3782895406	1.4579998391

H	3.2697038989	-0.4705588564	-2.7830584349
H	3.1733846883	-2.7409005171	-1.9221719511
H	-0.1565926905	-1.0120004370	-2.8188676458
H	-0.1053688357	-2.2413291972	-0.7371552652
H	3.0240260247	-1.4564238971	3.3986103675
H	0.4427096769	0.8861851376	3.0346445856
H	-0.8600307937	-0.8905247532	1.9978636678
H	2.0681687724	-2.8922552555	1.6869845811

Minimum Energy Conical Intersection Geometry: CASPT2

Si	-0.1192242854	0.7364505877	-0.0811724165
Si	0.4032810387	-1.0578970230	-1.4879158019
Si	2.7084686557	-1.3330712252	-1.7390193333
Si	3.7422512478	-0.6432139294	0.2313855973
Si	3.7670616545	1.6691455692	0.4650839694
Si	1.5778996290	2.3637886258	0.0317513004
Si	0.5609836394	-0.0262854832	2.2076964414
Si	2.5153149546	-1.3076414614	2.1036212770
H	5.1037031003	-1.2141658462	0.3662786456
H	1.3934553491	2.7414669651	-1.4088778949
H	1.0871291571	3.4358968699	0.9227306675
H	4.6871023782	2.3737976283	-0.4536194346
H	4.0501939097	2.0147397847	1.8796550198
H	3.1988096313	-0.4994144211	-2.8611251836
H	2.9820426933	-2.7670386272	-1.9869845725
H	-0.3522223701	-0.9081025827	-2.7502572773
H	-0.1567305919	-2.1776160481	-0.6907728979
H	3.2305277194	-1.0044233646	3.3672386735
H	0.3885099101	1.0571774858	3.1906315545
H	-0.7476323310	-0.6951986692	1.8839049231
H	2.0440058357	-2.7092686409	2.0582267568

Excited State Minimum Geometry (S₁min): CASSCF

Si	-0.1430278800	0.2773864267	0.1754255847
Si	0.5830825619	-0.7082461165	-1.8595022388
Si	2.8212425513	-1.4210230618	-1.6234058600
Si	3.7553899757	-0.5334049719	0.3395411730
Si	3.5967500109	1.8085956517	0.2996212355
Si	1.3630288466	2.4672597160	-0.0551048629
Si	0.5438897516	-0.2305817452	2.3889155589
Si	2.6056346016	-1.3538262520	2.2169023868
H	5.1878751152	-0.8799275606	0.4187962709
H	0.9422375749	2.8301825819	-1.4146074247
H	0.6562182711	3.2392945063	0.9752630010
H	4.3390822843	2.4104871529	-0.8215645601

H	3.9755516251	2.4217259015	1.5840956297
H	3.5706992419	-0.9657074971	-2.8079232860
H	2.8176332641	-2.8921743554	-1.5399153987
H	0.4127565899	0.3368555359	-2.8812412456
H	-0.3674093247	-1.8136557070	-2.0743645117
H	3.3673341625	-1.1263984508	3.4571556163
H	0.6741171850	1.0741951583	3.0608328986
H	-0.5449317915	-1.0216694201	2.9843662665
H	2.3234913005	-2.7887182209	2.0283753916

Excited State Minimum Geometry (S₁min): CASPT2

Si	0.0064923337	0.6284062532	0.3976189538
Si	0.5494716864	-0.7155730996	-1.5273516725
Si	2.8469212123	-1.1099260268	-1.6693456725
Si	3.7627264812	-0.4733503573	0.3763141303
Si	3.4800424502	1.8311897475	0.5508800557
Si	1.4623190207	2.3154315382	-0.5332334762
Si	0.6613442453	-0.2220249513	2.4597732352
Si	2.5288780136	-1.5588547423	2.0290537265
H	5.2012784706	-0.8281875580	0.4201998189
H	1.5391845712	2.1356455839	-2.0011938135
H	0.7161067868	3.5486812984	-0.1746164103
H	4.5256505690	2.5877516728	-0.1788824372
H	3.3327595856	2.2852036455	1.9523063240
H	3.3548997765	-0.2933773838	-2.7956818575
H	3.0041120172	-2.5633910914	-1.9098316949
H	-0.1335207801	-0.1009826108	-2.6834481898
H	-0.2495118516	-1.8297555311	-0.9256456357
H	3.3044180427	-1.7422453561	3.2774316584
H	1.0391092839	1.0028215842	3.2105080775
H	-0.4881651648	-0.9140709795	3.0813850614
H	2.0361291678	-2.8527423636	1.4954214436

Geometries of The Negative DB System (in Angstrom)

Ground State Minimum Energy Geometry

Si	-0.4385050473	0.8554082689	0.0845600986
Si	0.3606141735	-0.7184353268	-1.5285870368
Si	2.6754190644	-1.3002997274	-1.6482335406
Si	3.7497268922	-0.5457877982	0.3171928626
Si	3.6090581589	1.8127435360	0.3078763780
Si	1.3392783390	2.4438999879	-0.0949363810
Si	0.3122065537	-0.2724730685	2.0551757030
Si	2.4649284824	-1.3051698825	2.1490410088

H	5.1718560784	-1.0211728910	0.3947950334
H	1.3654732528	3.0385553509	-1.4763097397
H	1.1124797069	3.6306479236	0.8002742814
H	4.5634602879	2.3627372270	-0.7121880312
H	4.1049550163	2.3257433264	1.6281672944
H	3.3497385465	-0.6671076323	-2.8298816806
H	2.9055606940	-2.7752573051	-1.8074875060
H	0.0015076419	-0.3033948799	-2.9285430424
H	-0.3385999029	-2.0389685900	-1.3562465330
H	3.2016424719	-1.0155035816	3.4246621975
H	0.3104198591	0.6718884414	3.2256545643
H	-0.6459990541	-1.3553314676	2.4680684259
H	2.3724947843	-2.8015499109	2.0809916435

Minimum Energy Conical Intersection Geometry: CASSCF

Si	0.1193919937	0.6563068509	0.1438079796
Si	0.3541821729	-0.7638414154	-1.6775449345
Si	2.6038816367	-1.4731685017	-1.5199495280
Si	3.5282937904	-0.3785341491	0.3421204295
Si	3.5519769613	1.9269493618	-0.1539618223
Si	1.4817222092	3.0485176031	-0.1712877589
Si	0.0217678708	-0.6616874446	2.0440970439
Si	2.3447194865	-1.1084309875	2.2503046803
H	4.9435197298	-0.8302626692	0.4973134795
H	1.8897669643	4.4247599183	-0.7276285296
H	1.1454694199	3.3915901171	1.2364504757
H	4.2245937341	2.0083556856	-1.4841170325
H	4.4918883715	2.6057754921	0.7830646551
H	3.3761110016	-1.1133486515	-2.7384926100
H	2.7227592283	-2.9499797699	-1.3934662563
H	0.2390967504	-0.0103778703	-2.9540061427
H	-0.5260182978	-1.9527835868	-1.8386259558
H	2.9003730223	-0.4361356129	3.4566060697
H	-0.3855553431	0.0817478875	3.2666930774
H	-0.7409844363	-1.9416656870	2.1021673585
H	2.6455186318	-2.5591398061	2.4172096329

Minimum Energy Conical Intersection Geometry: CASPT2

Si	0.1373945108	0.7735781544	0.1771909391
Si	0.3776059456	-0.6821695406	-1.6058162596
Si	2.5916771479	-1.4356604029	-1.4887878530
Si	3.5312695211	-0.3679223555	0.3441293232
Si	3.5336706122	1.9191323106	-0.1130536074
Si	1.4334202049	2.9500768253	-0.2112889366
Si	0.0402461470	-0.7223918127	1.9595725726

Si	2.3454961812	-1.0832677284	2.2160060026
H	4.9382843514	-0.8472406843	0.5015937404
H	1.9129353302	4.2893425751	-0.8649566928
H	1.1654233896	3.4233208519	1.1902285108
H	4.1997032499	2.0155230326	-1.4528751155
H	4.5017713947	2.5539245567	0.8361063832
H	3.3547068268	-1.0775184516	-2.7202757548
H	2.6749364982	-2.9208184631	-1.3472532010
H	0.2393256241	0.0368587394	-2.9074043019
H	-0.5166605813	-1.8750962064	-1.6887290727
H	2.8854011396	-0.4065962526	3.4319470471
H	-0.3843697242	0.0160994871	3.1875151043
H	-0.6606795100	-2.0514589321	2.0426065342
H	2.6309167787	-2.5430690614	2.3942982833

Excited State Minimum Geometry (S₁min-1): CASSCF

Si	-0.0158721454	0.6489973166	0.1317444333
Si	0.3948077623	-0.8869043167	-1.5789545724
Si	2.7269463925	-1.2419872146	-1.6656679167
Si	3.6757895587	-0.5096145219	0.3543331703
Si	3.5714829729	1.8361961058	0.3922006421
Si	1.3810373372	2.4928820207	-0.1910027979
Si	0.3880640569	-0.2220483460	2.2737600170
Si	2.4013071660	-1.4303382119	2.1099012277
H	5.0916355368	-0.9509902083	0.4245074160
H	1.3808381210	2.9084452454	-1.6146814004
H	0.9573069893	3.6552871774	0.6200926009
H	4.5508591745	2.4254104046	-0.5543731363
H	3.9035462530	2.3359140232	1.7458119628
H	3.2884861374	-0.4792590983	-2.8082985699
H	3.0323785422	-2.6736560525	-1.8974637773
H	-0.0742011599	-0.3892725436	-2.8937181290
H	-0.2932868145	-2.1669050597	-1.3049118878
H	3.1778166724	-1.4126228313	3.3634889668
H	0.6111024595	0.9483152450	3.1459955982
H	-0.7289751757	-1.0317741301	2.7699627714
H	2.1266461627	-2.8349030035	1.7313193810

Excited State Minimum Geometry (S₁min-1): CASPT2

Si	-0.0158721454	0.6489973166	0.1317444333
Si	0.3948077623	-0.8869043167	-1.5789545724
Si	2.7269463925	-1.2419872146	-1.6656679167
Si	3.6757895587	-0.5096145219	0.3543331703
Si	3.5714829729	1.8361961058	0.3922006421
Si	1.3810373372	2.4928820207	-0.1910027979

Si	0.3880640569	-0.2220483460	2.2737600170
Si	2.4013071660	-1.4303382119	2.1099012277
H	5.0916355368	-0.9509902083	0.4245074160
H	1.3808381210	2.9084452454	-1.6146814004
H	0.9573069893	3.6552871774	0.6200926009
H	4.5508591745	2.4254104046	-0.5543731363
H	3.9035462530	2.3359140232	1.7458119628
H	3.2884861374	-0.4792590983	-2.8082985699
H	3.0323785422	-2.6736560525	-1.8974637773
H	-0.0742011599	-0.3892725436	-2.8937181290
H	-0.2932868145	-2.1669050597	-1.3049118878
H	3.1778166724	-1.4126228313	3.3634889668
H	0.6111024595	0.9483152450	3.1459955982
H	-0.7289751757	-1.0317741301	2.7699627714
H	2.1266461627	-2.8349030035	1.7313193810

Excited State Minimum Geometry (S₁min): CASSCF

Si	0.1218980737	0.8040695986	0.2199092664
Si	0.3436900369	-0.7490432711	-1.4742126684
Si	2.6305766366	-1.2085843430	-1.6540091873
Si	3.5804857938	-0.4973020621	0.3447470942
Si	3.5578016381	1.8332389254	0.2905028597
Si	1.5037056833	2.6152246241	-0.4977152893
Si	0.2009292615	-0.5435404971	2.2142948081
Si	2.3957081616	-1.3501668648	2.1632417999
H	4.9966134873	-0.9773589271	0.4125264960
H	1.8022219753	3.3139975432	-1.8248226460
H	1.1036062759	3.7545256338	0.3860102226
H	4.6908951647	2.2894521157	-0.5798821493
H	3.8844546519	2.3217349598	1.6637651252
H	3.2415427565	-0.4467119876	-2.7828926310
H	2.9102542588	-2.6538869338	-1.9106885812
H	-0.1726809550	-0.3191666887	-2.8075560902
H	-0.3331151226	-2.0401721889	-1.1421555609
H	3.1976478143	-1.0192758898	3.3816469735
H	0.1247244471	0.4549622586	3.3240890110
H	-0.6192594102	-1.7155211295	2.7462259748
H	2.3860153707	-2.8453028756	2.0810211720

Excited State Minimum Geometry (S₁min): CASPT2

Si	0.1218980737	0.8040695986	0.2199092664
Si	0.3436900369	-0.7490432711	-1.4742126684
Si	2.6305766366	-1.2085843430	-1.6540091873
Si	3.5804857938	-0.4973020621	0.3447470942
Si	3.5578016381	1.8332389254	0.2905028597

Si	1.5037056833	2.6152246241	-0.4977152893
Si	0.2009292615	-0.5435404971	2.2142948081
Si	2.3957081616	-1.3501668648	2.1632417999
H	4.9966134873	-0.9773589271	0.4125264960
H	1.8022219753	3.3139975432	-1.8248226460
H	1.1036062759	3.7545256338	0.3860102226
H	4.6908951647	2.2894521157	-0.5798821493
H	3.8844546519	2.3217349598	1.6637651252
H	3.2415427565	-0.4467119876	-2.7828926310
H	2.9102542588	-2.6538869338	-1.9106885812
H	-0.1726809550	-0.3191666887	-2.8075560902
H	-0.3331151226	-2.0401721889	-1.1421555609
H	3.1976478143	-1.0192758898	3.3816469735
H	0.1247244471	0.4549622586	3.3240890110
H	-0.6192594102	-1.7155211295	2.7462259748
H	2.3860153707	-2.8453028756	2.0810211720

REFERENCES

REFERENCES

1. Canham, L. T., Silicon Quantum Wire Array Fabrication by Electrochemical and Chemical Dissolution of Wafers. *Appl Phys Lett* **1990**, *57*, 1046-1048.
2. Takagi, H.; Ogawa, H.; Yamazaki, Y.; Ishizaki, A.; Nakagiri, T., Quantum Size Effects on Photoluminescence in Ultrafine Si Particles. *Appl Phys Lett* **1990**, *56*, 2379-2380.
3. Fernandez, B. G.; Lopez, M.; Garcia, C.; Perez-Rodriguez, A.; Morante, J. R.; Bonafos, C.; Carrada, M.; Claverie, A., Influence of average size and interface passivation on the spectral emission of Si nanocrystals embedded in SiO₂. *J Appl Phys* **2002**, *91*, 798-807.
4. Gelloz, B.; Kojima, A.; Koshida, N., Highly efficient and stable luminescence of nanocrystalline porous silicon treated by high-pressure water vapor annealing. *Appl Phys Lett* **2005**, *87*, 031107.
5. Meyer, B. K.; Petrovakoch, V.; Muschik, T.; Linke, H.; Omling, P.; Lehmann, V., Electron-Spin-Resonance Investigations of Oxidized Porous Silicon. *Appl Phys Lett* **1993**, *63*, 1930-1932.
6. Pi, X. D.; Mangolini, L.; Campbell, S. A.; Kortshagen, U., Room-temperature atmospheric oxidation of Si nanocrystals after HF etching. *Phys Rev B* **2007**, *75* (8), 177.
7. Brawand, N. P.; Voros, M.; Galli, G., Surface dangling bonds are a cause of B-type blinking in Si nanoparticles. *Nanoscale* **2015**, *7*, 3737-3744.
8. Gelloz, B.; Koshida, N., Electroluminescence with high and stable quantum efficiency and low threshold voltage from anodically oxidized thin porous silicon diode. *J Appl Phys* **2000**, *88*, 4319-4324.
9. Lalic, N.; Linnros, J., Characterization of a porous silicon diode with efficient and tunable electroluminescence. *J Appl Phys* **1996**, *80*, 5971-5977.
10. Valenta, J.; Lalic, N.; Linnros, J., Electroluminescence microscopy and spectroscopy of silicon nanocrystals in thin SiO₂ layers. *Opt Mater* **2001**, *17*, 45-50.
11. Walters, R. J.; Bourianoff, G. I.; Atwater, H. A., Field-effect electroluminescence in silicon nanocrystals. *Nat Mater* **2005**, *4*, 143-146.
12. Li, H. S.; Wu, Z. G.; Lusk, M. T., Dangling Bond Defects: The Critical Roadblock to Efficient Photoconversion in Hybrid Quantum Dot Solar Cells. *J Phys Chem C* **2014**, *118*, 46-53.

13. Haider, M. B.; Pitters, J. L.; DiLabio, G. A.; Livadaru, L.; Mutus, J. Y.; Wolkow, R. A., Controlled Coupling and Occupation of Silicon Atomic Quantum Dots at Room Temperature. *Phys Rev Lett* **2009**, *102*, 046805.
14. Schofield, S. R.; Studer, P.; Hirjibehedin, C. F.; Curson, N. J.; Aeppli, G.; Bowler, D. R., Quantum engineering at the silicon surface using dangling bonds. *Nat Commun* **2013**, *4*, 1649.
15. Livadaru, L.; Xue, P.; Shaterzadeh-Yazdi, Z.; DiLabio, G. A.; Mutus, J.; Pitters, J. L.; Sanders, B. C.; Wolkow, R. A., Dangling-bond charge qubit on a silicon surface. *New J Phys* **2010**, *12*, 083018.
16. Lopinski, G. P.; Wayner, D. D. M.; Wolkow, R. A., Self-directed growth of molecular nanostructures on silicon. *Nature* **2000**, *406*, 48-51.
17. Dogel, S. A.; DiLabio, G. A.; Zikovsky, J.; Pitters, J. L.; Wolkow, R. A., Experimental and theoretical studies of trimethylene sulfide-derived nanostructures on p- and n-type h-silicon(100)-2 x 1. *J Phys Chem C* **2007**, *111*, 11965-11969.
18. Esch, M. P.; Shu, Y. N.; Levine, B. G., A Conical Intersection Perspective on the Low Nonradiative Recombination Rate in Lead Halide Perovskites. *J Phys Chem A* **2019**, *123*, 2661-2673.
19. Shu, Y. A.; Levine, B. G., Communication: Non-radiative recombination via conical intersection at a semiconductor defect. *J Chem Phys* **2013**, *139*, 081102.
20. Shu, Y. A.; Levine, B. G., Do Excited Silicon-Oxygen Double Bonds Emit Light? *J Phys Chem C* **2014**, *118*, 7669-7677.
21. Shu, Y. N.; Kortshagen, U. R.; Levine, B. G.; Anthony, R. J., Surface Structure and Silicon Nanocrystal Photoluminescence: The Role of Hypervalent Silyl Groups. *J Phys Chem C* **2015**, *119*, 26683-26691.
22. Shu, Y. N.; Levine, B. G., Nonradiative Recombination via Conical Intersections Arising at Defects on the Oxidized Silicon Surface. *J Phys Chem C* **2015**, *119*, 1737-1747.
23. Shu, Y. N.; Levine, B. G., First-Principles Study of Nonradiative Recombination in Silicon Nanocrystals: The Role of Surface Silanol. *J Phys Chem C* **2016**, *120*, 23246-23253.
24. Shu, Y. N.; Fales, B. S.; Levine, B. G., Defect-Induced Conical Intersections Promote Nonradiative Recombination. *Nano Lett* **2015**, *15*, 6247-6253.
25. Peng, W. T.; Fales, B. S.; Shu, Y. N.; Levine, B. G., Dynamics of recombination via conical intersection in a semiconductor nanocrystal. *Chem Sci* **2018**, *9*, 681-687.

26. Shu, Y. N.; Fales, B. S.; Peng, W. T.; Levine, B. G., Understanding Nonradiative Recombination through Defect-Induced Conical Intersections. *J Phys Chem Lett* **2017**, *8*, 4091-4099.
27. Berthe, M.; Urbieto, A.; Perdigo, L.; Grandidier, B.; Deresmes, D.; Delerue, C.; Stievenard, D.; Rurali, R.; Lorente, N.; Magaud, L.; Ordejon, P., Electron transport via local polarons at interface atoms. *Phys Rev Lett* **2006**, *97*, 206801.
28. Wolkin, M. V.; Jorne, J.; Fauchet, P. M.; Allan, G.; Delerue, C., Electronic states and luminescence in porous silicon quantum dots: The role of oxygen. *Phys Rev Lett* **1999**, *82*, 197-200.
29. Schmidt, T.; Chizhik, A. I.; Chizhik, A. M.; Potrick, K.; Meixner, A. J.; Huisken, F., Radiative exciton recombination and defect luminescence observed in single silicon nanocrystals. *Phys Rev B* **2012**, *86*, 125302.
30. Garcia, C.; Garrido, B.; Pellegrino, P.; Ferre, R.; Moreno, J. A.; Morante, J. R.; Pavesi, L.; Cazzanelli, M., Size dependence of lifetime and absorption cross section of Si nanocrystals embedded in SiO₂. *Appl Phys Lett* **2003**, *82*, 1595-1597.
31. Sychugov, I.; Juhasz, R.; Valenta, J.; Linnros, J., Narrow luminescence linewidth of a silicon quantum dot. *Phys Rev Lett* **2005**, *94*, 087405.
32. Levine, B. G.; Peng, W. T.; Esch, M. P., Locality of Conical Intersections in Semiconductor Nanomaterials. *Phys Chem Chem Phys* **2019**, *21*, 10870.
33. Becke, A. D., Density-Functional Thermochemistry .3. The Role of Exact Exchange. *J Chem Phys* **1993**, *98*, 5648-5652.
34. Lee, C. T.; Yang, W. T.; Parr, R. G., Development of the Colle-Salvetti Correlation-Energy Formula into a Functional of the Electron-Density. *Phys Rev B* **1988**, *37*, 785-789.
35. Ben-Nun, M.; Quenneville, J.; Martinez, T. J., Ab initio multiple spawning: Photochemistry from first principles quantum molecular dynamics. *J Phys Chem A* **2000**, *104*, 5161-5175.
36. Levine, B. G.; Coe, J. D.; Virshup, A. M.; Martinez, T. J., Implementation of ab initio multiple spawning in the MOLPRO quantum chemistry package. *Chem Phys* **2008**, *347*, 3-16.
37. Knowles, P. J.; Werner, H. J., An Efficient 2nd-Order Mc Scf Method for Long Configuration Expansions. *Chem Phys Lett* **1985**, *115*, 259-267.

38. Roos, B. O.; Taylor, P. R.; Siegbahn, P. E. M., A Complete Active Space Scf Method (Casscf) Using a Density-Matrix Formulated Super-Ci Approach. *Chem Phys* **1980**, *48*, 157-173.
39. Werner, H. J.; Knowles, P. J., A 2nd Order Multiconfiguration Scf Procedure with Optimum Convergence. *J Chem Phys* **1985**, *82*, 5053-5063.
40. Wadt, W. R.; Hay, P. J., Abinitio Effective Core Potentials for Molecular Calculations - Potentials for Main Group Elements Na to Bi. *J Chem Phys* **1985**, *82*, 284-298.
41. Hampel, C.; Peterson, K. A.; Werner, H. J., A Comparison of the Efficiency and Accuracy of the Quadratic Configuration-Interaction (Qcisd), Coupled Cluster (Ccsd), and Brueckner Coupled Cluster (Bccd) Methods. *Chem Phys Lett* **1992**, *190*, 1-12.
42. Korona, T.; Werner, H. J., Local treatment of electron excitations in the EOM-CCSD method. *J Chem Phys* **2003**, *118*, 3006-3019.
43. Sekino, H.; Bartlett, R. J., A Linear Response, Coupled-Cluster Theory for Excitation-Energy. *Int J Quantum Chem* **1984**, 255-265.
44. Gour, J. R.; Piecuch, P., Efficient formulation and computer implementation of the active-space electron-attached and ionized equation-of-motion coupled-cluster methods. *J Chem Phys* **2006**, *125*, 4107.
45. Gour, J. R.; Piecuch, P.; Wloch, M., Active-space equation-of-motion coupled-cluster methods for excited states of radicals and other open-shell systems: EA-EOMCCSDt and IP-EOMCCSDt. *J Chem Phys* **2005**, *123*, 4113.
46. Piecuch, P.; Wloch, M., Renormalized coupled-cluster methods exploiting left eigenstates of the similarity-transformed Hamiltonian. *J Chem Phys* **2005**, *123*, 4105.
47. Wloch, M.; Gour, J. R.; Piecuch, P., Extension of the renormalized coupled-cluster methods exploiting left eigenstates of the similarity-transformed Hamiltonian to open-shell systems: A benchmark study. *J Phys Chem A* **2007**, *111*, 11359-11382.
48. Celani, P.; Werner, H. J., Multireference perturbation theory for large restricted and selected active space reference wave functions. *J Chem Phys* **2000**, *112*, 5546-5557.
49. Shiozaki, T.; Gyorffy, W.; Celani, P.; Werner, H. J., Communication: Extended multi-state complete active space second-order perturbation theory: Energy and nuclear gradients. *J Chem Phys* **2011**, *135*, 081106.
50. Werner, H. J., Third-order multireference perturbation theory - The CASPT3 method. *Mol Phys* **1996**, *89*, 645-661.

51. Knowles, P. J.; Werner, H. J., An Efficient Method for the Evaluation of Coupling-Coefficients in Configuration-Interaction Calculations. *Chem Phys Lett* **1988**, *145*, 514-522.
52. Langhoff, S. R.; Davidson, E. R., Configuration Interaction Calculations on Nitrogen Molecule. *Int J Quantum Chem* **1974**, *8*, 61-72.
53. Werner, H. J.; Knowles, P. J., An Efficient Internally Contracted Multiconfiguration Reference Configuration-Interaction Method. *J Chem Phys* **1988**, *89*, 5803-5814.
54. Meek, G. A.; Levine, B. G., Evaluation of the Time-Derivative Coupling for Accurate Electronic State Transition Probabilities from Numerical Simulations. *J Phys Chem Lett* **2014**, *5*, 2351-2356.
55. Meek, G. A.; Levine, B. G., Accurate and efficient evaluation of transition probabilities at unavoided crossings in ab initio multiple spawning. *Chem Phys* **2015**, *460*, 117-124.
56. Werner, H. J.; Knowles, P. J.; Knizia, G.; Manby, F. R.; Schutz, M.
<http://www.molpro.net>.
57. Gordon, M. S.; Schmidt, M. W., Advances in electronic structure theory: GAMESS a decade later. *Theory and Applications of Computational Chemistry: The First Forty Years* **2005**, 1167-1189.
58. Schmidt, M. W.; Baldrige, K. K.; Boatz, J. A.; Elbert, S. T.; Gordon, M. S.; Jensen, J. H.; Koseki, S.; Matsunaga, N.; Nguyen, K. A.; Su, S. J.; Windus, T. L.; Dupuis, M.; Montgomery, J. A., General Atomic and Molecular Electronic-Structure System. *J Comput Chem* **1993**, *14*, 1347-1363.
59. Levine, B. G.; Coe, J. D.; Martinez, T. J., Optimizing conical intersections without derivative coupling vectors: Application to multistate multireference second-order perturbation theory (MS-CASPT2). *J Phys Chem B* **2008**, *112*, 405-413.

CHAPTER 5 SIMULATING ELECTRON DYNAMICS OF COMPLEX MOLECULES WITH TIME-DEPENDENT COMPLETE ACTIVE SPACE CONFIGURATION INTERACTION

Reproduced with permission from “Simulating Electron Dynamics of Complex Molecules with Time-Dependent Complete Active Space Configuration Interaction”, W.-T. Peng, B. S. Fales, B. G. Levine, *J. Chem. Theory Comput.*, 14, 4129, 2018. Copyright 2018 American Chemical Society.

5.1 Introduction

Ultrafast, strong, and shaped laser pulses have been shown to drive a wealth of interesting and often still poorly understood physical phenomena.¹⁻⁵ Experiments based on these pulses motivate the development of computational methods for modeling electronic dynamics in real time. (For a nice recent review see ref⁶.) Such methods enable ultrafast experiments to be modeled directly, providing detailed information about the motions of individual electrons which cannot be directly observed experimentally. Because the time-dependent wave function or electron density is explicitly modeled, interactions with the field are included to infinite order. Time-dependent electronic structure methods have also seen use in conjunction with nonadiabatic molecular dynamics schemes⁷⁻⁹ and for efficient computation of linear spectra.¹⁰

Among real-time electronic structure methods, real-time time-dependent density functional theory (RT-TDDFT) is the most popular choice for medium to large systems due to its favorable balance between cost and accuracy.¹¹⁻¹⁴ RT-TDDFT has enabled a microscopic, time-dependent view of electronic motions in light harvesting complexes, plasmonic materials, and other applications.^{10, 15-20} Though exact in principle, in practice RT-TDDFT suffers from a number of issues arising from the approximate functional used to describe exchange and correlation effects, in particular the adiabatic approximation (i.e. neglect of the history dependence of the functional) and the use of the ground state functional to describe nonstationary densities.²¹⁻²⁹ For example, RT-TDDFT predicts physically incorrect two-electron Rabi oscillations.²² The nonlinear dependence of the Kohn-Sham operator on the current state of the

system also causes the method to fail to predict full population inversion during Rabi oscillations and results in unphysical energy peak shifting.^{21, 24} In principle the exact history-dependent functional would correct these issues, but practical approaches to develop approximate functionals that solve these problems remain elusive.

Real-time time-dependent configuration interaction (TD-CI) methods, on the other hand, do not suffer these problems because the electronic Hamiltonian, a linear operator which is independent of the current state of the system, drives the dynamics.^{22, 24} In recent years, TD-CI and related Green's function approaches have enabled the computation of nonlinear response properties and dynamics of molecules in strong or shaped laser pulses.³⁰⁻⁴⁵ Time-dependent multiconfigurational self-consistent field (TD-MCSCF) calculations, in which both CI coefficients and orbitals are propagated in time, show promise for modeling high-harmonic generation, as well.⁴⁶⁻⁴⁸ Time-dependent equation-of-motion coupled cluster methods offer similar advantages to TD-CI, but within the faster converging framework of coupled cluster theory.^{36, 49-53} Though promising, TD-CI calculations have limitations. Within the often employed configuration interaction singles (CIS) approximation, TD-CI is limited to the singly excited electronic states of systems without strong electron correlation. TD-CI approaches based on higher-order expansions have typically been limited to small systems and/or short propagation times by computational cost. In addition, many schemes cannot practically be scaled to large configuration spaces because they require full diagonalization of the CI Hamiltonian prior to propagation, which becomes intractable for large configuration spaces.

A high-performance TD-CI implementation would open opportunities to accurately model electronic dynamics in medium-to-large molecular systems over long time scales. In this study, we present an implementation of TD-CI based on a complete active space expansion⁵⁴ of the electronic wave function (TD-CASCI). Rather than requiring diagonalization of the Hamiltonian prior to propagation, it is based on the on-the-fly calculation of $\mathbf{H}\mathbf{c}$, akin to direct configuration interaction strategies used to solve the time-independent electronic structure problem.⁵⁵⁻⁵⁶ Graphics processing unit (GPU) acceleration enables extension to large systems and configuration spaces. In the next section, we describe our numerical procedure for integrating the TDSE. In the Results and Discussion section we analyze the stability and

accuracy of our implementation and demonstrate its utility by predicting the dynamics of a large, strongly correlated molecule (decacene) in a series of shaped laser pulses. Finally, we conclude and discuss future prospects for GPU-accelerated TD-CASCI.

5.2 Method

Here we describe our graphics processing unit (GPU-) accelerated implementation of TD-CASCI. In TD-CI, the time-dependent electronic wave function, $\Psi(t)$, may be represented as a linear combinations of Slater determinants, $\{\Phi_I\}$, with time-dependent expansion coefficients $C_I(t)$,

$$\Psi(t) = \sum_I C_I(t) \Phi_I. \quad (1)$$

A complete active space expansion, familiar from time-independent quantum chemistry,⁵⁴ is used in this work, though the propagation scheme described below is general to any TD-CI expansion. The wave function is propagated by numerically solving the time-dependent Schrodinger equation,

$$i\dot{\mathbf{C}}(t) = \mathbf{H}(t)\mathbf{C}(t) \quad (2)$$

where the overdot indicates differentiation with respect to time. The formal solution of equation (2) can be written as

$$\mathbf{C}(t) = e^{-i\int_0^t \mathbf{H}(t) dt} \mathbf{C}(0). \quad (3)$$

However, solving the equation in this form requires exponentiating the CI Hamiltonian matrix, which is prohibitively expensive for large configuration spaces. Thus, different propagation schemes to approximate the exponentiation steps have been proposed.⁵⁷⁻⁵⁸ In this study, we used a second-order symplectic split operator integrator.⁵⁹ It is well-known that the time-dependent Schrodinger equation can be recast in symplectic form,

$$\dot{\mathbf{q}} = \mathbf{H}\mathbf{p} \quad (4)$$

$$\dot{\mathbf{p}} = -\mathbf{H}\mathbf{q}, \quad (5)$$

where the expansion coefficients have been split into their real and imaginary parts according to

$$\mathbf{C}(t) = \mathbf{q}(t) + i\mathbf{p}(t). \quad (6)$$

Propagation proceeds as follows. First we obtain initial conditions. In this work, all simulations start from the ground state solution of the field-free Hamiltonian matrix, \mathbf{H}_0 . The propagation occurs in a leap-frog fashion analogous to the velocity-Verlet integrator familiar in classical dynamics. Below h is the integration time step. At the first step:

$$\dot{\mathbf{p}}(0) = -\mathbf{H}(0)\mathbf{q}(0) \quad (7)$$

$$\mathbf{p}\left(\frac{1}{2}h\right) = \mathbf{p}(0) + \frac{1}{2}h\dot{\mathbf{p}}(0) \quad (8)$$

$$\dot{\mathbf{q}}\left(\frac{1}{2}h\right) = \mathbf{H}\left(\frac{1}{2}h\right)\mathbf{p}\left(\frac{1}{2}h\right) \quad (9)$$

$$\mathbf{q}(h) = \mathbf{q}(0) + h\dot{\mathbf{q}}\left(\frac{1}{2}h\right). \quad (10)$$

Then, for each subsequent time step the following four assignments are repeated:

$$\dot{\mathbf{p}}(t) = -\mathbf{H}(t)\mathbf{q}(t) \quad (11)$$

$$\mathbf{p}\left(t + \frac{1}{2}h\right) = \mathbf{p}\left(t - \frac{1}{2}h\right) + h\dot{\mathbf{p}}(t) \quad (12)$$

$$\dot{\mathbf{q}}\left(t + \frac{1}{2}h\right) = \mathbf{H}\left(t + \frac{1}{2}h\right)\mathbf{p}\left(t + \frac{1}{2}h\right) \quad (13)$$

$$\mathbf{q}(t+h) = \mathbf{q}(t) + h\dot{\mathbf{q}}\left(t + \frac{1}{2}h\right). \quad (14)$$

For the final step:

$$\dot{\mathbf{p}}(t) = -\mathbf{H}(t)\mathbf{q}(t) \quad (15)$$

$$\mathbf{p}(t) = \mathbf{p}\left(t - \frac{1}{2}h\right) + \frac{1}{2}h\dot{\mathbf{p}}(t). \quad (16)$$

The symplectic symmetry of the integrator will in many cases result in long-time norm conservation—though the norm may fluctuate on short timescales. Beyond the advantages of symplectic symmetry, this integrator also offers minimal storage requirements, enabling propagation in large CI spaces. Extension to higher order is straight forward, but comes at the expense of additional storage. Chebyshev propagation⁶⁰ and other symplectic integrators⁶¹ would both likely also provide robust and efficient integration.

The most time-consuming step of this algorithm is the evaluation of matrix-vector multiplications $\mathbf{H}\mathbf{p}$ and $\mathbf{H}\mathbf{q}$ at every time step. This step is equivalent to the σ -vector formation operation in the iterative Davidson scheme for solution of the time-independent Schrodinger equation (TISE). In this work, this operation is efficiently performed via the algorithm

developed by Knowles and Handy,⁶² one of several fast algorithms that have been proposed.^{54, 63-65} To achieve high performance, we will use the GPU-accelerated implementation of this algorithm recently reported by two of the authors⁶⁶ to evaluate equations (7), (9), (11), (13), and (15). We implemented our algorithm into a development version of the TeraChem GPU-accelerated electronic structure package.⁶⁷⁻⁶⁸ All floating point calculations are performed in double (64-bit) precision.

It is important to note that only the CI vector is propagated in this scheme; the orbitals remain frozen. Others have implemented propagation schemes that allow both the CI coefficients and orbital coefficients to evolve (TD-MCSCF).⁴⁶⁻⁴⁸ Though orbital propagation is certainly of benefit in applications where the time-dependent electronic wave function would not be representable in the initial active space at all times, it comes at a significant cost. Many of the disadvantages of RT-TDDFT relative to TD-CI arise from the orbital-dependence of the Kohn-Sham matrix. Orbital propagation necessarily involves a similar Fock matrix, and therefore would likely exhibit similar difficulties. For example, we suspect that the detuning of Rabi oscillations observed in RT-TDDFT as discussed in the introduction will be observed in time-dependent multi-configurational self-consistent field calculations as well.^{21, 24} The extent to which this behavior is a serious problem in the context of multi-configurational wave function theory would be an interesting topic for further study.

Given this limitation, we choose to eschew orbital propagation and judiciously apply our method to model dynamics that can reasonably be expected to be well described in an active space of orbitals. We expect, for example, that quantum control of the population of low-lying excited states can be modeled in a typical active space calculation, but ionization and high-harmonic generation, which would require population of high energy virtual orbitals, cannot. Extension of the TD-CI ansatz to include single excitations to the virtual space will enable modeling of these higher energy processes. This extension will be described in a subsequent publication.

The electric field is represented in the electric dipole approximation,

$$\hat{H}(t) = \hat{H}_0 - \hat{\mathbf{m}} \cdot \mathbf{d}E(t), \quad (17)$$

in which \hat{H}_0 is the field-free CI Hamiltonian, $\hat{\mathbf{m}}$ is the molecular dipole operator, the scalar function, $E(t)$, is the time-dependent external field strength, and \mathbf{d} is the unit vector in the field polarization direction. Magnetic field effects, which are neglected here, become prominent in ultra-intense fields,⁶⁹⁻⁷⁰ and under such conditions one must also consider a relativistic treatment.⁷¹ Four different pulse shapes are used in this work: 1) δ -function pulse,

$$E(t) = E_0 \delta(t), \quad (18)$$

2) continuous wave (CW),

$$E(t) = E_0 \sin(\omega t), \quad (19)$$

3) transform-limited (TL) pulse,

$$E(t) = E_0 \exp\left(\frac{t-t_0}{2\sigma^2}\right) \sin(\omega(t-t_0)), \quad (20)$$

and 4) chirped pulse,

$$E(t) = E_0 \exp\left(\frac{t-t_0}{2\sigma^2}\right) \sin\left(\left(\omega + \frac{1}{2}\beta(t-t_0)\right)(t-t_0)\right), \quad (21)$$

where ω is the carrier frequency, σ is the pulse width, and β is the chirp parameter. For numerical convenience, \hat{H}_0 is shifted such that the ground state energy of the system is zero.

The energy spectrum of the electronic wave function following excitation can be extracted from the time correlation function,

$$R(t) = \mathbf{C}(\varepsilon)^\dagger \mathbf{C}(\varepsilon + t), \quad (22)$$

where ε is a time immediately after the end of the pulse. Given a δ -function pulse, the Fourier transform of $R(t)$ yields the electronic absorption spectrum. When a large number of excited states are of interest, this approach yields an appealing alternative to the solution of the TISE, which may become intractable due to the memory requirements associated with the storage of a large number of electronic wave functions. In this case, TD-CI can provide a memory-efficient means of computing the energy spectrum, because only a single complex electronic wave function need be stored. This is similar to the way that RT-TDDFT can outperform linear response (LR-) TDDFT in obtaining excitation energies in large systems with high densities of states.¹⁰

In this work, the population of a given adiabatic electronic state is often reported as a function of time. This is computed by projection of the time-dependent wave function onto the electronic eigenstates as computed by solution of the TISE,

$$P_i(t) = \left| \psi_i^\dagger \mathbf{C}(t) \right|^2, \quad (23)$$

where ψ_i is the electronic eigenstate of interest.

Calculations are reported for two systems. We model the absorption spectrum and the ultrafast dynamics of decacene ($C_{42}H_{24}$; picture in Figure 5.1). Decacene was chosen because a) it is larger than most molecules that have previously been studied via TD-CI, b) it is known to possess strong electron correlation and thus benefits from a multireference description of the electronic structure,⁷²⁻⁷⁴ and c) with its large conjugated system, it is relatively rigid in its low-lying electronic excited states and thus electronic dynamics alone can be expected to provide a reasonable description of its response to a light field. The decacene calculations were performed using an orbital basis of state-averaged CIS natural orbitals (CISNO).⁷⁵⁻⁷⁶ CISNO-CASCI has been shown to reproduce the low-lying excited states of various molecules with semiquantitative accuracy (similar to state-averaged CASSCF) and, unlike state-averaged CASSCF, offers a rigorously size-intensive description of excitations in large systems. An active space of 10 electrons in 10 orbitals and the 6-31G(d) basis set were used. This active space was chosen to include all orbitals that contribute to strong correlation as predicted by density matrix renormalization group calculations.⁷² The decacene geometry was taken from ref. ⁷² where it was optimized at the UB3LYP/6-31G* level. In order to assess the accuracy of population transfer probabilities computed from our integration scheme, we have computed Rabi oscillations in a simpler system: ethylene (C_2H_4). Ethylene was optimized at the B3LYP/6-31G(d,p) level. A 2-electron, 2-orbital active space, STO-3G basis, and Hartree-Fock (HF) orbitals were used for the TD-CI calculations. A future study will investigate the accuracy of various possible orbital choices for TD-CASCI.

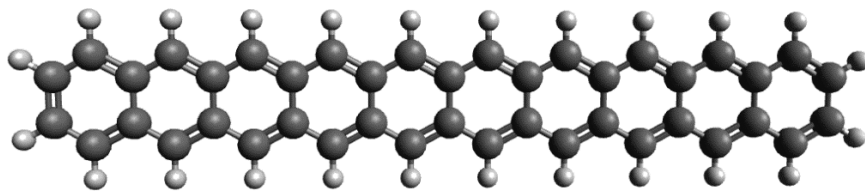


Figure 5.1. Molecule of decacene. Dark gray: carbons. Light gray: hydrogens.

Throughout this work, time-dependent calculations will be abbreviated TD-*<orbital determination scheme>*-CASCI (e.g. TD-CISNO-CASCI). Analogous time-independent calculation (traditional electronic structure calculations) will be abbreviated with the prefix TI for clarity (e.g. TI-CISNO-CASCI). Active spaces with M electrons and N orbitals are abbreviated (M,N) . Various integration time steps are used in different calculations and are mentioned with each result. Throughout this work adiabatic state labels are used (S_0 for the singlet ground state, S_1 for the first singlet excited state, etc.).

5.3 Results and Discussion

5.3.1 Absorption Spectrum

To demonstrate the applicability and numerical accuracy of our TD-CI scheme, we have computed the electronic absorption spectrum of decacene, a large molecule with a strongly correlated electronic ground state. This spectrum was computed as described above using a δ -function pulse polarized along the short in-plane molecular axis (the vertical direction in Figure 5.1). The resulting spectrum up to 6 eV is shown in Figure 5.2. The spectrum is based on 100 fs of propagation using a 1 attosecond (as) integration time step. The excitation energies are taken to be the points of maximum absorbance. These excitation energies are reported in Table 5.1. Given accurate numerical propagation, these energies should closely match those obtained by solution of the analogous time-independent electronic structure problem, TI-CISNO-CASCI, with the same basis and active space.

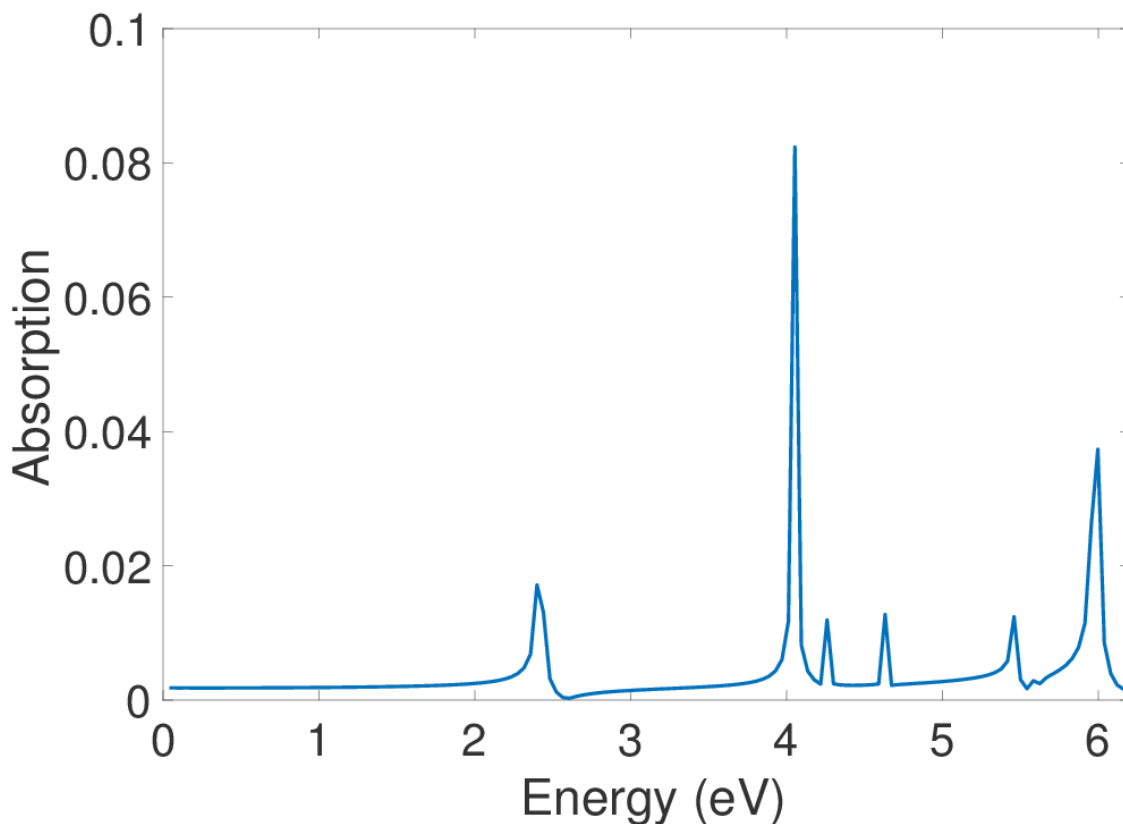


Figure 5.2. The absorption spectrum of decacene computed at the TD-CISNO-CASCI level as described in the text.

Table 5.1. Comparison of the excitation energies (eV) of decacene calculated via TD-CISNO-CASCI and TI-CISNO-CASCI. Only the states with non-zero transition dipole moment in the polarization direction (μ_y ; atomic units) are listed. Absolute errors are reported in eV.

	$S_0 \rightarrow S_2$	$S_0 \rightarrow S_8$	$S_0 \rightarrow S_9$	$S_0 \rightarrow S_{13}$	$S_0 \rightarrow S_{23}$	$S_0 \rightarrow S_{25}$	$S_0 \rightarrow S_{32}$
TD-CASCI	2.357	4.012	4.218	4.591	5.418	5.542	5.955
TI-CASCI	2.378	4.007	4.217	4.592	5.435	5.566	5.940
Error	0.021	0.005	0.001	0.001	0.017	0.024	0.015
μ_y	1.04	1.51	0.51	0.52	0.49	0.13	0.96

As shown in Table 5.1, our TD-CASCI implementation reproduces the excitation energies with only minor discrepancies. The maximum error is 0.024 eV ($S_0 \rightarrow S_{25}$). This discrepancy is of the order expected due to the Fourier relationship between the dynamics and

the energy spectrum; upon Fourier transformation of the correlation function computed from this 100 fs dynamic simulation, the resulting spectrum is discretized with an energy interval of 0.041 eV. That the maximum error is roughly half of this quantity suggests that the errors are due to the finite length of the dynamic simulations.

The dependence of the computed spectrum on the integration time step has been analyzed by considering the peak energies as a function of time step. We find that the energies of the peaks below 6 eV are invariant to the time step (to within the 0.041 eV accuracy for a 100 fs simulation) for time steps from 1 to 19 as. A 20 as time step results in catastrophic failure; the norm of the wave function diverges to infinity. This is in contrast to the 19 as time step, in which the norm of the wave function remains 1.006 after 100 fs of simulation. Details can be found in Table D1.

The smallest time step for which such divergence is observed is likely determined by the energy of the highest-energy state populated during the dynamics. This is because the high energy states rotate rapidly in the complex plane, and this rotation requires a short time step to integrate accurately. Obviously the choice of a large (e.g. (10,10)) active space creates the opportunity for some very high energy states to be populated. Here we consider the same system (decacene) but with a smaller active space (2,2) to investigate how the size of the active space influences the choice of integration time step. Note that there is only one bright transition available. The energy of this transition remains identical for time steps ranging from 1 to 100 as (2.151 eV, compared to a TI-CISNO-CASCI value of 2.157). Error increases with increasing time step (see Table D2), but the norm is well conserved even for a 450 as time step. Thus, the time step required to accurately predict the absorption spectrum depends strongly on the choice of active space, or more generally on the range of energies of the populated eigenstates. We also note that the norm is not a sensitive measure of the accuracy of integration.

5.3.2 Rabi Oscillations

A well-known failing of RT-TDDFT is that Rabi oscillations are not correctly described, both because energies detune as the Kohn-Sham matrix evolves^{21, 24} and because the mean-field

nature of RT-TDDFT results in electrons transitioning between orbitals in pairs (two-electron Rabi oscillations).²² Due to the many-body nature of CI and the linearity of the Hamiltonian driving the dynamics, these problems do not arise in TD-CI.^{22, 24} Here we again demonstrate this advantage of TD-CI and use the well-defined Rabi oscillations as a model to further investigate the accuracy of our integration scheme.

The period of Rabi oscillations between two states, i and j , is

$$T_{ij} = \frac{2\pi}{\Omega_{ij}} \quad (24)$$

with Rabi oscillation frequency

$$\Omega_{ij} = \frac{\mathbf{m}_{ij} \cdot \mathbf{E}}{\hbar} \quad (25)$$

where \mathbf{m}_{ij} is the transition dipole vector and \mathbf{E} is the electric field strength vector.

Here we study ethylene, with simulation parameters as described above. A continuous wave field polarized along the C=C bond is applied with an intensity of 10^{12} W/cm² and a field frequency of 3.444×10^{15} Hz. This corresponds to the energy difference between the S_0 and S_1 states ($\pi \rightarrow \pi^*$ transition) as calculated at the TI-HF-CASCI level. The exact Rabi oscillation period computed for this system according to equations (24) and (25) is 21.506 fs. The state populations as a function of time drawn from a simulation with a 1 as time step are shown in Figure 5.3a. Qualitatively correct one-electron Rabi oscillations are observed. The observed oscillation frequency (21.507 fs) is in excellent agreement with the exact value (21.506 fs)

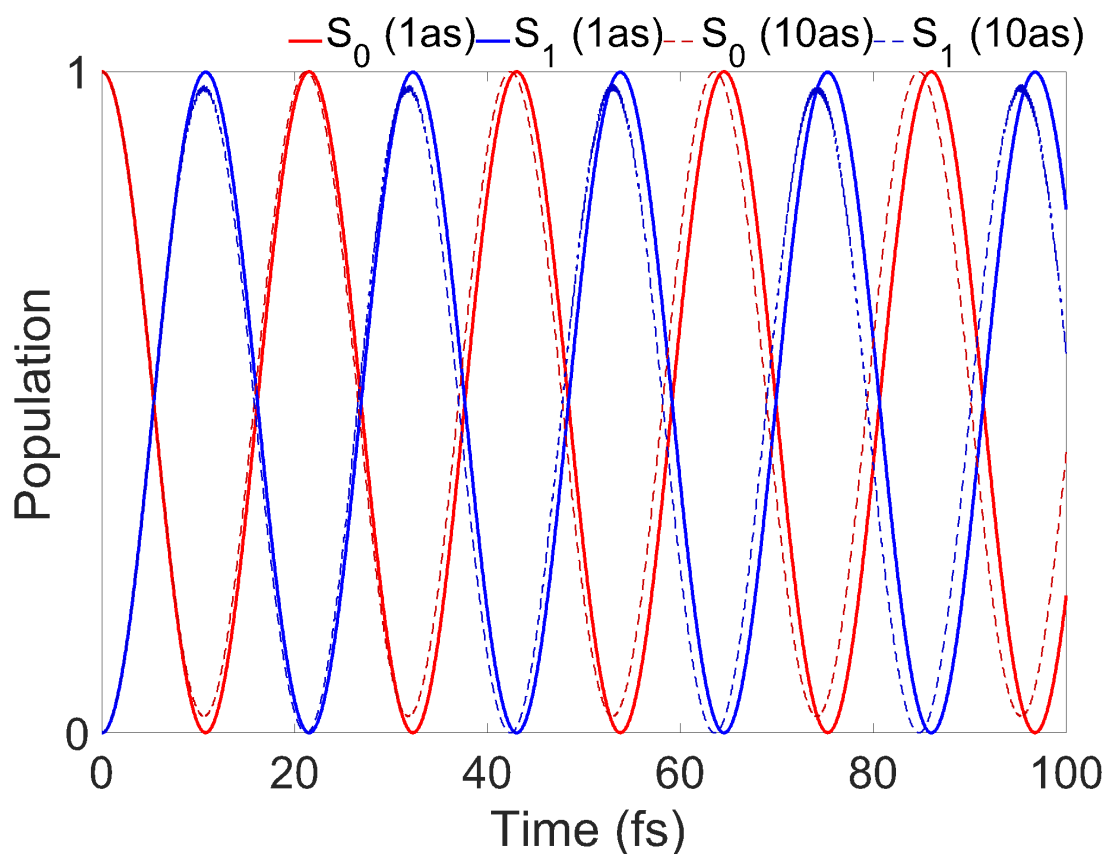


Figure 5.3. The populations of the S_0 and S_1 states as a function of time from calculations of the dynamics of ethylene in a resonant CW field, as described in the text. Calculations are performed with time steps of 1 as (solid) and b) 10 as (dashed).

Because Rabi oscillations are an exactly solvable problem, they provide us with an opportunity to examine the influence of time step on the accuracy of population dynamics. Three different measures of the integration error are reported in Table 5.2. The population error (“Pop. Err.” in Table 5.2) measures whether full population inversion is achieved. We define the population error as the minimum population of S_0 observed during the Rabi oscillation cycle. Each simulation includes multiple such minima. The largest error observed in each simulation is reported. The error in the period (ΔT in Table 5.2) is defined as the difference between the exact Rabi oscillation period, 21.506 fs, and the period as predicted by TD-CASCI (determined by measuring the peak-to-peak distance for the first oscillation). Finally, the norm of the wave function after 100 fs of propagation is reported.

We find that the accurate calculation of population dynamics requires a finer time step than was needed to reproduce the absorption spectrum. As shown in the Table 5.2, the error in the population dynamics increases from 0.0002 to 0.0292 as the time step is increased from 1 to 10 as. Integration error results in population dynamics comparable to interaction with a field that is slightly off resonance (Figure 5.3). In addition, the calculated period of the Rabi oscillations increases by 0.316 fs as the time step is increased from 1 to 10 as. Note that the norm is well conserved in all simulations (Table 5.2), and therefore is not a sensitive measure of the accuracy of the population dynamics.

Table 5.2. The error in the population (Pop. Err.), error in the Rabi oscillation period (ΔT) relative to the exact value (21.506 fs), and norm of the wave function after 100 fs of propagation for simulations of ethylene in a resonant CW field as a function of the integration time step. Simulation details are presented in the text.

	1 as	2 as	4 as	6 as	8 as	10 as
Pop. Err.	0.0002	0.0004	0.0013	0.0042	0.0110	0.0292
ΔT (fs)	0.001	0.011	0.020	0.062	0.162	0.316
norm	1.000	1.000	1.001	1.001	1.000	0.997

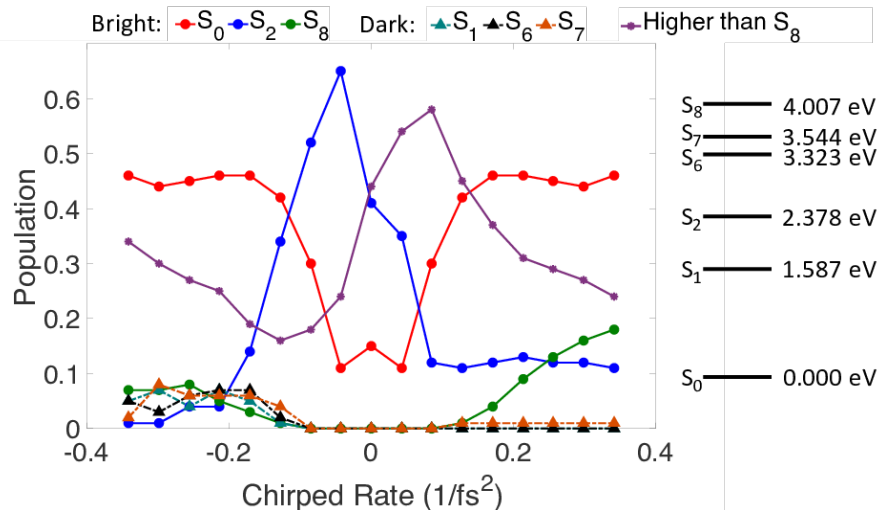


Figure 5.4. The final state populations obtained from 100 fs simulations of decacene (TD-CISNO-CASCI(10/10)/6-31G(d)) in a series of laser pulses with chirp ranging from $\beta = -0.342$ fs^{-2} to $\beta = 0.342$ fs^{-2} . All pulses have a FWHM of 10 fs and a maximum intensity of 3×10^{12} W/cm^2 . The populations of bright and dark states up to S_8 are shown with solid lines and dashed lines, respectively. The populations in all states above S_8 are summed into a single (purple) line. Populations of states with negligible population in all simulations (S_3 - S_5) are not shown. A Jablonski diagram on the right shows the energies of the populated states up to S_8 .

5.3.3 Control by Shaped Pulses

Here we demonstrate our implementation of TD-CISNO-CASCI by modeling the electronic dynamics of decacene in a series of chirped laser pulses. All pulses are polarized along the short in-plane molecular axis and have a 10 fs FWHM, a maximum intensity of 3×10^{12} W/cm^2 , and a carrier frequency matching the gap between the S_0 and S_2 states (2.378 eV; the lowest allowed transition for decacene for the chosen polarization direction). Figure 5.4 shows the populations of all significantly populated electronic states after the pulse decays for chirp parameters ranging from $\beta = -0.342$ fs^{-2} to $\beta = 0.342$ fs^{-2} (-0.0002 a.u. to 0.0002 a.u.). Clearly the populations depend strongly on the chirp parameter. Specifically, positive chirp rates (meaning that the frequency increases with time) result in a significant increase in the population of higher energy states. This includes S_8 , which is bright with respect to the ground state, and states higher than S_8 , many of which are dipole-forbidden with respect to the ground state. For

less chirped pulses ($\beta \approx 0.1 \text{ fs}^{-2}$) more population is seen in states above S_8 , whereas for more chirped pulses ($\beta \approx 0.3 \text{ fs}^{-2}$) more population is observed in S_8 itself. In contrast, negatively chirped pulses result in either more population in S_2 (for $\beta \approx -0.05 \text{ fs}^{-2}$) or in low energy states that are dark relative to the ground electronic state (S_1 , S_6 , and S_7 ; for $\beta < -0.1 \text{ fs}^{-2}$). For pulses that are nearly transform limited ($\beta \approx 0.0 \text{ fs}^{-2}$) the ground states is more strongly depleted than for pulses with larger positive or negative chirps.

In order to understand the dependence of the electron state populations on pulse shape, we examine the population dynamics driven by several different pulses. First we consider TL pulses at two different intensities to investigate the probability of multiphoton processes. The middle and bottom panels of Figure 5.5 present the electronic state populations as a function of time for decacene in TL pulses with maximum intensities of $1 \cdot 10^{12} \text{ W/cm}^2$ and $3 \cdot 10^{12} \text{ W/cm}^2$, respectively. Both pulses have FWHM of 10 fs. For the weaker pulse ($1 \cdot 10^{12} \text{ W/cm}^2$; middle panel), most of the population (75 %) transfers from the ground state to the S_2 state with less than 8% of the population on other (higher) states after the pulse. When the intensity is tripled, however, maintaining the same duration and carrier frequency, only 41.5% of the population stays on the S_2 state. A similarly large fraction of the population (44%) is promoted to states higher in energy than S_8 . Examination of the populations shows that in this more intense field the molecule tends to absorb multiple photons, climbing a ladder of states: $S_0 \rightarrow S_2 \rightarrow S_{18} \rightarrow S_{57}$. Each of these transitions has a large transition dipole ($>1 \text{ a.u.}$) and the transition energies are roughly resonant with the carrier frequency (2.378 eV for $S_0 \rightarrow S_2$, 2.684 eV for $S_2 \rightarrow S_{18}$, and 2.151 eV for $S_{18} \rightarrow S_{57}$). Note that the $S_0 \rightarrow S_{18}$ transition is dipole forbidden. The $S_0 \rightarrow S_{57}$ transition is dipole allowed, but the energy of this transition is 7.213 eV, large enough so as to preclude direct excitation from S_0 . These higher states are not populated until after S_2 is significantly populated, consistent with the proposed ladder-climbing behavior. Thus, at this intensity strong nonlinear effects are observed.

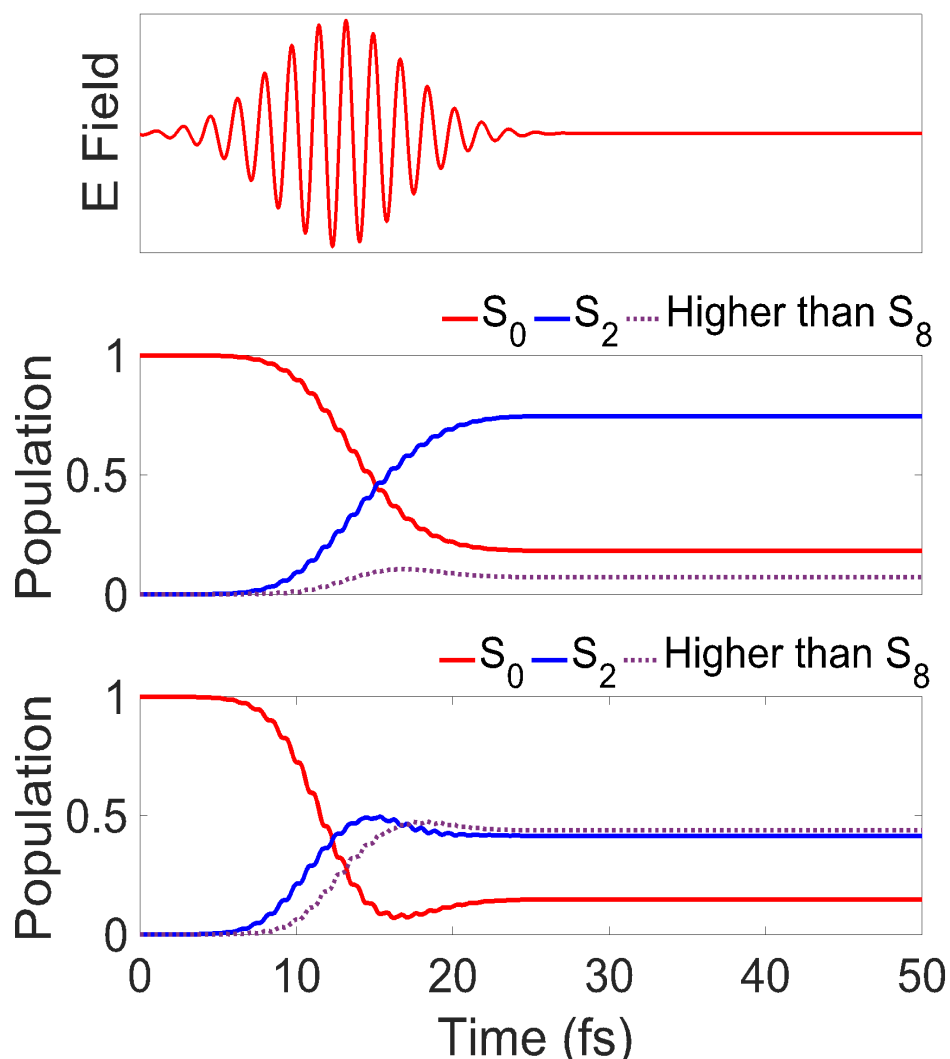


Figure 5.5. The electronic state populations as a function of time for decacene (TD-CISNO-CASCI(10,10)/6-31G(d)) in 10 femtosecond (FWHM) TL pulses with maximum intensities of $1 \cdot 10^{12}$ W/cm² (middle panel) or $3 \cdot 10^{12}$ W/cm² (bottom panel). The electric field as a function of time is shown in the top panel (arbitrary units). This pulse is resonant with the $S_0 \rightarrow S_2$ transition. Only states up to S_8 that contain non-negligible population at the end of the simulations are shown. The sum of all population in states higher than S_8 is represented by a dotted purple line.

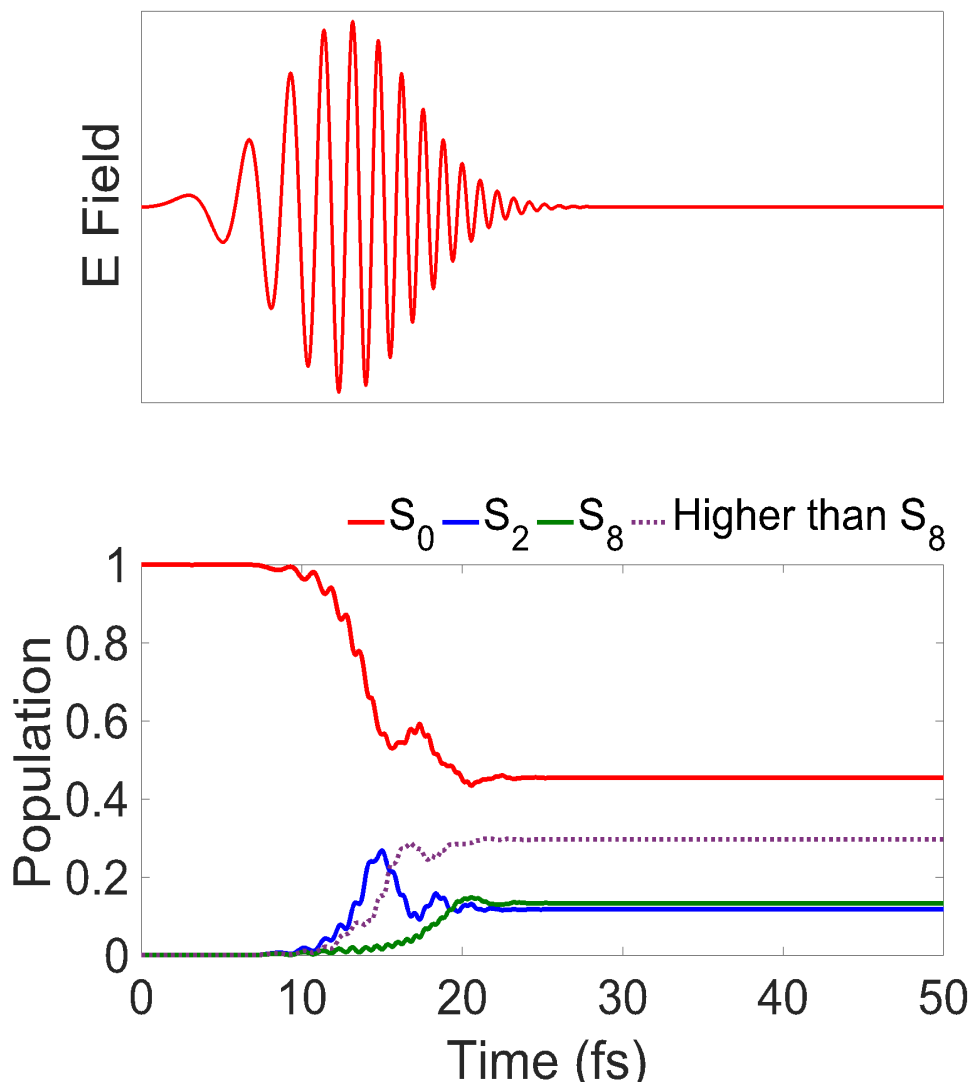


Figure 5.6. The electronic state populations as a function of time for decacene (TD-CISNO-CASCI(10,10)/6-31G(d)) in 10 fs (FWHM) chirped pulses with $\beta = 0.256 \text{ fs}^{-2}$ and an intensity of $3 \times 10^{12} \text{ W/cm}^2$ are shown in the bottom panel. The electric field as a function of time is illustrated in the top panel. Only populations of states up to S_8 that contain non-negligible population at the end of the simulation are shown. The sum of all population in states higher than S_8 is represented by a dotted purple line.

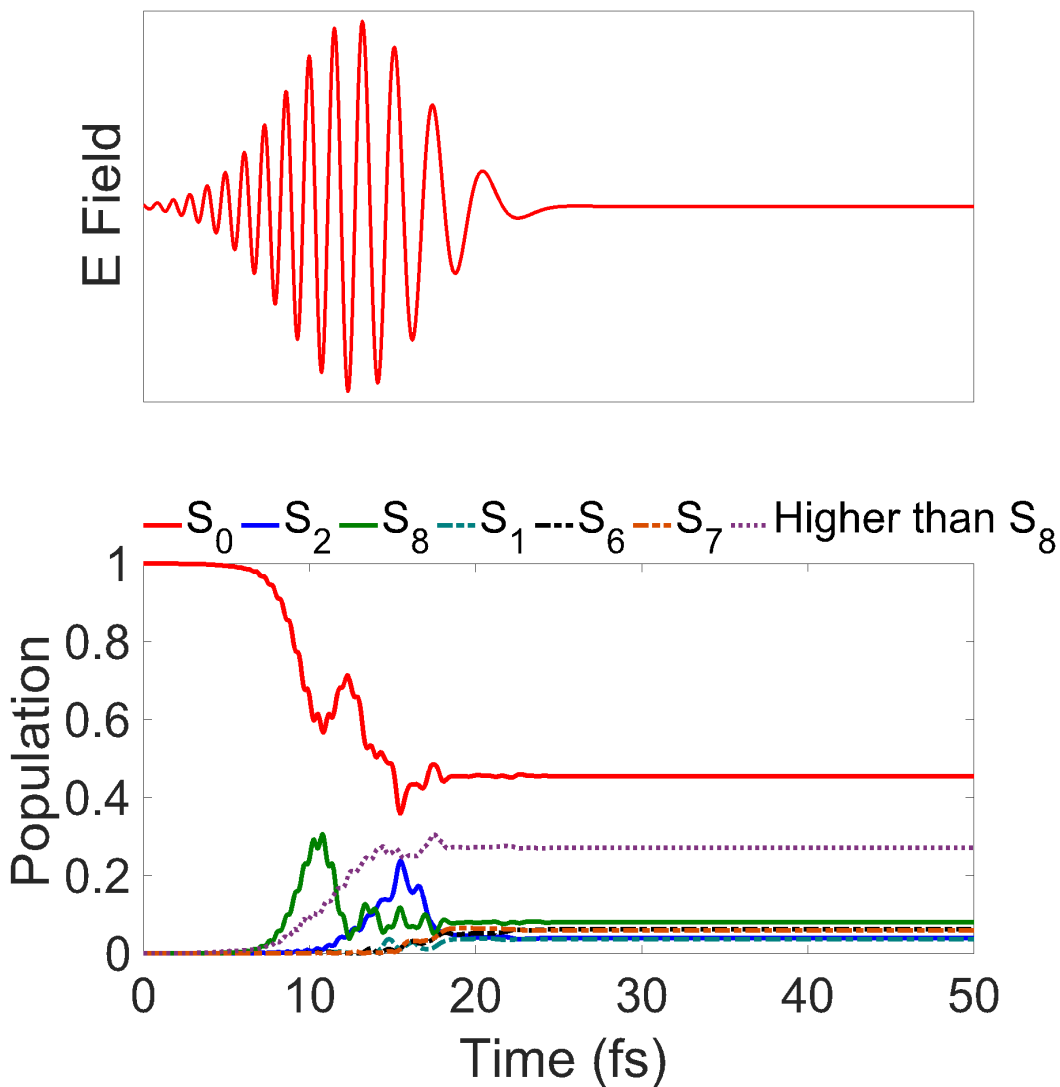


Figure 5.7. The electronic state populations as a function of time for decacene (TD-CISNO-CASCI(10,10)/6-31G(d)) in 10 fs (FWHM) chirped pulses with $\beta = -0.256 \text{ fs}^{-2}$ and an intensity of $3 \times 10^{12} \text{ W/cm}^2$ are shown in the bottom panel. The electric field as a function of time is illustrated in the top panel. Only populations of states up to S_8 that contain non-negligible population at the end of the simulation are shown. States that are dark with respect to the electronic ground state (S_1 , S_6 , and S_7) are shown with dashed lines. The sum of all population in states higher than S_8 is represented by a dotted purple line.

Now we consider the detailed dynamics of decacene in chirped pulses. Figures 5.6 and 5.7 show the electronic state populations as a function of time when decacene is exposed to chirped pulses with a carrier frequency resonant with the $S_0 \rightarrow S_2$ transition and chirp rates of 0.256 fs^{-2} and -0.256 fs^{-2} (0.00015 to -0.00015 a.u.), respectively. First we consider the positively chirped pulse. As noted above, the S_2 and S_8 states are the lowest-lying dipole-allowed transitions from S_0 . Significant population is observed in the two dipole allowed states (S_2 and S_8), the ground state, and states above S_8 . The S_2 state accumulates populations first, followed by the S_8 state. This is not surprising given a positively chirped pulse. The frequency increases with time, so the $S_0 \rightarrow S_2$ transition is resonant first, and the $S_0 \rightarrow S_8$ transition is resonant later. Population in states above S_8 largely arises due to ladder-climbing from S_2 , similar to that observed in the TL pulse above. As can be seen in Figure 5.4, larger positive chirp results in more population in S_8 , consistent with the fact that a pulse with a larger chirp parameter reaches resonance with the $S_0 \rightarrow S_8$ transition while its intensity remains large and before the ground state population is depleted by the $S_0 \rightarrow S_2$ transition.

The dynamics in the negatively chirped pulse (Figure 5.7) are more complex than in the positively chirped pulse. Population transfer to S_8 is observed before transfer to S_2 , as one would expect for a negatively chirped pulse. Subsequent population transfer is observed to several states that are dark relative to S_0 : S_1 , S_6 , and S_7 . In all three cases population transfer begins once the population of S_2 becomes significant. The $S_2 \rightarrow S_1$, $S_2 \rightarrow S_6$ and $S_2 \rightarrow S_7$ transitions energies (0.791 eV , 0.945 eV , and 1.116 eV , respectively) are all lower than the energy of $S_0 \rightarrow S_2$ and these three transitions all have a significant transition dipole moment. As the frequency of the negatively chirped field decreases with time, it reaches resonance with these transitions. Thus, these states are populated via a two-photon process: resonant two-photon absorption in the case of S_6 and S_7 and stimulated electronic Raman scattering in the case of S_1 . Population of these dark states is not observed for positively chirped pulses because the lower frequencies resonant with the $S_2 \rightarrow S_n$ ($n=1,6,7$) transitions precede population of S_2 . As can be seen in Figure 5.4, the populations of all of these states depends intricately on the value of the chirp parameter (β). Less negatively chirped pulses are so low in intensity by the time the frequency reaches resonance with the $S_2 \rightarrow S_n$ transitions that these two-photon processes are not observed with significant probability. The dependence of the dynamics on active space was

investigated by running an identical calculation with an expanded (12,12) active space. Qualitatively similar dynamics were observed, with small quantitative differences in the final populations of the various states. See Figure D1 for details.

To investigate the convergence of the population dynamics with respect to time step, we have modeled the dynamics of decacene in a pulse with a chirp rate of -0.256 fs^{-2} , a (10/10) active space, and all other parameters as above using time steps ranging from 1 to 16 as. We find that the final population as predicted with a 16 as time step is in error by less than 0.001 for all states. As the time step decreases, the population converges nicely toward the zero time step limit, suggesting that future studies could utilize time step extrapolation to minimize integration errors. Data can be found in Figures D2-D7.

In all of the above cases, the dynamics observed are limited to the active space. Thus, only valence electronic dynamics are observed and processes involving high energy virtual orbitals (e.g. ionization and high harmonic generation) are not. As mentioned above, the use of a TD-CASSCF approach could circumvent this limitation because the occupied orbitals can rotate into the virtual space, but TD-CASSCF would suffer from many of the difficulties associated with RT-TDDFT. As will be discussed in the conclusion, application to higher energy processes can also be achieved by extension of the configuration space.

Table 5.3. The wall time to solution for several of the calculations. The propagation time is 100 femtosecond and the time step is 1 as for all simulations shown.

Field Type	Molecule	Method	Active Space	Wall Time (seconds)
CW	ethylene	TD-HF-CASCI/STO-3G	(2,2)	146 (2.43 min)
δ -function	decacene	TD-CISNO-CASCI/6-31G(d)	(10,10)	8328 (2.31 hr)
TL	decacene	TD-CISNO-CASCI/6-31G(d)	(10,10)	8612 (2.39 hr)
Chirped pulse	decacene	TD-CISNO-CASCI/6-31G(d)	(10,10)	8536 (2.37 hr)
Chirped pulse	decacene	TD-CISNO-CASCI/6-31G(d)	(12,12)	72473 (20.1 hr)

5.3.4 Performance

Table 5.3 reports the wall time to solution for a representative set of the calculations mentioned above. All calculations were performed on a single NVIDIA K40 GPU. For the smaller ethylene system (TD-HF-CASCI(2,2)/STO-3G) the CW field calculation took less than 2.5 minutes to propagate for 100 femtosecond using a 1 as time step. The larger decacene simulations with δ -function, TL, and chirped fields (TD-CISNO-CASCI(10,10)/6-31G(d)) required less than 2.5 hours to propagate for 100 fs using a 1 as time step. Of the 2.5 hours, approximating one hour is required to compute the TI-CISNO-CASCI(10,10)/6-31G(d) ground state for use as the initial wave function and higher energy eigenstates for subsequent population projections. Extrapolating from these benchmarks, the 17 simulations of decacene used to create Figure 5.4 require less than 2 days on a single GPU. One additional calculation based on a (12,12) active space is shown. Even with this large active space (853776 determinants) integration for 100 fs requires only 20.1 hr.

5.4 Conclusions

In this study, we implemented a new algorithm to efficiently perform TD-CASCI calculations with the aid of GPUs. We found that when employed with a sufficiently short time step this algorithm provided robust predictions of absorption spectra and population dynamics (i.e. Rabi oscillations). The dynamics of decacene with a large (10,10) active space can be simulated for 100 fs in less than 2.5 hours on an NVidia K40 GPU. This new tool was employed to explore how shaped laser pulses can be used to control the population of dipole-forbidden states in decacene.

Because excitations to the virtual orbitals outside the CAS space are not possible in TD-CASCI, our current method is limited to dynamics that do not leave the set of valence excited electronic states. In future work we will extend our method to high-energy processes by inclusion of single excitations to the virtual orbital space. We will also investigate the choice of orbital determination methods^{75, 77-79} on the accuracy of TD-CASCI calculations and couple our

GPU-accelerated TD-CI method to a nonadiabatic molecular dynamics scheme in order to model full molecular dynamics in dense manifolds of states.

APPENDIX

SUPPORTING INFORMATION FOR: SIMULATING ELECTRON DYNAMICS OF COMPLEX MOLECULES WITH TIME-DEPENDENT COMPLETE ACTIVE SPACE CONFIGURATION INTERACTION

Table D1. Comparison of the wave function norm at the end of 100 fs simulations of decacene after excitation by a δ -function pulse calculated using different time steps. Calculations are performed with the TD-CISNO-CASCI/6-31G(d) basis set with a (10,10) active space.

Time Step	Norm
1 as	1.000
10 as	1.002
15 as	1.003
19 as	1.006
20 as	Inf

Table D2. The first excitation energies (in eV) of decacene obtained with TI-CISNO-CASCI and TD-CISNO-CASCI methods with 6-31G(d) basis set and a (2,2) active space. TD-CISNO-CASCI calculations were performed with a series of time steps from 1 to 500 as. The norm at the end of the 100 fs simulations is also presented.

	TI-CISNO-CASCI	1 as	100 as	200 as	300 as	400 as	450 as	500 as
E_{ex}	2.157	2.151	2.151	2.192	2.303	2.358	2.426	---
norm	---	1.000	1.001	1.002	1.005	1.012	1.014	Inf

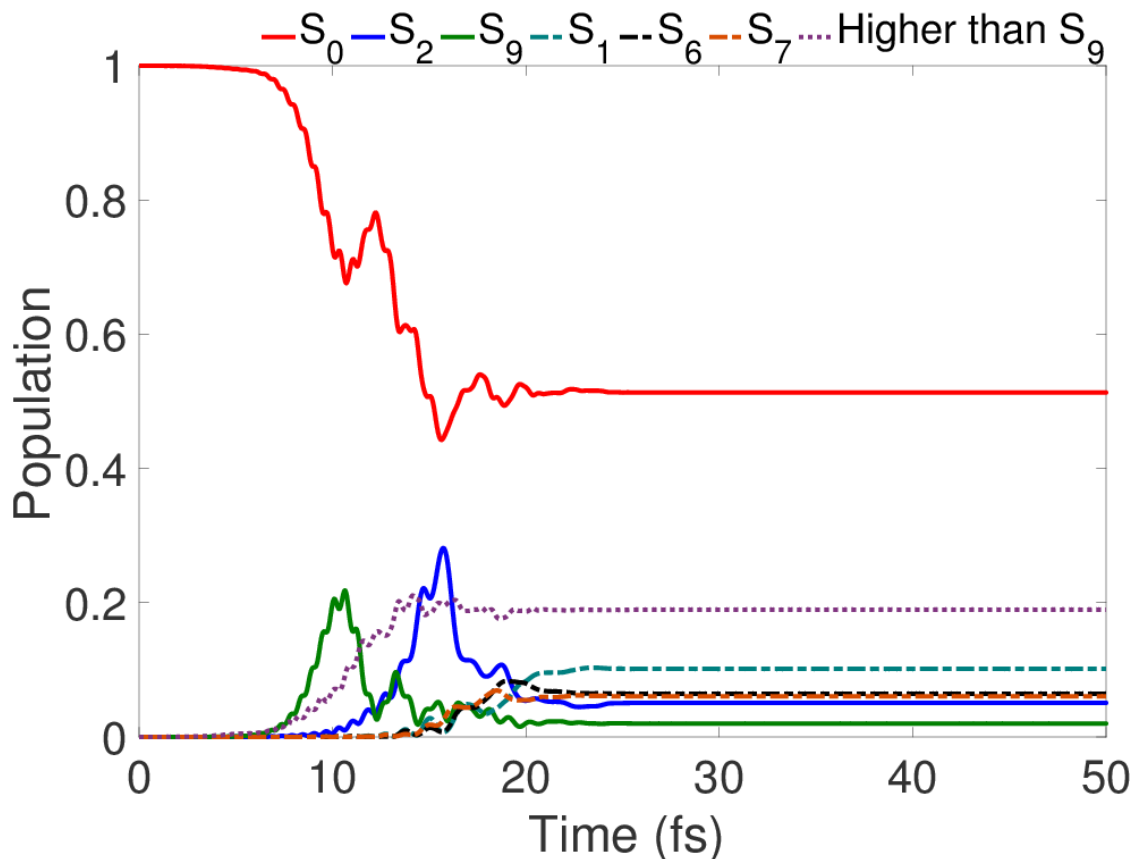


Figure D1. The electronic state populations as a function of time for decacene (TD-CISNO-CASCI(12,12)/6-31G(d)) in 10 fs (FWHM) chirped pulses with $\beta = -0.256 \text{ fs}^{-2}$ and an intensity of $3 \times 10^{12} \text{ W/cm}^2$. Only populations of states up to S_9 that contain non-negligible population at the end of the simulation are shown. Note that S_9 in this active space corresponds to S_8 in the (10,10) active space used throughout this work. States that are dark with respect to the electronic ground state (S_1 , S_6 , and S_7) are shown with dashed lines. The sum of all population in states higher than S_9 is represented by a dotted purple line.

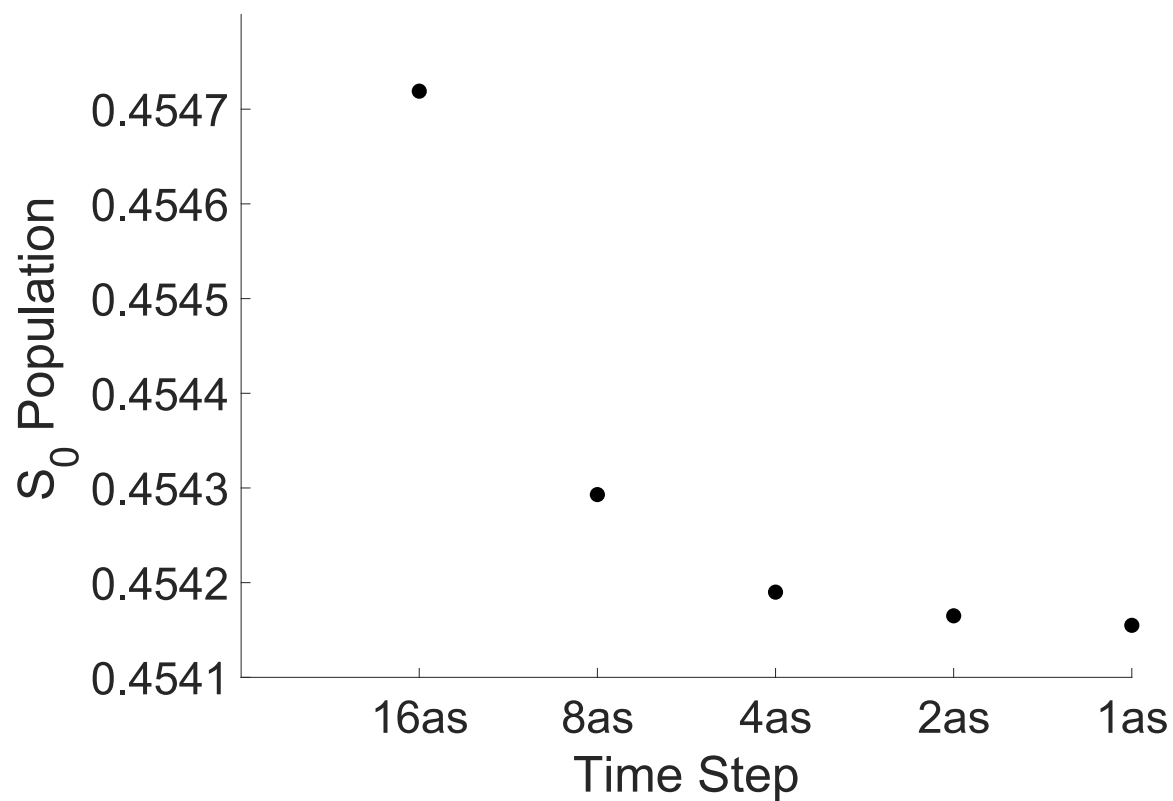


Figure D2. The final population on S₀ for a simulation of decacene with a (10,10) active space in a pulse with a chirp rate of -0.256 fs^{-2} as a function of time step. All other simulation parameters are as described in the main text.

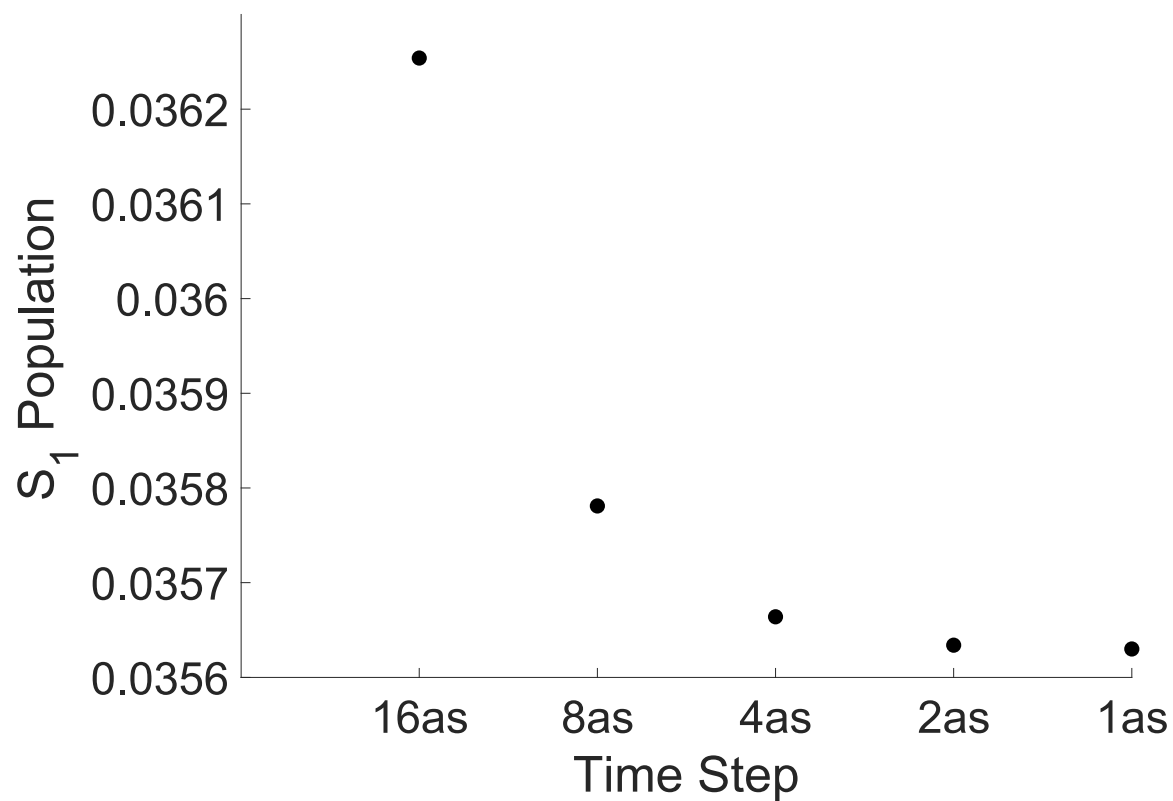


Figure D3. The final population on S₁ for a simulation of decacene with a (10,10) active space in a pulse with a chirp rate of -0.256 fs^{-2} as a function of time step. All other simulation parameters are as described in the main text.

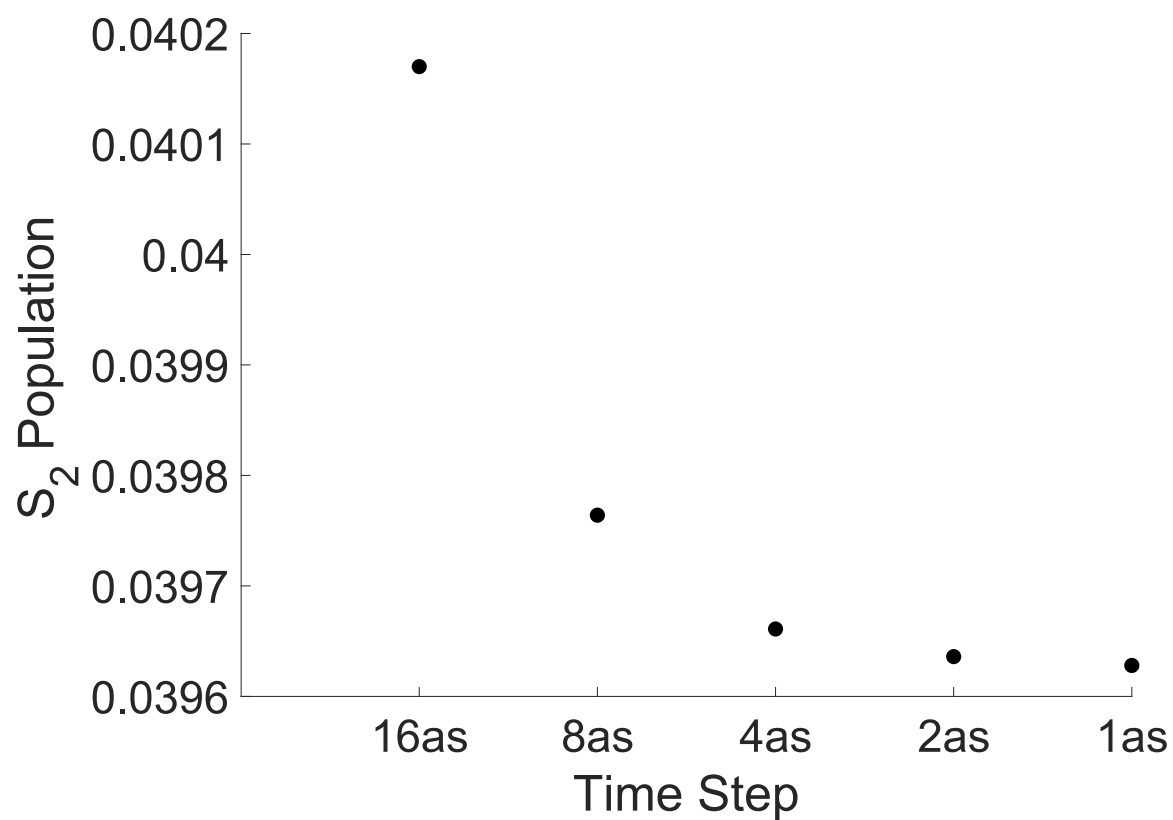


Figure D4. The final population on S₂ for a simulation of decacene with a (10,10) active space in a pulse with a chirp rate of -0.256 fs^{-2} as a function of time step. All other simulation parameters are as described in the main text.

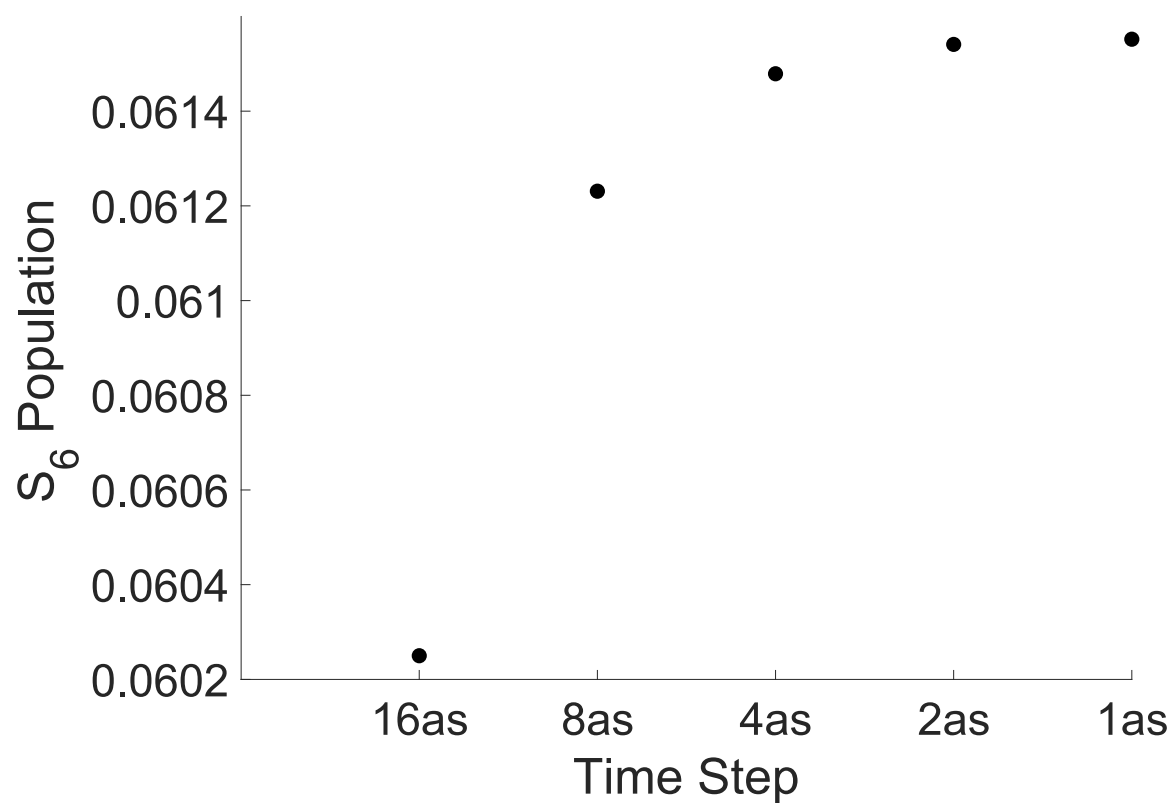


Figure D5. The final population on S₆ for a simulation of decacene with a (10,10) active space in a pulse with a chirp rate of -0.256 fs^{-2} as a function of time step. All other simulation parameters are as described in the main text.

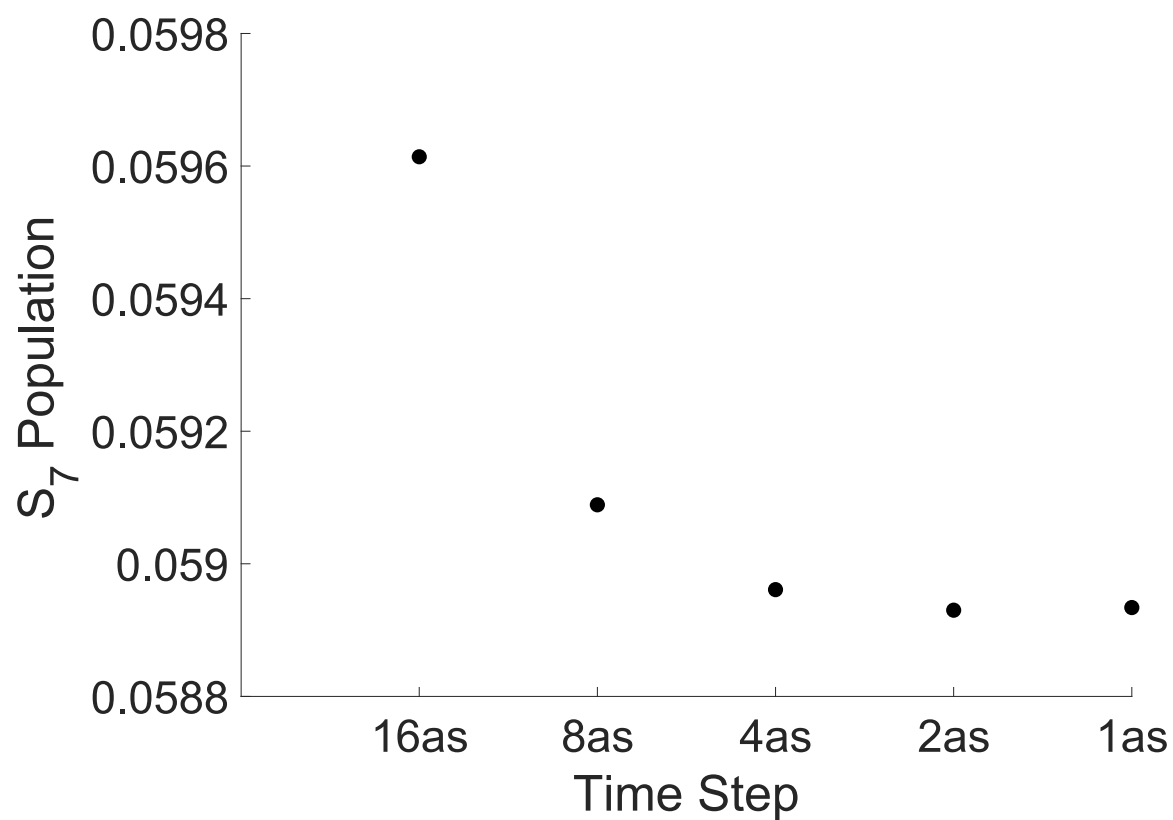


Figure D6. The final population on S₇ for a simulation of decacene with a (10,10) active space in a pulse with a chirp rate of -0.256 fs^{-2} as a function of time step. All other simulation parameters are as described in the main text.

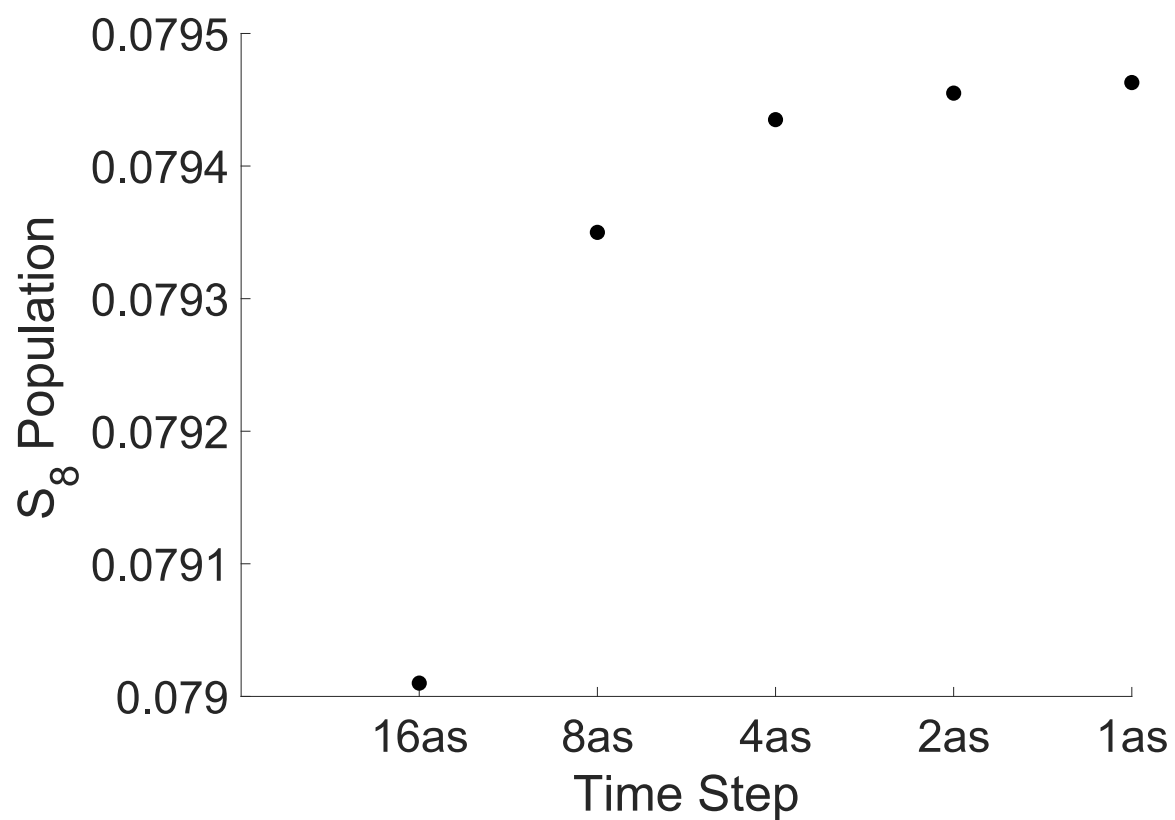


Figure D7. The final population on S₈ for a simulation of decacene with a (10,10) active space in a pulse with a chirp rate of -0.256 fs^{-2} as a function of time step. All other simulation parameters are as described in the main text.

Geometries (in Angstrom)

Ethylene, B3LYP/6-31G**

C	-0.66500	0.00000	0.00000
C	0.66500	0.00000	0.00000
H	-1.23780	0.92380	0.00000
H	-1.23780	-0.92380	0.00000
H	1.23780	0.92380	0.00000
H	1.23780	-0.92380	0.00000

Decacene, UB3LYP/6-31G* singlet (from Hachmann, J.; Dorando, J. J.; Aviles, M.; Chan, G. K. L., The radical character of the acenes: A density matrix renormalization group study. *J. Chem. Phys.* **2007**, *127* (13), 134309.)

C	-12.286459	0.713204	0.000000
C	-12.286459	-0.713204	0.000000
H	-13.232858	-1.247136	0.000000
H	-13.232858	1.247136	0.000000
C	-11.104552	1.407441	0.000000
C	-11.104552	-1.407441	0.000000
C	-9.848699	0.724254	0.000000
C	-9.848699	-0.724254	0.000000
H	-11.102098	2.494931	0.000000
H	-11.102098	-2.494931	0.000000
C	-8.626957	1.405881	0.000000
C	-8.626957	-1.405881	0.000000
C	-7.395009	0.727344	0.000000
C	-7.395009	-0.727344	0.000000
H	-8.627386	2.494068	0.000000
H	-8.627386	-2.494068	0.000000
C	-6.158121	1.408266	0.000000
C	-6.158121	-1.408266	0.000000
C	-4.934211	0.730243	0.000000
C	-4.934211	-0.730243	0.000000
H	-6.158802	2.496330	0.000000
H	-6.158802	-2.496330	0.000000
C	-3.693580	1.409318	0.000000
C	-3.693580	-1.409318	0.000000
C	-2.468192	0.731552	0.000000
C	-2.468192	-0.731552	0.000000
H	-3.693840	2.497387	0.000000
H	-3.693840	-2.497387	0.000000
C	-1.231033	1.409431	0.000000
C	-1.231033	-1.409431	0.000000
C	-0.000005	0.731841	0.000000

C	-0.000005	-0.731841	0.000000
H	-1.231077	2.497521	0.000000
H	-1.231077	-2.497521	0.000000
C	1.231025	1.409431	0.000000
C	1.231025	-1.409431	0.000000
C	2.468184	0.731552	0.000000
C	2.468184	-0.731552	0.000000
H	1.231052	2.497521	0.000000
H	1.231052	-2.497521	0.000000
C	3.693573	1.409317	0.000000
C	3.693573	-1.409317	0.000000
C	4.934206	0.730244	0.000000
C	4.934206	-0.730244	0.000000
H	3.693823	2.497385	0.000000
H	3.693823	-2.497385	0.000000
C	6.158118	1.408263	0.000000
C	6.158118	-1.408263	0.000000
C	7.395010	0.727345	0.000000
C	7.395010	-0.727345	0.000000
H	6.158798	2.496327	0.000000
H	6.158798	-2.496327	0.000000
C	8.626961	1.405879	0.000000
C	8.626961	-1.405879	0.000000
C	9.848706	0.724254	0.000000
C	9.848706	-0.724254	0.000000
H	8.627398	2.494066	0.000000
H	8.627398	-2.494066	0.000000
C	11.104563	1.407439	0.000000
C	11.104563	-1.407439	0.000000
C	12.286471	0.713205	0.000000
C	12.286471	-0.713205	0.000000
H	11.102124	2.494928	0.000000
H	11.102124	-2.494928	0.000000
H	13.232869	1.247141	0.000000
H	13.232869	-1.247141	0.000000

REFERENCES

REFERENCES

1. Zewail, A. H. Femtochemistry: Atomic-scale dynamics of the chemical bond. *J. Phys. Chem. A* **2000**, *104*, 5660-5694.
2. Krausz, F.; Ivanov, M. Attosecond physics. *Rev. Mod. Phys.* **2009**, *81*, 163-234.
3. Lin, C. D.; Le, A. T.; Chen, Z. J.; Morishita, T.; Lucchese, R. Strong-field rescattering physics-self-imaging of a molecule by its own electrons. *J. Phys. B-At. Mol. Opt. Phys.* **2010**, *43*, 122001.
4. Popmintchev, T.; Chen, M. C.; Arpin, P.; Murnane, M. M.; Kapteyn, H. C. The attosecond nonlinear optics of bright coherent X-ray generation. *Nat. Photonics* **2010**, *4*, 822-832.
5. Koch, C. P.; Shapiro, M. Coherent Control of Ultracold Photoassociation. *Chem. Rev.* **2012**, *112*, 4928-4948.
6. Goings, J. J.; Lestrangle, P. J.; Li, X. S. Real-time time-dependent electronic structure theory. *WIREs Comput. Mol. Sci.* **2018**, *8*, e1341.
7. Li, X. S.; Tully, J. C.; Schlegel, H. B.; Frisch, M. J. Ab initio Ehrenfest dynamics. *J. Chem. Phys.* **2005**, *123*, 084106.
8. Jaeger, H. M.; Fischer, S.; Prezhdo, O. V. Decoherence-induced surface hopping. *J. Chem. Phys.* **2012**, *137*, 22A545.
9. Nguyen, T. S.; Parkhill, J. Nonadiabatic Dynamics for Electrons at Second-Order: Real-Time TDDFT and OSCF2. *J. Chem. Theory Comput.* **2015**, *11*, 2918-2924.
10. Tussupbayev, S.; Govind, N.; Lopata, K.; Cramer, C. J. Comparison of Real-Time and Linear-Response Time-Dependent Density Functional Theories for Molecular Chromophores Ranging from Sparse to High Densities of States. *J. Chem. Theory Comput.* **2015**, *11*, 1102-1109.
11. Runge, E.; Gross, E. K. U. DENSITY-FUNCTIONAL THEORY FOR TIME-DEPENDENT SYSTEMS. *Phys. Rev. Lett.* **1984**, *52*, 997-1000.
12. Bertsch, G. F.; Iwata, J. I.; Rubio, A.; Yabana, K. Real-space, real-time method for the dielectric function. *Phys. Rev. B* **2000**, *62*, 7998-8002.
13. Marques, M. A. L.; Gross, E. K. U. Time-dependent density functional theory. *Annu. Rev. Phys. Chem.* **2004**, *55*, 427-455.

14. Li, X. S.; Smith, S. M.; Markevitch, A. N.; Romanov, D. A.; Levis, R. J.; Schlegel, H. B. A time-dependent Hartree-Fock approach for studying the electronic optical response of molecules in intense fields. *Phys. Chem. Chem. Phys.* **2005**, *7*, 233-239.
15. Cheng, C. L.; Evans, J. S.; Van Voorhis, T. Simulating molecular conductance using real-time density functional theory. *Phys. Rev. B* **2006**, *74*, 155112.
16. Chen, H. N.; Ratner, M. A.; Schatz, G. C. Time-Dependent Theory of the Rate of Photo-induced Electron Transfer. *J. Phys. Chem. C* **2011**, *115*, 18810-18821.
17. De Giovannini, U.; Brunetto, G.; Castro, A.; Walkenhorst, J.; Rubio, A. Simulating Pump-Probe Photoelectron and Absorption Spectroscopy on the Attosecond Timescale with Time-Dependent Density Functional Theory. *Chemphyschem* **2013**, *14*, 1363-1376.
18. Ding, F. Z.; Guidez, E. B.; Aikens, C. M.; Li, X. S. Quantum coherent plasmon in silver nanowires: A real-time TDDFT study. *J. Chem. Phys.* **2014**, *140*, 244705.
19. Falke, S. M.; Rozzi, C. A.; Brida, D.; Maiuri, M.; Amato, M.; Sommer, E.; De Sio, A.; Rubio, A.; Cerullo, G.; Molinari, E.; Lienau, C. Coherent ultrafast charge transfer in an organic photovoltaic blend. *Science* **2014**, *344*, 1001-1005.
20. Nguyen, T. S.; Parkhill, J. Nonradiative Relaxation in Real-Time Electronic Dynamics OSCF2: Organolead Triiodide Perovskite. *J. Phys. Chem. A* **2016**, *120*, 6880-6887.
21. Fuks, J. I.; Helbig, N.; Tokatly, I. V.; Rubio, A. Nonlinear phenomena in time-dependent density-functional theory: What Rabi oscillations can teach us. *Phys. Rev. B* **2011**, *84*, 075107.
22. Habenicht, B. F.; Tani, N. P.; Provorse, M. R.; Isborn, C. M. Two-electron Rabi oscillations in real-time time-dependent density-functional theory. *J. Chem. Phys.* **2014**, *141*, 184112.
23. Helbig, N.; Fuks, J. I.; Tokatly, I. V.; Appel, H.; Gross, E. K. U.; Rubio, A. Time-dependent density-functional and reduced density-matrix methods for few electrons: Exact versus adiabatic approximations. *Chem. Phys.* **2011**, *391*, 1-10.
24. Provorse, M. R.; Habenicht, B. F.; Isborn, C. M. Peak-Shifting in Real-Time Time-Dependent Density Functional Theory. *J. Chem. Theory Comput.* **2015**, *11*, 4791-4802.
25. Fuks, J. I.; Luo, K.; Sandoval, E. D.; Maitra, N. T. Time-Resolved Spectroscopy in Time-Dependent Density Functional Theory: An Exact Condition. *Phys. Rev. Lett.* **2015**, *114*, 183002.
26. Ruggenthaler, M.; Bauer, D. Rabi Oscillations and Few-Level Approximations in Time-Dependent Density Functional Theory. *Phys. Rev. Lett.* **2009**, *102*, 233001.

27. Elliott, P.; Fuks, J. I.; Rubio, A.; Maitra, N. T. Universal Dynamical Steps in the Exact Time-Dependent Exchange-Correlation Potential. *Phys. Rev. Lett.* **2012**, *109*, 266404.
28. Fuks, J. I.; Elliott, P.; Rubio, A.; Maitra, N. T. Dynamics of Charge-Transfer Processes with Time-Dependent Density Functional Theory. *J. Phys. Chem. Lett.* **2013**, *4*, 735-739.
29. Provorse, M. R.; Isborn, C. M. Electron dynamics with real-time time-dependent density functional theory. *Int. J. Quantum Chem.* **2016**, *116*, 739-749.
30. Cederbaum, L. S.; Zobeley, J. Ultrafast charge migration by electron correlation. *Chem. Phys. Lett.* **1999**, *307*, 205-210.
31. Rohringer, N.; Gordon, A.; Santra, R. Configuration-interaction-based time-dependent orbital approach for ab initio treatment of electronic dynamics in a strong optical laser field. *Phys. Rev. A* **2006**, *74*, 043420.
32. Krause, P.; Klamroth, T.; Saalfrank, P. Molecular response properties from explicitly time-dependent configuration interaction methods. *J. Chem. Phys.* **2007**, *127*, 034107.
33. Schlegel, H. B.; Smith, S. M.; Li, X. S. Electronic optical response of molecules in intense fields: Comparison of TD-HF, TD-CIS, and TD-CIS(D) approaches. *J. Chem. Phys.* **2007**, *126*, 244110.
34. Greenman, L.; Ho, P. J.; Pabst, S.; Kamarchik, E.; Mazziotti, D. A.; Santra, R. Implementation of the time-dependent configuration-interaction singles method for atomic strong-field processes. *Phys. Rev. A* **2010**, *82*, 023406.
35. Pabst, S.; Greenman, L.; Ho, P. J.; Mazziotti, D. A.; Santra, R. Decoherence in Attosecond Photoionization. *Phys. Rev. Lett.* **2011**, *106*, 053003.
36. Sonk, J. A.; Caricato, M.; Schlegel, H. B. TD-CI Simulation of the Electronic Optical Response of Molecules in Intense Fields: Comparison of RPA, CIS, CIS(D), and EOM-CCSD. *J. Phys. Chem. A* **2011**, *115*, 4678-4690.
37. Ulusoy, I. S.; Nest, M. Correlated Electron Dynamics: How Aromaticity Can Be Controlled. *J. Am. Chem. Soc.* **2011**, *133*, 20230-20236.
38. Hochstuhl, D.; Bonitz, M. Time-dependent restricted-active-space configuration-interaction method for the photoionization of many-electron atoms. *Phys. Rev. A* **2012**, *86*, 053424.
39. Luppi, E.; Head-Gordon, M. Computation of high-harmonic generation spectra of H-2 and N-2 in intense laser pulses using quantum chemistry methods and time-dependent density functional theory. *Mol. Phys.* **2012**, *110*, 909-923.

40. Bauch, S.; Sorensen, L. K.; Madsen, L. B. Time-dependent generalized-active-space configuration-interaction approach to photoionization dynamics of atoms and molecules. *Phys. Rev. A* **2014**, *90*, 062508.
41. Nguyen-Dang, T. T.; Couture-Bienvenue, E.; Viau-Trudel, J.; Sainjon, A. Time-dependent quantum chemistry of laser driven many-electron molecules. *J. Chem. Phys.* **2014**, *141*, 244116.
42. Schonborn, J. B.; Saalfrank, P.; Klamroth, T. Controlling the high frequency response of H-2 by ultra-short tailored laser pulses: A time-dependent configuration interaction study. *J. Chem. Phys.* **2016**, *144*, 044301.
43. White, A. F.; Heide, C. J.; Saalfrank, P.; Head-Gordon, M.; Luppi, E. Computation of high-harmonic generation spectra of the hydrogen molecule using time-dependent configuration-interaction. *Mol. Phys.* **2016**, *114*, 947-956.
44. Lestrangle, P. J.; Hoffmann, M. R.; Li, X. Time-Dependent Configuration Interaction Using the Graphical Unitary Group Approach: Nonlinear Electric Properties. *Adv. Quant. Chem.* **2018**, *76*, 295-313.
45. Breidbach, J.; Cederbaum, L. S. Migration of holes: Numerical algorithms and implementation. *J. Chem. Phys.* **2007**, *126*, 034101.
46. Miyagi, H.; Madsen, L. B. Time-dependent restricted-active-space self-consistent-field theory for laser-driven many-electron dynamics. *Phys. Rev. A* **2013**, *87*, 062511.
47. Miyagi, H.; Madsen, L. B. Time-dependent restricted-active-space self-consistent-field theory for laser-driven many-electron dynamics. II. Extended formulation and numerical analysis. *Phys. Rev. A* **2014**, *89*, 063416.
48. Sato, T.; Ishikawa, K. L.; Brezinova, I.; Lackner, F.; Nagele, S.; Burgdorfer, J. Time-dependent complete-active-space self-consistent-field method for atoms: Application to high-order harmonic generation. *Phys. Rev. A* **2016**, *94*, 023405.
49. Huber, C.; Klamroth, T. Explicitly time-dependent coupled cluster singles doubles calculations of laser-driven many-electron dynamics. *J. Chem. Phys.* **2011**, *134*, 054113.
50. Sonk, J. A.; Schlegel, H. B. TD-CI Simulation of the Electronic Optical Response of Molecules in Intense Fields II: Comparison of DFT Functionals and EOM-CCSD. *J. Phys. Chem. A* **2011**, *115*, 11832-11840.
51. Kvaal, S. Ab initio quantum dynamics using coupled-cluster. *J. Chem. Phys.* **2012**, *136*, 194109.

52. Nascimento, D. R.; DePrince, A. E. Linear Absorption Spectra from Explicitly Time-Dependent Equation-of-Motion Coupled-Cluster Theory. *J. Chem. Theory Comput.* **2016**, *12*, 5834-5840.
53. Nascimento, D. R.; DePrince, A. E. Simulation of Near-Edge X-ray Absorption Fine Structure with Time Dependent Equation-of-Motion Coupled-Cluster Theory. *J. Phys. Chem. Lett.* **2017**, *8*, 2951-2957.
54. Olsen, J.; Roos, B. O.; Jorgensen, P.; Jensen, H. J. A. DETERMINANT BASED CONFIGURATION-INTERACTION ALGORITHMS FOR COMPLETE AND RESTRICTED CONFIGURATION-INTERACTION SPACES. *J. Chem. Phys.* **1988**, *89*, 2185-2192.
55. Roos, B. NEW METHOD FOR LARGE-SCALE CI CALCULATIONS. *Chem. Phys. Lett.* **1972**, *15*, 153-159.
56. Sherrill, C. D.; Schaefer, H. F., The configuration interaction method: Advances in highly correlated approaches. In *Advances in Quantum Chemistry, Vol 34*, Lowdin, P. O.; Sabin, J. R.; Zerner, M. C.; Brandas, E., Eds. Elsevier Academic Press Inc: San Diego, 1999; Vol. 34, pp 143-269.
57. Kormann, K.; Holmgren, S.; Karlsson, H. O. Accurate time propagation for the Schrodinger equation with an explicitly time-dependent Hamiltonian. *J. Chem. Phys.* **2008**, *128*, 184101.
58. Leforestier, C.; Bisseling, R. H.; Cerjan, C.; Feit, M. D.; Friesner, R.; Guldborg, A.; Hammerich, A.; Jolicard, G.; Karrlein, W.; Meyer, H. D.; Lipkin, N.; Roncero, O.; Kosloff, R. A Comparison of Different Propagation Schemes for the Time-Dependent Schrodinger-Equation. *J. Comput. Phys.* **1991**, *94*, 59-80.
59. Blanes, S.; Casas, F.; Murua, A. Symplectic splitting operator methods for the time-dependent Schrodinger equation. *J. Chem. Phys.* **2006**, *124*, 234105.
60. Chen, R. Q.; Guo, H. The Chebyshev propagator for quantum systems. *Comput. Phys. Commun.* **1999**, *119*, 19-31.
61. Gray, S. K.; Manolopoulos, D. E. Symplectic integrators tailored to the time-dependent Schrodinger equation. *J. Chem. Phys.* **1996**, *104*, 7099-7112.
62. Knowles, P. J.; Handy, N. C. A NEW DETERMINANT-BASED FULL CONFIGURATION-INTERACTION METHOD. *Chem. Phys. Lett.* **1984**, *111*, 315-321.
63. Harrison, R. J.; Zarrabian, S. AN EFFICIENT IMPLEMENTATION OF THE FULL-CI METHOD USING AN (N-2)-ELECTRON PROJECTION SPACE. *Chem. Phys. Lett.* **1989**, *158*, 393-398.

64. Zarrabian, S.; Sarma, C. R.; Paldus, J. VECTORIZABLE APPROACH TO MOLECULAR CI PROBLEMS USING DETERMINANTAL BASIS. *Chem. Phys. Lett.* **1989**, *155*, 183-188.
65. Bendazzoli, G. L.; Evangelisti, S. A VECTOR AND PARALLEL FULL CONFIGURATION-INTERACTION ALGORITHM. *J. Chem. Phys.* **1993**, *98*, 3141-3150.
66. Fales, B. S.; Levine, B. G. Nanoscale Multireference Quantum Chemistry: Full Configuration Interaction on Graphical Processing Units. *J. Chem. Theory Comput.* **2015**, *11*, 4708-4716.
67. Titov, A. V.; Ufimtsev, I. S.; Luehr, N.; Martinez, T. J. Generating Efficient Quantum Chemistry Codes for Novel Architectures. *J. Chem. Theory Comput.* **2013**, *9*, 213-221.
68. Ufimtsev, I. S.; Martinez, T. J. Quantum Chemistry on Graphical Processing Units. 3. Analytical Energy Gradients, Geometry Optimization, and First Principles Molecular Dynamics. *J. Chem. Theory Comput.* **2009**, *5*, 2619-2628.
69. Walser, M. W.; Keitel, C. H.; Scrinzi, A.; Brabec, T. High harmonic generation beyond the electric dipole approximation. *Phys. Rev. Lett.* **2000**, *85*, 5082-5085.
70. Kylstra, N. J.; Worthington, R. A.; Patel, A.; Knight, P. L.; de Aldana, J. R. V.; Roso, L. Breakdown of stabilization of atoms interacting with intense, high-frequency laser pulses. *Phys. Rev. Lett.* **2000**, *85*, 1835-1838.
71. Goings, J. J.; Kasper, J. M.; Egidi, F.; Sun, S. C.; Li, X. S. Real time propagation of the exact two component time-dependent density functional theory. *J. Chem. Phys.* **2016**, *145*, 104107.
72. Hachmann, J.; Dorando, J. J.; Aviles, M.; Chan, G. K. L. The radical character of the acenes: A density matrix renormalization group study. *J. Chem. Phys.* **2007**, *127*, 134309.
73. Jiang, D. E.; Dai, S. Electronic ground state of higher acenes. *J. Phys. Chem. A* **2008**, *112*, 332-335.
74. Chai, J. D. Density functional theory with fractional orbital occupations. *J. Chem. Phys.* **2012**, *136*, 154104.
75. Shu, Y. A.; Hohenstein, E. G.; Levine, B. G. Configuration interaction singles natural orbitals: An orbital basis for an efficient and size intensive multireference description of electronic excited states. *J. Chem. Phys.* **2015**, *142*, 024102.

76. Fales, B. S.; Shu, Y. N.; Levine, B. G.; Hohenstein, E. G. Complete active space configuration interaction from state-averaged configuration interaction singles natural orbitals: Analytic first derivatives and derivative coupling vectors. *J. Chem. Phys.* **2017**, *147*, 094104.
77. Potts, D. M.; Taylor, C. M.; Chaudhuri, R. K.; Freed, K. F. The improved virtual orbital-complete active space configuration interaction method, a "packageable" efficient ab initio many-body method for describing electronically excited states. *J. Chem. Phys.* **2001**, *114*, 2592-2600.
78. Abstracts of Papers of the American Chemical Society Slavicek, P.; Martinez, T. J. Ab initio floating occupation molecular orbital-complete active space configuration interaction: An efficient approximation to CASSCF. *J. Chem. Phys.* **2010**, *132*, 234102.
79. Lu, Z.; Matsika, S. High-Multiplicity Natural Orbitals in Multireference Configuration Interaction for Excited States. *J. Chem. Theory Comput.* **2012**, *8*, 509-517.

CHAPTER 6 ANALYTICAL EXPRESSION FOR A MOLECULE-CENTERED COMPLEX ABSORBING POTENTIAL USING GAUSSIAN BASIS SETS

6.1 Introduction

Experimental techniques for generating ultrafast, intense laser pulses open up the possibilities of new spectroscopic methods with unprecedented spatial and temporal resolution. For example, laser-induced electron diffraction (LIED) experiments have reached a few femtosecond and sub-angstrom resolutions, allowing the real-time observations of the structural change of a single chemical bond.¹⁻⁵ Another example is orbital tomography, which reaches similar resolutions for electron dynamics.⁶ In addition, nonlinear optical phenomena such as high harmonic generation (HHG)⁷⁻⁸ and above-threshold ionization (ATI)⁹ are now routinely explored. With HHG, extreme ultraviolet (XUV) or soft x-ray attosecond pulses have been made possible and have been applied to study electron dynamics in atoms, molecules and solids.¹⁰⁻¹⁴

Despite the advancements in the experimental methods, the theoretical description of the microscopic mechanisms for ultrafast dynamics driven by intense lasers remain challenging. Various real-time time-dependent methods for electron dynamics under external fields have been developed by numerically propagating electronic wavefunctions or electron densities.¹⁵ Among them, real-time time-dependent density functional theory (RT-TDDFT) is one of the most popular methods because of its balance treatment of electron correlation with favorable computational cost. However, the exact density functional form is unknown and approximated functionals are used, which make them inaccurate or inapplicable in many applications. On the other hand, wave function-based methods can be systematically improved to include both dynamical and static electron correlation. There are many wave function-based time-dependent electronic structure methods that have been developed including time-dependent configuration interaction based methods (TD-CIS, TD-CISD, ... etc.),¹⁶⁻²⁹ time-dependent multiconfigurational self-consistent field methods (TD-MCSCF),³⁰⁻³² and time-dependent equation-of-motion coupled cluster methods (TD-EOM-CC).³³⁻³⁴ Although higher accuracy for a higher tier method, the computational cost limits their applications to large systems. Recently, we have developed a TD-CASCI method based on a direct CI scheme, which can be accelerated by graphics processing

units (GPUs).³⁵ The approach is promising for large systems and systems where static electron correlation is important. By extending to consider all single excitations from a multiconfigurational reference state (a CASCI state),³⁶ the method becomes the time-dependent multireference configuration interaction singles (TD-MRCIS) method, which is able to describe ionization processes via high single excitations. Another advantage of the TD-MRCIS method is that it restores part of the dynamical electron correlation missing in CASCI.

In this study, we are looking to further develop a method in conjunction with the TD-MRCIS approach for simulating electron dynamics under intense laser radiation. The electrons in a system can be driven to move far away from their original locations under a strong laser field. Since finite Gaussian basis sets are used in our TD-MRCIS method, the electrons may reach the boundary of the basis in a simulation, resulting in unphysical events such as reflection due to the insufficiency of the basis sets. To include adequate basis sets for all high-lying Rydberg states as well as the continuum states is computationally infeasible. One route to remedy these unphysical events and to treat the ionization processes without adding excessive diffuse basis functions is to place an absorbing potential on a defined boundary of the system. When an electron arrives at the boundary, it will be absorbed by the potential and considered ionized. The complex absorbing potential (CAP) has been developed to remove unphysical effects from finite boundaries when numerically solving the time-dependent Schrodinger equation.³⁷⁻⁴³ CAP has been applied to study the photoionization processes with TD-CI methods.^{19, 44-45} For atom-centered Gaussian basis sets, a similar heuristic model that treats electrons in the ionizing states which have energies above the ionization potential with an energy-dependent lifetime to account for the loss of electrons.⁴⁶⁻⁴⁷ In addition, the equation-of-motion coupled cluster methods have been coupled to CAP for studying resonance states.⁴⁸⁻⁴⁹ Recently, Schlegel et al. developed a numerical scheme to add CAP to atom-centered gaussian basis sets.⁴⁴ These methods have been used for studying HHG^{47, 50} and charge resonance-enhanced ionization (CREI)⁴⁴ among other processes.

The goal of this study is to develop an analytical form of the CAP which can be evaluated efficiently. In conjunction with the TD-MRCIS method, we aim at an efficient approach for simulating electron dynamics under intense laser fields in large systems. In order to reach this

goal, we consider a molecule-centered CAP as shown in Figure 6.1. The CAP is zero within the boundary and has quadratic form beyond the boundary. The derivations of the CAP are presented in the method section.

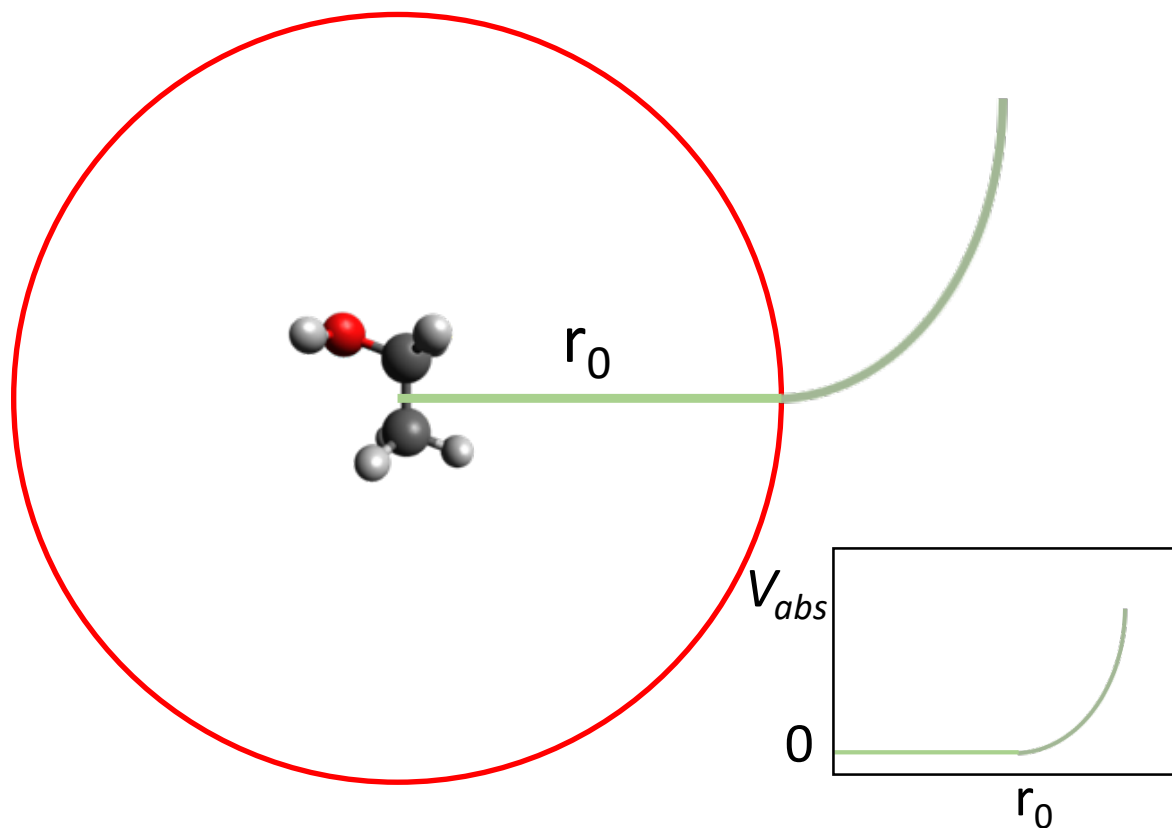


Figure 6.1. A representation of the molecule-centered complex absorbing potential developed in this work. The radius, r_0 , from the center of the molecule is defined for the boundary (shown in red). Beyond the boundary, a quadratic form of absorbing potential is applied (shown in the green line and in the inserted figure). Within the boundary, the potential is zero.

6.2 Method

As in the TD-CASCI method (Chapter 5), our goal is to solve the time-dependent electronic Schrodinger equation with TD-CI expansion,

$$i\dot{\mathbf{C}}(t) = \mathbf{H}(t)\mathbf{C}(t), \quad (1)$$

where $\mathbf{C}(t)$ is the time-dependent CI vector and $\mathbf{H}(t)$ is the time-dependent Hamiltonian. To include the CAP, we added a complex potential to the Hamiltonian

$$\mathbf{H}(t) = \mathbf{H}_0 - \hat{\boldsymbol{\mu}} \cdot \mathbf{d}E(t) - i\mathbf{V}_{abs}, \quad (1)$$

where the \mathbf{H}_0 is the time-independent CI Hamiltonian, $-\hat{\boldsymbol{\mu}} \cdot \mathbf{d}E(t)$ is the applied electric field described in the dipole approximation, and the last term $-i\mathbf{V}_{abs}$ is the complex absorbing potential, the matrix element of which can be written as

$$V_{ij} = \langle i | \hat{V}_{abs} | j \rangle = \int_0^\infty \boldsymbol{\chi}_i(\mathbf{r}) \hat{V}_{abs}(\mathbf{r}) \boldsymbol{\chi}_j(\mathbf{r}) d\mathbf{r}. \quad (2)$$

By adding the CAP, the Hamiltonian is no longer a Hermitian matrix, thus the conservation of the norm of the wave functions will not be guaranteed. When the electron travels to the defined boundary, the CAP will annihilate the electronic wavefunction that touches it. In this study, we are looking for a CAP with a quadratic form beyond the boundary,

$$\hat{V}_{abs}(\mathbf{r}) = b(\mathbf{r} - \mathbf{r}_0)^2 \text{ for } r > r_0, \quad V_{abs} = 0 \text{ for } r \leq r_0. \quad (3)$$

In equation (4), the parameter \mathbf{r}_0 is the radius of the CAP from the center of the molecule and the parameter b controls the curvature of the CAP. Thus, we define a molecule-centered CAP with a spherical boundary (Figure 6.1). $\boldsymbol{\chi}_i(\mathbf{r})$ and $\boldsymbol{\chi}_j(\mathbf{r})$ in equation (3) are molecule-centered diffused Gaussian functions which we introduce to the system to describe ionization processes. The low-lying valence electrons that are bounded to the molecules are treated with normal atom-centered basis sets. Given their limited spatial extent, the valence electrons are not annihilated by the CAP. The radius r_0 can be adjusted to make sure all of the atom-centered basis functions decay to near zero at the boundary of CAP. Molecule-centered diffuse functions can then be added to describe the higher-lying states. With the gaussian basis functions, equation (3) can be written as

$$V_{ij} = \int_{r_0}^{\infty} \int_0^{\pi} \int_0^{2\pi} b(r-r_0)^2 x_A^i y_A^j z_A^k e^{-ar^2} r^2 \sin \theta dr d\theta d\phi. \quad (4)$$

To integrate equation (5), we rewrite the Cartesian components in spherical coordinates,

$$x_A^i y_A^j z_A^k = (r \sin \theta \cos \phi)^i (r \sin \theta \sin \phi)^j (r \cos \theta)^k. \quad (5)$$

Then the integration of equation (5) can be separated into three contributions,

$$F_{\theta} = \int_0^{\pi} (\sin \theta)^{i+j+1} (\cos \theta)^k d\theta \quad (6)$$

$$F_{\phi} = \int_0^{2\pi} (\cos \phi)^i (\sin \phi)^j d\phi \quad (7)$$

$$F_r = \int_{r_0}^{\infty} r^{i+j+k+2} (r-r_0)^2 e^{-ar^2} dr. \quad (8)$$

These three terms can be integrated analytically, and the results can be expressed as

$$F_{\theta} = \frac{(1+(-1)^k) \Gamma\left[\frac{1}{2}(2+i+j)\right] \Gamma\left[\frac{1+k}{2}\right]}{2\Gamma\left[\frac{1}{2}(3+i+j+k)\right]} \quad (9)$$

$$F_{\phi} = \frac{(1+(-1)^i)(1+(-1)^{i+j}) \Gamma\left[\frac{1+i}{2}\right] \Gamma\left[\frac{1+j}{2}\right]}{2\Gamma\left[\frac{1}{2}(2+i+j)\right]} \quad (10)$$

$$F_r = \frac{a^{\frac{(-i-j-k-5)}{2}}}{e^{ar_0^2} (2(i+j+k+3))} \left\{ -2a^{\frac{(i+j+k+5)}{2}} r_0^{i+j+k+5} - 2\sqrt{a} r_0 e^{ar_0^2} (i+j+k+3) \Gamma \left[\frac{1}{2}(i+j+k+4), ar_0^2 \right] \right. \\ \left. + e^{ar_0^2} (2ar_0^2 + i+j+k+3) \Gamma \left[\frac{1}{2}(i+j+k+5), ar_0^2 \right] \right\} \quad (11)$$

We implemented equations (10), (11), and (12) for the evaluation of the matrix elements of the CAP into the TeraChem software package.

In addition, since the imaginary potential breaks the symplectic symmetry of the Schrodinger equation for the TD-CI method, the previously implemented symplectic split operator integrator becomes inappropriate for applications requiring the CAP. Instead, we implemented a fourth order Runge-Kutta (RK4) integrator for TD-CI propagation with the CAP. The RK4 algorithm is implemented in its standard form, as shown in the following,

$$\mathbf{k}_1 = \Delta t \frac{\mathbf{H}(t)}{i\hbar} \mathbf{C}(t) \quad (12)$$

$$\mathbf{k}_2 = \Delta t \frac{\mathbf{H}(t + \frac{\Delta t}{2})}{i\hbar} \left(\mathbf{C}(t) + \frac{\mathbf{k}_1}{2} \right) \quad (13)$$

$$\mathbf{k}_3 = \Delta t \frac{\mathbf{H}(t + \frac{\Delta t}{2})}{i\hbar} \left(\mathbf{C}(t) + \frac{\mathbf{k}_2}{2} \right) \quad (14)$$

$$\mathbf{k}_4 = \Delta t \frac{\mathbf{H}(t + \Delta t)}{i\hbar} (\mathbf{C}(t) + \mathbf{k}_3) \quad (15)$$

$$\mathbf{C}(t + \Delta t) = \mathbf{C}(t) + \frac{\mathbf{k}_1}{6} + \frac{\mathbf{k}_2}{3} + \frac{\mathbf{k}_3}{3} + \frac{\mathbf{k}_4}{6}. \quad (16)$$

In order to verify our derivations and the implementation of the evaluation of matrix elements V_{ij} , we considered an s shell Gaussian basis for a molecule-centered diffuse function. In this situation, the integration of the equation (7) and the equation (8) can be done by hand (where $i = j = k = 0$), giving values $F_\theta = 2$ and $F_\phi = 2\pi$. We can compare to the values

evaluating from our implementation in the TeraChem package using equation (10) and equation (11) to verify the derivations and our implementations. For the F_r term expressed in equation (12), we evaluate using Matlab and compare it to our implementations. We used a diffuse function with exponent $a = 0.0256$, and the CAP boundary is set to $r_0 = 20$ a.u.. For the angular parts, we got a value of $F_\theta F_\phi = 12.566371 = 4\pi$ from our TeraChem implementation, which suggests our derivations and implementations are correct for F_θ and F_ϕ . For the radius part, we got a value of $F_r = 1.18610403 \times 10^{-7}$ from our implementations and a value of $F_r = 1.18636726 \times 10^{-7}$ from the Matlab evaluation, which verified our implementations for the F_r . Coupling the efficient molecule-centered CAP approach to the TD-MRCIS method, we will be able to investigate electronic dynamics of atoms and molecules driven by strong light fields with the multireference configuration interaction level of theory in the near future.

REFERENCES

REFERENCES

1. Meckel, M.; Comtois, D.; Zeidler, D.; Staudte, A.; Pavicic, D.; Bandulet, H. C.; Pepin, H.; Kieffer, J. C.; Dorner, R.; Villeneuve, D. M.; Corkum, P. B., Laser-induced electron tunneling and diffraction. *Science* **2008**, *320*, 1478-1482.
2. Okunishi, M.; Niikura, H.; Lucchese, R. R.; Morishita, T.; Ueda, K., Extracting Electron-Ion Differential Scattering Cross Sections for Partially Aligned Molecules by Laser-Induced Rescattering Photoelectron Spectroscopy. *Phys Rev Lett* **2011**, *106*, 032027.
3. Pullen, M. G.; Wolter, B.; Le, A. T.; Baudisch, M.; Hemmer, M.; Senftleben, A.; Schroter, C. D.; Ullrich, J.; Moshhammer, R.; Lin, C. D.; Biegert, J., Imaging an aligned polyatomic molecule with laser-induced electron diffraction. *Nat Commun* **2015**, *6*, 7262.
4. Ray, D.; Ulrich, B.; Bocharova, I.; Maharjan, C.; Ranitovic, P.; Gramkow, B.; Magrakvelidze, M.; De, S.; Litvinyuk, I. V.; Le, A. T.; Morishita, T.; Lin, C. D.; Paulus, G. G.; Cocke, C. L., Large-angle electron diffraction structure in laser-induced rescattering from rare gases. *Phys Rev Lett* **2008**, *100*, 143002.
5. Xu, J. L.; Chen, Z. J.; Le, A. T.; Lin, C. D., Self-imaging of molecules from diffraction spectra by laser-induced rescattering electrons. *Phys Rev A* **2010**, *82*, 033403.
6. Haessler, S.; Caillat, J.; Salieres, P., Self-probing of molecules with high harmonic generation. *J Phys B-at Mol Opt* **2011**, *44*, 203001.
7. Lhuillier, A.; Balcou, P., High-Order Harmonic-Generation in Rare-Gases with a 1-Ps 1053-Nm Laser. *Phys Rev Lett* **1993**, *70*, 774-777.
8. Mcpherson, A.; Gibson, G.; Jara, H.; Johann, U.; Luk, T. S.; McIntyre, I. A.; Boyer, K.; Rhodes, C. K., Studies of Multiphoton Production of Vacuum Ultraviolet-Radiation in the Rare-Gases. *J Opt Soc Am B* **1987**, *4*, 595-601.
9. Agostini, P.; Fabre, F.; Mainfray, G.; Petite, G.; Rahman, N. K., Free-Free Transitions Following 6-Photon Ionization of Xenon Atoms. *Phys Rev Lett* **1979**, *42*, 1127-1130.
10. Calegari, F.; Ayuso, D.; Trabattoni, A.; Belshaw, L.; De Camillis, S.; Anumula, S.; Frassetto, F.; Poletto, L.; Palacios, A.; Decleva, P.; Greenwood, J. B.; Martin, F.; Nisoli, M., Ultrafast electron dynamics in phenylalanine initiated by attosecond pulses. *Science* **2014**, *346*, 336-339.
11. Cavalieri, A. L.; Muller, N.; Uphues, T.; Yakovlev, V. S.; Baltuska, A.; Horvath, B.; Schmidt, B.; Blumel, L.; Holzwarth, R.; Hendel, S.; Drescher, M.; Kleineberg, U.; Echenique, P. M.; Kienberger, R.; Krausz, F.; Heinzmann, U., Attosecond spectroscopy in condensed matter. *Nature* **2007**, *449*, 1029-1032.

12. Drescher, M.; Hentschel, M.; Kienberger, R.; Uiberacker, M.; Yakovlev, V.; Scrinzi, A.; Westerwalbesloh, T.; Kleineberg, U.; Heinzmann, U.; Krausz, F., Time-resolved atomic inner-shell spectroscopy. *Nature* **2002**, *419*, 803-807.
13. Lepine, F.; Ivanov, M. Y.; Vrakking, M. J. J., Attosecond molecular dynamics: fact or fiction? *Nat Photonics* **2014**, *8*, 195-204.
14. Schiffrin, A.; Paasch-Colberg, T.; Karpowicz, N.; Apalkov, V.; Gerster, D.; Muhlbrandt, S.; Korbman, M.; Reichert, J.; Schultze, M.; Holzner, S.; Barth, J. V.; Kienberger, R.; Ernstorfer, R.; Yakovlev, V. S.; Stockman, M. I.; Krausz, F., Optical-field-induced current in dielectrics. *Nature* **2013**, *493*, 70-74.
15. Goings, J. J.; Lestrangle, P. J.; Li, X. S., Real-time time-dependent electronic structure theory. *Wires Comput Mol Sci* **2018**, *8*, e1341.
16. Schlegel, H. B.; Smith, S. M.; Li, X. S., Electronic optical response of molecules in intense fields: Comparison of TD-HF, TD-CIS, and TD-CIS(D) approaches. *J Chem Phys* **2007**, *126*, 244110.
17. Krause, P.; Klamroth, T.; Saalfrank, P., Molecular response properties from explicitly time-dependent configuration interaction methods. *J Chem Phys* **2007**, *127*, 034107.
18. Rohringer, N.; Gordon, A.; Santra, R., Configuration-interaction-based time-dependent orbital approach for ab initio treatment of electronic dynamics in a strong optical laser field. *Phys Rev A* **2006**, *74*, 043420.
19. Greenman, L.; Ho, P. J.; Pabst, S.; Kamarchik, E.; Mazziotti, D. A.; Santra, R., Implementation of the time-dependent configuration-interaction singles method for atomic strong-field processes. *Phys Rev A* **2010**, *82*, 023406.
20. Pabst, S.; Greenman, L.; Ho, P. J.; Mazziotti, D. A.; Santra, R., Decoherence in Attosecond Photoionization. *Phys Rev Lett* **2011**, *106*, 053003.
21. Sonk, J. A.; Caricato, M.; Schlegel, H. B., TD-CI Simulation of the Electronic Optical Response of Molecules in Intense Fields: Comparison of RPA, CIS, CIS(D), and EOM-CCSD. *J Phys Chem A* **2011**, *115*, 4678-4690.
22. Ulusoy, I. S.; Nest, M., Correlated Electron Dynamics: How Aromaticity Can Be Controlled. *J Am Chem Soc* **2011**, *133*, 20230-20236.
23. Hochstuhl, D.; Bonitz, M., Time-dependent restricted-active-space configuration-interaction method for the photoionization of many-electron atoms. *Phys Rev A* **2012**, *86*, 053424.

24. Luppi, E.; Head-Gordon, M., Computation of high-harmonic generation spectra of H-2 and N-2 in intense laser pulses using quantum chemistry methods and time-dependent density functional theory. *Mol Phys* **2012**, *110*, 909-923.
25. Bauch, S.; Sorensen, L. K.; Madsen, L. B., Time-dependent generalized-active-space configuration-interaction approach to photoionization dynamics of atoms and molecules. *Phys Rev A* **2014**, *90*, 062508.
26. Nguyen-Dang, T. T.; Couture-Bienvenue, E.; Viau-Trudel, J.; Sainjon, A., Time-dependent quantum chemistry of laser driven many-electron molecules. *J Chem Phys* **2014**, *141*, 244116.
27. Schonborn, J. B.; Saalfrank, P.; Klamroth, T., Controlling the high frequency response of H-2 by ultra-short tailored laser pulses: A time-dependent configuration interaction study. *J Chem Phys* **2016**, *144*, 044301.
28. White, A. F.; Heide, C. J.; Saalfrank, P.; Head-Gordon, M.; Luppi, E., Computation of high-harmonic generation spectra of the hydrogen molecule using time-dependent configuration-interaction. *Mol Phys* **2016**, *114*, 947-956.
29. Lestrangle, P. J.; Hoffmann, M. R.; Li, X. S., Time-Dependent Configuration Interaction Using the Graphical Unitary Group Approach: Nonlinear Electric Properties. *Adv Quantum Chem* **2018**, *76*, 295-313.
30. Miyagi, H.; Madsen, L. B., Time-dependent restricted-active-space self-consistent-field theory for laser-driven many-electron dynamics. *Phys Rev A* **2013**, *87*, 062511.
31. Miyagi, H.; Madsen, L. B., Time-dependent restricted-active-space self-consistent-field theory for laser-driven many-electron dynamics. II. Extended formulation and numerical analysis. *Phys Rev A* **2014**, *89*, 063416.
32. Sato, T.; Ishikawa, K. L.; Brezinova, I.; Lackner, F.; Nagele, S.; Burgdorfer, J., Time-dependent complete-active-space self-consistent-field method for atoms: Application to high-order harmonic generation. *Phys Rev A* **2016**, *94*, 023405.
33. Nascimento, D. R.; DePrince, A. E., Linear Absorption Spectra from Explicitly Time-Dependent Equation-of-Motion Coupled-Cluster Theory. *J Chem Theory Comput* **2016**, *12*, 5834-5840.
34. Nascimento, D. R.; DePrince, A. E., Simulation of Near-Edge X-ray Absorption Fine Structure with Time Dependent Equation-of-Motion Coupled-Cluster Theory. *J Phys Chem Lett* **2017**, *8*, 2951-2957.
35. Peng, W. T.; Fales, B. S.; Levine, B. G., Simulating Electron Dynamics of Complex Molecules with Time-Dependent Complete Active Space Configuration Interaction. *J Chem Theory Comput* **2018**, *14*, 4129-4138.

36. Fales, B. S.; Levine, B. G., unpublished results.
37. Kosloff, R.; Kosloff, D., Absorbing Boundaries for Wave-Propagation Problems. *J Comput Phys* **1986**, *63*, 363-376.
38. Neuhasuer, D.; Baer, M., The Time-Dependent Schrodinger-Equation - Application of Absorbing Boundary-Conditions. *J Chem Phys* **1989**, *90*, 4351-4355.
39. Child, M. S., Analysis of a Complex Absorbing Barrier. *Mol Phys* **1991**, *72*, 89-93.
40. Vibok, A.; Balintkurti, G. G., Parametrization of Complex Absorbing Potentials for Time-Dependent Quantum Dynamics. *J Phys Chem-Us* **1992**, *96*, 8712-8719.
41. Vibok, A.; Balintkurti, G. G., Reflection and Transmission of Waves by a Complex Potential - a Semiclassical Jeffreys-Wentzel-Kramers-Brillouin Treatment. *J Chem Phys* **1992**, *96*, 7615-7622.
42. Macias, D.; Brouard, S.; Muga, J. G., Optimization of Absorbing Potentials. *Chem Phys Lett* **1994**, *228*, 672-677.
43. Riss, U. V.; Meyer, H. D., Investigation on the reflection and transmission properties of complex absorbing potentials. *J Chem Phys* **1996**, *105*, 1409-1419.
44. Krause, P.; Sonk, J. A.; Schlegel, H. B., Strong field ionization rates simulated with time-dependent configuration interaction and an absorbing potential. *J Chem Phys* **2014**, *140*, 174113.
45. Krause, P.; Schlegel, H. B., Strong-field ionization rates of linear polyenes simulated with time-dependent configuration interaction with an absorbing potential. *J Chem Phys* **2014**, *141*, 174104
46. Klinkusch, S.; Saalfrank, P.; Klamroth, T., Laser-induced electron dynamics including photoionization: A heuristic model within time-dependent configuration interaction theory. *J Chem Phys* **2009**, *131*, 114304.
47. Luppi, E.; Head-Gordon, M., The role of Rydberg and continuum levels in computing high harmonic generation spectra of the hydrogen atom using time-dependent configuration interaction. *J Chem Phys* **2013**, *139*, 164121.
48. Jagau, T.-C.; Krylov, A. I., Complex absorbing potential equation-of-motion coupled-cluster method yields smooth and internally consistent potential energy surfaces and lifetimes for molecular resonances. *J Phys Chem Lett* **2014**, *5*, 3078-3085.
49. Ghosh, A.; Vaval, N.; Pal, S.; Bartlett, R. J., Complex absorbing potential based equation-of-motion coupled cluster method for the potential energy curve of CO₂⁻ anion. *J Chem Phys* **2014**, *141*, 4113.

50. White, A. F.; Heide, C. J.; Saalfrank, P.; Head-Gordon, M.; Luppi, E., Computation of high-harmonic generation spectra of the hydrogen molecule using time-dependent configuration-interaction. *Mol Phys* **2016**, *114*, 947-956.

CHAPTER 7 THE EHRENFEST MOLECULAR DYNAMICS IN CONJUNCTION WITH TIME-DEPENDENT CONFIGURATION INTERACTION ELECTRONIC WAVE FUNCTIONS

7.1 Introduction

Ab initio molecular dynamics (AIMD) methods model nuclear motion under the forces generated by electronic wave functions which are determined from ab initio quantum mechanical calculations on-the-fly. AIMD methods allow researchers to study chemical processes without prior knowledge of or extensive assumptions about the shape of the potential energy surfaces (PES). When the PES of multiple states are involved, the nonadiabatic effects need to be considered in the simulations. The ab initio multiple spawning (AIMS) method,¹⁻² surface hopping method³ and Ehrenfest dynamics⁴⁻⁶ are prevalent approaches for the study of such nonadiabatic dynamics. On the other hand, although the nonadiabatic AIMD methods for the low-lying excited states are well-developed, tools for calculating dynamics in high-lying excited states such as Rydberg and continuum states are less mature. Due to the dense manifold of adiabatic electronic states in these cases, conventional nonadiabatic dynamical methods are not applicable as the computational cost generally grows with the number of states involved and the need to evaluate numerous nonadiabatic couplings between each state. The mean field nature of the Ehrenfest dynamics method provides a route to sidestep these hurdles.

With high intensity, ultrafast laser pulses, many intriguing dynamics in this dense manifold regime are discovered experimentally. We aim at developing a time-dependent configuration interaction (TD-CI)⁷ -based Ehrenfest dynamics method in the present work for simulating such systems. In order to account for light-matter interactions in nonadiabatic dynamics simulations, the time-dependent electronic wave functions are propagated explicitly with an applied external fields in our approach. The time-dependent electronic wave functions are represented as linear combinations of configurational states, where the expansion coefficients are evolved in time as the responses to the external field. As a result, the TD-CI wave functions can be deemed as the weighted sums of adiabatic electronic states, avoiding the explicit calculations of the dense manifold of electronic states. The intramolecular coordinates are

subjected to the mean field potential generated by the TD-CI wavefunction, hence the ions move according to the mean force acting on them. In this work, we develop Ehrenfest dynamics in conjunction with time-dependent complete active space configuration interaction method (TD-CASCI-Ehrenfest) as a first step toward modeling dense manifold systems. Although excitations from active space to high-lying virtual orbitals are required for processes including high-lying states, e.g. ionization process, we noted that the extension to Ehrenfest dynamics with time-dependent multireference configuration interaction singles (TD-MRCIS-Ehrenfest) is straightforward when the force generated from the TD-MRCIS electronic wave function can be evaluated efficiently. The detailed algorithms of the TD-CASCI-Ehrenfest method are explained in the method section.

7.2 Method

In this work, we developed a nonadiabatic Ehrenfest dynamics method that can be applied to elucidate laser-induced dynamics. The electronic dynamics are propagated with the TD-CASCI method, and the molecular dynamics are simulated using the velocity Verlet (VV) algorithm, where the forces experienced by the molecules are generated from the TD-CASCI wave functions (TD-CASCI-Ehrenfest). Noting that the electrons move much faster than the nuclei, we employed two time step sizes $\Delta\tau$ and Δt for the electronic and nuclear dynamics, respectively, in which $\Delta\tau \ll \Delta t$. Given an initial geometry \mathbf{R}_0 , an initial momentum \mathbf{p}_0 , and an electronic wavefunction Ψ , the algorithm for the TD-CASCI-Ehrenfest approach can be outlined in the following and is summarized in the Figure 7.1. The detailed descriptions of the algorithm are presented in the following paragraphs and the cited references therein.

(i). Calculate the force $\mathbf{F} = -\frac{d}{d\mathbf{R}}\langle\Psi|\mathbf{H}|\Psi\rangle$.

(ii). Propagate the momentum with $\mathbf{p}_{\frac{\Delta t}{2}} = \mathbf{p}_0 + \frac{1}{2}\mathbf{F}\Delta t$ (or $\mathbf{p}_{t+\frac{\Delta t}{2}} = \mathbf{p}_{t-\frac{\Delta t}{2}} + \mathbf{F}\Delta t$ for $t \neq 0$)

(iii). Propagate the position with $\mathbf{R}_{\Delta t} = \mathbf{R}_0 + \frac{\mathbf{p}_{\frac{\Delta t}{2}}}{m}\Delta t$ (or $\mathbf{R}_{t+\Delta t} = \mathbf{R}_t + \frac{\mathbf{p}_{t+\frac{\Delta t}{2}}}{m}\Delta t$ for $t \neq 0$)

(iv). Obtain the orbitals at new geometry $\mathbf{R}_{\Delta t}$ (or $\mathbf{R}_{t+\Delta t}$).

- (v). Diabatize the orbitals to have largest overlap with orbitals from previous molecular time step Δt (describe below).
- (vi). Use the new set of orbitals to build the electronic Hamiltonian and start TD-CASCI propagation for the electronic wavefunction Ψ with time steps $\Delta \tau$.
- (vii). Repeat steps (i)-(vi) until the desired propagation time reached.

The initial condition for the position and momentum ($\mathbf{R}_0, \mathbf{p}_0$) can be sampled from a Wigner distribution corresponding to the ground vibrational state in the harmonic approximation or from classical molecular dynamics simulations on the ground state. With the initial \mathbf{R}_0 , the initial electronic wave function is obtained by a user-selected CASCI approach such as Hartree-Fock CASCI (HF-CASCI), the floating occupation molecular orbital CASCI (FOMO-CASCI)⁸⁻⁹ or the configuration interaction singles natural orbital CASCI (CISNO-CASCI),¹⁰⁻¹¹ in which the HF, FOMO and CISNO methods are the orbital determination approaches for the CASCI method. To calculate the force at each nuclear coordinate (step (i)),

$$\mathbf{F} = -\frac{d}{d\mathbf{R}} \langle \Psi | \mathbf{H} | \Psi \rangle. \quad (1)$$

Notice that the wave function is a complex vector in the TD-CASCI,

$$\Psi = \mathbf{q} + i\mathbf{p}. \quad (2)$$

As a result, the separation of the calculations of the force which are contributed from the real and imaginary parts of the wave function (CI vector) is performed,

$$\mathbf{F} = -\frac{d}{d\mathbf{R}} \langle \Psi | \mathbf{H} | \Psi \rangle = -\left(\frac{d}{d\mathbf{R}} \langle \mathbf{q} | \mathbf{H} | \mathbf{q} \rangle + \frac{d}{d\mathbf{R}} \langle \mathbf{p} | \mathbf{H} | \mathbf{p} \rangle \right). \quad (3)$$

The analytical energy gradients for the HF-CASCI, FOMO-CASCI, and CISNO-CASCI methods can be obtained from the GPU-accelerated implementations,^{8, 10} where the equation (42) in reference 8 or the equation (56) in reference 10 are employed, depends on which CASCI method is applied. Note that the real and imaginary parts of the CI vectors along with other parameters (parameters that define the wave functions and depend on \mathbf{R} , but are not propagated by the TD-CASCI method, e.g. the orbital coefficients matrix $\mathbf{C}_{\mu p}$ for all three CASCI methods or the configuration interaction singles eigenvectors for the CISNO-CASCI method) are used for the analytical energy gradient calculations. After the force is calculated, the VV algorithm (steps (ii) and (iii)) is performed to update the momentum and position for the nucleus.¹² With the new

nuclear geometry $\mathbf{R}_{t+\Delta t}$, the selected orbital determination scheme (HF, FOMO or CISNO) is applied for a new set of orbitals (step (iv)). The electronic structure changes when the nuclear geometry is updated. In order to account for the electronic structure which is coupled to the nuclear motion, an orbital diabaticization scheme that is described as following equations is performed (step (v)).

$$\psi'_{i,t+\Delta t} = \sum_j c_j^i \psi_{j,t+\Delta t}, \quad (4)$$

in which the orbitals $\psi_{j,t+\Delta t}$ are rotated to a new set of orbitals $\psi'_{i,t+\Delta t}$ with the following constrain

$$\langle \psi'_{i,t+\Delta t} | \psi_{j,t} \rangle = 0 \text{ for } i \neq j. \quad (5)$$

As a result, the coefficients c_j^i can be obtained from

$$c_j^i = \langle \psi_{j,t+\Delta t} | \psi_{i,t} \rangle. \quad (6)$$

Overall, the orbital diabaticization scheme can be written with the coefficient matrices C and the overlap matrix $S_{\mu\nu}(t + \Delta t | t)$ between basis functions at time $t + \Delta t$ and time t ,

$$C'_{\mu i}(t + \Delta t) = C_{\mu j}(t + \Delta t) C_{\mu j}^\dagger(t + \Delta t) S_{\mu\nu}(t + \Delta t | t) C_{\nu i}(t). \quad (7)$$

In equation (4), the i, j denote for the molecular orbitals in the active space and μ, ν denote for the atomic basis sets. With the new set of molecular orbitals and applied external field, the electronic Hamiltonian is built and the electronic degrees of freedom are propagated via the TD-CASCI method (step (vi)). Steps (i)-(vi) are repeated until the desired propagation time is reached. The TD-CASCI-Ehrenfest dynamics method is implemented in the TeraChem software package.⁷⁻¹⁴ The extension of this approach to the TD-MRCIS-Ehrenfest will be straightforward when the analytical energy gradient of the MRCIS method (or other efficient means for retrieving the forces from the MRCIS method) is available. In addition, schemes for correcting the Ehrenfest dynamics method for decoherence in the dense manifold regime are being developed in the Levine's group.

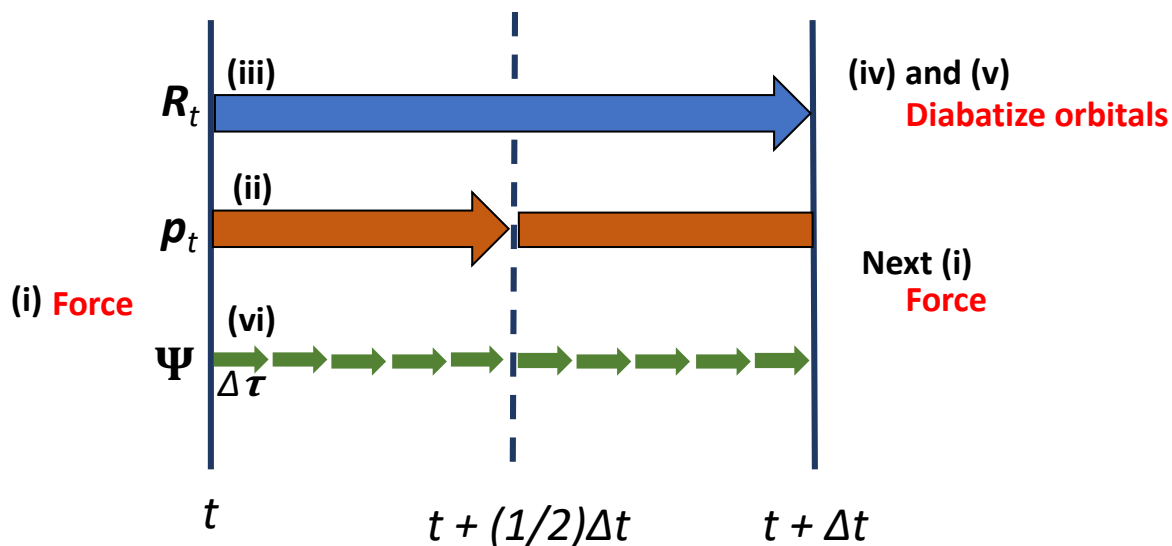


Figure 7.1. The schematic representation of the Ehrenfest dynamics algorithm. The steps (i)-(vi) mentioned in the text are labeled. The orange and blue arrows indicate the velocity-Verlet algorithm with time steps Δt for propagating momentum and position respectively. The smaller green arrows indicate the time steps $\Delta\tau$ for propagating electronic dynamics in the TD-CI calculations. For the feedback between electronic and nuclear dynamics, the force calculation and orbital diabatization (both indicated in red words) are performed.

REFERENCES

REFERENCES

1. Ben-Nun, M.; Quenneville, J.; Martinez, T. J., Ab initio multiple spawning: Photochemistry from first principles quantum molecular dynamics. *J Phys Chem A* **2000**, *104*, 5161-5175.
2. Levine, B. G.; Coe, J. D.; Virshup, A. M.; Martinez, T. J., Implementation of ab initio multiple spawning in the MOLPRO quantum chemistry package. *Chem Phys* **2008**, *347*, 3-16.
3. Tully, J. C., Molecular-Dynamics with Electronic-Transitions. *J Chem Phys* **1990**, *93*, 1061-1071.
4. Parandekar, P. V.; Tully, J. C., Mixed quantum-classical equilibrium. *J Chem Phys* **2005**, *122*, 094102.
5. Andrade, X.; Castro, A.; Zueco, D.; Alonso, J. L.; Echenique, P.; Falceto, F.; Rubio, A., Modified Ehrenfest Formalism for Efficient Large-Scale ab initio Molecular Dynamics. *J Chem Theory Comput* **2009**, *5*, 728-742.
6. Hack, M. D.; Truhlar, D. G., Nonadiabatic trajectories at an exhibition. *J Phys Chem A* **2000**, *104*, 7917-7926.
7. Peng, W. T.; Fales, B. S.; Levine, B. G., Simulating Electron Dynamics of Complex Molecules with Time-Dependent Complete Active Space Configuration Interaction. *J Chem Theory Comput* **2018**, *14*, 4129-4138.
8. Hohenstein, E. G.; Bouduban, M. E. F.; Song, C. C.; Luehr, N.; Ufimtsev, I. S.; Martinez, T. J., Analytic first derivatives of floating occupation molecular orbital-complete active space configuration interaction on graphical processing units. *J Chem Phys* **2015**, *143*, 014111.
9. Slavicek, P.; Martinez, T. J., Ab initio floating occupation molecular orbital-complete active space configuration interaction: An efficient approximation to CASSCF. *J Chem Phys* **2010**, *132*, 234102.
10. Fales, B. S.; Shu, Y. N.; Levine, B. G.; Hohenstein, E. G., Complete active space configuration interaction from state-averaged configuration interaction singles natural orbitals: Analytic first derivatives and derivative coupling vectors. *J Chem Phys* **2017**, *147*, 094104.
11. Shu, Y. A.; Hohenstein, E. G.; Levine, B. G., Configuration interaction singles natural orbitals: An orbital basis for an efficient and size intensive multireference description of electronic excited states. *J Chem Phys* **2015**, *142*, 024102.

12. Ufimtsev, I. S.; Martinez, T. J., Quantum Chemistry on Graphical Processing Units. 3. Analytical Energy Gradients, Geometry Optimization, and First Principles Molecular Dynamics. *J Chem Theory Comput* **2009**, *5*, 2619-2628.
13. Fales, B. S.; Levine, B. G., Nanoscale Multireference Quantum Chemistry: Full Configuration Interaction on Graphical Processing Units. *J Chem Theory Comput* **2015**, *11*, 4708-4716.
14. Song, C. C.; Wang, L. P.; Martinez, T. J., Automated Code Engine for Graphical Processing Units: Application to the Effective Core Potential Integrals and Gradients. *J Chem Theory Comput* **2016**, *12*, 92-106.